IECM Technical Documentation Updates

Final Report

DE-AC26-04NT41917

November 2009

Disclaimer

This report was prepared as an account of work sponsored by an agency of the United States Government. Neither the United States Government nor any agency thereof, nor any of their employees, makes any warranty, express or implied, or assumes any legal liability or responsibility for the accuracy, completeness, or usefulness of any information, apparatus, product, or process disclosed, or represents that its use would not infringe privately owned rights. Reference therein to any specific commercial product, process, or service by trade name, trademark, manufacturer, or otherwise does not necessarily constitute or imply its endorsement, recommendation, or favoring by the United States Government or any agency thereof. The views and opinions of authors expressed therein do not necessarily state or reflect those of the United States Government or any agency thereof.

IECM Technical Documentation Updates
Final Report

_____

DE-AC26-04NT41917

RDS Subtask 404.01.03:
Development and Application of the Integrated Environmental Control Model

Prepared for:

Office of Systems, Analyses and Planning
National Energy Technology Laboratory
Department of Energy
Pittsburgh, PA 15236
www.netl.doe.gov

Prepared by:
Michael B. Berkenpas
Karen Kietzke
Hari Mantripragada
Sean McCoy
Edward S. Rubin (PI)
Peter L. Versteeg
Haibo Zhai

Carnegie Mellon University
Pittsburgh, PA 15213
www.iecm-online.com

November 2009

This document brings together the five Technical Reports prepared under this contract to document enhancements made to the Integrated Environmental Control Model (IECM). Additional documentation of the model prepared under previous contracts is available at the IECM Web site: http://www.iecm-online.com.

Table of Contents

IECM Technical Documentation: Volume I
Wet Cooling Tower

DE-AC26-04NT41917

November 2009

NETL

Disclaimer

IECM Technical Documentation: Volume I
Wet Cooling Tower

_____

DE-AC26-04NT41917

RDS Subtask 404.01.03:
Development and Application of the Integrated Environmental Control Model

Prepared for:

Office of Systems, Analyses and Planning
National Energy Technology Laboratory
Department of Energy
Pittsburgh, PA 15236
www.netl.doe.gov

Prepared by:
Haibo Zhai
Michael B. Berkenpas
Edward S. Rubin
Carnegie Mellon University
Pittsburgh, PA 15213
www.iecm-online.com

November 2009

Table of Contents

List of Figures

List of Tables

Acknowledgements

Wet Cooling Tower

Nomenclature

A_V = surface area of water droplets (sq ft per cu ft)

c_w = specific heat of water, Btu per (lb) (^{o}F)

$c_{p,a}$ = specific heat at constant pressure of moist air, Btu per (lb of dry air) (^{o}F)

$C_{blowdown}$ = concentration of traces in tower blowdown (mg/l)

C_{cs} = concentration of traces in cooling water (mg/l)

C_{drift} = concentration of traces in drift loss (mg/l)

C_{evap} = concentration of traces in evaporation water (mg/l)

C_{makeup} = concentration of traces in makeup water (mg/l)

CC = cycle of concentration for cooling system

Cw_{heat} = steam cycle heat rejected to the cooling system (Btu/hr)

h = enthalpy of moist air, Btu per lb of dry air

h_c = convection heat transfer coefficient, Btu per (hr) (sq ft) (^{o}F)

h_D = convection mass transfer coefficient, lb_w per (hr) (sq ft) (lb_w per lb_a)

h_f = specific enthalpy of saturated liquid water, Btu per lb; $h_{f,w}$ evaluated at t_w

h_g = specific enthalpy of saturated water vapor, Btu per lb; $h_{g,w}$ evaluated at t_w

$h_{fg,w}$ = $h_{g,w} - h_{f,w}$, Btu per lb

Hr_s = steam cycle heat rate not including auxiliary power requirements (Btu/kWh)

Le = Lewis number, dimensionless

m_a = mass rate of flow of dry air (tons/hr)

$m_{blowdown}$ = cooling tower blowdown (tons/hr)

m_{drift} = cooling tower drift loss (tons/hr)

m_{evap} = cooling tower evaporation loss (tons/hr)

m_{makeup} = makeup water for the cooling tower system (tons/hr)

m_w = recirculation cooling water (tons/hr)

MWg = plant (steam-side) gross electrical output (MW)

t = dry-bulb temperature of moist (^{o}F)

t_w = temperature of water (^{o}F)

$t_{w,i}$ = inlet water temperature for cooling tower (^{o}F)

$t_{w,o}$ = outlet water temperature for cooling tower (^{o}F)

t_{wet} = air wet bulb temperature (^{o}F)

ΔT_w = temperature drop range of cooling water across the condenser (^{o}F)

V = volume (cu ft)

V_{cw} = cooling water flow (gpm)

W = humidity ratio of moist air, lb of water vapor per lb of dry air

$W_{s,w}$ = humidity ratio of saturated moist air at t_w, lb of water vapor per lb of dry air

W_1 = tower inlet moist air humidity ratio, lb of water vapor per lb of dry air

W_2 = tower outlet moist air humidity ratio, lb of water vapor per lb of dry air

α = water-air ratio of flow rate for the cooling water versus tower inlet air

η_{aux} = heat load for auxiliary equipment as a percentage of condenser rejected heat (%)

ε = tower performance efficiency (%)

MWh = megawatt - hours

Abstract

Thermoelectric power plants require significant quantities of cooling water to support electricity generation. The largest design impact of the Clean Water Act, Section 316(b) regulation is to promote the wide use of cooling towers in most new power plants. The principal objective of this study is to systematically evaluate the performance and cost of cooling water systems equipped with wet cooling towers for pulverized coal (PC) and integrated gasification combined cycle (IGCC) power plants.

The effects of individual components in a PC or IGCC plant on performance and cost of the cooling system are investigated. In addition to case studies, this system-level analysis explores a broad range of net plant size for three major PC plant types: subcritical, supercritical and ultra-supercritical plants. Average makeup water consumption usage normalized by net plant size is 565 gallons per MWh, 506 gallons per MWh, and 420 gallons per MWh for subcritical, supercritical, and ultra-supercritical PC plants, respectively. Total plant costs (TPCs) normalized by net electricity output range from $54 per kW to $72 per kW for the cooling system in the three types of PC plants. For the GE-based IGCC plant, makeup water usage is 265 gallons per MWh and the TPC is $35 per kW, while for the Shell-based IGCC case, makeup water required is 327 gallons per MWh and the TPC is $43 per kW. Makeup water required and capital costs of cooling systems are therefore smaller for IGCC plants than those for PC plants.

Meteorology affects evaporation loss. The tower evaporation loss shows seasonal patterns. However, evaporation loss estimation for the cooling tower based on annual average air temperatures may well represent overall annual evaporation loss. Because of this importance, normalized makeup water usage is recommended as a key water consumption factor in water resource planning for thermal power generation.

Introduction

Thermoelectric power plants require significant quantities of water for generating electrical energy. Thermoelectric generation accounted for approximately 39% of freshwater withdrawals as an industry, ranking only slightly behind agricultural irrigation as the largest source of freshwater withdrawals in the United States in 2000 (Feeley *et al.*, 2006a; NETL, 2007a). Large amount of water in thermoelectric power plants is primarily used for cooling purpose in the main steam condenser and auxiliary cooling equipment, standard equipment used to support the generation of electricity (Feeley *et al.*, 2008).

Surface water is a major supply source of thermoelectric-power water consumption (USGS, 2008). Regulation of cooling water intake structures, established under the CWA Section 316(b) requires that the location, design, construction and capacity of cooling water intake structures reflect the best technology available for minimizing adverse environmental impact (EPA, 2008). The largest design impact of 316(b) compliance is that most new power plants will be required to implement closed-loop cooling systems. Because the Clean Water Act (CWA) requires the regulation of water thermal discharge from cooling water systems (EPA, 2008), the current use of the once-through cooling system may be replaced by a wider use of cooling towers (Feeley *et al.*, 2006a; Feeley *et al.*, 2006b). As part of the cooling system of a power plant, cooling towers are generally used to dissipate large heat loads to the atmosphere and lower the temperature of the recirculating cooling water used for condensers and heat exchangers. Because if its importance, the evaluation on the performance and cost of cooling systems in general and cooling towers in particular are needed to understand the implications on water resource planning for thermal power plants.

The Electric Power Research Institute (EPRI)'s PISCES model was designed to estimate toxic emissions from coal-based power plants to air, water and land (EPRI, 1999). It considers water use in and around major components of PC power plants. Recently, the U.S. Department of Energy's (DOE) National Energy Technology Laboratory (NETL) conducted a broad water usage and loss study for integrated gasification combined cycle (IGCC) and pulverized coal (PC) power plants (NETL, 2007b). In this baseline study for fossil energy plants, makeup water usage and costs were estimated (NETL, 2007c). However, makeup water usage estimates for the cooling system in the PISCES and NETL studies were both based on the simplified empirical assumption for evaporation water losses instead of detailed water-air mass and thermal balance simulation for cooling towers (Bedillion *et al.*, 1997; NETL, 2007b; NETL, 2007c). These studies did not sufficiently reflect the impacts of variations for many factors including water temperature drop range, boiler type, and air dry and wet bulb temperatures on cooling system performance.

The majority of cooling towers utilize freshwater as their makeup water, which has water quality requirements to minimize operating problems such as scaling, corrosion and biological fouling (EPRI, 1982). Makeup water typically contains soluble minerals and low concentrations of organic compounds, depending on the source water quality. These constituents control the allowable operating chemical concentration of cooling tower, water consumption and wastewater generation (EPRI, 2003). Therefore, performance assessments for the cooling system should take into account the inherent relationship between water usage and water quality.

Objectives

The major objectives of this study are to:

1. systematically establish water performance models of cooling systems in coal-based PC and integrated gasification combined-cycle (IGCC) power plants and evaluate water usage and loss issues

2. estimate the cooling system costs corresponding to their performance

3. address the impacts of some key factors including the effects of power generation technology and meteorology on cooling system performance and cost

The performance and cost models will be incorporated into the Integrated Environmental Control Model (IECM) developed by Carnegie Mellon University for the NETL. The IECM is a computer-modeling program that performs systematic cost and performance analyses of environmental control equipment at coal-fired power plants (Rubin *et al.*, 2007). The addition of cooling water models will enable IECM users to evaluate the performance and cost of a power plant with sensitivity to the presence of the cooling water system.

Performance Model

An evaluation of the performance of a cooling water system begins by determining the flow rate of the recirculating cooling water, then estimates various water usage and losses based on mass and energy balances, and finally an analysis of the water quality around the cooling system. Capital costs and annual operation and maintenance (O&M) costs for cooling water systems can then be estimated based on the performance modeling results. The explicit linking of performance parameters to cost models is an important aspect of the integrated structure of the IECM.

Recirculating Water in Cooling System

A typical power plant contains two important water systems: (1) a recirculating steam cycle system and (2) a cooling water system. In the PC plant, water in the steam cycle is used to capture heat generated during combustion by converting water to steam. In the IGCC plant, hot exhaust from a gas turbine is fed to a heat recovery steam generator where heat is recovered to generate steam. The high energy steam is transported to the steam turbine, where the latent heat in steam is converted to electrical energy as it passes through. However, not all the latent heat is recoverable, resulting in a low quality steam exiting the steam turbine. This low quality steam must be condensed back into a liquid before being recirculated back to the boiler. This conversion of low quality steam to water is done in the condenser, where the latent heat is taken from the steam and passed to the cooling water system. The heat transferred to the cooling system results in a temperature increase, which must be reduced before being recirculated back into the condenser.

In the condenser, the latent heat of the turbine exhaust steam is transferred to the cooling water. The calculation of flows for the cooling system begins with the heat rejected in the condenser. A lesser amount of heat being rejected from other parts of the power plant by auxiliary equipment is also considered here. For a given type of power plant, the amount of heat that must be rejected to the cooling system, excluding the heat rate of 3413 Btu per kWh used for generating electricity, is estimated as (Bedillion *et al.*, 1997):

$$Cw_{heat} = (Hr_s - 3413) \cdot MW_g \cdot 1000 \cdot (1 + \eta_{aux}) \tag{1}$$

where

Hr_s = the steam cycle heat rate, determined by the thermal efficiency of the Rankine cycle

1000   = converts MW to kW

η_{aux} = the fraction of the total steam cycle load required for auxiliary cooling

Considering the temperature drop possible across the cooling tower, the recirculating water flow rate for the cooling system can now be calculated:

$$m_w = \frac{Cw_{heat}}{\Delta T_w \cdot 2000} \tag{2}$$

Water Balance around Wet Cooling Tower

A majority of the cooling water is recirculated through the cooling tower and back to the condenser. However, water losses can occur in three areas: (1) evaporation, (2) drift, and (3) blowdown. The losses are mainly from the evaporation and blowdown.

Most of the water losses are due to evaporation of the cooling water itself. In wet cooling towers, water has direct contact with ambient air and cooling is achieved mainly by the evaporation process in which some of the water

leaves with the air. In case studies performed by NETL, evaporative loss is empirically estimated as 0.8% of the circulating water flow rate per 10°F of range (NETL, 2007b; NETL, 2007c).

Because water evaporated in the cooling tower consists of pure water, the concentration of salts or other impurities will increase in the recirculating water. To avoid a high concentration and subsequent scaling of the surface within the tower, it is necessary to blow down a portion of the water and replace it with fresh water (Li and Priddy, 1985). Tower blowdown water may be reused in the power plant to sluice bottom ash or fly ash.

A relatively small amount of entrained water lost as fine droplets in the air discharge from a tower, which is frequently referred to as tower drift loss. The drift loss is about 0.001% of the recirculating water (NETL, 2007c). Total water loss depends on the water-cooling range.

The cooling tower operation is maintained by making up fresh water at the same rate as the water losses from the tower. Based on water mass balance for the cooling tower, total tower makeup water is:

$$m_{makeup} = m_{evap} + m_{drift} + m_{blowdown} \qquad (3)$$

All these loss terms may be empirically expressed as a percentage of the recirculating water flow rate. In addition, the amount of chemical components and impurities in the losses is equal to that in the makeup water. The mass balance of chemical traces dissolved in water for the cooling tower is expressed as:

$$m_{makeup} \cdot C_{makeup} = m_{evap} \cdot C_{evap} + m_{drift} \cdot C_{drift} + m_{blowdown} \cdot C_{blowdown} \qquad (4)$$

Since the concentrations of all impurities in the evaporation water are assumed to be zero ($C_{evap} = 0$), and the concentrations of impurities dissolved in drift and blowdown losses are equal to those for the cooling water ($C_{drift} = C_{blowdown} = C_{cs}$), rearranging Equation (4) above gives:

$$CC = \frac{C_{cs}}{C_{makeup}} = \frac{m_{makeup}}{m_{drift} + m_{blowdown}} = 1 + \frac{m_{evap}}{m_{drift} + m_{blowdown}} \qquad (5)$$

The term CC is called the cycle of concentration. It is a measure of the number of times water recirculates before being removed from the cooling water as blowdown. From Equation (5), the tower blowdown loss is estimated as:

$$m_{blowdown} = \frac{m_{evap}}{CC - 1} - m_{drift} \qquad (6)$$

As implicated in Equation (6), the evaporation process is the largest source of cooling tower water losses, which is estimated based on the mass and energy balance model described in the next section. The operation at a higher cycle of concentration reduces cooling tower blowdown. However, there is a strict requirement for water quality, and the complex makeup water treatment processes may have to be applied, which increases the cost of water use. The cycle of concentration reflects the effect of water quality on makeup water usage, which is determined through water quality analysis for makeup water.

Water Evaporation Loss

A more detailed tool will be established to accurately estimate evaporation loss, as evaporation is the largest source of water loss. A schematic diagram for counter-flow cooling tower is given in Figure 1(Threlkeld, 1970). In a counter-flow cooling tower, air flows upward: opposite to the downward motion of the water. Wet cooling towers mainly rely on the latent heat of water evaporation to exchange heat between the process and the air passing through the cooling tower, although there is some sensible heat transfer to the air when the air temperature is low. Water temperature decreases whereas the moisture content of the air passing through the cooling tower increases. In practice, the change range of inlet and outlet water temperatures is generally 10 to 30°F for wet cooling towers (McCabe *et al*., 2001).

A mathematical model based on mass and energy balance has been established for wet cooling towers. Major assumptions that derive the basic modeling process under steady-flow conditions for a wet counter flow cooling tower are:

- ignore heat transfer through the walls of the tower

- constant water and dry air specific heats

- constant heat and mass transfer coefficients throughout the tower

- uniform temperature throughout the water stream at any cross-section

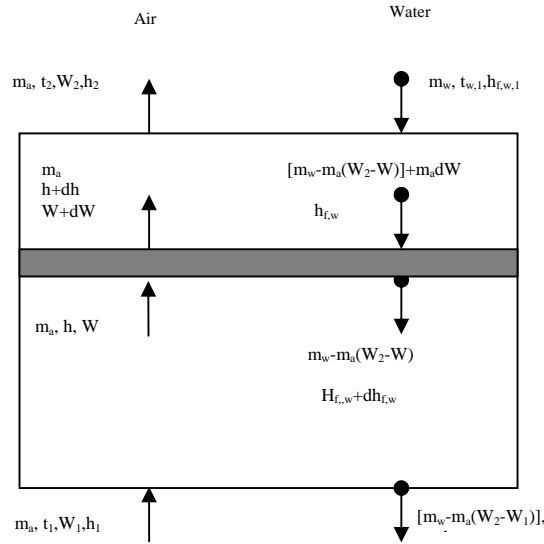- constant value of Lewis number through the tower

Figure 1. Schematic diagram of counterflow wet cooling tower (Threlkeld, 1970)

The following equation is based on steady-state energy and mass balances for the differential volume segment (Threlkeld, 1970):

$$m_a dh = -[m_w - m_a(W_2 - W)]dh_{f,w} + (m_a dW)h_{f,w}$$ (7)

or approximately

$$m_a dh = -m_w dh_{f,w} + (m_a dW)h_{f,w}$$ (8)

Also, the water energy balance can be written in terms of heat- and mass- transfer coefficient as:

$$-m_w dh_{f,w} = h_c A_V dV(t_w - t) + h_D A_V dV(W_{s,w} - W)h_{fg,w}$$ (9)

and the air-side water-vapor mass balance as:

$$m_a dW = h_D A_V dV(W_{s,w} - W)$$ (10)

By substitution of $Le = \dfrac{h_c}{h_D c_{p,a}}$ in Equation (9), we can rewrite it as:

$$-m_w dh_{f,w} = h_D A_V dV[Le\, c_{p,a}(t_w - t) + (W_{s,w} - W)h_{fg,w}]$$ (11)

Combining and rearranging Equations (8), (10) and (11), we get :

$$\frac{dh}{dW} = Le\, c_{p,a}\frac{(t_w - t)}{W_{s,w} - W} + h_{g,w}$$ (12)

Because of (Threlkeld, 1970)

$$h_{s,w} - h = c_{p,a}(t_w - t) + 1061(W_{s,w} - W) \tag{13}$$

Equation (12) may then be written as:

$$\frac{dh}{dW} = Le\,\frac{\left(h_{s,w} - h\right)}{\left(W_{s,w} - W\right)} + \left(h_{g,w} - 1061Le\right) \tag{14}$$

Equation (14) describes the condition line on the psychometric chart for the changes in state of moist air passing through the tower. In other words, this equation describes the state of the moist air passing through the tower (Qureshi et al, 2006). When the inlet water temperature, temperature drop range of cooling water, water flow rate, air flow rate or water-air flow ratio, and dry and wet bulb temperature of tower inlet moist air under standard atmosphere pressure are known, the outlet state of the air can be determined. Then, the evaporation loss can be calculated according to the inlet and outlet air humidity, and air flow rate. The solution is iterative with respect to the air humidity ratio and temperatures.

The model starts by locating the state of the inlet air and saturated air in equilibrium with the leaving water. The quantity of dh/dW is calculated using Equation (14). The enthalpy of inlet air is then increased by a small amount (Δh) in the second step. The resulting incremental change in water temperature is estimated as (Threlkeld, 1970; Khan *et al.*, 2001):

$$-\Delta t_w = \frac{m_a}{m_w c_w}\left(\Delta h - \Delta W\, h_{f,w}\right) = \frac{1}{\alpha\, c_w}\left(\Delta h - \Delta W\, h_{f,w}\right) \tag{15}$$

In the immediate subsequent step, the state of saturated air in equilibrium with water temperature is determined at this increased water temperature. The procedure is repeated until the water temperature is equal to the water inlet temperature. A computer model has been added to the IECM to perform this procedure. In the model, properties of air-water vapor mixtures and moist air are calculated using the property equations given by the American Society of Heating, Refrigerating, and Air-Conditioning Engineers (ASHRAE) (ASHRAE, 1997). In addition, the Lewis number is estimated based on the method recommended by Kusuda (Kusuda, 1965; Threlkeld, 1970). Once the humidity ratio is determined for inlet and outlet air, the evaporation water loss is:

$$m_{evap} = m_a(W_2 - W_1) \tag{16}$$

Then, the evaporation loss is expressed as a function of the recirculating cooling water:

$$m_{evap} = \frac{m_w}{\alpha} \cdot (W_2 - W_1) \tag{17}$$

In a brief summary, the evaporation loss can be estimated, given inlet and outlet cooling water temperatures, inlet air dry and wet temperatures, inlet air humidity, the recirculating cooling water and water-air mass flow rate ratio[*].

Finally, the cooling tower performance efficiency can be expressed as (Ren, 2006):

$$\varepsilon = \frac{t_{w,i} - t_{w,o}}{t_{w,i} - t_{wet}} \cdot 100\% \tag{18}$$

Effect of Meteorology on Evaporation Loss

The evaporation process is affected by water and air temperatures. The impacts of meteorological conditions on evaporation loss are quantified and evaluated in this section. Local monthly meteorological data from the city of Pittsburgh available from the National Climatic Data Center (NCDC, 2008) is used for these case studies. The monthly mean air dry and wet bulb temperature are 28.1ºF and 26.3ºF in January, whereas dry and wet bulb temperatures are 72.5ºF and 65.5ºF in July. The annual average monthly air dry and wet temperatures are 51ºF and 46ºF. To investigate the effect of monthly air conditions on evaporation loss, the temperature drop range for the cooling tower will be maintained at 20ºF for all scenarios. Since the air wet bulb temperature is the minimum

---

[*] A value of 1.0 will be assumed in this study for the air mass flow ratio

temperature that the cooling water leaving from the cooling tower can reach (Threlkeld, 1970), the temperature of the cooling water entering the cooling tower is supposed to be 90°F in order to maintain the same water temperature drop range for each monthly scenario.

The evaporation loss based on monthly air temperatures is estimated and shown in Figure 2 and Figure 3. As shown in Figure 2, the evaporation loss displays apparent trends that larger loss occurs in summer whereas less loss occurs in winter, which is similar to the finding of other study (Levy *et al.*, 2006). Figure 3 shows the sensitivity of evaporation loss to the temperature approach, defined as the difference between tower outlet water temperature and inlet air wet bulb temperature. Evaporation loss decreases with temperature approach. In summer, the temperature approach becomes low and the cooling tower has high performance efficiency resulting in more evaporation.
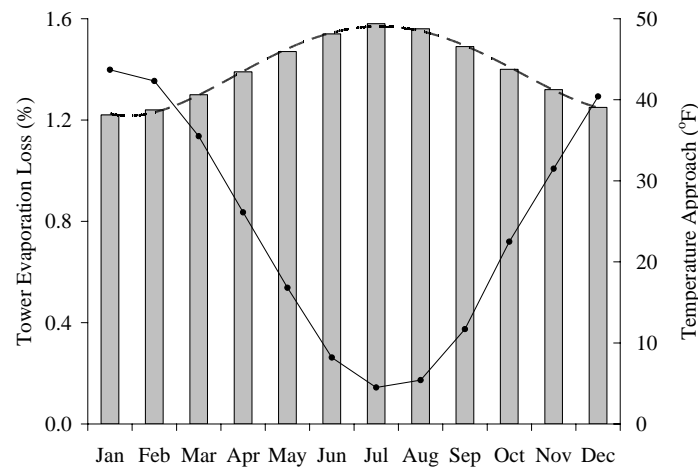

Figure 2. Effect of meteorology on evaporation loss for cooling tower: the effect of monthly air conditions on evaporation loss
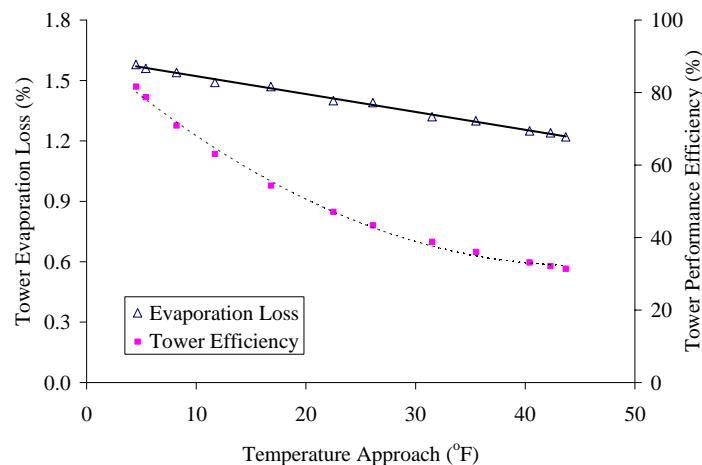
Figure 3. Effect of meteorology on evaporation loss for cooling tower: the effect of temperature approach on evaporation loss

The average monthly evaporation loss shown in Figure 2 is 1.44 percent of the recirculating cooling water. In addition, evaporation loss based on annual average monthly air dry and wet temperatures is estimated to be 1.44 percent of the cooling water, which is almost same as average monthly evaporation loss. This result implies that the estimation of evaporation loss only based on the annual average air temperature may represent the overall evaporation loss for the cooling water system throughout the year.

Water Quality Analysis

Water quality assessment includes three steps:

1. Identify and characterize the source water

2. Evaluate constituents of concern and water quality index

3. Design cooling system operations and water treatment procedures

River water is assumed in this report as the source of makeup water for the cooling system. A representative analysis of raw water based on the Mississippi river that EPRI's Technical Assessment Guide (TAG) provides is adopted in water quality assessment and given in Table 1 (EPRI, 1993). The cooling system may encounter various problems related to water properties such as scaling formation, corrosion and organic growth. Specifically, water quality is typically expressed by the calcium hardness, alkalinity, pH and temperature of makeup water, all of which may produce tower scaling and corrosion problems (Cheremisinoff *et al.*, 1981). EPRI has developed criteria for water chemistry given in Table 1 for cooling tower evaluation (EPRI, 1982; EPRI, 2003). Each chemical constituent that can affect cooling system performance is compared with water chemistry criteria separately to determine its maximum allowable concentration in the cooling system. As shown in Table 1, the minimum ratio of concentration for the criteria versus the raw water is 4.8 for calcium. Therefore, in this study we will designate a cycle of concentration (CC) of 4, which will also be used in the performance modeling for the cooling system operation.

In performing a water quality analysis for the cooling water, the Langelier Saturation Index (LSI) and Ryznar Stability Index (RSI) are often used to predict the scale-forming and corrosion tendencies of cooling water (EPRI, 2003). However, these indices are considered very conservative. They serve as guides rather than as absolute control methods as uneven temperatures exist throughout a cooling system (Cheremisinoff *et al.*, 1981). If the LSI is zero, water is believed to be in chemical balance; if the LSI is positive, scale-forming tendency is indicated; and if the LSI is negative, corrosive tendency is indicated (Cheremisinoff *et al.*, 1981). If the RSI is less than 6.5, the water is scale-forming; if the RSI ranges from 6.5 to 7.0, the water is in a good range; and if the RSI is more than 7.0, the water is corrosive (Cheremisinoff *et al.*, 1981). The LSI for the cooling system is 1.1 under the designed CC when the temperature is assumed to be 80°F, which implies the scaling tendency in the cooling water and thus, requirement of scale inhibitor.

Table 1. Water quality analysis for the cooling water system

Parameter	Unit	Water quality criteria	Makeup water quality [a]	Allowable Cycle of concentration
Calcium (Ca)	$mg/l \ CaCO_3$	900	189	4.8
Magnesium (Mg)	$mg/l \ CaCO_3$	N/A [b]	66.0	
Silica (SiO_2)	mg/l	150	6.8	22.1
Sulfate (SO_4)	$mg/l \ CaCO_3$	N/A [b]	58.0	
$Mg \times SiO_2$	$mg/l \ CaCO_3 \times mg/l$	35,000	448.8	78.0
$Ca \times SO_4$	$(mg/l)^2 \ CaCO_3$	500,000	10,962	45.6
Bicarbonate	$mg/l \ CaCO_3$	N/A [b]	202.0	
pH		7.8-8.4	8.0	
Chloride	mg/l	700	26	26.9
Total dissolved solids	mg/l	70,000	457.0	153.2
Temperature	°F	N/A [b]	40-80	

[a] The alkalinity is assumed to only be bicarbonate alkalinity as no data is available.

[b] Not available.

Chemicals are typically added to the cooling water system to control scaling, corrosion and fouling, which are determined by the dosage of chemicals and the cooling water usage and loss. Acid, usually sulfuric, is added to control the pH and alkalinity concentration of the circulating water for prevention of calcium carbonate scale. Acid is used together with scale inhibitors to simultaneously reduce scale formation. Cooling tower pH is typically maintained at about 8.0 and alkalinity maintained at approximately 150 mg/l as $CaCO_3$ (EPRI, 1992). When the actual influent alkalinity of makeup water is greater than the allowable alkalinity, the makeup water alkalinity is

neutralized with sulfuric acid. At the designed cycle of concentration, the allowable alkalinity in the cooling water is 37.5 mg/l as $CaCO_3$. The excess alkalinity of 164.5 mg/l as $CaCO_3$ should be neutralized.

A biocide such as chlorine or chlorine dioxide is added to prevent biological fouling. For algae and bacterial growth control, the normal amount of chlorine needed is 1 ppm every 4 hours daily, which is equivalent to 0.2 ppm in continuous control (Cheremisinoff *et al.*, 1981).

Calcium carbonate scale formation can be controlled by pH and alkalinity adjustments. It is frequently coupled with the use of scale inhibitors (EPRI, 1982). The phosphonates are effective in $CaCO_3$ inhibition (Vetter, 1971, Nowack, 2003) and used as scale inhibitors at 2 to 10 ppm in cooling water (Cheremisinoff *et al.*, 1981). The loss of phosphonates is due to cooling tower blowdown and drift.

Capital Cost

The total plant cost (TPC) for the cooling system is estimated based on the procedure recommended by EPRI's TAG (EPRI, 1993), consisting of process facility cost (PFC), general facilities capital (GFC), engineering and home office overhead including fees, and project and process contingencies.

NETL estimated the capital costs in 2006 for the cooling system with the 20°F temperature drop range in IGCC and PC power plants in case studies (NETL, 2007c). The cost for the cooling system included cooling tower, circulating water pumps, circulating water system auxiliaries, piping, makeup water system, component cooling water system, and system foundation and structure. In the case studies of PC power plants, project and process contingency costs were about 15% and 0% of PFC, respectively. The GFC was ignored. Based on the NETL's twelve case studies, the regression model of the PFC as a function of the recirculating cooling water is developed as follows:

$$PFC(\$, 2006) = (1.18E+2) \cdot v_{cw} + (4.51E-5) \cdot v_{cw}^2 - (1.56E-10) \cdot v_{cw}^3 \quad (r^2 = 0.978)$$ (19)

Thus, the cost model is directly linked by the amount of the recirculating cooling water determined by the performance model of the cooling water system developed above. In the cost estimate, multiple cooling towers may be required when the recirculating water is more than the maximum value of about 600,000 gallon per minute (gpm).

Assumptions regarding fixed O&M cost are made as follows: total maintenance cost of a cooling system is assumed to be 2% of TPC (EPRI, 2004); and for cooling system operation, there is one job per shift and 4.75 shifts per day. The operating labor rate is $33.0 per hour.

Case Studies

Case studies are illustrated below to evaluate the performance and costs of the cooling systems for pulverized coal-fired (PC) power plants and IGCC plants. Three types of PC plants are included for evaluation and comparison: subcritical, supercritical and ultra-supercritical plants, whereas IGCC plants include GE and Shell types. Environmental controls in the PC plants include selective catalytic reduction, electrostatic precipitator and flue gas desulfurization whereas they include Selexol for hydrogen sulfide control and sulfur plant in the IGCC plants.

The thermal efficiency for the steam cycle is estimated based on the NETL's plant system design (NETL, 2007c). All PC plants with the single reheat employ a boiler and a steam turbine. Power plant performances were modeled using the IECM (Rubin *et al.*, 2007). The air dry and wet bulb temperatures, and the temperatures of the cooling water entering and leaving the tower are assumed to be the same as NETL designed, which are summarized in Table 2. The standard atmosphere pressure is assumed in this study (14.7 psi). The cooling water temperature drop range is 20°F. The tower performance efficiency is 70%. The designed four cycles of concentration are consistent with the setting of the NETL study (NETL, 2007c). The performance and costs of cooling water systems are evaluated under the designed conditions, with the results given in Table 2.

The evaporation loss is 1.5% of the recirculating cooling water flow rate for all types of power plants, which is somewhat less than the NETL's empirical assumption (1.6%) (NETL, 2007b; NETL, 2007c). The total makeup water for the cooling system is 2.0% of the recirculating cooling water flow rate. Makeup water normalized by net electrical output for PC plants changes from 420 gallons per net MWh to 565 gallons per net MWh, which are less

than those estimated by NETL because of NETL's higher evaporation loss and additional cooling duty assumptions (NETL, 2007c). Makeup water required by cooling systems in combined-cycle plants is about 265 gallons per net MWh for GE IGCC plant and 327 gallons per net MWh for Shell IGCC plant. At the designed cycle of concentration, 75% of the makeup water is used to supplement evaporation loss whereas 25% of the makeup water is to supplement the tower blowdown loss. The drift loss is too small and ignored.

The power generation type also affects the amount of makeup water required. Compared to a subcritical power plant, the makeup water consumption decreases by 10% for a supercritical power plant and by 26% for an ultra-supercritical power plant. The water requirements are summarized in Table 2. These results also show that the thermal efficiencies for both the supercritical and ultra-supercritical power plants are higher than those of the subcritical power plant. We can deduce from these results that the heat duties rejected in the cooling systems for supercritical and ultra-supercritical power plants are smaller, compared to subcritical PC plants.

Table 2. Summary for performance of power plant and performance and cost of cooling water systems

Unit Name	Parameter	PC Plants			IGCC Plants	
		Sub.	Super.	Ultra-super.	GE	Shell
Power Plant	Net plant efficiency (%)	35.93	38.25	42.24	35.48	47.04
	Steam Cycle Heat Rate (Btu/kWh)	7790	7359	6705	9000	9000
	Gross Electricity Output (MW)	539.4	536.3	533.0	659.8	733.9
	Net Electricity Output (MW)	500	500	500	571.7	655.8
Air	Dry Bulb Temperature (°F)	60.0	60.0	60.0	60.0	60.0
	Wet Bulb Temperature (°F)	51.5	51.5	51.5	51.5	51.5
Cooling Water	Tower Inlet Temperature (°F)	80.0	80.0	80.0	80.0	80.0
	Tower Outlet Temperature (°F)	60.0	60.0	60.0	60.0	60.0
Cooling System	Evaporation Loss (gpm)	3530	3164	2624	1894	2682
	Blowdown Loss (gpm)	1174	1052	873	630	892
	Drift Loss (gpm)	2	2	2	1	2
	Total Makeup Water (gpm)	4708	4217	3498	2526	3576
	Makeup Water (gallons/ net MWh)	565	506	420	265	327
	Total Plant Cost ($,2007/net kW) [a]	73	66	55	35	43
	Fixed O&M Cost ($,2007/net kW)	2.5	2.4	2.1	1.6	1.6

[a] Assumption: GFC is zero, engineering overhead and home office fee is 9.3% of PFC, and 15% of PFC for contingency cost.

The costs in this study are given in 2007 year dollars and are normalized by net electricity output. The normalized TPC for the cooling system calculated by IECM decrease by 10% for the supercritical power plant and by 25% for the ultra-supercritical power plant, based on the TPC of $73/kW for the subcritical power plant. However, NETL obtained the same value of $68/kW TPC for both subcritical and supercritical PC plants (NETL, 2007c). The differences of the normalized TPC estimates between the NETL result and our study mainly come from the differences in evaporation loss estimate and the cost model residual that could not be explained by the regression model of the PFC based on the NETL case studies. For IGCC plants, the normalized TPC of cooling systems is just about $35/kW for the GE case and $43/kW for the Shell case.

There is a similar relative cost trend for annual O&M costs between the different plant types. In other words, the O&M costs for a subcritical plant is higher than the costs of the supercritical and ultra-supercritical plant types. PC plants have larger O&M costs for cooling systems than IGCC plants.

Effects of Power Plant Type and Size on Performance and Cost

In evaluating performance and estimating cost for the cooling water system, power plant size and power generation technology have to be considered as they directly affect the heat load and the makeup water consumption for the cooling system.

Except for plant size and boiler type, other parameters such air temperature, cooling water temperature and temperature drop range are kept the same as assumed in the case studies above. The makeup water and cost for the cooling system are systematically estimated for each type of PC plant within a range of net plant outputs, as shown in Figure 4 and Figure 6.
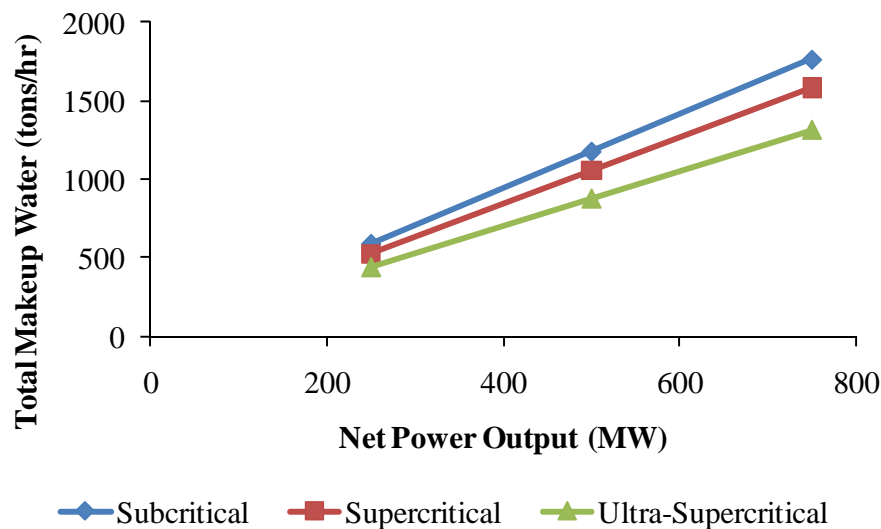

Figure 4. Makeup water consumption for the cooling water system

Figure 4 shows the sensitivity of makeup water usage for the three boiler types to the net plant size. When the net plant size ranges from 250 MW to 750 MW, the makeup water for subcritical PC consistently increases from 590 tons per hour to 1765 tons per hour, which is more than the other two types of power plants at any particular plant size. Although the makeup water usage (gpm) increases with plant size, the normalized makeup water usage does not change with plant size for each type of PC plant. The average normalized makeup water usage as reported by IECM are 565 gallons/MWh, 506 gallons/MWh, and 420 gallons/MWh for subcritical, supercritical, and ultra-supercritical PC plants, respectively, which are all more than makeup water required by cooling system in IGCC plants. These are the same as the findings of the case studies performed and reported by NETL. In summary, the subcritical PC plant consumes the most water, mostly because its low energy efficiency results in more demand of the steam and cooling water flow while generating the same electricity as the other PC plant types.
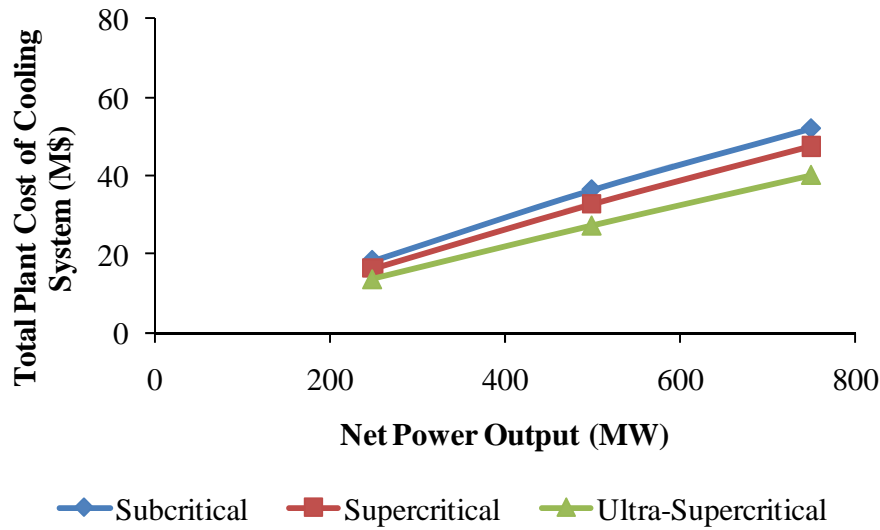
Figure 5. Total absolute value of plant cost for the cooling water system

Figure 5 show the sensitivity of the TPC for a given boiler type as a function of net plant size and boiler type. The TPC monotonically increases with the net plant size for any type of PC plants. Due to larger water consumption, the subcritical PC plant has a higher TPC than the other PC plants for any level of the net plant size.
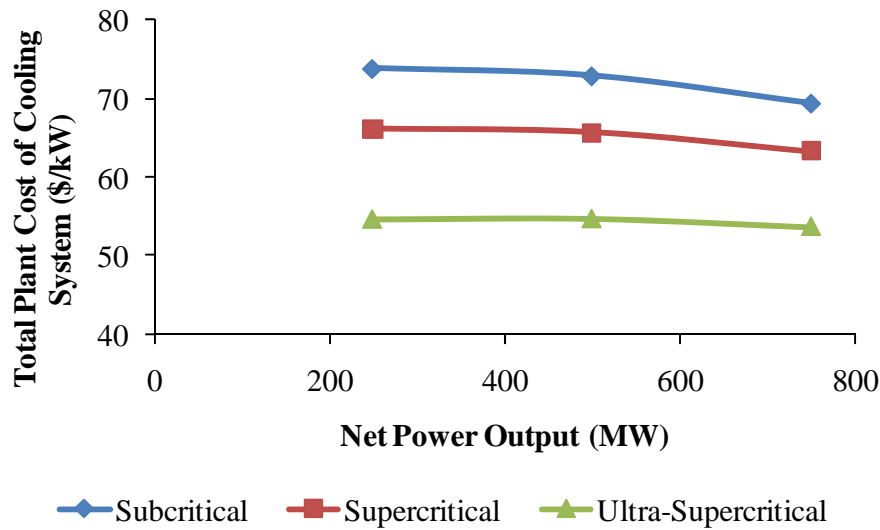

Figure 6. Total normalized plant cost for the cooling water system

The TPC displayed in Figure 5 was normalized by net plant size. Figure 6 shows that the normalized TPC decreases moderately when the net plant size increases from 250 MW to 750 MW. The differences between the maximum and minimum normalized TPCs are $1/kW to $5/kW within the range of net plant sizes for the cooling system. The average normalized TPC across the range of net plant sizes is $72/kW, $65/kW, and $54/kW for subcritical, supercritical and ultra-supercritical PC plants, respectively.

Conclusions

This report systematically evaluates performance and cost of the cooling water system for coal-based power plants. The makeup water for the cooling system is mainly used to supplement the loss due to evaporation and blowdown.

The tower performance affects evaporation loss. The cooling system operation, in particular for blowdown control, cooling water quality, and makeup water usage, is highly related to the quality of source makeup water. High quality of makeup water can decrease blowdown and then reduce makeup water usage. Case studies show the agreement of cooling system performance modeling with the NETL baseline study. Because of higher steam cycle heat rate, the subcritical PC plant requires more recirculating cooling water and makeup water usage, and more costs for the cooling system than supercritical and ultra-supercritical PC plants.

The effects of the plant size and type on performance and cost, and the effects of meteorological conditions on evaporation loss are highlighted. Although the absolute amounts of makeup water usage and cost increase with the net plant size for any type of PC plants, the normalized makeup water does not significantly vary with net plant size, whereas the normalized TPC moderately decreases. Makeup water and capital cost for cooling systems are larger in PC plants than in IGCC plants. The resulting average normalized makeup water usage can be used as water consumption factors in water resource planning for power generation plants. In addition, the cooling tower has higher performance efficiency in summer and results in more evaporation loss. Estimation of evaporation loss for the cooling tower based on annual average air temperatures may be sufficient enough to represent overall annual evaporation loss.

References

ASHRAE. ASHRAE Fundamentals Handbook. American Society of Heating, Refrigerating, and Air-Conditioning Engineers, Inc., 1997.

Bedillion, M.; Berkenpas, M.B.; Kietzke, K.; and Rubin, E.S. PISCES Power Plant Chemical Assessment Model Technical Documentation. Prepared by Carnegie Mellon University for the Electric Power Research Institute, July 1997.

Cheremisinoff, Nicholas P.; Cheremisinoff, Paul N. Cooling Towers Selection, Design and Practice. Ann Arbor Science Publishers, Inc., Ann Arbor, Michigan, 1981.

EPA. Economic and Engineering Analyses of the Proposed 316(b) New Facility Rule. EPA-821-R-00-019, U.S. Environmental Protection Agency, Washington, DC, August 2000.

EPA. Technical Development Document for the Final Regulations Addressing Cooling Water Intake Structures for New Facilities. EPA-821-R-01-036, U.S. Environmental Protection Agency, Washington, DC, November 2001.

EPA. Cooling Water Intake Structures- CWA §316(b). U.S. Environmental Protection Agency. http://www.epa.gov/waterscience/316b/ Accessed on July 7, 2008.

EPRI. Design and Operating Guidelines Manual for Cooling Water Treatment. Report No. EPRI CS-2276, Electric Power Research Institute, Palo Alto, CA, March 1982.

EPRI. Wastewater Treatment Manual for Coal Gasification Combined Cycle Power Plants Volume 2: Process Design and Cost Guide. Report No.TR-101788, Electric Power Research Institute, Palo Alto, CA, December 1992.

EPRI. *TAG™ Technical Assessment Guide: Electricity Supply - 1993,* Volume 1, Rev. 7, Report No. TR-102276, Electric Power Research Institute , Palo Alto, CA, June 1993.

EPRI. PISCES: Power Plant Chemical Assessment Model (3.03): User Documentation; Report No CM-112347, Electric Power Research Institute, Palo Alto, CA, 1999.

EPRI. Water & Sustainability (Volume 3):U.S. Water Consumption for Power Production— The Next Half Century; Report No 1006786, Electric Power Research Institute, Palo Alto, CA, March 2002.

EPRI. *Use of Degraded Water Sources as Cooling Water in Power Plants. Report No.* 1005359, Electric Power Research Institute, Palo Alto, CA, 2003.

EPRI. Comparison of Alternate Cooling Technologies for U.S. Power Plants: Economic, Environmental, and Other Tradeoffs. Report No. 1005358, Electric Power Research Institute, Palo Alto, CA, August 2004.

Feeley III, T. J.; Green, L.; McNemar, A.; Carney, B.A. and Pletcher, S. *Department of Energy/Office of Fossil Energy's Water-Energy Interface Research Program*. DOE/FE's Power Plant Water Management R&D

Program Summary, April 2006a. http://www.netl.doe.gov/technologies/coalpower/ewr/ref-shelf.html#Water. Accessed on July 7, 2008.

Feeley III, T. J.; Pletcher, S.; Carney, B. and McNemar, A. T. *Department of Energy/National Energy Technology Laboratory's Power Plant-Water R&D Program*, 2006b. http://www.netl.doe.gov/technologies/coalpower/ewr/ref-shelf.html#Water. Accessed on July 7, 2008.

Feeley III, T,J.; Skone, T. J.; Stiegel Jr., G. J.; McNemar, A.; Nemeth, M.; Schimmoller, B.; Murphy, James T.; Manfredo, L. Water: A Critical Resource in the Thermoelectric Power Industry. *Energy*, 2008, 33:1-11.

Khan, J.R. and Zubair, S.M. An Improved Design and Rating Analyses of Counter Flow Wet Cooling Towers, *Journal of Heat Transfer*, 123(4), 2001:770-778.

Levy, E.K.; Sarunac, N.; Bilirgen, H.; Caram, H. Use of Coal Drying to Reduce Water Consumed in Pulverized Coal Power Plants. Final Report, Prepared by Leigh University for U.S. Department of Energy, March 2006.

National Climatic Data Center. Local Climatological Data Publication. http://www7.ncdc.noaa.gov/IPS/lcd/lcd.html. Accessed on September 16, 2008.

NETL. National Energy Technology Laboratory. *Estimating Freshwater Needs to Meet Future Thermoelectric Generation Requirements*. DOE/NETL-400/2007/1304, U.S. Department of Energy National Energy Technology Laboratory. September 2007a.

NETL. *Power Plant Water Usage and Loss Study*. U.S. Department of Energy National Energy Technology Laboratory. August 2005, Revised May 2007b.

NETL, *Cost and Performance Baseline for Fossil Energy Plants*. Report DOE/NETL-2007/1281, U.S. Department of Energy National Energy Technology Laboratory. August 2007c.

Nowack, B. Environmental Chemistry of Phosphonates. *Water Research*, 2003, 37(11): 2533-2546.

McCabe, W. L.; Smith, J. C.; Harriott, P. Unit Operations of Chemical Engineering, 6th edition. McGraw-Hill Higher Education, 2001.

Qureshi, B.A.; Zubair, S.M. Prediction of Evaporation Losses in Wet Cooling Towers. Heat Transfer Engineering, 2006, 27(9):86-92.

Ren, C. An Analytical Approach to the Heat and Mass Transfer Processes in Counterflow Cooling Towers, Transactions of the ASME, 2006, 128:1142-1148.

Rubin, E.S.; Berkenpas, M.B.; and Zaremsky, C.J. Integrated Environmental Control Model (IECM) with Carbon Capture and Storage (CCS). Prepared by Carnegie Mellon University for U.S. DOE National Energy Technology Laboratory, Pittsburgh, PA, May 2007.

Threlkeld, J.L. Thermal Environmental Engineering, 2nd edition. Prentice-Hall, Inc., 1970.

U.S. Geological Survey. Thermoelectric-Power Water Use. http://ga.water.usgs.gov/edu/wupt.html Accessed on July 6, 2008.

Vetter, O.J. Evaluation of Scale Inhibitors. Society of Petroleum Engineers of AIME, 8th Permian Basin Oil Recovery Conference. May 6-7 1971, Midland, Tex.

IECM Technical Documentation: Volume II
Air Cooled Condenser

DE-AC26-04NT41917

November 2009

NETL

Disclaimer

This report was prepared as an account of work sponsored by an agency of the United States Government. Neither the United States Government nor any agency thereof, nor any of their employees, makes any warranty, express or implied, or assumes any legal liability or responsibility for the accuracy, completeness, or usefulness of any information, apparatus, product, or process disclosed, or represents that its use would not infringe privately owned rights. Reference therein to any specific commercial product, process, or service by trade name, trademark, manufacturer, or otherwise does not necessarily constitute or imply its endorsement, recommendation, or favoring by the United States Government or any agency thereof. The views and opinions of authors expressed therein do not necessarily state or reflect those of the United States Government or any agency thereof.

IECM Technical Documentation: Volume II
Air Cooled Condenser

_____

DE-AC26-04NT41917

RDS Subtask 404.01.03:
Development and Application of the Integrated Environmental Control Model

Prepared by:
Haibo Zhai
Michael B. Berkenpas
Edward S. Rubin
Carnegie Mellon University
Pittsburgh, PA 15213
www.iecm-online.com

November 2009

Table of Contents

List of Figures

List of Tables

Acknowledgements

Air Cooled Condenser

Nomenclature

a_1, a_2 = functions of the suction Reynolds number

A_c = inside tube area exposed to the condensing steam, m^2

A_{fr} = effective front area, m^2

A_{ti} = inside area of tube per unit length, m

c_{pa} = air specific heat rate, J/kgK

d_e = hydraulic diameter of tube, m

e = effectiveness

h_{ae} = air-side heat transfer coefficient, W/m^{2}K

h_c = condensation heat transfer coefficient, W/m^{2}K

H_t = inside height of tube, m

i_{fg} = heat of the latent, J/kg

k_a = thermal conductivity, W/mK

k_c = condensate thermal conductivity, W/mK

K_c = contraction loss coefficient

K_{sd} = loss coefficient for the steam duct system

L_t = length of finned tube, m

m_a = air flow rate, kg/s

m_c = condensate flow rate, kg/s

n_b = number of bundle per cell

n_{tb} = number of tubes per bundle

Ny = characteristic heat transfer parameter, m^{-1}

ΔP = steam pressure drop, N/m^2

Pr_a = Prandtl number for air

P_{sd} = mean steam pressure out of the turbine considered as backpressure, N/m^2

P_{vi} = mean steam pressure inside the inlet of the finned tubes, N/m^2

$\overline{P}_{vm}$ = mean static pressure in the flattened tubes, N/m^2

Q = cooling duty of air cooled condensers, MWt

Q_a = heat transferred to air, W_t

Q_o = reference cooling duty, 288 MWt

Re_{vi} = Reynolds number

Re_{vn} = normal suction Reynolds number

Ry = characteristic flow parameter, m^{-1}

T_{ai} = inlet air temperature, K

T_{vi} = temperature corresponding to P_{vi}, K

T_{vm} = mean steam temperature corresponding to $\overline{P}_{vm}$, K

U_c = condensate-side overall heat transfer coefficient, W/m^2K

UA = overall heat transfer coefficient for the tubes, W/K

v_{vi} = steam velocity in the tube, m/s

W_t = inside width of tube, m

ρ_c = condensate density, kg/m^3

ρ_{vi} = steam density, kg/m^3

μ_a = air dynamic viscosity, kg/ms

μ_{vi} = steam dynamic viscosity, kg/ms

θ = apex angle of A-frame

σ = the tube inlet contraction area ratio

Abstract

Water use is becoming an important issue at thermoelectric power plants where significant quantities of water are required for the purpose of cooling. The pressure on water resource availability and conservation leads to increasing employment of dry cooling systems in thermoelectric power plants. In order to facilitate preliminary evaluation and policy analysis regarding air-cooled condenser (ACC) technologies, simplified engineering and economic models are developed based on detailed thermodynamic process analyses. The initial temperature difference (ITD) between inlet steam and air is identified as one of significant parameters affecting ACC performance and economics. When ACCs are used, the steam turbine in general operates with a high backpressure. The increase of the backpressure leads to the reduction of steam cycle thermal efficiency with an energy penalty, while higher backpressure leads to increases of ITD and thermal capacity of ACCs. Both dry cooling system size and capital cost significantly vary by a factor of about four over a wide range of ITD generally from 20°F to 80°F. Meanwhile, the capital cost ratios for

ACC versus wet cooling tower technologies vary by a factor approximately from two to six, strongly dependent on ITD, which indicate large capital cost associated with the dry cooling technology.

Introduction

Water use is becoming an important issue at thermoelectric power plants where significant quantities of cooling water are required to condense exhaust steam and support electricity generation. Thermoelectric generation accounted for approximately 39% of freshwater withdrawals as an industry, ranking only slightly behind agricultural irrigation as the largest source of freshwater withdrawals in the United States (U.S.) in 2000 (Feeley et al., 2008). In particular, water use of power plants in water-short or arid regions becomes increasingly contentious. When the U.S. southeast experienced particularly acute drought conditions in August 2007, nuclear and coal-fired plants within the Tennessee Valley Authority system were forced to shut down some reactors as the levels of water resources fall near or below the level of the water intakes drawing cooling water (NETL, 2009). Water demands of power plants have to be met sometime in a water-constraint environment. A conflict of water use may arise among power generation industries and others such as agriculture and residence. The pressure on water resource availability and conservation leads to increasing employment of dry cooling systems in thermoelectric power plants as the dry cooling systems can significantly reduce the cooling water use.

A dry cooling system utilizes the sensible heating of atmospheric air passed across finned-tube heat exchangers to reject heat (EPRI, 2005). There are generally two types of dry cooling systems: direct and indirect. An indirect cooling system condenses the steam in a surface condenser, but the heated cooling water is cooled in an air-cooled heat exchanger, whereas a direct cooling system uses air-cooled condensers (ACCs) to reject exhaust heat (EPRI, 2005). The direct cooling system has been used in power plants of the United States and become much more common in recent years. In the U.S., the total capacity of power plants equipped with ACCs through the end of the 20th century was less than 2500 MWe, whereas the capacity of power plants that ACCs served dramatically increased up to approximately 7000 MWe in 60 power generation units by late 2004 (EPRI, 2005).

Mathematical models were presented to evaluate the performances of the dry cooling systems used in power plants (Conradie and Kroger, 1996). Korger (2004) presented detailed analytical and empirical tools in relevant to designing air-cooled heat exchangers and evaluating their technical performances. Recently, the Electric Power Research Institute (EPRI) compared alternate cooling technologies for U.S. power plants (EPRI, 2002 and EPRI, 2004). The ACC-based dry cooling systems are found to have much higher capital costs requirement than wet cooling tower systems, depending on site location and operation specifications. Capital cost ratio of ACC-based dry cooling system versus wet cooling tower ranges from 4.5 at a hot arid site to about 3.5 at more moderate sites in the combined-cycle power plants (EPRI, 2004). Design, specification, and operation guidelines of the ACC were also presented by EPRI to offer perspective on the most important economic and performance issues (EPRI, 2005). The guidelines indicate that the choices of backpressure and ambient temperature essentially determine the ACC design size and cost for a given heat load. Most steam turbines in plants equipped with ACCs are restricted to operating at backpressures below 8.0 inch mercury (Hg_a). Dry system performance decreases as air dry bulb temperature increases. Under high air temperature conditions coincident with peak summer loads, dry cooling can impose a substantial energy penalty on the system. The performance design of the dry cooling system is frequently characterized by the initial temperature difference (ITD) between condensing temperature and inlet air temperature. The design choices of ITDs are reported to be mostly in the mid-40°F range for modern ACCs (EPRI, 2005).

Although sophisticated thermodynamic models are available for ACCs, those design processes are much more complicated as detailed geometrical dimensions of heat exchangers and fans have to be provided and various heat transfer parameters or relationships and energy loss coefficients have to experimentally measured, prior to thermodynamic simulation. In order to facilitate preliminary evaluation and policy analysis regarding dry cooling technologies used in power plants, simplified engineering and economic tools are needed. The objectives of this study are therefore to:

1. develop simplified technical models or tools to investigate the performance of the ACC-based dry cooling system for coal-based power plants

2. identify key factors and quantify the impacts of their operation designs on the ACC performance and cost

The simplified models incorporate key processes and are developed based on detailed thermodynamic process analyses. The performance and cost models will be incorporated into the Integrated Environmental Control Model (IECM) developed by Carnegie Mellon University for the NETL. IECM is a computer-modeling program that performs systematic cost and performance analyses of environmental control equipment at fossil fuel power plants (Rubin et al., 2007). The addition of dry cooling system models will enable IECM users to evaluate the performance and cost of a power plant equipped with ACC and make technical and cost comparisons among different cooling technologies.

Configuration and Geometry

ACC configuration and geometry are briefly introduced in this section prior to technical performance analyses. Details about configuration and geometry can be found elsewhere (Larinoff et al., 1978, Kroger, 2004, EPRI, 2005). As shown in Figure 1, ACC is comprised of fin tube bundles grouped together in parallel and arranged in an A-frame configuration. A typical full-scale ACC-based dry cooling system consists of numerous lanes. Each lane consists of several cells. Each cell consists of multiple bundles of finned tubes. A large axial flow fan located at the floor of each cell provides forced-draft cooling air to the finned-tube heat exchangers. In the direct dry cooling system, the steam is ducted from the steam turbine exit to ACC where steam from the distribution manifold enters parallel flow fin tube bundles at the top, condenses on the inner tube walls and flows downward to condensate headers at the bottom of the bundles. The condensate flow is received by a condensate tank from which it is pumped back to the boiler.
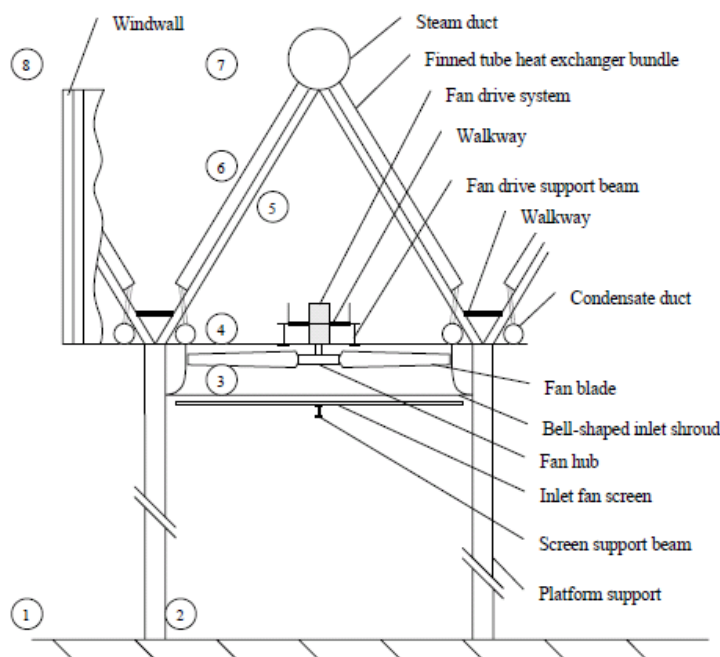

Figure 1 A-Frame Air-Cooled Condenser Unit (Bredell and Kroger, 2006)

An ACC cell has plan dimension of 12×12 meters or less, at the floor of which the large axial flow fan is typically 8.5 to 10 meters in diameter (EPRI, 2005). A number of different heat exchangers are offered by industries, including single-row and multiple-row fin tube bundles. For a multiple-row exchanger, the tubes may be arranged in a staggered or aligned pattern. Finned tube shapes may be circular, elliptical and flattened. The finned tubes of the bundle are typically 9 to 12 meters in length, and are typically clustered in 2.5-meter wide bundles (EPRI, 2005).

Thermodynamic Analysis

The performance evaluation of ACC is based on the fundamental thermodynamics theory. Heat transferred from the exhaust steam to the air flowing through a multiple-row ACC is estimated as:

$$q = \sum_{n=1}^{N} m_a c_a^{(n)} \left(T_a^{o(n)} - T_a^{i(n)} \right) \tag{1}$$

The effectiveness of each tube row is given as:

$$e^{(n)} = 1 - \exp\left(\frac{-UA^{(n)}}{m_a c_a^{(n)}} \right) \tag{2}$$

With the effectiveness, the rejected heat by ACC is estimated as:

$$q' = \sum_{n=1}^{N} e^{(n)} m_a c_a^{(n)} \left(T_{vm}^{(n)} - T_a^{i(n)} \right) \tag{3}$$

where

$c_a^{(n)}$ = the heat specific heat rate of the air through the tube row n

$e^{(n)}$ = the effectiveness of the tube row n

q and q' = the rejected heat from the exhaust steam to the air

m_a = the air mass flow rate;

$T_a^{i(n)}$, = the air inlet temperature for the tube row n

$T_a^{o(n)}$ = the air outlet temperature for the tube row n

$T_{vm}^{(n)}$ = the vapor mean temperature for the tube row n

$UA^{(n)}$ = the overall heat transfer coefficient between the steam and the air at the tube row n.

When the cooling air moves through upstream and downstream obstacles such as structure supports and screen support beams, and the exchanger bundles, it experiences energy loss. A fan must appropriately deliver cooling air flow rate to satisfy the requirement of heat rejection duty. A detailed derivation of the draft equation is given elsewhere (Kroger, 2004). The draft equation of ACC is:

$$P_{a1} \left[\{ 1 - 0.00975 (H_7 - H_6)/T_{a6} \}^{3.5} - \{ 1 - 0.00975 (H_7 - H_6)/T_{a1} \}^{3.5} \right]$$
$$=$$
$$K_{ts} \frac{(m_a/A_{fr})^2}{2\rho_{a1}} + K_{up} \frac{(m_a/A_e)^2}{2\rho_{a3}} - K_{Fs} \frac{(m_a/A_c)^2}{2\rho_{a3}} + K_{do} \frac{(m_a/A_e)^2}{2\rho_{a3}} + K_{\theta t} \frac{(m_a/A_{fr})^2}{2\rho_{a56}} \tag{4}$$

where

A_e = the effective flow area through the fan (m^2)

A_c = the fan casing area (m^2)

A_{fr} = the effective area of the bundles (m^2)

H = the height at different location (m)

K_{ts} = the loss coefficient for the platform supports

K_{up} = the loss coefficient for the upstream obstacles

K_{do} = the loss coefficient for the downstream obstacles

$K_{\theta t}$ = the total loss coefficient across the heat exchanger bundles

K_{Fs} = the fan static pressure coefficient

P_{a1} = the ambient pressure (N/m^2)

ρ_a = the air density at different location (kg/m^3)

T_a = the air temperature at different location (K)

The energy and draft equations are inherently coupled and must be satisfied simultaneously. In the calculation of a given ACC, initial estimates of air mass flow rate and air temperature out of the heat exchanger are given and then adjusted until ACC heat duties estimated using Equations (1) and (3) agree with each other. Meanwhile, in addition to air temperatures through the heat exchanger, air mass flow rate has to be adjusted to ensure that the left side and right side of the draft equation also agree with each other. It is an iterative process to determine the ACC performance. Kroger (2004) provides empirical functions and relationships to characterize fan performance and estimate various heat transfer parameters and loss coefficients, and detailed analytical process for different types of ACCs. Key parameters and heat transfer coefficients estimates are given in the Appendix.

Effect of Air-Cooled Condenser on Steam Cycle Performance

The range of turbine back pressures varies depending on the choice of cooling systems (either wet or dry) used in power plants. The backpressure of conventional steam turbine in power plants installed with once-through or wet tower cooling system is typically designed with 1.5 to 2.0 inch Hg$_a$ and less than 5.0 inch Hg$_a$ (EPRI, 2004). When an ACC-based dry cooling system is used in the power plant, the steam turbine may operate with a high backpressure to enlarge the capacity of the cooling system. The design of modifying the conventional turbine is the currently preferred choice for plants equipped with ACCs. The conventional turbine is modified to be capable of operating at higher backpressure up to 8.0 inch Hg$_a$ (EPRI, 2004). Thus, there are heat rate penalties due to turbine modification and higher backpressure operation relative to the conventional turbine. EPRI (2004) presented the ratios of heat rates for the steam cycles with large backpressure versus the basis of 2.0 inch Hg$_a$ backpressure. That heat ratio relationship as a function of the backpressure is used to estimate the steam cycle heat rate for the power plant using the ACCs.

The temperature of exhaust steam out of the turbine varies with the backpressure. It is empirically estimated as a function of the backpressure as follows (EPRI, 2005):

$$T_s = -0.01210 \cdot P_b{}^4 + 0.3948 \cdot P_b{}^3 - 4.9013 \cdot P_b{}^2 + 32.6369 \cdot P_b + 51.8006 \tag{5}$$

where

T_s = the exhaust steam temperature out of the turbine (°F)

P_b = the turbine backpressure (inch Hga)

For a given plant size, total heat rejected in the dry cooling system and condensate flow rate are estimated as, respectively:

$$Q = (Hr_s - 3413) \cdot MWg \cdot 10^3 \tag{6}$$

$$m_c = \frac{Q}{i_{fg,T_s} \cdot 2000} \tag{7}$$

where

Hr_s = the heat rate of the steam cycle equipped with the ACC, a function of the backpressure (Btu/kWh)

i_{fg,T_s} = the latent heat of vaporization at the temperature T_s (Btu/lb)

MWg = the gross electricity output (MW)

m_c = the condensate flow rate (tons/hr)

Q = the total heat rejected in the dry cooling system (Btu/hr)

The heat rate of 3,413 Btu/ kWh is used for generating electricity. The latent heat of vaporization is estimated at the condensing steam temperature out of the turbine. Although actual condensing steam temperature in the tubes may be less than the exhaust steam temperature out of the turbine due to steam pressure drop during the condensation in the tubes, their difference is too small to ignore when the latent heat is estimated. This point is further illustrated later.

Performance Thermodynamics Modeling and Characterization

Performance characterization for the selected dry cooling system is investigated based on the analysis for detailed thermodynamics modeling results.

Thermodynamics Modeling for Various Design Scenarios

Thermodynamic analyses are carried out for the dry cooling system consisting of ACCs with two-row staggered plate-finned flat tubes. This type of ACC is selected as empirical functions based experimental results for characteristic heat transfer parameters, loss coefficient across the heat exchanger bundles, fan static pressure and power are available for detailed process modeling (Kroger, 2004). An A-frame cell served by a large fan with 9.145-meter diameter consists of 8 bundles. Each bundle has an effective frontal area of 27.55 m^2. Detailed finned tube bundle and fan installation geometries and specifications are available elsewhere (Kroger, 2004). Once inlet ambient air and steam conditions including temperature and pressure are given, the ACC performance can be modeled.

This analysis investigated forty-eight scenarios with different combinations of steam turbine backpressure and air inlet temperature under three kinds of ambient pressure (84.6 kPa, 91.0 kPa and 101.3 kPa). The temperature of the exhaust steam before entering the ACC is calculated using Equation (5) in terms of the turbine backpressure. The resulting ITDs range basically from 20 ^{o}F to 80 ^{o}F. Figure 2 shows that for a given inlet temperature, ITD increases when the steam turbine backpressure increases, whereas it decreases for a given backpressure when the inlet air temperature increases.
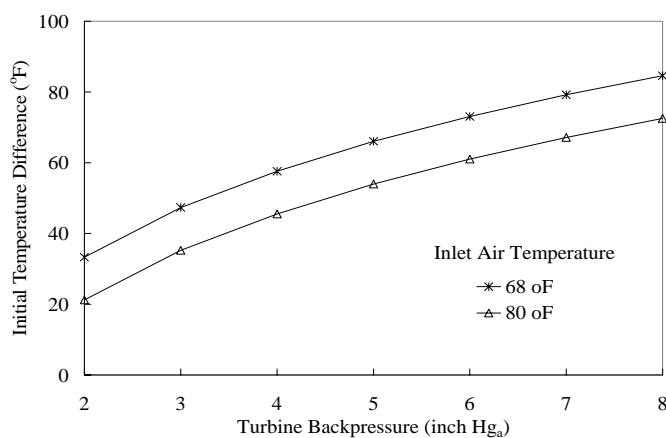

Figure 2 Initial Temperature Difference between Inlet Air and Steam Temperatures in Case Studies

As discussed above, those energy and draft equations are solved simultaneously to determine the performance characteristics such as heat load, air mass flow rate and fan shaft power. The ACC surface or plot area and fan power use are divided by ACC heat load for each scenario. The normalized ACC size and fan electricity use are then compared among scenarios to quantify and characterize technical performance impacts of such operation design conditions as temperatures and pressures of the inlet steam and air. Figure 3 shows the thermodynamic modeling results for those scenarios under the barometric pressure of 84.6 kPa. As shown in Figure 3(a), the normalized ACC size decreases when the steam turbine backpressure increases for a given air temperature. Meanwhile, it increases with the air inlet temperature and then leads to large space requirement for the dry cooling system. These results indicate that hot weather produces a penalty associated with the ACC capability. As shown in Figure 3(b), the fan electricity requirement shows similar sensitivities to the backpressure and inlet air temperature as the normalized ACC size does. There are similar trends on the normalized ACC size and energy use under other ambient pressures. These results under different design conditions consistently indicate the significant effects of ambient air condition and exhaust steam pressure on the ACC size and energy requirement.
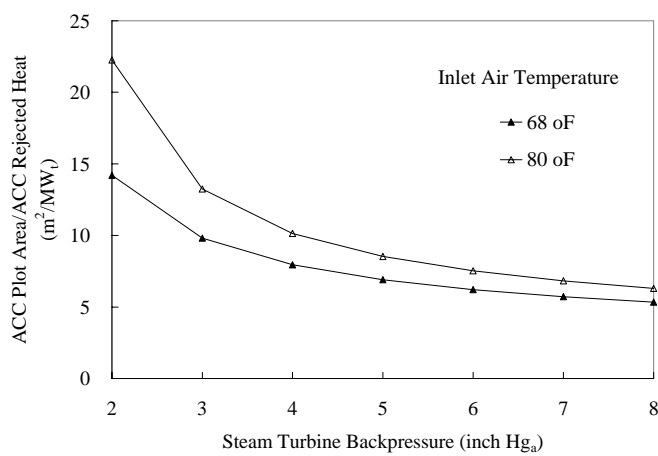
(a)
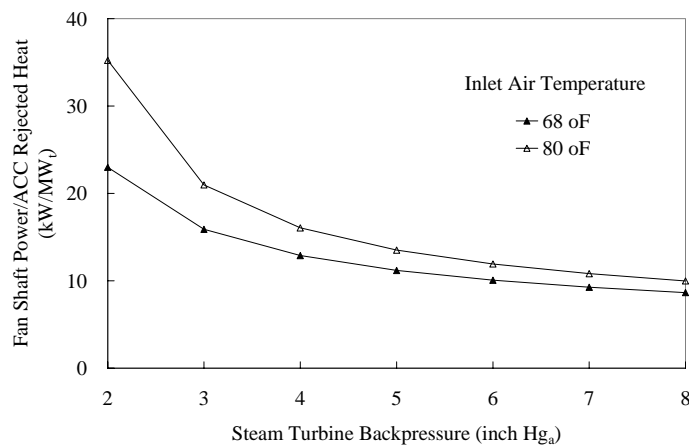
(b)

Figure 3 Performance Evaluation of Selected ACC under Ambient Pressure of 84.6 kPa

Since ITD directly associates the inlet air temperature with the turbine backpressure, the relationships between the ITD and the normalized plot area and electricity are visually explored with the help of scatter plots. Figure 4 shows that the normalized cell plot area and corresponding fan electricity requirement decrease with an increase of ITD under each given ambient pressure. For a given heat load, the cell size and electricity usage are inversely related to ITD. ITD aggregates the individual effects of inlet air temperature and backpressure on the ACC cooling capacity

and energy requirement. Meanwhile, Figure 4 also demonstrates that the ambient barometric pressure affects the ACC performances, especially the ACC plot area. As the ambient pressure increases, the air density increases under the same temperature condition, and more air flow rates for the same ITD scenarios are required to satisfy with the draft equation. The resulting heat rejected by the given ACC increases and corresponding fan electricity requirement increases. Thus, the normalized cell plot area decreases with an increase of the barometric pressure.
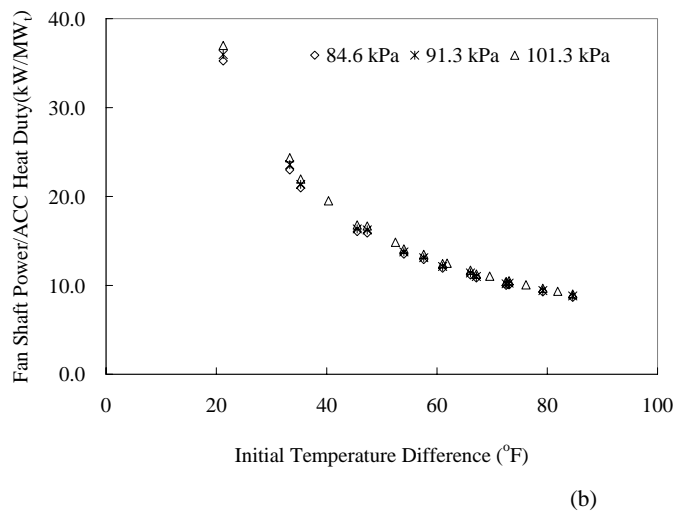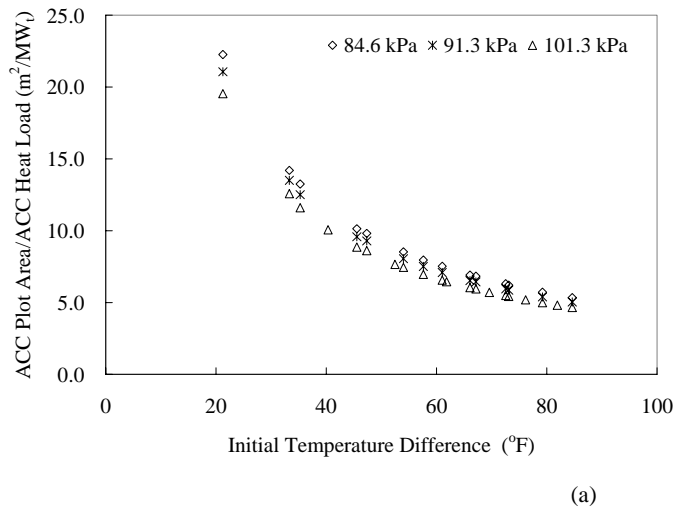

(a)

(b)

Figure 4 Air-Cooled Condenser Performance Characterizations

The mean temperature of steam in the tubes decreases, compared to the temperature of inlet exhaust steam due to steam pressure drop in the tubes. However, case studies above show that temperature drops are generally less than 1.5%. Therefore, there is no significant error in estimating condensate flow rate in terms of the temperature of exhaust steam just out of the turbine.

Performance Characterization Quantification

A number of thermodynamic process modeling scenarios covering a reasonable range of values for the key parameters have been conducted. The ACC plot area and fan shaft power normalized by ACC rejected heat are found to be functions of ITD and ambient barometric pressure. Based on all scenarios results obtained from the thermodynamic process modeling, these empirical relationships are quantified using the multivariate nonlinear regression and given as follow:

$$\bar{a} = 462.346 \times ITD^{-1.0344} \times \left(\frac{P_{ambient}}{101.3}\right)^{-0.7401} \qquad R^2 = 0.999$$	(8)
$$\bar{e} = 848.024 \times ITD^{-1.0227} \times \left(\frac{P_{ambient}}{101.3}\right)^{0.2709} \qquad R^2 = 0.999$$	(9)

where

$\bar{a}$ = the ACC plot area normalized by ACC rejected heat (m^2/MW_t)

$\bar{e}$ = the required fan shaft power normalized by ACC rejected heat (kW/MW_t)

ITD = the initial temperature difference between inlet air and steam (^{o}F)

$P_{ambient}$ = the ambient barometric pressure (kPa)

Those relationships characterizing the performance can be used to provide preliminary assessment for an ACC-based dry cooling system. Once ITD is designed at a specific site, the normalized plot area per cell and fan electricity requirement can be estimated using those empirical functions above. When heat load of a dry cooling system is calculated for a given plant size using Equation (6), the total ACC plot area or surface size and electricity usage are estimated as the product of the corresponding values of the normalized performance parameters and the heat duty of dry cooling system. The number of ACC cells is determined either. Those empirical functions greatly simplify the design process of sizing the dry cooling system and estimating energy requirement.

Performance Comparisons between Different ACCs

An on-line ACC sizing calculator to model the multiple-row ACC performance is available (GEA, 2009). Once steam turbine exhaust flow rate, temperature and steam quality, and ambient air temperature and pressure are given by users, the plot area and fan shaft power requirement are calculated for the ACC-based dry cooling system. Numerous scenarios with various combinations of steam turbine exhaust and ambient air conditions are modeled using that on-line sizing calculator under the standard atmospheric pressure. The resulting ACC plot area and fan shaft power requirement are normalized by corresponding heat load for each scenario. The results are shown in Figure 5.

Comparisons of technical performances are made between different ACC models. Figure 5 shows that for a given ITD, the GEA ACC model requires more plot area but less fan shaft power than the selected ACC model above that is named Kroger ACC in the figure. The performance differences between two ACCs may be due to the differences of ACC configuration and geometry specifications, and selected fan character. However, these differences cannot be quantitatively accounted for herein because no technical document providing the GEA ACC with configuration and geometry specifications is available online. In spite of some differences, both ACCs show very similar performance trends as power functions of ITD.
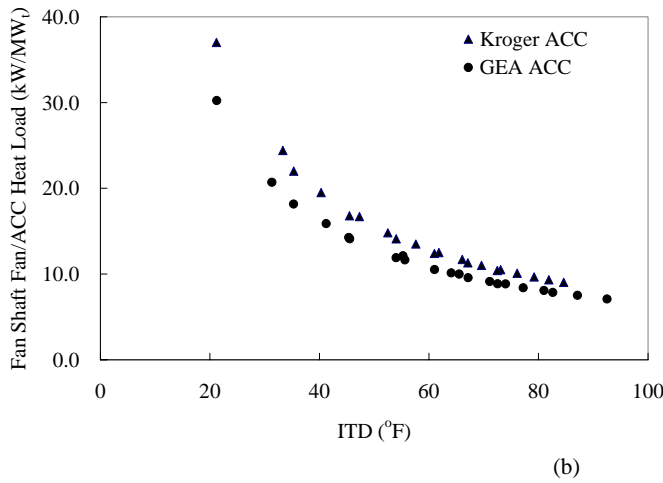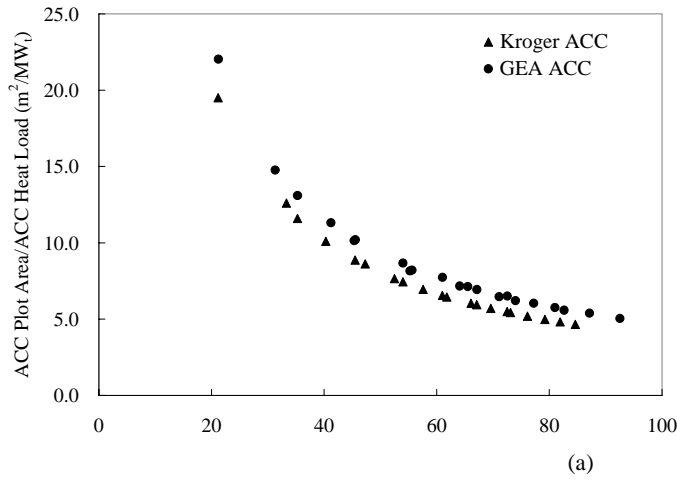
(a)

(b)

Figure 5 Performance Comparisons between Two ACCs under Standard Pressure

Capital Cost

Major capital cost elements for the ACC-based dry cooling system include: ACC equipment, equipment installation, steam duct support and column foundation, electrical and control equipment, cleaning system for finned tube surfaces and auxiliary cooling (EPRI, 2002, and EPRI, 2004). Typically, the auxiliary cooling cost is estimated at 7.5% of the sum of the equipment, erection and electrical/control costs. As the most important element, the equipment capital cost of the dry cooling system covers these costs for finned tube heat exchanger elements, fans and motors, ACC support structure, steam exhaust duct, piping and valves, air removal equipment and support for start-up, training, and testing (EPRI, 2002 and 2004). EPRI (2002 and 2004) estimated the equipment cost (regarded as the 2003 US dollars) for 500MW combine cycle power plants with 170 MW at steam side using cost data originally provided by major ACC vendors. Based on the cost estimates from EPRI case studies, the equipment capital cost normalized by power plant size at the steam side is regressed as a function of ITD and estimated as:

$$C_{equip}\,(M\$) = 663.4\,ITD^{-1.0055}\left(\frac{Q}{Q_o}\right) \qquad\qquad R^2 = 0.856 \qquad (10)$$

The capital cost for a dry cooling system is strongly dependent on the ITD choice and power plant size. In addition, the equipment erection cost regarded as another significant item was estimated at approximately 30% of the sum of

the equipment and erection cost (EPRI, 2004); and electrical and control equipment cost were estimated at the range from $20,000 to $35,000 per cell.

The cost sum of the equipment, erection, electrical/control, and auxiliary cooling is regarded as process facility cost (PFC). The total plant cost (TPC) for the dry cooling system is also estimated based on the procedure recommended by the EPRI's Technical Assessment Guide (EPRI, 1993), consisting of PFC, general facilities capital (GFC), engineering and home office overhead including fees, and project and process contingencies.

Case Studies for Pulverized Coal Power Plants

Illustrative case studies are carried out for pulverized coal (PC) plants equipped with the dry cooling systems. The technical design assumptions and inputs for the PC power plants and dry cooling systems are given in Table 1. IECM is used to model the plant performance based on the steam cycles referred to, such as the net electricity output, coal use and pollutant emissions. The ACC plot area and electricity requirement are estimated according to the operation design inputs and performances of power plant and cooling system. Then, the impacts of operation design inputs including steam turbine backpressure and ambient conditions on technical performance and cost of the dry cooling system are discussed.

Table 1 Technical design assumptions for pulverized coal power plants and dry cooling systems

Parameter	Value
Coal	
HHV	13,260 Btu/lb
Carbon	73.81 wt%
Ash	7.24 wt%
Moisture	5.05 wt%
Base plant and Environmental Control	
Plant type	Subcritical
Environmental control	SCR+ ESP + FGD
Net electricity output	550.0 MW
Dry cooling system	
Ambient barometric pressure	101.3 kPa
ACC configuration	A-frame, 8 bundles per cell
Auxiliary cooling	5% of main cooling heat load
Fan drive system efficiency	90%
Fan diameter	9.145 meter
Capital cost for cooling system	
Steam duct support unit cost	$ 136,360 per 1.0 MM lb/hr steam
Electrical and control equip. unit cost	$ 30,000.0 per cell
Clearing system unit cost	$ 880/MW$_{e,gross}$
Engineering & home office overhead fee	9.3% of process facility cost
Project contingency cost	15.0% of process facility cost
Process contingency cost	0.0% of process facility cost
Cost year	2007

To cover a broad range of ACC operation conditions, the turbine backpressure is designed to vary from 2.0 inch Hg$_a$ to 8.0 inch Hg$_a$, while the dry cooling system operates under two ambient conditions. The ITDs between the inlet air

and steam for the ACCs studies cover a large range. Table 2 summarizes key technical performance and cost results for subcritical PC power plants.

Table 2 Performance and cost results of dry cooling systems for subcritical pulverized coal plants

Case Study No.	1	2	3	4	5	6	7	8
Gross electricity outputs (MW)	621.4	599.9	596.6	595.6	607.9	596.7	594.6	594.1
Turbine backpressure (inch Hg$_a$)	2	4	6	8	2	4	6	8
Steam cycle heat rate (Btu/kWh)	7856	8023	8242	8514	7856	8023	8242	8514
Ambient air temperature (^{o}F)	80	80	80	80	70	70	70	70
Initial temperature difference between inlet steam and air (^{o}F)	20.4	46.1	60.8	71.8	30.4	56.1	70.8	81.8
Condensate flow rate (tons/hr)	1398	1421	1492	1584	1368	1413	1487	1580
ACC system plot area (ft^2)	1.87e5	8.05e4	6.30e4	5.60e4	1.21e5	6.54e4	5.44e4	4.88e4
Fan electricity requirement (% of MWg)	5.89	2.67	2.10	1.87	3.92	2.18	1.80	1.64
Total plant cost (TPC) (M$)	237.28	105.62	83.7	74.85	155.89	86.52	71.78	65.68
Normalized TPC ($/kW$_{net}$)	431.4	192.04	152.2	136.10	283.44	157.32	130.51	119.42

The size and capital cost of the dry cooling system significantly change with the inlet air and steam conditions. Higher turbine backpressure and lower air ambient temperature jointly help decrease the cooling system size and capital cost. As shown in Figure 6, the number of ACC cells installed in the dry cooling system decreases from 157 to 41 when ITD changes from 20.4°F to 81.8°F. In addition, comparisons of the cooling system size between the PC plants operating with the same backpressure display that the capacity of the cooling system decreases under the hot weather. The TPC normalized by net electricity output significantly varies from $431.4 kWe to $119.4 kWe in the 2007 US dollars for such a large ITD range. Ratios of the normalized TPCs and cooling system size between two cases of maximum versus minimum ITDs are about a factor of four. The big ratio factor further shows the significance of the ITD as a design parameter for the dry cooling system.
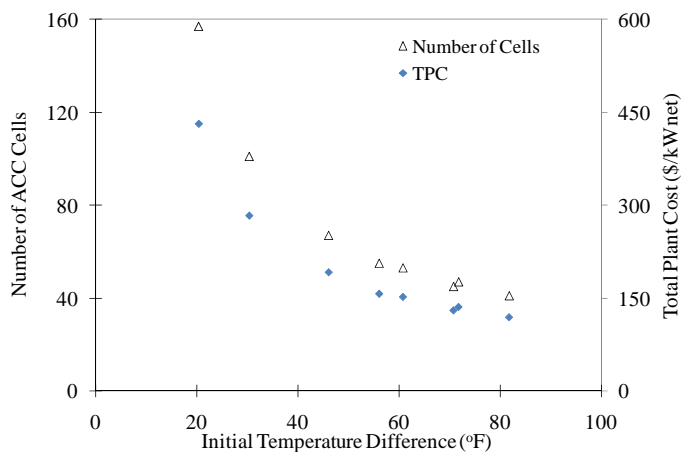

Figure 6 Effect of initial temperature difference design on dry cooling system size and capital cost in 550 MWnet pulverized coal power plant

The dry cooling system produces energy penalties associated with the steam cycle. For a given ambient condition, the electricity use required by the dry cooling system decreases as ITD becomes larger, when the turbine backpressure increases. However, thermal efficiency of the steam cycle decreases from 43.4% to 40.1%. Therefore, the turbine backpressure has dual effects on the performances of power plants equipped with dry cooling systems.

The increase of ambient air temperature leads to more energy required by large fans for operation when the steam turbine works with a fixed backpressure. This result provides evidence that the hot weather is not favorable to the operation of the dry cooling system.

Comparisons of capital cost are made between dry and wet cooling systems to provide insight into different cooling technologies for coal-based power plants. The normalized TPC of wet cooling tower was estimated by the National Energy Technology Laboratory (NETL) in terms of a 20^oF temperature decrease of cooling water across the tower to be \$68/kWe (NETL, 2007). Figure 7 gives the normalized TPC ratios for dry versus wet cooling systems. The TPC ratio for dry versus wet cooling systems varies by factor approximately from two to six, strongly depending on ITD. In contrast to the wet cooling system, the dry cooling system can result in an increase of electricity production cost, in spite of its evident advantage in reducing water consumption.
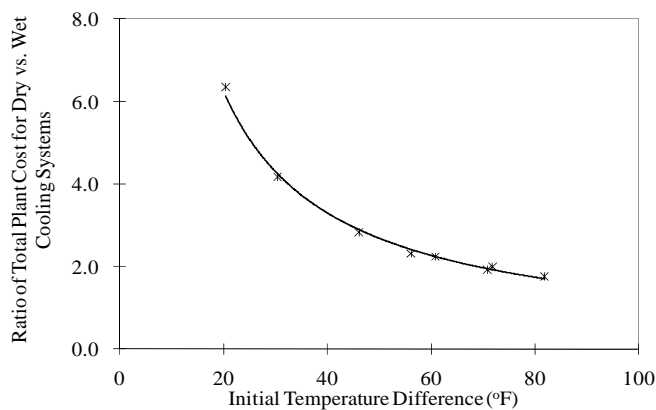

Figure 7 Effect of initial temperature difference design on ratio of total plant costs for dry versus wet cooling systems in pulverized coal power plant

Conclusion

This report systematically evaluates performance and cost of the direct dry cooling system for coal-based power plants. Thermodynamics analyses demonstrate sensitivities of technical performance and cost to critical inputs including ambient air conditions and turbine backpressure designated point. A series of empirical exploratory recognizes such crucial design input parameter as ITD that links multiple input variables and aggregates their joint effects on technical performance of the ACC-based cooling system. Technical performances are characterized by ITD and ambient barometric pressure based on the thermodynamics simulation. Simplified performance models respond appropriately to critical inputs and provide crucial technical information that is used to facilitate preliminary assessment and strategic planning analysis. The dry cooling system size and energy use are reversely related to ITD, which strongly depend on the designated ITD value and show large variability associated with ITD.

When ACCs are used as the cooling system in coal-based power plants, the steam turbine backpressure in general operates in a higher level than the one in a wet cooling system. The design of the backpressure generates different effects on plant steam cycle and dry cooling system, respectively. The increase of the backpressure leads to the reduction of steam cycle thermal efficiency with an energy penalty, while higher backpressure leads to a larger ITD and thermal capacity of ACCs subsequently increases. Both dry cooling system size and capital cost vary by a factor of about four over a wide range of ITD generally from 20°F to 80°F. Comparison of capital costs between dry and wet cooling technologies displays a large sacrifice of capital cost highly dependent on the ITD to achieve the evident advantage of the dry cooling system in water conservation. The design of ITD indeed has profound technical and economic influences on the direct dry cooling system.

References

Bredell, J.R. and Kroger, D.G. Numerical Investigation of Fan Performance in A Forced Draft Air-Cooled Steam Condenser. Report No. CEC-500-2006-113, California Energy Commission, PIER Energy-Related Environmental Research, CA, December 2006.

Conradie, A.E. and Kroger, D.G. Performance Evaluation of Dry-Cooling Systems for Power Plant Evaluations. *Applied Thermal Engineering*, 1996, 16(3):219-232.

EPRI. TAG™ Technical Assessment Guide: Electricity Supply - 1993, Volume 1, Rev. 7, Report No. TR-102276-VIR7, Electric Power Research Institute, Palo Alto, CA, June 1993.

Electric Power Research Institute. Comparison of Alternate Cooling Technologies for California Power Plants: Economic, Environmental and Other Tradeoffs. Prepared by Electric Power Research Institute for California Energy Commission, Report No. 500-02-079F, EPRI, Palo Alto, CA, February 2002.

Electric Power Research Institute. Comparison of Alternate Cooling Technologies for U.S. Power Plants: Economic, Environmental, and Other Tradeoffs. Report No. 1005358, EPRI, Palo Alto, CA, August 2004.

Electric Power Research Institute. Air-Cooled Condenser Design, Specification, and Operation Guidelines. Report No. 1007688, EPRI, Palo Alto, CA, December 2005.

Feeley III, T,J.; Skone, T. J.; Stiegel Jr., G. J.; McNemar, A.; Nemeth, M.; Schimmoller, B.; Murphy, James T.; Manfredo, L. Water: A Critical Resource in the Thermoelectric Power Industry. *Energy*, 2008, 33:1-11.

GEA Aircooled Systems (Pty) Ltd. Aircooled Condenser Calculator. http://www.geapowercooling.com.mx/opencms/opencms/gem/en/calculators/ACC_Calculator.html. Accessed on May 18, 2009.

Kroger, D.G. Air-Cooled Heat Exchangers and Cooling Towers. Penwell Corp., 2004.

Larinoff, M.W.; Moles, W.E.; Reichhelm, R. Design and Specification of Air-Cooled Steam Condensers. *Chemical Engineering* (New York), 1978, 85(12):86-94.

NETL, Cost and performance baseline for fossil energy plants. Report DOE/NETL-2007/1281, U.S. Department of Energy National Energy Technology Laboratory, August 2007.

National Energy Technology Laboratory. Impact of Drought on U.S. Steam Electric Power Plant Cooling Water Intakes and Related Water Resource Management Issues.DOE/NETL-2009/1364, April 2009.

Rubin, E.S.; Berkenpas, M.B.; and Zaremsky, C.J. Integrated Environmental Control Model (IECM) with Carbon Capture and Storage (CCS). Prepared by Carnegie Mellon University for U.S. DOE National Energy Technology Laboratory, Pittsburgh, PA, May 2007.

Appendix

Parameters

Some key parameters and heat transfer coefficents estimates are briefly summarized in the appendix. Much more details are available from the technical textbook authored by Kroger (2004).

Air-Side Heat Transfer

Considering the reduced effective frontal area, the air-side characteristic flow is estimated as:

$$Ry = \frac{m_a}{\mu_a A_{fr}} \tag{11}$$

The corresponding heat transfer parameters for two individual plat-finned flat tube rows are experimentally estimated as:

$$Ny_1 = 366.007945 Ry^{0.433256} \tag{12}$$

$$Ny_2 = 360.588007 Ry^{0.470373} \tag{13}$$

Then, the corresponding effective heat transfer coefficient is estimated as:

$$h_{ae} A_a = k_a \Pr_a^{0.333} A_{fr} Ny \tag{14}$$

Steam-Side Heat Transfer

The drop in pressure between the inlet to the steam supply duct and a point just inside the inlet to the condenser tubes is estimated as:

$$\Delta P = 0.5 \rho_{vi} v_{vi}^2 \left(1 - \sigma^2 + K_c + K_{sd}\right) \tag{15}$$

The mean saturation pressure of the steam inside the inlet of the finned tubes is obtained by subtracting pressure drop from the mean saturation steam pressure at the turbine outlet (P_{sd}):

$$P_{vi} = P_{sd} - \Delta P \tag{16}$$

The saturation temperature of the steam corresponding to this pressure above is:

$$T_{vi} = \frac{5149.6889682}{\ln(\frac{1.020472843 \times 10^{11}}{P_{vi}})} \tag{17}$$

The thermophysical properties of statured steam at this temperature can be calculated. The mean static pressure in the flattened tubes can be determined as follows:

$$\text{Re}_{vi} = \frac{\rho_{vi} v_{vi} d_e}{\mu_{vi}}$$

(18)

$$\text{Re}_{vn} = \text{Re}_{vi} W_t /(2 L_t)$$

(19)

$$\overline{P}_{vm} = P_{vi} - \frac{0.1582 \mu_{vi}^2 L_t}{\rho_{vi} d_e^3 \text{Re}_{vi}} \left(0.267 a_1 \text{Re}_{vi}^{2.75} + 0.364 a_2 \text{Re}_{vi}^{1.75}\right) + \frac{2}{3} \rho_{vi} v_{vi}^2$$

(20)

where

$$a_1 = 1.0649 + 1.041 \times 10^{-3} \text{Re}_{vn} - 2.011 \times 10^{-7} \times \text{Re}_{vn}^3$$

(21)

$$a_2 = 290.1479 + 59.3153 \text{Re}_{vn} + 1.5995 \times 10^{-2} \times \text{Re}_{vn}^3$$

(22)

Then, the corresponding mean steam temperature (T_{vm}) is estimated using Equation (17). The thermo-physical properties of the condensate in the first tube row are estimated in terms of the corresponding mean steam temperature. The condensate flow rate is estimated as:

$$m_c = \frac{Q_a}{i_{fg}}$$

(23)

The condensation heat transfer coefficient is estimated as:

$$h_c = 0.9245 \left[\frac{L_t k_c^3 \rho_c^3 g \cos(90^0 - \theta) i_{fg}}{\mu_c m_a c_{pa} (T_{vm} - T_{ai}) \left[1 - \exp\left\{ -\frac{U_c H_t L_t}{m_a c_{pa}} \right\} \right]} \right]^{0.333}$$

(24)

where

$$U_c H_t L_t = \frac{h_{ae} A_a}{2 n_{tb} n_b}$$

(25)

The inside tube area exposed to the condensing steam is:

$$A_c = n_{tb} n_b A_{ti} L_t$$

(26)

Thus, the overall heat transfer coefficient for the tubes is:

$$UA = \left[\frac{1}{(h_{ae} A_a)} + \frac{1}{(h_c A_c)} \right]^{-1}$$

(27)

And, the effectiveness for the condenser tubes is:

$$e = 1 - \exp(-UA/(m_a c_{pa)}))$$

(28)

Thus, the heat transfer rate for the tubes is:

$$Q_a = m_a c_{pa} (T_{vm} - T_{ai}) e$$

(29)

IECM Technical Documentation: Volume III
Plant Water Usage

DE-AC26-04NT41917

November 2009

NETL

Disclaimer

IECM Technical Documentation: Volume III
Plant Water Usage

_____

DE-AC26-04NT41917

RDS Subtask 404.01.03:
Development and Application of the Integrated Environmental Control Model

Prepared for:

Office of Systems, Analyses and Planning
National Energy Technology Laboratory
Department of Energy
Pittsburgh, PA 15236
www.netl.doe.gov

Prepared by:
Haibo Zhai
Michael B. Berkenpas
Edward S. Rubin
Carnegie Mellon University
Pittsburgh, PA 15213
www.iecm-online.com

November 2009

Table of Contents

List of Figures

List of Tables

Acknowledgements

Plant Water Usage

Background

Thermoelectric power plants utilize significant quantities of water to support electricity generation. Thermoelectric generation accounted for 39% of all freshwater withdraws in the United States in 2000, second only to irrigation (Feeley *et al.*, 2008). 80 to 99% of water is primarily used for cooling purposes in thermoelectric power plants (NETL, 2005). The remaining water supports the operation of boiler and environmental control facilities, such as flue gas desulfurization (FGD) and electrostatic precipitator (ESP) technologies. Currently, carbon dioxide (CO_2) capture is receiving considerable attention as an option to mitigate greenhouse gas emissions from power plants (Rubin *et al*., 2007). Confronted with the large proportion of coal-based power plants, post-combustion CO_2 capture system is an important strategic option to reduce CO_2 emissions, where absorption processes based on monoethanolamine (MEA) solvents are currently the preferred option (Rao and Rubin, 2002; IPCC, 2005). Cooling water is needed in the amine-based CO_2 capture system to reduce the flue gas and solvent temperatures down to the levels required for efficient absorption of CO_2 (IPCC, 2005).

Cooling water intake structures cause adverse environmental impact by pulling large numbers of fish and shellfish or their eggs into a power plant's cooling system. There, the organisms may be killed or injured by heat, physical stress, or by chemicals used to clean the cooling system. Larger organisms may be killed or injured when they are trapped against screens at the front of an intake structure. Section 316(b) of the Clean Water Act grants the US Environmental Protection Agency (EPA) authority to regulate thermoelectric power plants with cooling water intake structures to assure that they reflect the "best technology available" (BTA) for minimizing adverse environmental impacts from these facilities. BTA options vary widely, from modifications of existing screens to expensive cooling tower retrofits and other flow control measures.

Since 1977, determinations of BTA for cooling water intake structures have been governed by EPA draft guidance, and state permitting authorities are allowed a key role in determining what control requirements will satisfy the BTA criterion. Because technologies whose costs are "wholly disproportionate" to their benefits are not considered to be BTA, a site-specific cost-benefit assessment has been a critical component of a BTA determination. Phase I was implemented in 2001 to cover new facilities; Phase II was implemented in 2004 to cover large existing power plants; and Phase III was instituted in 2006 to cover other existing facilities.

Under the requirement of Section 316(b) of the Clean Water Act, most new power plants will implement closed-loop cooling systems (i.e., zero discharge), which may discourage the use of the once-through cooling system and promote the wide use of cooling towers (Feeley *et al.*, 2006a and Feeley *et al.*, 2006b).

The U.S. Department of Energy's (DOE) National Energy Technology Laboratory (NETL) is sponsoring a research and development (R&D) program to reduce freshwater withdrawal and consumption from thermoelectric power generating facilities and estimate freshwater needs to meet future thermoelectric generation requirements (NETL, 2005; NETL, 2007a and 2007b; Feeley *et al.*, 2008).

With emphasis on estimating hazards or toxic emissions for coal-based power plants, the Electric Power Research Institute (EPRI)'s PISCES model estimates water balances around major operation units (EPRI, 1999). The cooling system in the PISCES model is based on simplified empirical relationships instead of thermodynamic relationships

under various meteorological conditions. In addition, the PISCES water models lack the capability to evaluate the impacts of power generation technology options and environmental controls on water consumption.

Objectives

The objectives of this study are to:

1. Develop the systematical approaches to estimate water usage for major operation units in pulverized coal (PC) power plants

2. Evaluate the impact of power generation technology options (e.g., subcritical versus supercritical) on water usage

3. Evaluate the effect of the amine-based CO_2 capture on water usage in different types of PC power plants

Water Configuration

The steam cycle in a power plant operates on the Rankine cycle utilizing a phase change between vapor and liquid. As shown in Figure 1 for PC plants, major operation units for electricity generation and environmental controls include the boiler, steam turbine, condenser, wet FGD, ESP, and cooling tower (wet), with and without a CO_2 capture system. An ash pond with overflow recirculation to sluice ash is used for solid waste management. The water configuration for PC plants mainly consists of makeup water for the cooling system, boiler and FGD, in addition to sluice water required for bottom and fly ash management from the boiler and ESP, respectively.
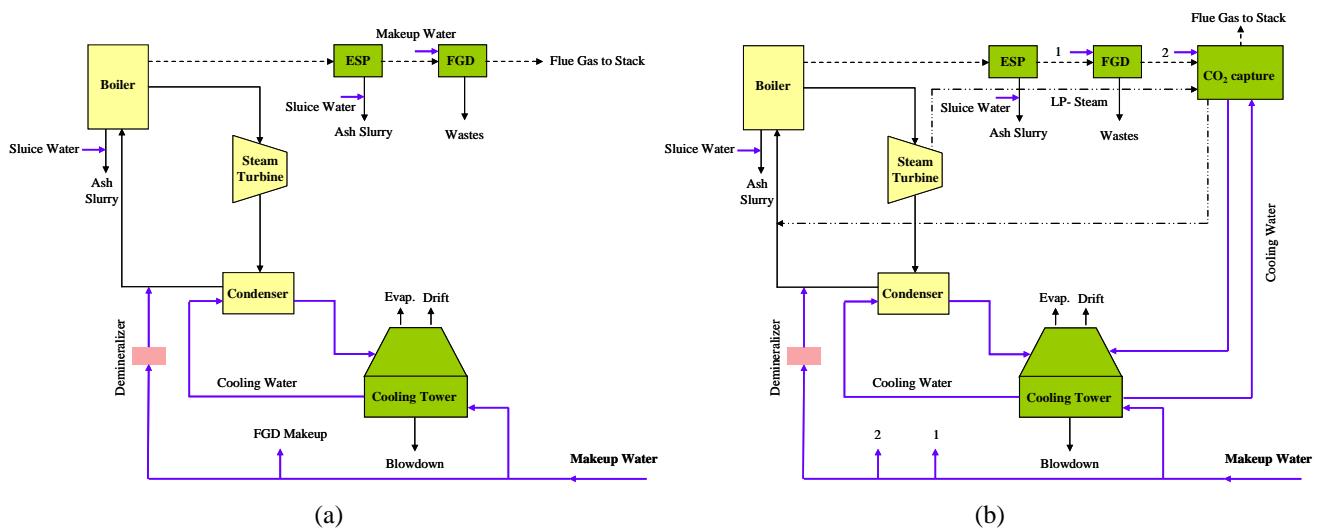

Figure 1 Conceptual water configuration of pulverized coal power plants: (a) without carbon dioxide capture; (b) with amine-based carbon dioxide capture

The CO_2 capture process is an amine-based system for PC plants. This system consists of two major elements: an absorber and a stripper. The capture process uses MEA as a solvent. The lean solvent absorbs CO_2 from the flue gas and leaves the bottom of the absorber with the absorbed CO_2. The stripper separates CO_2 from the rich solvent. A more detailed description of the amine-based CO_2 capture system performance model is available elsewhere (Rao and Rubin 2002). The capture system requires a significant amount of cooling water for flue gas cooling, reflux condenser duty, lean solvent cooling, and CO_2 compression interstage cooling. As shown in Figure 1(b), cooling water to support the CO_2 capture process is provided by the primary cooling system of the power plant. To assist the regeneration of CO_2, low-pressure (LP) or intermediate-pressure (IP) steam is extracted from the steam turbine to maintain the reboiler, which leads to a thermal energy penalty. Reboiler heat duty typically varies from 1500 Btu/lb CO_2 to 2350 Btu/lb CO_2 (NETL, 2007a and 2007c; Aroonwilas and Veawab, 2007; Knuutila *et al.*, 2009).

Water Performance Models

To account for the many factors that affect the overall water system performance, the Integrated Environmental Control Model (IECM) will be employed. The IECM is developed by Carnegie Mellon University for the NETL and publicly available through the website: http://www.iecm-online.com/index.html. The IECM includes an amine-based CO_2 capture process (Rao and Rubin, 2002; Rao and Rubin, 2006). Steam cycle performance is analyzed before presenting analytical methods for water performance. Water performance models are then developed based on fundamental mass and energy balances for major individual operation units in PC power plants.

Steam Cycle

Steam produced from a boiler flows to a steam turbine. Exhaust steam from the turbine condenses to liquid water in a condenser. A feedwater pump returns the condensed liquid to the boiler. The heat rejected around the condenser is transferred to the cooling system that in turn delivers the rejected heat either to the atmosphere through a cooling tower or to the surface water through a once-through system.

The thermal efficiency is the ratio of the new work produced to the energy input, and is determined by a thermodynamics analysis for a Rankine cycle. It is affected by boiler technology. Raising the steam pressure or steam temperature improves the efficiency. However, if the LP or IP steam is extracted for use in a CO_2 capture system, the thermal efficiency for the cycle decreases and the steam cycle heat rate increases. Steam cycle heat rate is defined as the quantity of input heat required to generate one unit of electrical power:

$$Hr_s = \frac{3413}{\eta} \tag{1}$$

where,

Hr_s = the steam cycle heat rate (Btu/Kwh)

η = the thermal efficiency of the steam cycle (%)

3413 = the equivalent heat rate for generating one unit of electricity (Btu/Kwh)

Total heat generated from the steam cycle is then estimated as the product of the steam cycle heat rate and the gross electricity output of the power plant (Bedillion *et al.*, 1997).

Cooling Water

Cooling water is used primarily for extracting the excess heat remaining in the exhaust steam of the steam cycle and also for the equipment in the process areas of the CO_2 capture system. These are discussed in the following sections.

Base Plant

The cooling system is used to cool the main condenser and any auxiliary heat exchanger. In the condenser, the latent heat of the turbine exhaust steam is transferred to the cooling water. The amount of cooling water required to reject the heat around the condenser is estimated as (Bedillion *et al.*, 1997):

$$m_c = \frac{(Hr_s - 3413) \cdot MWg \cdot 1000 \cdot (1 + \mu_{aux})}{\Delta T_w \cdot 2000} \tag{2}$$

where,

m_c = recirculating cooling water (tons/hr)

ΔT_w = cooling water temperature drop across the cooling tower (ºF)

MWg = gross electricity output of the power plant (MW)

μ_{aux} = percent of the primary steam cycle heat for auxiliary equipment cooling

The amine-based CO_2 capture system affects plant performance in two process areas: steam cycle and cooling system. When CO_2 is captured, the heat rejected around the condenser in the steam cycle does not include the amount of LP or IP steam heat used in the reboiler for CO_2 regeneration. Taking into account additional cooling water usage for the CO_2 capture process, the total cooling water required in the power plant is estimated as:

$$m_c' = \frac{(Hr_s' - 3413) \cdot MWg' \cdot 1000 \cdot (1 + \eta_{aux}) - Q_s^{LP}}{\Delta T_w \cdot 2000} + m_c^{CO_2} \qquad (3)$$

where,

Hr_s' = steam cycle heat rate with LP or IP steam extraction (Btu/Kwh)

MWg' = gross electricity output from power plant with CO_2 capture (MW)

Q_s^{LP} = heat required by the reboiler for CO_2 regeneration

$m_c^{CO_2}$ = cooling water used by the amine-based CO_2 capture system (to be further illustrated later)

CO_2 Capture System

Cooling water is required in an amine-based CO_2 capture system to support the operations of a direct contact cooler (DCC), the absorption and stripping processes, and CO_2 product compression. Cooling water is provided from the plant cooling system and returned to the plant cooling tower.

The DCC cools the flue gas before it enters the CO_2 absorber in order to improve the absorption of CO_2 by the amine sorbent, to minimize sorbent losses, and to avoid excessive loss of moisture in the exhaust gases. The cooling water required for the DCC is estimated based on the energy balance as (Rao *et al*., 2004):

$$m_c^{DCC} = \frac{M_{fg} \cdot Cs_{fg} \cdot (T_{fg,in} - T_{fg,out})}{Cs_w \cdot \Delta T_w} \qquad (4)$$

where,

Cs_{fg} = specific heat values of the flue gas ($kJ / kg \cdot {}^o C$)

Cs_w = specific heat values of the water respectively ($kJ / kg \cdot {}^o C$)

m_c^{DCC} = cooling water flow rate for the DCC (tons/hr)

M_{fg} = flue gas mass flow rate (tons/hr)

$T_{fg,in}$ = temperatures of flue gas entering the direct contact cooler (ºF)

$T_{fg,out}$ = temperatures of flue gas exiting the direct contact cooler (ºF)

Lean solvent from the stripper is cooled against rich solvent in the solvent cross exchanger, and then further cooled in the lean solvent cooler against cooling water; and the overhead vapor from the stripper is cooled in the reflux condenser against cooling water (FLUOR, 2005a and 2005b). The cooling water required by the absorption and stripping processes is estimated as:

$$m_c^{process} = \varphi \cdot M_{CO_2\,Product} \qquad (5)$$

where,

$m_c^{process}$ = cooling water for absorption and stripping processes (tons/hr)

$M_{CO_2\,Product}$ = captured CO_2 product (tons/hr)

φ = a normalized parameter (grams of cooling water / gram of CO_2 product)

φ is estimated in terms of the total capture process cooling water requirement divided by the compressed CO_2 product. In this study, the normalized φ is estimated based on FLUOR company studies for the amine-based capture process (FLUOR, 2005a and 2005b).

The CO_2 product is compressed and dried using a multi-stage compressor with interstage cooling. Cooling water is required for CO_2 compression interstage cooling where CO_2 is cooled against cooling water. Based on the design of a six-stage centrifugal compressor by NETL (NETL, 2007a), this compression is modeled using the ASPEN-Plus software to estimate the total heat rejected in the compression and then determine required cooling water (Aspen, 2003). Total cooling water usage ($m_c^{CO_2}$) for the amine-based system is the sum of cooling water for the DCC, absorption and stripping processes, and CO_2 product compression.

Makeup Water

Makeup water is used to replenish water evaporated or removed from any particular process. This does not include water recirculated or returned to the general plant water system.

Cooling System

A cooling tower may be used to remove the heat in the recirculating cooling water, decreasing the temperature of the cooling water. The cooling tower operation is maintained by adding fresh water at the same rate as the water losses due to evaporation, blowdown and drift from the cooling tower. The blowdown from the cooling tower can be collected for use as sluice water for bottom and fly ash. The evaporation process is the largest source of cooling tower water losses, depending on cooling water and air temperatures, the water temperature drop across the tower, and the water quality. The blowdown replies on cooling water quality that can be measured by a cycle of concentration for cooling water. The tower drift is often empirically estimated as a percent of the recirculating cooling water. The detailed performance models of cooling system are available elsewhere (Zhai *et al*., 2009).

Makeup water for the cooling system increases with the recirculating cooling water. In particular, when an amine-based system is present, makeup water for the cooling system may substantially increase due to the additional cooling water requirement in the CO_2 capture process as discussed above.

Boiler

The boiler in the power plant is a steam generating system that transfers the heat from coal combustion to water, producing steam. The steam flow depends on the steam cycle heat rate, gross electricity output and boiler design, according to:

$$m_s = \frac{Hr_s \times MWg \times 10^3}{\left\{\left(h_s^{super} - h_w^{Boiler}\right) + \phi_{reheat} \cdot \left(h_{s,out}^{reheat} - h_{s,in}^{reheat}\right)\right\} \times 2000} \qquad (6)$$

where,

m_s = steam flow rate (tons/hr)

h_s^{super} = boiler superheat steam enthalpy (Btu/lb)

h_w^{Boiler} = boiler feedwater enthalpy (Btu/lb)

$h_{s,out}^{reheat}$ = steam enthalpy after the reheat (Btu/lb)

$h_{s,in}^{reheat}$ = steam enthalpy prior to the reheat (Btu/lb)

ϕ_{reheat} = mass fraction of reheat steam

The denominator term in Equation (6) represents the net heat added in the boiler to one unit of steam (Btu/lb), affected by steam generation designs such as superheat and reheat steam temperatures and pressures (NETL, 2007a).

To maintain the boiler operations, the boiler blowdown stream is necessary to remove dissolved salts and suspended solids from the boiler. Makeup water required for the boiler operation is empirically estimated based on the boiler blowdown rate and miscellaneous losses in the steam cycle. The blowdown rate is defined as a percent of the boiler feedwater. Depending on water quality, it typically ranges from 4% to 8% of boiler feedwater flow rate, but can be as high as 10%, and even up to 20% when makeup water has high solids content (Harrell, 2004; EERE, 2006). Boiler feedwater flow rate is the sum of steam flow rate and boiler blowdown. Depending on the amount of generated steam from the cycle, boiler makeup water is estimated as:

$$m_{bmw} = \frac{\beta}{1-\beta} m_s + \eta_{steam} \cdot m_s \qquad (7)$$

where,

m_{bmw} = boiler makeup water (tons/hr)

m_s = steam flow rate (tons/hr)

β = boiler blowdown rate (%)

η_{steam} = a percent of steam accounting for miscellaneous loss

Makeup water for the boiler often needs to be treated due to a high requirement for water quality. When the demineralizer is used to treat water, the amount of makeup water for the demineralizer can be found based on the required boiler makeup water and the fraction of water entering the demineralizer that is lost as waste (EPRI, 1999).

Flue Gas Desulfurization

Wet FGD is widely used to remove sulfur dioxide (SO_2) from the exhaust flue gases in coal-based power plants. In the FGD, water is lost mainly due to evaporation in the scrubber. A module in the IECM determines the evaporation loss based on an energy balance that the sensible energy released by the flue gas entering the scrubber has to equal the energy needed to evaporate the water evaporated and raise it to the exit temperature (Bedillion *et al.*, 1997). Makeup water is required principally to offset the evaporative loss. Makeup water for the FGD is estimated using the IECM (Berkenpas *et al.*, 2007).

Ash Sluice Water

Bottom and fly ash are two types of ash residue produced by coal combustion in a coal-based power plant. Bottom ash is collected at the bottom of the boiler. In a wet sluicing system, bottom ash is sluiced with water and transported to a bottom ash pond where the ash settles in the pond. Fly ash is entrained in the flue gas and removed by air pollution control system equipment. For example, an ESP is often installed to reduce particle emissions from the PC plant.

This study assumes that fly ash is sluiced by water and mixed with the bottom ash slurry. Ash is sluiced in the U.S. at a solid content of 5 to 15% by weight (EPRI, 1987). Depending on percent water in the ash waste and the amount of emitted ash, the combined sluice makeup water for bottom and fly ash mix management is estimated as:

$$m_{sluice} = m_{bottom}^{dry} \cdot \frac{f_{bottom}}{1 - f_{bottom}} + m_{fly}^{dry} \cdot \frac{f_{fly}}{1 - f_{fly}} \qquad (8)$$

where,

m_{sluice} = ash sluice makeup water (tons/hr)

m_{bottom}^{dry} = dry bottom ash and fly ash mass flow rate (tons/hr)

m_{fly}^{dry} = dry bottom ash and fly ash mass flow rate (tons/hr)

f_{bottom} = water content in bottom ash slurry (%)

f_{fly} = water content in fly ash slurry (%)

As shown in Figure 2, the mass flows into the bottom ash pond include the bottom and fly ash slurry. The mass flows out of the ash pond include overflow, leachate and evaporation.
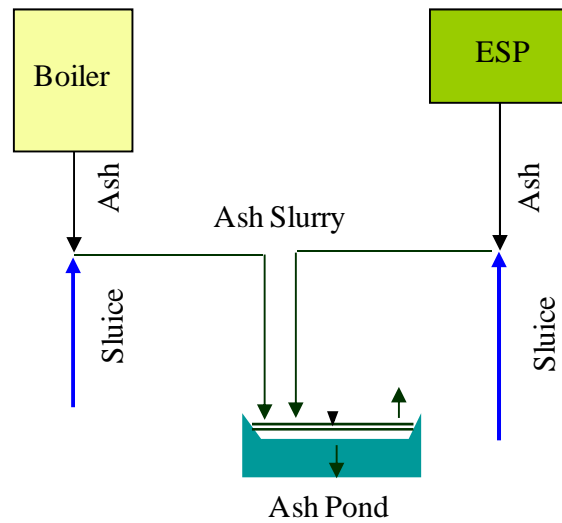

Figure 2 Bottom and fly ash mix management in pulverized coal power plant

The sluice makeup water for bottom ash and fly ash management is estimated based on the algorithm of water balance around the ash pond in the PISCES (Bedillion *et al*., 1997; EPRI, 1999).

Case Studies

To evaluate water usage for major operation units and water impacts of electricity generation and CO_2 capture, case studies are based on comparisons of several PC plants with the same net 550 MW electricity output. The single-reheat Rankine cycles designed by NETL for PC plants are referred to and analyzed (NETL, 2007a). The PC cases are evaluated with and without carbon capture and sequestration (CCS). The wet tower is used in the cooling system. The demineralizer treats makeup water for the boiler. The wet FGD is used to remove SO_2, whereas the amine-based system is used to capture CO_2 if applied. Other environmental control technologies include SCR and ESP. The fly ash slurry is co-treated with the bottom ash slurry in the ash pond. The technical design assumptions for PC power plants and environmental controls are given in Table 1.

The IECM is used to model the plant performance based on the steam cycles referred to, such as the gross electricity output, coal use and pollutant emissions. Makeup water usage for major operation units is quantified and characterized according to the plant performance. Then, the impacts of power generation technology and CO_2 capture on makeup water usage are evaluated and discussed.

PC Power Plant Performance

The plant performance evaluation starts by estimating thermal efficiencies. The key performance results are summarized in Table 2. The thermal efficiencies of the steam cycle for supercritical power plants increase by about 2 to 3 percent due to higher temperature and steam pressure generated compared to subcritical power plants. When CO_2 is captured, the thermal efficiency for the steam cycle decreases due to the steam extraction from the steam turbine. For a given type of PC plant, net plant efficiency of the plant with the CO_2 capture decreases by about 12%, compared to the PC plant without CO_2 capture.

Table 1 Design assumptions for pulverized coal power plant

Parameter	Value
Coal	
HHV	13260 Btu/lb
Carbon	73.81, wt%
Ash	7.24, wt%
Moisture	5.05, wt%
Steam cycle	
Boiler type	Subcritical/Supercritical
Boiler blowdown rate	6% of steam flow
Miscellaneous steam loss	0.4% of steam flow [a]
Demineralizer regenerant wastes	8.5% of boiler makeup water [a]
Cooling system	
Tower inlet water temperature	80ºF
Tower outlet water temperature	60ºF
Dry bulb air temperature	60ºF
Wet bulb air temperature	51.5ºF
Cycle of concentration	4
Drift loss	0.001% of cooling water [b]
Cooling load of auxiliary equipment	1.41% of heat rejected by steam cycle [a]
Bottom and fly ash	
water content in wet bottom ash waste	60%
water content in wet fly ash waste	60%
Flue gas desulfurization	
Reagent type	Limestone
Oxidation type	Forced
Amine system	
Sorbent used	Advanced Amine (FG+)
Makeup wash water for wash section above the absorber	0.8% of mass flow rate of flue gas entering the absorber [c]
Cooling water usage of capture process alone	79.5 tons cooling water per ton of CO_2 compressed product [c,d]
CO_2 removal efficiency	90%
CO_2 product purity	99.5%

[a] (EPRI, 1999) , [b] (NETL, 2007a), [c] (FLUOR 2005a and 2005b), [d] The capture process cooling duty is estimated corresponding to the cooling water temperature change of 20ºF across the tower.

All subcritical and supercritical cases are controlled to have the same net electricity output, with and without CCS. Table 2 shows that in addition to the same net electricity output, the subcritical PC plant has somewhat larger gross power outputs than the supercritical plant. For the same net electricity output, the gross electricity output increases by 17% on average when the advanced amine-based CO_2 capture system is used.

The thermal performance of PC plants affects feed coal consumption and pollutant emissions. For the same net electricity output, subcritical PC plants have higher steam cycle heat rates than supercritical PC plants. As a result, the subcritical plants have larger feed coal flow rates, compared to the supercritical plants. There are higher bottom and fly ash emissions produced, and larger requirements for limestone in the subcritical PC plant. When the CO_2 capture system is used, there is a higher requirement for coal use, ash emissions and limestone. For example, feed coal consumption increases by 50% for the subcritical case and 45% for the supercritical case when CO_2 is captured

by the advanced amine system, compared to the plants without carbon capture. In addition, CO_2 captured product decreases by 9% for supercritical versus subcritical plants.

Table 2 Performance of pulverized coal power plants with and without carbon dioxide capture

Parameter	Pulverized Coal Power Plant			
Boiler	Subcritical	Supercritical	Subcritical	Supercritical
Amine-based CO_2 capture	Without	without	with	with
Plant gross electricity (MW)	591.4	588.1	696.0	680.9
Plant net electricity (MW)	550	550	550	550
Net plant efficiency (%)	36.35	38.69	24.28	26.67
Steam cycle heat rate (Btu/kWhr)	7790	7359	9908	9222
Coal (tons/hr)	194.7	182.9	291.4	265.3
CO_2 captured product (tons/hr)	-	-	716.7	652.5

Makeup Water Usage by Unit Operations

Makeup water usage is quantified for major units including the boiler, cooling system, SCR, FGD, and ash controls. Then, the distribution of makeup water usage in PC power plants is characterized by unit operations.

Makeup water usage for the major unit operations is shown in Figure 3. The total makeup water usage of a PC plant without CCS reaches 701 gallons/MWhr for the subcritical case and 637 gallons/ MWhr for the supercritical case. When CCS is used, the total makeup water usage significantly increases to 1,306 gallons/MWhr for the subcritical case and 1,159 gallons/MWhr for the supercritical case.
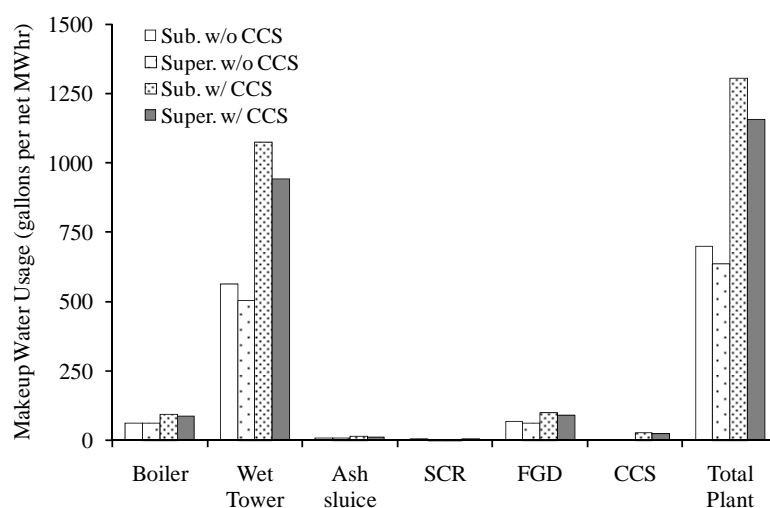

Figure 3 Makeup water usage normalized by net plant electricity output

Table 3 summarizes the distribution as a percent of the total makeup water usage by these unit operations, with and without CCS. The cooling system is the largest user of makeup water in PC power plants. Table 3 shows that approximately 80% of water is used for the cooling system, mainly due to cooling tower evaporation, drift and blowdown. The flue gas abatement technology units require the remaining makeup water. The FGD is the largest of the flue gas technologies consuming makeup water in PC plants. Compared to the FGD, the boiler requires less makeup water.

Table 3 Distribution of makeup water usage in pulverized coal power plant

Unit Operation	Subcritical		Supercritical	
	w/o CCS	w/ CCS	w/o CCS	w/ CCS
Boiler	8.8%	9.5%	7.0%	7.6%
Wet Tower	80.3%	79.2%	82.2%	81.4%
Ash sluice	1.3%	1.3%	1.0%	1.1%
SCR	0.1%	0.1%	0.1%	0.1%
FGD	9.5%	9.8%	7.6%	7.8%
CCS	0.0%	0.0%	2.0%	2.1%

When CO_2 is captured using the amine-based system, makeup water is required to replace the loss from contact cooler evaporation, dilute the makeup MEA, and supplement the reclaimer loss. A water wash section may be installed above the absorber to minimize solvent losses due to mechanical entrainment and evaporation (NETL, 2007a). The flue gas leaving from the absorber is contacted with a recirculating water stream for the removal of most of the lean solvent. Makeup water required to maintain the wash water level is empirically estimated as a percent of flue gas entering the amine-based system. The resulting makeup water including all factors above for the wash water is only 2.0% of the total water usage.

Effects of Power Generation Technology on Makeup Water Usage

Power generation technology of coal-based plants propagates the influences through the steam cycle (e.g. boiler and condenser) to environmental controls and the cooling system. Supercritical PC plants with higher thermal efficiencies burn less coal, and generate lower emissions of ash, CO_2 and sulfur dioxide (SO_2) than subcritical plants. Figure 4 demonstrates makeup water usage savings for supercritical versus subcritical PC plants, indicating the impacts of power generation technology on water.

Lower steam cycle heat rates of supercritical PC plants compared to subcritical PC plants lead to the smaller requirement of heat rejected around the condenser and reduce the amount of recirculating cooling water, which directly affects the makeup water usage.

In comparison with subcritical plant, makeup water required for the FGD in the supercritical plant reduces by 6% for the case without CCS and 9% for the case with CCS because SO_2 emissions generated are lower for the supercritical plants. As shown in Figure 4, makeup water savings of the cooling system for supercritical PC plant compared to subcritical PC plant reach 10% for the case without CCS and 12% for the case with CCS. As a short summary, the total makeup water usage of the plant for supercritical versus subcritical cases reduce by 9% for PC plant without CCS and 11% for PC plant with CCS.
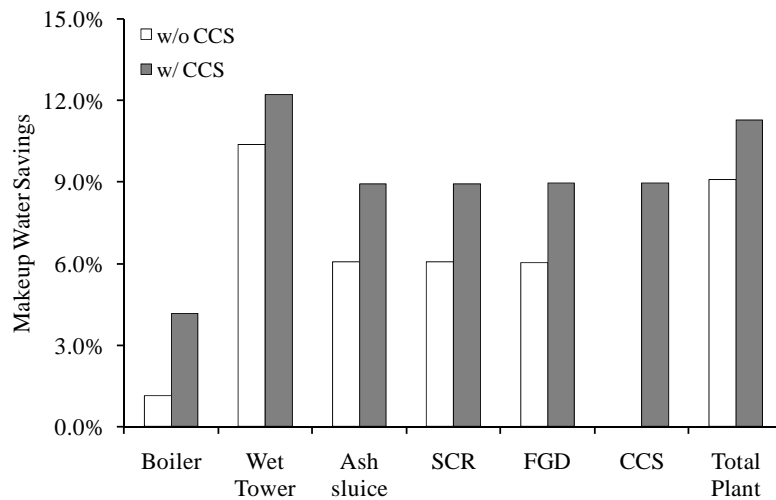
Figure 4 Makeup water savings for supercritical versus subcritical power plants

Effects of Amine-Based Capture System on Makeup Water Usage

The modeling results of amine-based CO_2 capture performance show that the reboiler regeneration heat required is 1,520 Btu/lb CO_2. That heat required to support CO_2 regeneration is provided by the steam extracted from plant steam cycle. The heat content change of steam across a reboiler is about 1,000 Btu/lb, which is same as the value in NETL baseline study for PC plants where the IP steam is used (NETL, 2007a). As a result, about forty percent of steam mass flow rate on average is extracted from the steam cycle. The steam extraction reduces the thermal efficiency and increases the steam cycle heat rate, in comparisons with the PC plants without CCS. In addition to the increased steam cycle heat rates, additional electricity requirements for the amine capture system substantially increase feed coal consumption, as shown in Table 2. As a result, net plant efficiency significantly decreases.
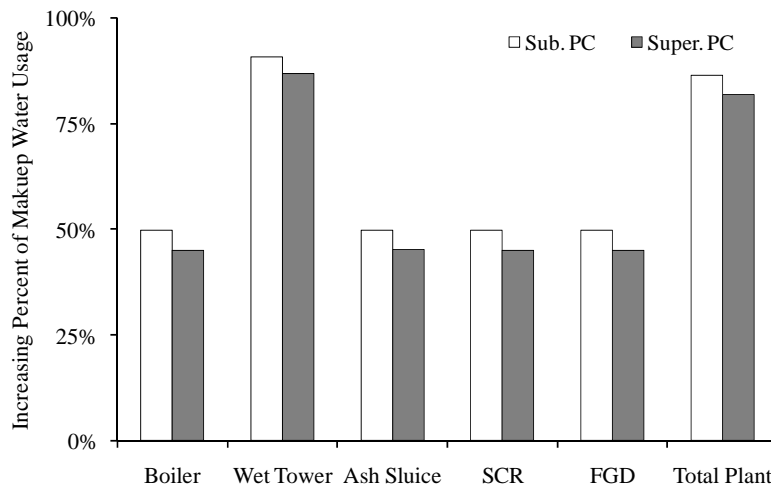

Figure 5 Effect of amine-based CO_2 capture on makeup water usage

The increased steam cycle heat rate and additional electricity requirements for CO_2 capture result in more steam, SO_2 and CO_2 emissions produced, which in turn lead to the significant increasing of makeup water usage for the boiler, FGD, and cooling system for maintaining CO_2 capture process. Figure 5 shows the changes of makeup water usage for both supercritical and subcritical PC plants to quantify water impacts of the amine-based CO_2 capture system. When CO_2 is captured, makeup water usage of the boiler and the FGD increase by approximately 45% to

---

50% for both types of PC plants; the makeup water of cooling systems increases by approximately 90 percent when CO_2 is capture. Overall, makeup water usage for the entire plant significantly increases by over 80% for subcritical and supercritical PC plants.

Conclusions

The IECM is exercised to examine the performance of PC power plants. Makeup water required for major units in PC plants under various environmental controls is quantified. The largest percent of makeup water supplied to the plants is used for the cooling system, followed by uses of makeup water for the FGD and the boiler. Makeup water required for SCR and ash sluice is relatively smaller.

The power generation technology and CO_2 capture system propagate their influences through the steam cycle to unit operations and environmental controls. Those influences on makeup water usage are highlighted and quantified. Supercritical PC plants have higher thermal efficiencies and require less makeup water for major units, compared to subcritical PC plants, which imply that improved thermodynamics of the steam cycle should help reduce water consumption for power plants. When the amine-based system is used to capture CO_2, thermal performance of the steam cycle gets worse due to the extraction of the LP or IP steam to support the operation of the reboiler. With additional cooling water for the amine-based system, makeup water of the cooling system significantly increases with the CO_2 capture. The CO_2 capture system has much more substantial impacts on makeup water consumption than the boiler technology.

References

Aroonwilas, A.; Veawab, A. Integration of CO_2 Capture Unit Using Single- and Blended-Amines into Supercritical Coal-fired Power Plants: Implications for Emission and Energy Management. *International Journal of Greenhouse Gas Control*, 2007, 1: 143-150.

Aspen. Aspen Plus 12.1 User Guide; Aspen Technology, Inc., Cambridge, MA, June 2003.

Bedillion, M.; Berkenpas, M.B.; Kietzke, K.; and Rubin, E.S. PISCES Power Plant Chemical Assessment Model Technical Documentation. Prepared by Carnegie Mellon University for the Electric Power Research Institute, Pittsburgh, PA, July 1997.

EERE. Energy Tips-Steam Sheet #9: *Minimize Boiler Blowdown*. Energy Efficiency and Renewable Energy, U.S. Department of Energy, January 2006.
http://www1.eere.energy.gov/industry/bestpractices/pdfs/steam9_blowdown.pdf. (accessed on May 22, 2008).

EPRI. Water Management System in Ash-Handling Systems; Report CS-5369, Electric Power Research Institute, Palo Alto, CA, 1987.

EPRI. PISCES: Power Plant Chemical Assessment Model (3.03): User Documentation; Report No CM-112347, Electric Power Research Institute, Palo Alto, CA, 1999.

Feeley III, T. J.; Green, L.; McNemar, A.; Carney, B.A. and Pletcher, S. *Department of Energy/Office of Fossil Energy's Water-Energy Interface Research Program*. DOE/FE's Power Plant Water Management R&D Program Summary, April 2006a. http://www.netl.doe.gov/technologies/coalpower/ewr/ref-shelf.html#Water. Accessed on July 7, 2008.

Feeley III, T. J.; Pletcher, S.; Carney, B.; and McNemar, A. T. *Department of Energy/National Energy Technology Laboratory's Power Plant-Water R&D Program*, 2006b. http://www.netl.doe.gov/technologies/coalpower/ewr/ref-shelf.html#Water. Accessed on July 7, 2008.

Feeley III, T,J.; Skone, T. J.; Stiegel Jr., G. J.; McNemar, A.; Nemeth, M.; Schimmoller, B.; Murphy, James T.; Manfredo, L. Water: A critical resource in the thermoelectric power industry. *Energy*, 2008, 33:1-11.

FLUOR. Study and Estimate for CO_2 Capture Facilities for the Proposed 800 MW Combined Cycle Power Plant-Tjeldbergodden, Norway. Final Report CB2005-0022, April 2005a.

FLUOR. CO_2 Capture Study at Mongstad. Final Report CB2005-0079, June 2005b.

Harrell, G. Boiler Blowdown Energy Recovery, *Energy Engineering*, 2004, 101 (5): 32-42.

IPCC. IPCC Special Report on Carbon Dioxide Capture and Storage. Prepared by Working Group III of the Intergovernmental Panel on Climate Change, Cambridge University Press, Cambridge, United Kingdom and New York, NY, USA, 2005.

Knuutila, H.; Svendsen, H. F.; and Anttila, M. CO_2 Capture from Coal-fired Power Plants Based on Sodium Carbonate Slurry; a Systems Feasibility and Sensitivity Study. *International Journal of Greenhouse Gas Control*, 2009, 3:143-151.

Rao, A.B.; and Rubin, E.S. A Technical, Economic, and Environmental Assessment of Amine-based CO_2 Capture Technology for Power Plant Greenhouse Gas Control. *Environmental Science and Technology* 2002, 36: 4467–4475.

Berkenpas, M. B.; Rubin, E. S. and Zaremsky, C. J. User Documentation: Integrated Environmental Control Model with Carbon Capture and Storage. Prepared by Carnegie Mellon University for U.S. DOE's National Energy Technology Laboratory, Pittsburgh, PA, May 2007.

NETL. Power Plant Water Usage and Loss Study. U.S. Department of Energy National Energy Technology Laboratory, August 2005. Revised May 2007.

NETL, Cost and Performance Baseline for Fossil Energy Plants. Report DOE/NETL-2007/1281, U.S. Department of Energy National Energy Technology Laboratory, August 2007a.

NETL. Estimating FreshWater Needs to Meet Future Thermoelectric Generation Requirements. DOE/NETL-400/2007/1304, U.S. Department of Energy National Energy Technology Laboratory, September 2007b.

NETL. Carbon Dioxide Capture from Existing Coal-Fired Power Plants. Report DOE/NETL-401/110907, National Energy Technology Laboratory, November 2007c.

Rao, Anand B.; Rubin, Edward S. and Berkenpas, M.B. Amine-based CO_2 Capture and Storage Systems for fossil Fuel Power Plant. Prepared by Carnegie Mellon University for U.S. DOE's National Energy Technology Laboratory, Pittsburgh, PA, March 2004.

Rao, A.B.; and Rubin, E.S. Identifying Cost-effective CO_2 Control Levels for Amine-based CO_2 Capture Systems. *Industrial and Engineering Chemistry Research*, 2006, 45(8):2421-2429.

Rubin, E.S.; Chao, C.; and Rao, A.B. Cost and Performance of Fossil Power Plants with CO_2 Capture and Storage. *Energy Policy*, 2007, 35:4444-4454.

Zhai, H.; M. Berkenpas, and E.S. Rubin, IECM Model Documentation: Wet Cooling Tower. Prepared by Carnegie Mellon University for U.S. Department of Energy's National Energy Technology Laboratory, Pittsburgh, PA, November, 2009.

IECM Technical Documentation: Volume IV
Pulverized Coal Power Plant Model
and IGCC Plant Model Updates

DE-AC26-04NT41917

Disclaimer

This report was prepared as an account of work sponsored by an agency of the United States Government. Neither the United States Government nor any agency thereof, nor any of their employees, makes any warranty, express or implied, or assumes any legal liability or responsibility for the accuracy, completeness, or usefulness of any information, apparatus, product, or process disclosed, or represents that its use would not infringe privately owned rights. Reference therein to any specific commercial product, process, or service by trade name, trademark, manufacturer, or otherwise does not necessarily constitute or imply its endorsement, recommendation, or favoring by the United States Government or any agency thereof. The views and opinions of authors expressed therein do not necessarily state or reflect those of the United States Government or any agency thereof.

IECM Technical Documentation: Volume IV
Pulverized Coal Power Plant Model
and IGCC Plant Model Updates

DE-AC26-04NT41917

Development and Application of the Integrated Environmental Control Model

Prepared for:

Prepared by:
Peter L. Versteeg
Hari Chandan Mantripragada
Haibo Zhai
Karen Kietzke
Edward S. Rubin
Carnegie Mellon University
Pittsburgh, PA 15213
www.iecm-online.com

November 2009

Table of Contents

Acknowledgements

List of Figures

List of Tables

PC Base Plant Updates

Overview of Base Plant Updates

The Base Plant module of the PC plant refers to plant with no environmental control systems. In the newest version of the IECM, a number of updates were made to the base plant. Specifically,

1. The default cooling system has been set to be a once-through system.
2. Ambient absolute air humidity is calculated in terms of given relative humidity.
3. A new process type, Steam Cycle has been added to the Set Parameter Base Plant screen.
4. The steam cycle heat rate has been updated based on the NETL 2007 Baseline Report and is now calculated as a function of boiler type, cooling technology, and CO_2 capture option.
5. Base plant power requirements are updated based on the NETL 2007 Baseline Report and are calculated as a function of boiler type and/or coal rank.
6. Leakage air at the preheater is updated based on recent guidelines [5]
7. The costs of all the pulverized coal power plant technologies were updated based on information available in the NETL 2007 Baseline Report.

The changes in the defaults are shown below in Table 1.

Table 1: Updated Base Plant Parameters

IECM Screen	Parameter	IECM 5.22 Defaults	IECM 6.2 Defaults	References
Configure Plant	Cooling System	Wet tower	Once-through	
Overall Plant	Ambient Air Humidity (lb H2O/lb dry air)	1.800e-02	9.879e-3 (Calc)	
Base Plant	Steam cycle heat rate (Btu/kWh)			
	Subcritical	7880	7790	[2]
	Supercritical	7098	7359	[2]
	Ultra-supercritical	6458	6705	
	Leakage Air at Preheater (%)	20	10	[5]
	Base Plant Power Requirements (% of MWg)			[2]
	Coal Pulverizer	0.6000	0.5105 (Calc)	
	Steam Cycle Pumps	0.6500	0.3100 (Calc)	
	Forced / Induced Draft Fans	1.500	1.408 (Calc)	
	Cooling System	1.800	0.4000 (Calc)	
	Miscellaneous	1.300	0.9900 (Calc)	

Updated Cost Correction Factors

For the new version of the IECM, the base process performance costs functions for all the pulverized coal power plant technologies were multiplied by a cost correction factor based on information available in the NETL 2007 Baseline Report [2]. This cost correction factor updates the costs of each technology. A summary table of the cost correction factors applied to each technology is shown in Table 2.

Table 2: Updated Cost Correction Factors by Technology

Technology	Cost Correction Factor
Base plant	1.12
SCR	0.99
TSP	0.86
FGD	1.59
Water System	1.01
CCS	1.60

Advanced Amine-Based CO$_2$ Capture System

Abstract

In response to growing interest in large scale carbon dioxide (CO$_2$) capture, Fluor and Mitsubishi Heavy Industries (MHI) have developed commercially available advanced CO$_2$ capture systems based on solutions of aqueous amines [1]. Fluor's most recent offering is the Econamine® FG+ process, which uses an aqueous mixture of monoethanolamine (MEA) and proprietary corrosion inhibitors [2]. The original IECM capture model is based on an MEA capture process that was representative of the state of the technology in 2002. In this updated version, a new CO$_2$ capture model based on the Fluor's Econamine® FG+ process is included in the IECM. For this new model, the performance of the original MEA model was adjusted to reflect process improvements in amine-based CO$_2$ capture. The corresponding costs have also been updated to reflect technology improvements and the current pricing environment.

Introduction

MEA is costly to replace, has a significant regeneration heat requirement and can be corrosive. Improvements in MEA-based CO$_2$ capture processes therefore have been focused at lowering solvent losses, providing improved heat integration, and research into additives that inhibit corrosion allowing for the use of carbon steel instead of more expensive stainless steel [3]. While many of these improvements are proprietary, the CO$_2$ capture system incorporated into the IECM can be modified to match the information publicly available on the performance and cost of these systems. The documentation that follows describes parameter updates made to the original MEA based CO$_2$ capture system that were applied for the advanced amine-based CO$_2$ capture system, model adjustments made for the advanced amine-based CO$_2$ capture system, menu updates for the capture models in the IECM in general, and a comparison between the MEA and advanced amine-based CO$_2$ capture system.

Parameter Updates for the Advanced Amine-Based CO_2 Capture System

The documentation in this section describes default parameter updates to the IECM MEA based CO_2 capture model that were made to represent the amine-based CO_2 capture processes in the DOE/NETL August 2007 Baseline Report, which is based on Fluor's Econamine® FG+ CO_2 capture system [2]. In the cases where the DOE/NETL August 2007 Baseline Report does not specify values for needed parameters, information was used from similar reports which included advanced amine-based CO_2 capture processes, or were transferred from the original MEA based CO_2 capture model. The existing and updated cost and performance parameters are shown in each of the Tables below. The IECM 6.2 defaults are shown when a new supercritical PC plant is chosen that has been configured with a Hot-Side SCR, Cost-Side ESP, Wet FGD, and an Amine System with Advanced Amine (FG+) selected as the solvent.

Table 3: Set Parameters > CO_2 Capture > CO_2 Capture System Process > Config Menu

	Parameter	IECM 5.22 Default	IECM 6.2 Default	References
Config	Sorbent Used	MEA	Adv. Amine	
	Auxiliary Natural Gas Boiler	None	None	
	CO_2 Product Compressor Used?	Yes	Yes	
	Flue Gas Bypass Control	No Bypass	No Bypass	
	Direct Contact Cooler (DCC) Used?	Yes	Yes	
	SO_2 Polisher Used?	N/A	Yes	[2]
	SO_2 Outlet Concentration (ppmv)	N/A	10	[2]
	Temperature Exiting DDC (F)	122F	113F	IECM[1]

Table 4: Set Parameters > CO_2 Capture > CO_2 Capture System Process > Performance Menu

	Parameter	IECM 5.22 Default	IECM 6.2 Default	References
Performance	Maximum CO_2 Removal Efficiency (%)	90%	90%	
	Scrubber Removal Efficiency (%)	90%	90%	[2]
	SO_2 Removal Efficiency (%)	99.50%	100%	[2]
	SO_3 Removal Efficiency (%)	99.50%	99.50%	
	NO_2 Removal Efficiency (%)	25%	25%	
	HCl Removal Efficiency (%)	95%	95%	
	PM Removal Efficiency (%)	50%	50%	
	Max Train CO_2 Capacity (tons/hr)	230	230	
	# Absorbers	2	3	IECM[1]
	Spare Absorbers	0	0	
	Max CO_2 Compressor Capacity (tons/hr)	330	330	
	No.of Operating CO_2 Compressors	2	2	
	No.of Spare CO_2 Compressors	0	0	
	Scrubber Power Requirement (%MWg)	14.00%	9.187%	IECM[1]

Table 5: Set Parameters > CO_2 Capture > CO_2 Capture System Process > Capture Menu

	Parameter	IECM 5.22 Default	IECM 6.2 Default	References
Capture	Sorbent concentration (%)	30%	30%	[4]

	Lean CO2 Loading (mol CO_2/mol sorb)	0.2	0.19	[4]
	Nominal Sorbent Loss (lb / ton CO_2)	3	0.6[2]	[2]
	Liq/Gas Ratio (Ratio)	2.876	3.072	IECM[1]
	Ammonia Generation (mol NH_3 / mol sorb.)	1	1	
	Gas Phase Pressure Drop (psia)	2	1	[4]
	ID Fan Efficiency (%)	75%	75%	
	Makeup Water for Wash Section (% raw flue gas)	N/A	0.8	IECM[1]
	Regenerator Heat Requirement (Btu / lb CO2)	1975	1516	[2]
	Steam Ht. Cont (Btu/lb Steam)	860.4	1397	[2]
	Heat to Electricity Efficiency	14%	22%[3]	[2]
	Solvent Pumping Head	30	30	
	Pump Efficiency	75%	75%	
	% Solids in Reclaimer Waste	40%	40%	
	Capture System Cooling Duty (ton H_2O/ton CO_2)	N/A	46.19	IECM[1]

Table 6: Set Parameters > CO_2 Capture > CO_2 Capture System Process > CO_2 Storage Menu

	Parameter	IECM 5.22 Default	IECM 6.2 Default	References
CO_2 Storage	CO_2 Product Pressure (psig)	2000	2000	
	CO_2 Compressor Efficiency (%)	80%	80%	
	CO_2 Unit Compression Energy (kWh/ton CO_2)	107	107	

Table 7: Set Parameters > CO_2 Capture > CO_2 Capture System Process > Retrofit Cost Menu

	Parameter	IECM 5.22 Default	IECM 6.2 Default	References
Retrofit Cost (All Units in retro $/new $)	SO2 Polisher/ Direct Contact Cooler	1	1	
	Flue Gas Blower	1	1	
	CO_2 Absorber Vessel	1	1	
	Heat Exchangers	1	1	
	Circulation Pumps	1	1	
	Sorbent Regenerator	1	1	
	Reboiler	1	1	
	Steam Extractor	1	1	
	Sorbent Reclaimer	1	1	
	Sorbent Processing	1	1	
	CO2 Drying and Compression Unit	1	1	
	Auxiliary Natural Gas Boiler	1	1	
	Auxiliary Steam Turbine	1	1	

Table 8: Set Parameters CO_2 Capture > CO_2 Capture System Process > Capital Cost Menu

	Parameter	IECM 5.22 Default	IECM 6.2 Default	References
Capital Cost	Construction Time (years)	3	3	
	General Facilities Capital (%PFC)	10	10	
	Engineering & Home Office Fees (%PFC)	7	7	

	Parameter		
	Project Contingency Cost (%PFC)	15	15	
	Process Contingency Cost (%PFC)	5	5	
	Royalty Fees (%PFC)	0.5	0.5	
	Months of Fixed O&M (months)	1	1	
	Months of Variable O&M (months)	1	1	
	Misc. Capital Cost (%TPI)	2	2	
	Inventory Capital (%TPC)	0.5	0.5	
	TCR Recovery Factor (%)	100	100	

Table 9: Set Parameters > CO$_2$ Capture > CO$_2$ Capture System Process > O&M Cost Menu

	Parameter	IECM 5.22 Default	IECM 6.2 Default	References
O&M Cost	Sorbent Cost ($/ton)	1379	2142	[2]
	Inhibitor Cost (% of MEA)	20	0	[2]
	Activated Carbon Cost ($/ton)	1411	2000	[2]
	Caustic (NaOH) Cost ($/ton)	666.6	413	[2]
	Water Cost ($/kgal)	0.8874	1.03	[2]
	Reclaimer Waste Disposal Cost ($/ton)	201.2	211.6	
	Electricity Price (Base Plant)	43.27	59.97	
	Number of Operating Jobs (jobs/shift)	2	2	
	Number of Operating Shifts (shifts/day)	4.75	4.75	
	Operating Labor Rate ($/hr)	24.82	33	[2]
	Total Maintenance Cost (%TPC)	2.5	2.5	
	Maint. Cost Allocated to Labor (% total)	40	40	
	Administrative & Support Cost (% total labor)	30	30	
	CO2 Transportation Cost ($/ton)	2.4	2.38	IECM[1]
	CO2 Storage Cost ($/ton)	5.75	6.047	IECM[1]

[1] The IECM calculates updated values based on other values supplied as inputs. These values may change with different plant configurations.

[2] For a more thorough explanation and for the calculation of Nominal Sorbent Loss, see below.

[3] For the calculation of the updated Heat-to-Electricity Efficiency, see below.

Model Adjustments for the Advanced Amine-Based CO$_2$ Capture System

Updated Heat Integration Equation

In order to reflect the new regeneration heat requirement of the Advanced Amine CO$_2$ capture process, the original regression equation was adjusted by a scaling factor. In the original model, regeneration heat is calculated based on the following regression equation:

Regen Heat (Btu/ lb CO$_2$) = Sorbent Circulation (tons/hr)* exp(2.5919 + 0.0259 * Reagent Concentration (%) - 6.3536 * Lean CO$_2$ Loading (mol CO$_2$/sorb) - 0.0015 * Actual CO$_2$ Removal Efficiency (%) - 0.0059 * CO$_2$ Flue Gas (lb moles/hr)*100/Total Gas (lb moles/hr) / Sorbent Molecular Weight (lb/lb*mole)/ CO$_2$ Captured (tons/hr)* 429.9046

This regression equation was multiplied by a scaling factor of 0.7639 to approximately match the updated regeneration energy of 1516 Btu/ lb CO_2 currently available by advanced amine-based CO_2 capture systems, from 1984 Btu/ lb CO_2 available for conventional MEA systems.

Updated Heat-to-Electricity Conversion Efficiency Equation

In previous versions of the IECM, the Heat-to-Electricity Conversion Efficiency (or equivalence factor) was selected from a range of values in the literature as 14%. In this new version of the IECM, the Heat-to-Electricity Conversion Efficiency was estimated from data obtained using the NETL 2007 Baseline report [2]. In the NETL Baseline report, the following data is available for a subcritical plant without CO_2 Capture:

Case 9 – Subcritical Plant without CO_2 Capture,
Gross Plant Size: 583 MW
Coal Flow Rate: 437,699 lb coal/hr

Therefore, approximately 750 lb coal/hr is burned for each gross MW produced for this plant. For a subcritical plant with CO_2 Capture:

Case 10 – Subcritical Plan with CO_2 Capture,
Gross Plant Size: 680 MW
Coal Flow Rate: 646,589 lb coal/hr

Based on 750 lb coal/hr per gross MW produced and the 646,589 lb coal/hr flow rate of coal, the plant in Case 10 should produce approximately 862 MW gross absent the CO_2 capture system. Therefore,
862 MW-680MW = approximately 182 gross MW lost due to the CO_2 capture system

For NETL Case 10, the subcritical plant with the CO_2 capture system, 1,995,300 lb steam/hr of quality 1397.7 Btu/lb is diverted from the low pressure turbine and this steam flows to the reboiler of the advanced amine-based CO_2 capture unit. Therefore the Heat-to-Electricity Conversion Efficiency can be calculated as:

$$\frac{182[\text{MW}]}{1995300[\text{lb steam/hr}]} * 1397.7[\text{Btu/lb steam}] * 2.93\text{E}^{-7}[\text{MW/(Btu/hr)}] = 0.222 \text{ or } 22\%,$$

Where 2.93E^{-7} [MW/(Btu/hr)] equals the MW equivalent of 1 Btu/hr.

Similar results are shown using NETL Cases 11 and 12 for supercritical plants. In the new version of the IECM, the Heat-to-Electricity Conversion Efficiency as well as the steam quality parameters were updated for both the MEA and Advanced Amine CO_2 capture systems to reflect these results.

Updated Equivalent Electrical Loss Due to the Capture System

In previous versions of the IECM, the electrical equivalent loss (energy penalty) from the conventional CO_2 capture system was based on multiplying the regeneration energy requirement by the Heat-to-Electricity Conversion Efficiency. In the updated version of the IECM, this calculation was modified to reflect a more realistic process. The electrical equivalent loss (MW) due to the steam requirements in the reboiler are calculated in two steps, first by calculating the steam flow rate directly, and then by using this value and the Heat-to-Electricity Conversion Efficiency to calculating the electrical equivalent loss:

1. The steam flow rate is calculated as:

$$\dot{M}_{Steam\ Flow} = \frac{E_{Regeneration} * CO_{2\,Flow}}{Enthalpy_{Steam\ Inlet} - Enthalpy_{Steam\ Condensate}}$$

Where:

$\dot{M}_{Steam\ Flow}$ = Steam Flow Rate [lb/hr]
$E_{Regeneration}$ = Regeneration Heat Energy [Btu/ lb CO_2]
$CO_{2\,Flow}$ = Flow Rate of CO_2 Captured [lb CO_2/hr]
$Enthalpy_{Steam\ Inlet}$ = Enthaly of Steam at Reboiler Inlet [Btu/lb CO_2]
$Enthalpy_{Steam\ Inlet}$ = Enthalpy of Steam at Reboiler Outlet [Btu/lb CO_2]

2. The equivalent electrical loss (MW) is calculated as:

$$MW_{Eq.} = (Heat - to - Electricity\ Efficiency) * \dot{M}_{Steam\ Flow} * Enthalpy_{Steam\ Inlet} * 2.97E^{-7}$$

Where:

$MW_{Eq.}$ = Equivalent Steam Usage [MW]
$Heat - to - Electricity\ Efficiency$ = Energy Conversion Efficiency [dimensionless]
$CO_{2\,Flow}$ = Flow Rate of CO_2 Captured [lb CO_2/hr]
$Enthalpy_{Steam\ Inlet}$ = Enthaly of Steam at Reboiler Inlet [Btu/lb CO_2]
$2.97E^{-7}$ = Conversion Factor for Btu to MW [MW/[Btu/hr]]

Updated Base Plant Cost Equations for the Case with CO_2 Capture

In past versions of the IECM, the costs of the equipment in the Base Plant depended on the gross power produced (MW) by the power plant. In the updated version of the IECM for cases with CO_2 capture, the majority of equipment in the Base Plant is instead sized on the gross power produced (MW) plus the equivalent electrical loss (MW), which is called the Gross Power Produced Effective internally in the IECM. This new calculation accounts for the steam produced by the base plant that is not used to generate electricity but is instead used to regenerate amine in the CO_2 capture system. The only exception is the Turbine Island, which is still sized based the gross power produced. The Turbine Island does not need be sized based on the equivalent electrical loss because it is not part of the set of equipment that produces steam. This adjustment more realistically captures the cost equations of the base plant equipment for cases with CO_2 capture.

Updated Amine Usage for the Advanced Capture System

For the advanced amine-based CO_2 capture system, the Nominal Sorbent Loss (lb/ton CO_2) represents the amount of sorbent that has been lost due to unwanted polymerization and oxidation reactions. The total sorbent loss, which requires makeup sorbent (called Sorbent (lb/hr)on the Get Results, CO_2 Capture, Diagram screen), represents the Nominal Sorbent Loss (lb/ ton CO_2) minus the amount of CO_2 regenerated in the reclaimer.

Menu Updates to the IECM CO₂ Capture System

Updated CO₂ Capture, Config Menu

The IECM CO₂ Capture screens have been updated to include the changes listed in this document. The updated Advanced Amine process has been included in the Set Parameters, CO₂ Capture, Config Menu, and the user can now select between traditional MEA and Advanced Amine (FG+). An additional update to the Set Parameters, CO₂ Capture, Config Menu is the inclusion of a polishing unit intended to lower the SO₂ concentration in the feed gas. SO₂ can react with MEA to produce undesirable and irreversible byproducts, therefore causing a loss of amine in the system that requires makeup [2]. The polishing unit uses caustic to capture the SO₂, reducing the cost of makeup chemicals. The user can choose whether or not to include the polishing unit. The updated Set Parameters, CO₂ Capture, Config Menu is shown in Figure 1.

Figure 1: Updated CO2 Capture, Config Menu.

Updated CO₂ Capture, Capture Menu

The CO₂ capture menu for the advanced amine system (Figure 2) has been updated to show only the Nominal Sorbent Loss. The Sorbent Oxidation Loss line has been collapsed into Nominal Sorbent Loss to reflect the lack of detailed information on this parameter available for advanced amine capture systems.
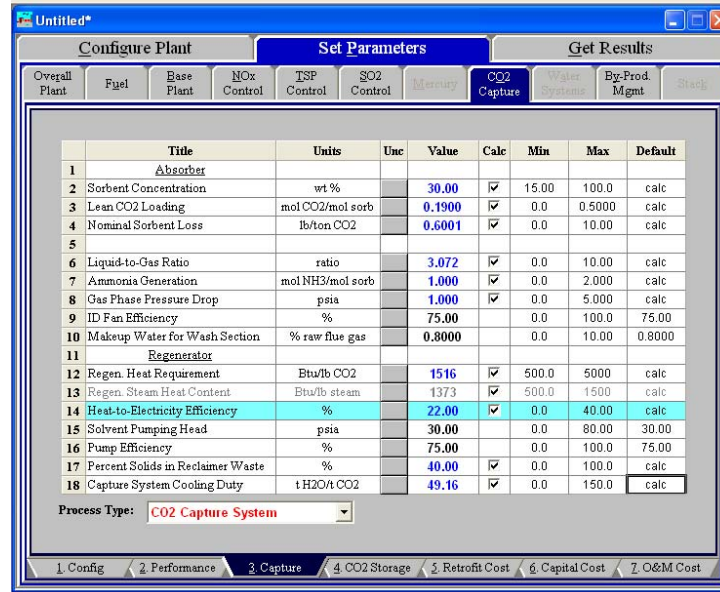
Figure 2:Updated CO₂ Capture, Capture Menu

Case Studies of PC Plants

Introduction to Case Studies

The NETL 2007 Baseline report presents four pulverized coal case studies: Subcritical PC plants with and without a CO_2 Capture System, carbon, and Supercritical PC plants with and without a CO_2 Capture System. For these case studies, parameters from the NETL 2007 Baseline Report [2] were duplicated in the IECM, and the results from the updated IECM are presented.

Case Study #1: PC Supercritical without CO₂ Capture

For the Supercritical plant without a CO_2 Capture System, a number of default parameters in the IECM were changed so that these parameters matched the NETL 2007 Baseline Report. These changes are shown in Table 10.

Table 10: IECM Parameters Changed for Case 1 - Supercritical Plants without CO₂ Capture

	Parameter	IECM Default	IECM Case 1
Configure Plant Overall Plant	NO_x Control	None	Hot-Side SCR
	Particulates	None	Fabric Filter
	SO_2 Control	None	Wet FGD
	Cooling System	None	Wet Cooling Tower

Fuel Properties	Fuel Name	Appalachian Medium Sulfur	Illinois #6
Overall Plant Performance	Capacity Factor (%)	75.00	85.00
	Ambient Air Temperature (Avg.) (°F)	77.00	70.00
Overall Plant Financing	Discount Rate (Before Taxes) (fraction)	0.103	1.0E-4
	Fixed Charge Factor (FCF) (fraction)	0.148	0.164
	Plant or Project Book Life (years)	30.00	20.00
Overall Plant O&M Cost	Natural Gas Cost ($/mscf)	5.99	7.58
Base Plant Performance	Gross Electrical Output (MWg)	500	580.2
	Unit Type:	Sub-Critical	Supercritical
	Boiler Efficiency (%)	88.89	89.00
	Leakage Air at Preheater (% stoich.)	10	5.5
Base Plant Capital Cost	General Facilities Capital (%PFC)	10.00	2.41
	Engineering & Home Office Fees (%PFC)	6.50	9.37
	Project Contingency Cost (%PFC)	11.67	13.8
	Process Contingency Cost (%PFC)	0.3	0.0
	Royalty Fees (%PFC)	7.00E-2	0.0
	Fixed Operating Cost (months)	1.00	0.0
	Variable Operating Cost (months)	1.00	0.0
	Misc. Capital Cost (%TPI)	2.0	0.0
	Inventory Capital (%TPC)	6.00E-2	0.0
Base Plant O&M Cost	Waste Disposal Cost ($/ton)	9.36	15.45
	Total Maintenance Cost (%TPC)	1.896	1.60
NO_x Control Performance	Actual NOx Removal Efficiency (%)	76.66	86.00
	Hot-Side SCR Power Requirement (% MWg)	0.5088	8.60E-3
NO_x Control Capital Cost	General Facilities Capital (%PFC)	10.00	2.41
	Engineering & Home Office Fees (%PFC)	6.50	9.37
	Project Contingency Cost (%PFC)	11.67	13.80
	Process Contingency Cost (%PFC)	0.3	0.0
	Royalty Fees (%PFC)	7.00E-2	0.0
	Months of Fixed O&M (months)	1	0
	Months of Variable O&M (months)	1	0
	Misc. Capital Cost (%TPI)	2	0
	Inventory Capital (%TPC)	0.5	0
NO_x Control O&M Cost	Total Maintenance Cost (%TPC)	2.00	1.60
TSP Control Performance	Particulate Removal Efficiency (%)	99.10	99.90
	Fabric Filter Power Requirement (% MWg)	0.1958	1.70E-2
TSP Control Capital Cost	General Facilities Capital (%PFC)	1.00	2.41
	Engineering & Home Office Fees (%PFC)	5	9.37
	Project Contingency Cost (%PFC)	20	13.80
	Process Contingency Cost (%PFC)	0	0.0
	Royalty Fees (%PFC)	0	0.0
	Fixed Operating Cost (months)	1.0	0.0
	Variable Operating Cost (months)	1.000	0.0
	Misc. Capital Cost (%TPI)	2.0	0.0
	Inventory Capital (%TPC)	0.5	0.0

TSP Control O&M Cost	Total Maintenance Cost (%TPC)	1.767	1.600
SO₂ Control Performance	Scrubber SO2 Removal Efficiency (%)	85.49	98.00
	Wet FGD Power Requirement (% MWg)	1.607	0.660
SO₂ Control Capital Cost	General Facilities Capital (%PFC)	10	2.41
	Engineering & Home Office Fees (%PFC)	10	9.37
	Project Contingency Cost (%PFC)	15	13.80
	Process Contingency Cost (%PFC)	2	0.0
	Royalty Fees (%PFC)	0.5	0.0
	Fixed Operating Cost (months)	1.0	0.0
	Variable Operating Cost (months)	1.00	0.0
	Misc. Capital Cost (%TPI)	2.0	0.0
	Inventory Capital (%TPC)	0.3545	0.0
SO₂ Control O&M Cost	Total Maintenance Cost (%TPC)	4.306	1.60
Water Systems Performance	Ambient Air Temp (Dry Bulb Avg.) (°F)	77.00	70.00
Water Systems Capital Cost	General Facilities Capital (%PFC)	10	2.410
	Engineering & Home Office Fees (%PFC)	10	9.370
	Project Contingency Cost (%PFC)	15	13.80
	Process Contingency Cost (%PFC)	0	0.0
	Royalty Fees (%PFC)	0.5	0.0
	Fixed Operating Cost (months)	1.0	0.0
	Variable Operating Cost (months)	1.000	0.0
	Misc. Capital Cost (%TPI)	2.0	0.0
	Inventory Capital (%TPC)	0.5	0.0
Water Systems O&M Cost	Total Maintenance Cost (%TPC)	2.0	1.600

The key results of this case study are shown below in summary Table 14.

Case Study #2: PC Supercritical with CO₂ Capture

For the Supercritical plant with a CO_2 Capture System, a number of default parameters in the IECM were changed so that these parameters matched the NETL 2007 Baseline Report. These changes are shown in Table 11.

Table 11: IECM Parameters Changed for Case 2 - Supercritical Plants with CO₂ Capture

	Parameter	IECM Default	IECM Case 2
Configure Plant Overall Plant	NOₓ Control	None	Hot-Side SCR
	Particulates	None	Fabric Filter
	SO₂ Control	None	Wet FGD
	CO₂ Capture	None	Amine System
	Cooling System	None	Wet Cooling Tower
Fuel Properties	Fuel Name	Appalachian Medium Sulfur	Illinois #6
Overall Plant	Capacity Factor (%)	75.00	85.00

Performance	Ambient Air Temperature (Avg.) (°F)	77.00	70.00
Overall Plant Financing	Discount Rate (Before Taxes) (fraction)	0.103	1.0E-4
	Fixed Charge Factor (FCF) (fraction)	0.148	0.175
	Plant or Project Book Life (years)	30.00	20.00
Overall Plant O&M Cost	Natural Gas Cost ($/mscf)	5.99	7.58
Base Plant Performance	Gross Electrical Output (MWg)	500	663.3
	Unit Type:	Sub-Critical	Supercritical
	Boiler Efficiency (%)	88.89	89.00
	Leakage Air at Preheater (% stoich.)	10	5.5
	Coal Pulverizer (% MWg)	0.5897	0.6700
Base Plant Capital Cost	General Facilities Capital (%PFC)	10.00	1.570
	Engineering & Home Office Fees (%PFC)	6.50	9.37
	Project Contingency Cost (%PFC)	11.67	16.38
	Process Contingency Cost (%PFC)	0.3	4.670
	Royalty Fees (%PFC)	7.00E-2	0.0
	Fixed Operating Cost (months)	1.00	0.0
	Variable Operating Cost (months)	1.00	0.0
	Misc. Capital Cost (%TPI)	2.0	0.0
	Inventory Capital (%TPC)	6.00E-2	0.0
Base Plant O&M Cost	Waste Disposal Cost ($/ton)	9.36	15.45
	Total Maintenance Cost (%TPC)	1.896	1.60
NO_x Control Performance	Actual NOx Removal Efficiency (%)	76.66	86.00
	Hot-Side SCR Power Requirement (% MWg)	0.6294	1.100e-2
NO_x Control Capital Cost	General Facilities Capital (%PFC)	10.00	1.57
	Engineering & Home Office Fees (%PFC)	10.00	9.37
	Project Contingency Cost (%PFC)	10.00	16.38
	Process Contingency Cost (%PFC)	6.397	4.670
	Royalty Fees (%PFC)	7.00E-2	0.0
	Months of Fixed O&M (months)	1	0
	Months of Variable O&M (months)	1	0
	Misc. Capital Cost (%TPI)	2	0
	Inventory Capital (%TPC)	0.5	0
NO_x Control O&M Cost	Total Maintenance Cost (%TPC)	2.00	1.60
TSP Control Performance	Particulate Removal Efficiency (%)	99.10	99.90
	Fabric Filter Power Requirement (% MWg)	0.1958	1.70E-2
TSP Control Capital Cost	General Facilities Capital (%PFC)	1.00	1.57
	Engineering & Home Office Fees (%PFC)	5	9.37
	Project Contingency Cost (%PFC)	20	16.38
	Process Contingency Cost (%PFC)	0	4.670
	Royalty Fees (%PFC)	0	0.0
	Fixed Operating Cost (months)	1.0	0
	Variable Operating Cost (months)	1.000	0
	Misc. Capital Cost (%TPI)	2.0	0
	Inventory Capital (%TPC)	0.5	0
TSP Control O&M Cost	Total Maintenance Cost (%TPC)	1.723	1.600

SO$_2$ Control Performance	Scrubber SO2 Removal Efficiency (%)	85.49	98.00
	Wet FGD Power Requirement (% MWg)	1.607	0.83
SO$_2$ Control Capital Cost	General Facilities Capital (%PFC)	10	1.57
	Engineering & Home Office Fees (%PFC)	10	9.37
	Project Contingency Cost (%PFC)	15	16.38
	Process Contingency Cost (%PFC)	2	4.670
	Royalty Fees (%PFC)	0.5	0.0
	Fixed Operating Cost (months)	1.0	0
	Variable Operating Cost (months)	1.00	0
	Misc. Capital Cost (%TPI)	2.0	0
	Inventory Capital (%TPC)	0.3545	0
SO$_2$ Control O&M Cost	Total Maintenance Cost (%TPC)	4.398	1.60
CO2 Capture Config	Sorbent Used	Conv. MEA	Adv. Amine (FG+)
CO$_2$ Capture Performance	Amine Scrubber Power Requirement (% MWg)	13.98	10.28
CO$_2$ Capture Capital Cost	General Facilities Capital (%PFC)	10	1.57
	Engineering & Home Office Fees (%PFC)	7	9.37
	Project Contingency Cost (%PFC)	15	16.38
	Process Contingency Cost (%PFC)	5	4.670
	Royalty Fees (%PFC)	0.5	0.0
	Fixed Operating Cost (months)	1.0	0
	Variable Operating Cost (months)	1.00	0
	Misc. Capital Cost (%TPI)	2.0	0
	Inventory Capital (%TPC)	0.5	0
CO$_2$ Capture O&M Cost	Reclaimer Waste Disposal Cost ($/ton)	211.6	0.0
	Total Maintenance Cost (%TPC)	2.5	1.600
	CO2 Transportation Cost ($/ton)	1.759	0.0
	CO2 Storage Cost ($/ton)	6.047	3.4
Water Systems Performance	Ambient Air Temp (Dry Bulb Avg.) (°F)	77.00	70.00
	Power Requirement (% MWg)	2.8	2.800
Water Systems Capital Cost	General Facilities Capital (%PFC)	10	1.57
	Engineering & Home Office Fees (%PFC)	10	9.37
	Project Contingency Cost (%PFC)	15	16.38
	Process Contingency Cost (%PFC)	0	4.670
	Royalty Fees (%PFC)	0.5	0.0
	Fixed Operating Cost (months)	1.0	0
	Variable Operating Cost (months)	1.000	0
	Misc. Capital Cost (%TPI)	2.0	0
	Inventory Capital (%TPC)	0.5	0
Water Systems O&M Cost	Total Maintenance Cost (%TPC)	2.0	1.600

The key results of this case study are shown below in summary Table 14.

Case Study #3: PC Subcritical without CO$_2$ Capture

For the Subcritical plant without a CO$_2$ Capture System, a number of default parameters in the IECM were changed so that these parameters matched the NETL 2007 Baseline Report. These changes are shown in Table 12.

Table 12: IECM Parameters Changed for Case 3 - Supercritical Plants without CO$_2$ Capture

	Parameter	IECM Default	IECM Case 3
Configure Plant Overall Plant	NO$_x$ Control	None	Hot-Side SCR
	Particulates	None	Fabric Filter
	SO$_2$ Control	None	Wet FGD
	Cooling System	None	Wet Cooling Tower
Fuel Properties	Fuel Name	Appalachian Medium Sulfur	Illinois #6
Overall Plant Performance	Capacity Factor (%)	75.00	85.00
	Ambient Air Temperature (Avg.) (°F)	77.00	70.00
Overall Plant Financing	Discount Rate (Before Taxes) (fraction)	0.103	1.0E-4
	Fixed Charge Factor (FCF) (fraction)	0.148	0.164
	Plant or Project Book Life (years)	30.00	20.00
Overall Plant O&M Cost	Natural Gas Cost ($/mscf)	5.99	7.58
Base Plant Performance	Gross Electrical Output (MWg)	500	583.2
	Unit Type:	Sub-Critical	Sub-Critical
	Boiler Efficiency (%)	88.89	89.00
	Leakage Air at Preheater (% stoich.)	10	5.5
	Coal Pulverizer (% MWg)	0.6425	0.58
Base Plant Capital Cost	General Facilities Capital (%PFC)	10.00	2.515
	Engineering & Home Office Fees (%PFC)	6.50	9.3
	Project Contingency Cost (%PFC)	11.67	13.8
	Process Contingency Cost (%PFC)	0.3	0.0
	Royalty Fees (%PFC)	7.00E-2	0.0
	Fixed Operating Cost (months)	1.00	0.0
	Variable Operating Cost (months)	1.00	0.0
	Misc. Capital Cost (%TPI)	2.0	0.0
	Inventory Capital (%TPC)	6.00E-2	0.0
Base Plant O&M Cost	Waste Disposal Cost ($/ton)	9.36	15.45
	Total Maintenance Cost (%TPC)	1.896	1.60
NO$_x$ Control Performance	Actual NOx Removal Efficiency (%)	76.66	86.00
	Hot-Side SCR Power Requirement (% MWg)	0.5088	8.60E-3
NO$_x$ Control Capital Cost	General Facilities Capital (%PFC)	10.00	2.515
	Engineering & Home Office Fees (%PFC)	6.50	9.3
	Project Contingency Cost (%PFC)	11.67	13.80
	Process Contingency Cost (%PFC)	0.3	0.0
	Royalty Fees (%PFC)	7.00E-2	0.0
	Months of Fixed O&M (months)	1	0
	Months of Variable O&M (months)	1	0

	Misc. Capital Cost (%TPI)	2	0
	Inventory Capital (%TPC)	0.5	0
NO$_x$ Control O&M Cost	Total Maintenance Cost (%TPC)	2.00	1.60
TSP Control Performance	Particulate Removal Efficiency (%)	99.10	99.90
	Fabric Filter Power Requirement (% MWg)	0.1958	1.70E-2
TSP Control Capital Cost	General Facilities Capital (%PFC)	1.00	2.515
	Engineering & Home Office Fees (%PFC)	5	9.30
	Project Contingency Cost (%PFC)	20	13.80
	Process Contingency Cost (%PFC)	0	0.0
	Royalty Fees (%PFC)	0	0.0
	Fixed Operating Cost (months)	1.0	0.0
	Variable Operating Cost (months)	1.000	0.0
	Misc. Capital Cost (%TPI)	2.0	0.0
	Inventory Capital (%TPC)	0.5	0.0
TSP Control O&M Cost	Total Maintenance Cost (%TPC)	1.767	1.600
SO$_2$ Control Performance	Scrubber SO2 Removal Efficiency (%)	85.49	98.00
	Wet FGD Power Requirement (% MWg)	1.607	0.71
SO$_2$ Control Capital Cost	General Facilities Capital (%PFC)	10	2.515
	Engineering & Home Office Fees (%PFC)	10	9.30
	Project Contingency Cost (%PFC)	15	13.80
	Process Contingency Cost (%PFC)	2	0.0
	Royalty Fees (%PFC)	0.5	0.0
	Fixed Operating Cost (months)	1.0	0.0
	Variable Operating Cost (months)	1.00	0.0
	Misc. Capital Cost (%TPI)	2.0	0.0
	Inventory Capital (%TPC)	0.3545	0.0
SO$_2$ Control O&M Cost	Total Maintenance Cost (%TPC)	4.388	1.60
Water Systems Performance	Ambient Air Temp (Dry Bulb Avg.) (°F)	77.00	70.00
	Power Requirement (% MWg)	1.41	1.410
Water Systems Capital Cost	General Facilities Capital (%PFC)	10	2.515
	Engineering & Home Office Fees (%PFC)	10	9.30
	Project Contingency Cost (%PFC)	15	13.80
	Process Contingency Cost (%PFC)	0	0.0
	Royalty Fees (%PFC)	0.5	0.0
	Fixed Operating Cost (months)	1.0	0.0
	Variable Operating Cost (months)	1.000	0.0
	Misc. Capital Cost (%TPI)	2.0	0.0
	Inventory Capital (%TPC)	0.5	0.0
Water Systems O&M Cost	Total Maintenance Cost (%TPC)	2.0	1.600

The key results of this case study are shown below in summary Table 14.

Case Study #4: PC Subcritical with CO$_2$ Capture

For the Subcritical plant with a CO_2 Capture System, a number of default parameters in the IECM were changed so that these parameters matched the NETL 2007 Baseline Report. These changes are shown in Table 13.

Table 13: IECM Parameters Changed for Case 4 - Supercritical Plants with CO_2 Capture

	Parameter	IECM Default	IECM Case 4
Configure Plant Overall Plant	NO_x Control	None	Hot-Side SCR
	Particulates	None	Fabric Filter
	SO_2 Control	None	Wet FGD
	CO_2 Capture	None	Amine System
	Cooling System	None	Wet Cooling Tower
Fuel Properties	Fuel Name	Appalachian Medium Sulfur	Illinois #6
Overall Plant Performance	Capacity Factor (%)	75.00	85.00
	Ambient Air Temperature (Avg.) (°F)	77.00	70.00
Overall Plant Financing	Discount Rate (Before Taxes) (fraction)	0.103	1.0E-4
	Fixed Charge Factor (FCF) (fraction)	0.148	0.175
	Plant or Project Book Life (years)	30.00	20.00
Overall Plant O&M Cost	Natural Gas Cost ($/mscf)	5.99	7.58
Base Plant Performance	Gross Electrical Output (MWg)	500	681.3
	Unit Type:	Sub-Critical	Sub-Critical
	Boiler Efficiency (%)	88.89	89.00
	Leakage Air at Preheater (% stoich.)	10	5.5
	Coal Pulverizer (% MWg)	0.5897	0.7300
Base Plant Capital Cost	General Facilities Capital (%PFC)	10.00	1.570
	Engineering & Home Office Fees (%PFC)	6.50	9.37
	Project Contingency Cost (%PFC)	11.67	16.38
	Process Contingency Cost (%PFC)	0.3	4.670
	Royalty Fees (%PFC)	7.00E-2	0.0
	Fixed Operating Cost (months)	1.00	0.0
	Variable Operating Cost (months)	1.00	0.0
	Misc. Capital Cost (%TPI)	2.0	0.0
	Inventory Capital (%TPC)	6.00E-2	0.0
Base Plant O&M Cost	Waste Disposal Cost ($/ton)	9.36	15.45
	Total Maintenance Cost (%TPC)	1.896	1.60
NO_x Control Performance	Actual NOx Removal Efficiency (%)	76.66	86.00
	Hot-Side SCR Power Requirement (% MWg)	0.6294	1.100e-2
NO_x Control Capital Cost	General Facilities Capital (%PFC)	10.00	1.57
	Engineering & Home Office Fees (%PFC)	10.00	9.37
	Project Contingency Cost (%PFC)	10.00	16.38
	Process Contingency Cost (%PFC)	6.397	4.670
	Royalty Fees (%PFC)	7.00E-2	0.0
	Months of Fixed O&M (months)	1	0
	Months of Variable O&M (months)	1	0
	Misc. Capital Cost (%TPI)	2	0
	Inventory Capital (%TPC)	0.5	0

NO$_x$ Control O&M Cost	Total Maintenance Cost (%TPC)	2.00	1.60
TSP Control Performance	Particulate Removal Efficiency (%)	99.10	99.90
	Fabric Filter Power Requirement (% MWg)	0.1958	1.40E-2
TSP Control Capital Cost	General Facilities Capital (%PFC)	1.00	1.57
	Engineering & Home Office Fees (%PFC)	5	9.37
	Project Contingency Cost (%PFC)	20	16.38
	Process Contingency Cost (%PFC)	0	4.670
	Royalty Fees (%PFC)	0	0.0
	Fixed Operating Cost (months)	1.0	0
	Variable Operating Cost (months)	1.000	0
	Misc. Capital Cost (%TPI)	2.0	0
	Inventory Capital (%TPC)	0.5	0
TSP Control O&M Cost	Total Maintenance Cost (%TPC)	1.723	1.600
SO$_2$ Control Performance	Scrubber SO2 Removal Efficiency (%)	85.49	98.00
	Wet FGD Power Requirement (% MWg)	1.607	0.89
SO$_2$ Control Capital Cost	General Facilities Capital (%PFC)	10	1.57
	Engineering & Home Office Fees (%PFC)	10	9.37
	Project Contingency Cost (%PFC)	15	16.38
	Process Contingency Cost (%PFC)	2	4.670
	Royalty Fees (%PFC)	0.5	0.0
	Fixed Operating Cost (months)	1.0	0
	Variable Operating Cost (months)	1.00	0
	Misc. Capital Cost (%TPI)	2.0	0
	Inventory Capital (%TPC)	0.3545	0
SO$_2$ Control O&M Cost	Total Maintenance Cost (%TPC)	4.398	1.60
CO$_2$ Capture Config	Sorbent Used	Conv. MEA	Adv. Amine (FG+)
CO$_2$ Capture Performance	Amine Scrubber Power Requirement (% MWg)	13.98	11.04
CO$_2$ Capture Capital Cost	General Facilities Capital (%PFC)	10	1.57
	Engineering & Home Office Fees (%PFC)	7	9.37
	Project Contingency Cost (%PFC)	15	16.38
	Process Contingency Cost (%PFC)	5	4.670
	Royalty Fees (%PFC)	0.5	0.0
	Fixed Operating Cost (months)	1.0	0
	Variable Operating Cost (months)	1.00	0
	Misc. Capital Cost (%TPI)	2.0	0
	Inventory Capital (%TPC)	0.5	0
CO$_2$ Capture O&M Cost	Reclaimer Waste Disposal Cost ($/ton)	211.6	0.0
	Total Maintenance Cost (%TPC)	2.5	1.600
	CO2 Transportation Cost ($/ton)	1.759	0.0
	CO2 Storage Cost ($/ton)	6.047	3.4
Water Systems Performance	Ambient Air Temp (Dry Bulb Avg.) (°F)	77.00	70.00
	Power Requirement (% MWg)	2.8	3.14
Water Systems	General Facilities Capital (%PFC)	10	1.57

Capital Cost	Engineering & Home Office Fees (%PFC)	10	9.37
	Project Contingency Cost (%PFC)	15	16.38
	Process Contingency Cost (%PFC)	0	4.670
	Royalty Fees (%PFC)	0.5	0.0
	Fixed Operating Cost (months)	1.0	0
	Variable Operating Cost (months)	1.000	0
	Misc. Capital Cost (%TPI)	2.0	0
	Inventory Capital (%TPC)	0.5	0
Water Systems O&M Cost	Total Maintenance Cost (%TPC)	2.0	1.600

The key results of this case study are shown below in summary Table 14.

Summary Results from Case Studies 1-4

The key results from Case Studies 1-4 are shown below in Table 14. The performance parameters in terms of net plant efficiency for the same gross power plant size match closely, as do the capital costs on a $/kW-net basis. The revenue required for the IECM for each of these cases is somewhat lower than in the NETL 2007 Baseline Report, owing primarily to an escalation in coal prices for all four cases in the Baseline Report, which is not done in this analysis in the IECM.

Table 14: Summary of Case Study Results

Cases	Gross Output (MW)		Net Plant Efficiency (%)		Capital Cost ($/kW -net)		Revenue Required ($/MWh)	
	IECM	NETL	IECM	NETL	IECM	NETL	IECM	NETL
PC Supercritical	580.2	580.2	39.1%	39.1%	1601	1575	60.4	63.3
PC Supercritical + CCS	663.3	663.4	27.1%	27.2%	2857	2870	108.4	114.8
PC Subcritical	583.2	583.3	36.8%	36.8%	1541	1549	60.1	64.0
PC Subcritical + CCS	681.3	679.9	24.8%	24.9%	2935	2895	112.5	118.8

Cost Sensitivity

A cost sensitivity analysis was done for different steam cycles (Subcritical, Supercritical, and Ultra Supercritical), for different coal types (Appalachian Medium Sulfur, Illinois #6, and Wyoming Powder River Basin), and for plants with and without CO_2 capture across a range of net plant sizes (250MW to 750MW). In each of these sensitivity studies, the defaults for the IECM were used with an SCR, ESP, and FGD system, and with an Advanced Amine CO_2 Capture System for the case with CO_2 capture. The results are presented below.

Cost Sensitivity to Steam Cycle Type

In the sensitivity analysis for the steam cycle, an IECM default plant was built with an SCR, ESP, and FGD system, but without a CO_2 capture system, and the coal used was Illinois #6. The net plant size was varied between 250 and 750 MW. The plant efficiencies were approximately constant through this range of plant sizes, with the Subcritical plant having an efficiency of 36.4%, the Supercritical plant having an efficiency of 38.7%, and the Ultra Supercritical plant having an efficiency of 42.7% (all HHV). The results from the sensitivity studies for Capital Cost and Revenue Required are shown in Figure 3 and Figure 4 below.
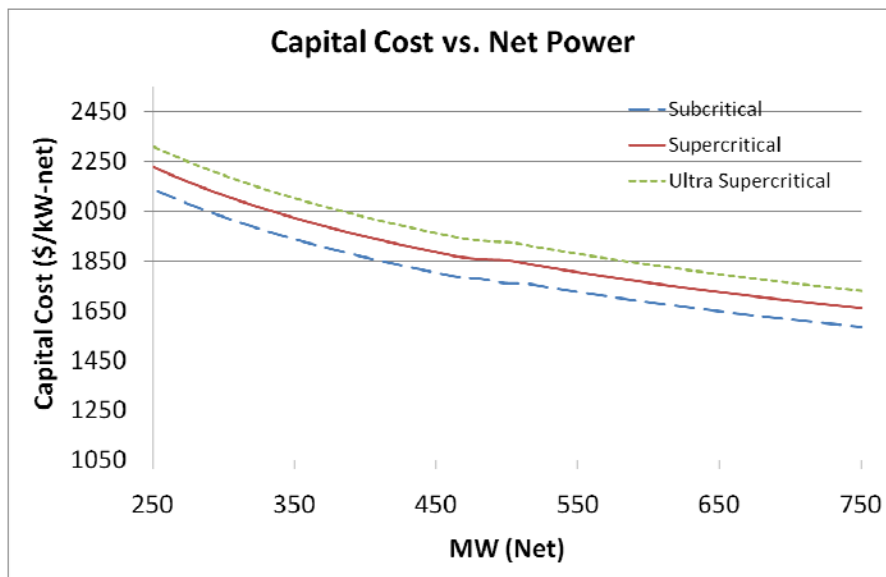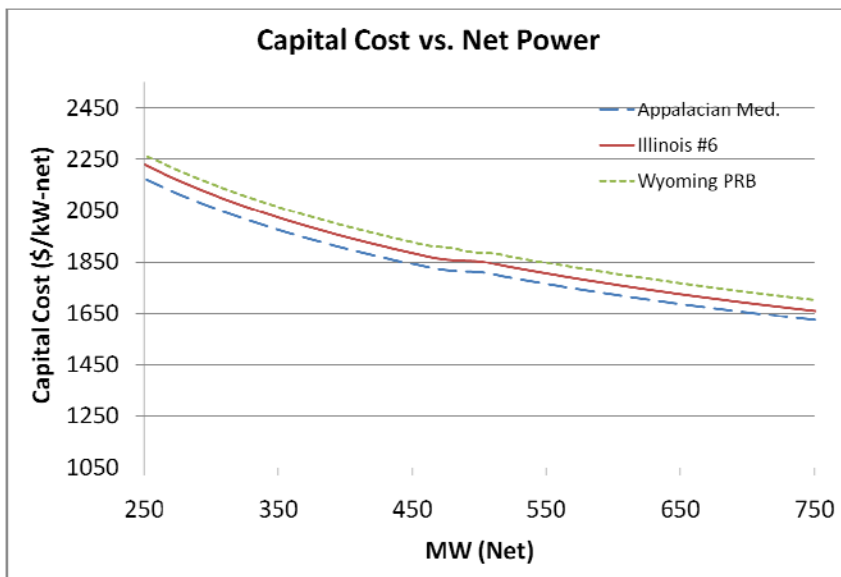

Figure 3: Capital Costs by Steam Cycle Type vs. Net Power Output
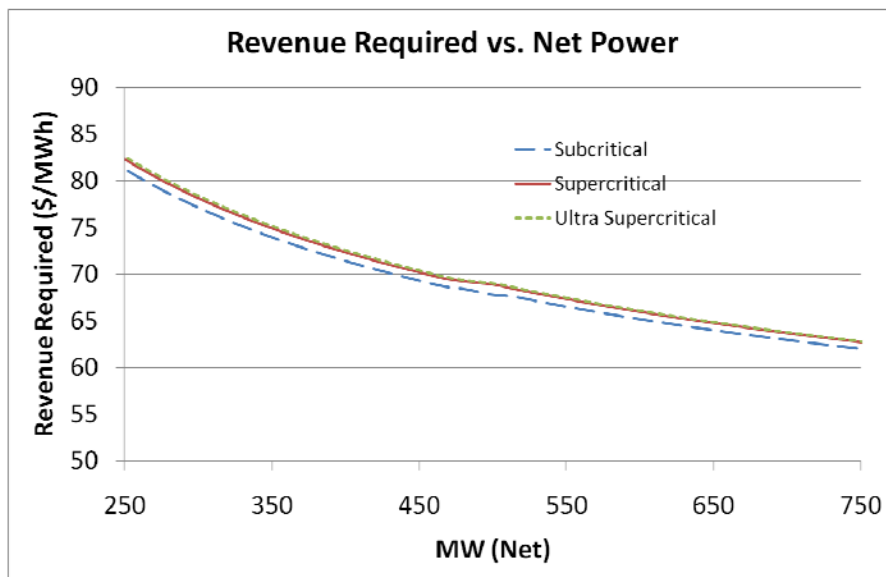
Figure 4: Revenue Required by Steam Cycle Type vs. Net Power Output

Sensitivity to Coal Type

In the sensitivity analysis for coal type, an IECM default plant was built with an SCR, ESP, and FGD system, but without a CO_2 capture system, and a Supercritical steam cycle was used. Three coals were chosen for this analysis, Appalachian Medium Sulfur, Illinois #6, and Wyoming Powder River Basin. The net plant size was varied between 250 and 750 MW. The results from the sensitivity studies for Capital Cost and Revenue Required are shown in Figure 5 and Figure 6 below.
.

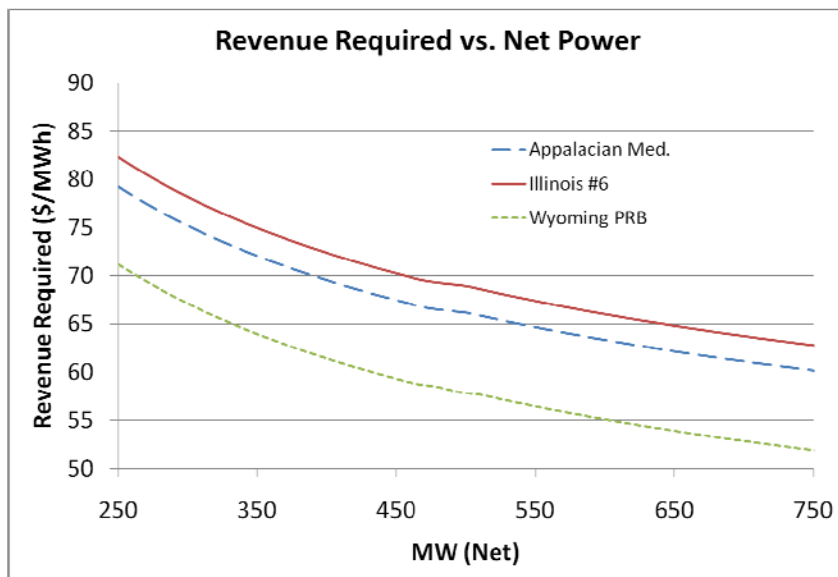*Figure 5: Capital Costs by Coal Type vs. Net Power Output*

Figure 6: Revenue Required by Coal Type vs. Net Power Output

Sensitivity to CO$_2$ Capture Technology

In the sensitivity analysis for CO$_2$ capture technology, an IECM default plant was built with an SCR, ESP, and FGD system, and a Supercritical steam cycle was used. The net plant size was varied between 250 and 750 MW with and without a CO$_2$ capture system. The results from the sensitivity studies for Capital Cost and Revenue Required are shown in Figure 7 and Figure 8 below. In Figure 7 and Figure 4, the costs for plants with CO$_2$ Capture generally decrease with increasing plant size until a new train is required in the CO$_2$ capture system, at which point the cost rises slightly.
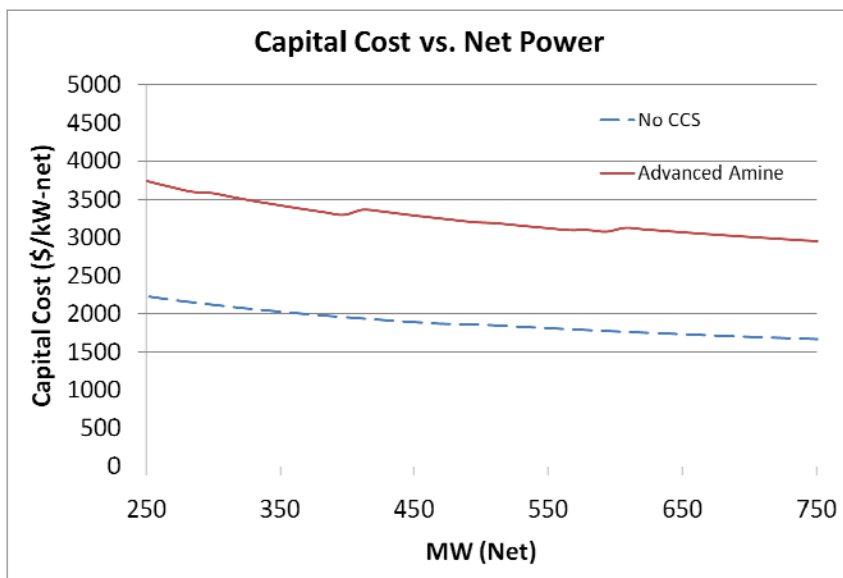

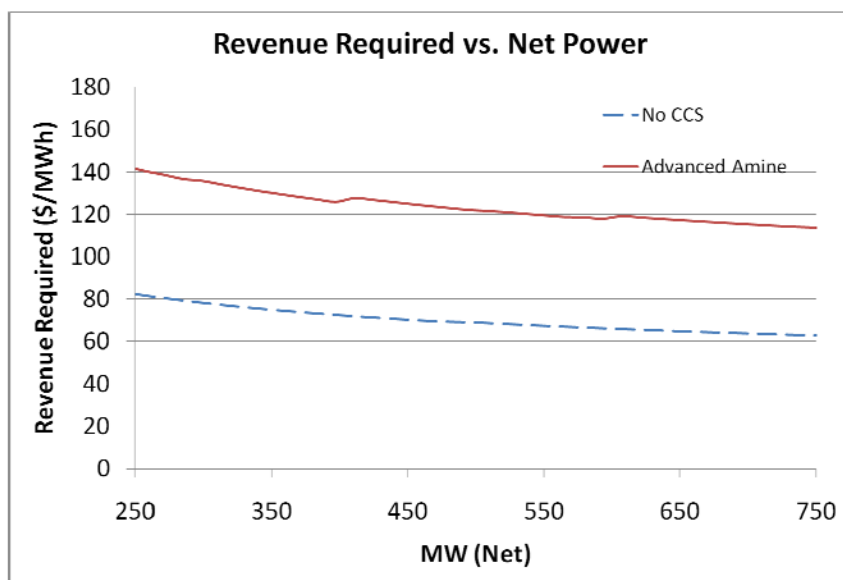*Figure 7: Capital Cost vs. Net Power Output with and without CCS*

Figure 8: Revenue Required vs. Net Power Output with and without CCS

Updates to IGCC models in IECM

Abstract

In this part of the report, updates done to the technologies, technical parameters and cost parameters for IGCC models in IECM are presented. Technologies such as Shell gasifier, Sulfinol sulfur removal and GE 7FB gas turbine are added to IECM. Cost models are updated to be in tune with recent figures. Case studies with application of IECM to different conditions are presented at the end. Documentation of process performance models developed using Aspen Plus is given in the Appendix.

Modifications to IECM – Technology Models

This section lists the technology-related modifications done to IECM. The modifications range from inclusion of new technologies to changing of technical parameters in the existing ones. Documentation of process performance model for Shell gasification technology is given in the Appendix.

Shell Gasification Technology

The earlier versions of IECM used only the GE quench type gasification technology in its IGCC models. Now, Shell gasification system, a dry-feed gasification technology, is also added. Radiant syngas cooling is used for non-capture cases and a quench cooling system is used for capture cases. Following is the description of modifications to IECM user-interface to include Shell technology as an option
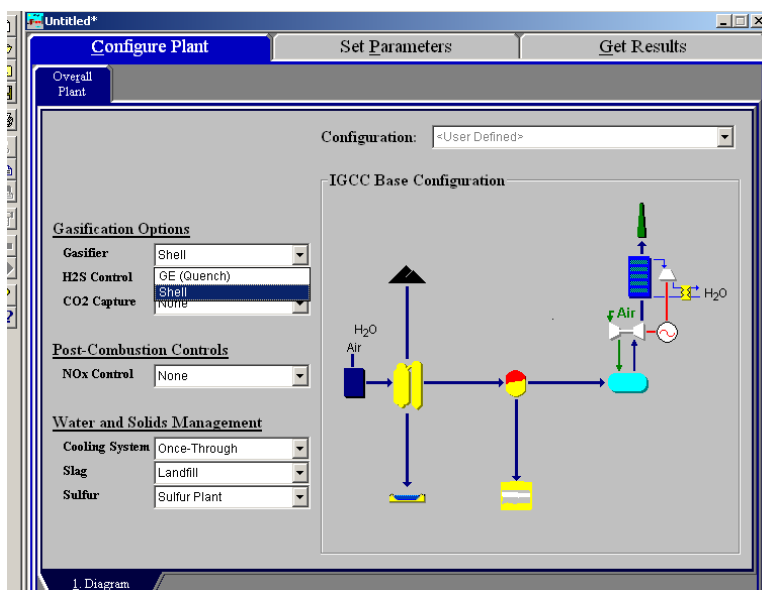

Figure 9: Gasifier type choices - GE (Quench) and Shell

Figure 9: Gasifier type choices - GE (Quench) and ShellFigure 9 shows the Configure Plant tab where the user can choose between GE (Quench) or Shell gasifier technologies.

By selecting the Shell gasifier technology, the gasifier area screen in the Set Parameters tab updates the variables correspondingly. Shell gasifier is a dry-feed gasifier, operating at a temperature of 2600 ^{o}F (line 2 in the Gasifier Area tab) and 615 psia (line 3 in the Gasifier Area tab. In IECM, temperature can be varied by +/- 100 ^{o}F, as shown in Figure 10.

Figure 10: Gasifier area: temperature is 2600 ^{o}F, with options of 2500 ^{o}F and 2700 ^{o}F

Figure 11 shows other default operating parameters. Shell gasifier is a dry-feed system. Bituminous coals have to be dried to 5% moisture content (line 4 in the Gasifier Area tab). Sub-bituminous coals and lignite are dried to 6% and 12% moisture levels respectively. A small amount of steam is also input to the gasifier, such that the mole ratio of water to carbon in coal is 0.15 (line 5 in the Gasifier Area tab). Oxygen input from the ASU is fixed such that the mole ratio of oxygen to carbon in coal is 0.4216 (line 6 the Gasifier Area tab). Total carbon loss is given as a function of carbon in slag. The default is 0.5% by weight but it can be changed to 1% or 1.5% (line 7 the Gasifier Area tab).

Figure 11: Default operating parameters of a Shell gasifier

Figure 12 shows the syngas composition for Illinois#6 coal, gasifier operating temperature of 2600 ^{o}F and carbon loss percentage of 0.5%. The composition changes when one or more of input specifications like coal type, gasifier temperature or carbon loss are changed. **Error! Reference source not found.** and **Error! Reference source not found.** show the diagrams of IGCC plant for non-capture and CO$_2$ capture cases, respectively.

Figure 12: Syngas composition at gasifier exit. This varies with the coal type and operating conditions like temperature and carbon loss percentage.

Sulfinol Sulfur Removal System

A Sulfinol sulfur removal system model is also added to the IGCC model. This is in addition to the Selexol system model that already exists in IECM. The user can choose between Sulfinol and Selexol proceses, as shown in Figure 13. When the Sulfinol option is selected, CO_2 capture option is deactivated. CO_2 capture works only if Selexol is chosen for H_2S capture.
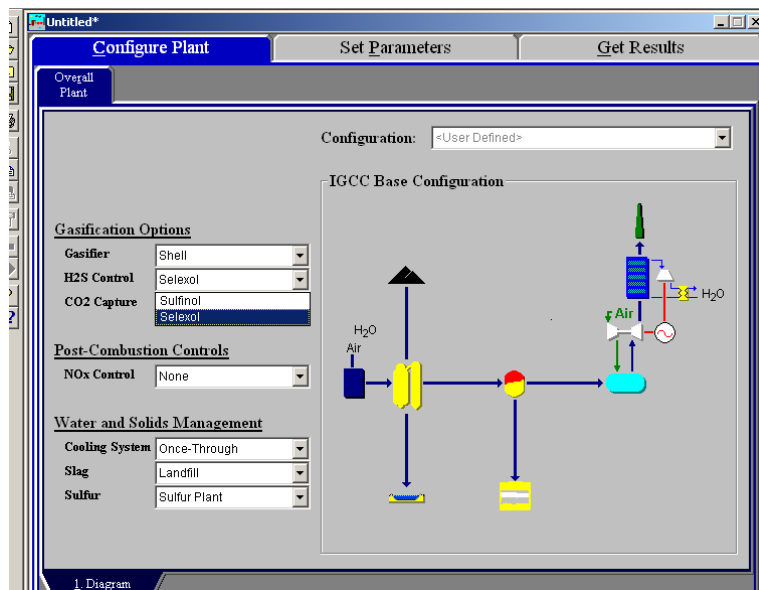
Figure 13: H2S control choices - Sulfinol and Selexol

Figure 14: Diagram of IGCC base configuration without CO2 capture

Figure 15: Diagram of IGCC plant with sour shift CO2 capture (this is activated only if Selexol is used for sulfur removal)
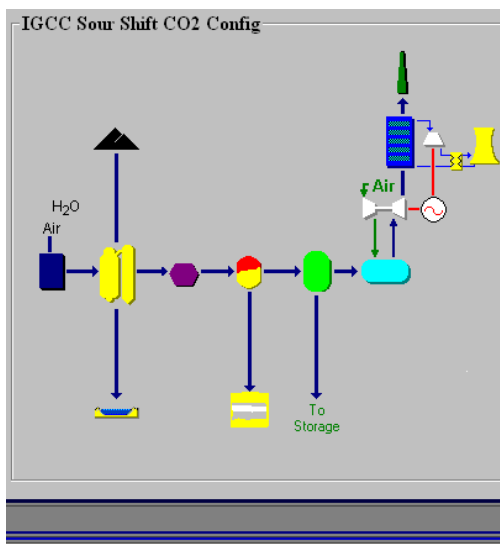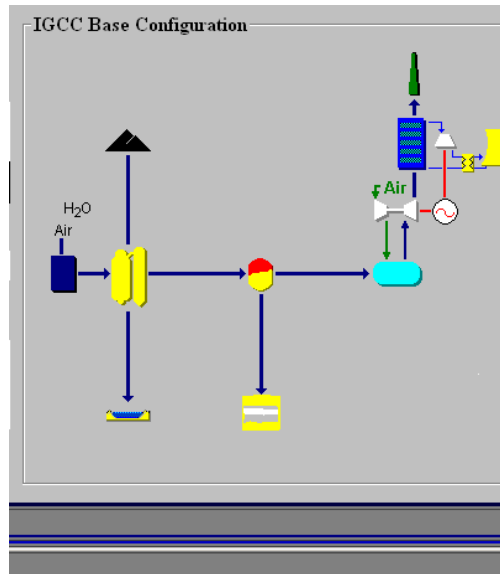
The range of H_2S removal efficiency has been modified to have a maximum value of 99.9% (line 4 in the Sulfur Removal tab). The sulfur removal block default parameters are shown in Figure 16.

Figure 16: Sulfur Removal block - range of removal efficiency modified to a maximum value of 99.9%

GE 7FB Gas Turbine

The updated IECM contains the option of GE 7FB gas turbine. The earlier version had only 7FA for a gas turbine. The user can select which turbine to use by clicking on the drop down menu for gas turbine model (line 2 in the Power Block tab), as shown in Figure 17. The figure also shows default values for other parameters. The firing temperature of a 7FB turbine is 2500 ^{o}F (line 6 in the Power Block tab) and the pressure ratio is 18.5 (line 12 in the Power Block tab) [12]. The defaults for adiabatic turbine efficiency (line 8 in the Power Block tab) and adiabatic compressor efficiency (line 13 in the Power Block tab) are chosen as 85.7 and 87.5 respectively. These values are arrived at by calibrating the model to match the simple cycle power output of 185 MW and net plant heat rate (LHV) of 9,469 kJ/kWh when the turbine is operated on natural gas as fuel [1].

Figure 17: Power Block - 7FB turbine added to IECM

The steam cycle also utilizes high pressure steam from the gas cooling section. To account for that, a heat rate factor was added to the code, for both capture and non-capture cases. The values for these factors were obtained by

---

calibrating this model with steam turbine output results in the NETL baseline report. Steam turbine output is calculated as follows:

$$MW_{Steamturbine} = \frac{\Delta H_{flue\,gas}}{HR_{steamcycle} \times factor \times (1 - \Delta T / T_{gasifier})}$$

where, $\Delta H_{flue\,gas}$ is the sensible heat recovered from flue gases in HRSG, $HR_{steamcycle}$ is the default steam cycle heat rate (9,000 BTU/kWh), and the factor in the denominator is the heat rate adjustment factor. The value of the factor is 0.6972 for non-capture cases, where a higher amount of steam is produced by radiant syngas cooling, compared to the quench cooling system in the capture case, where the factor has been estimated as 0.8756, when the gasification temperature is 2600 °F. The temperature term in the denominator adjusts the turbine output according to variation in gasification temperature. If the temperature is higher than 2600 °F, there will be more steam produced and hence more power output from the steam turbine and vice versa.

Modifications to IGCC Cost Models

New cost models were developed for new technologies and the existing cost models were updated using recent literature. This section lists the additions and modifications to IECM cost models for IGCC.

Shell Gasification System

Capital cost of shell gasifiers is different from other gasifiers. New cost models had to be developed for IECM shell gasifier cases. The exponential cost model is used here for gasifier cost equations.

$$C = C_{ref} \times \left(\frac{X}{X_{ref}} \right)^m$$

In doing cost estimation for slurry feed quench gasifiers, it was found that the cost varies with coal flow rate with an exponential factor of 0.943 [GE documentation IECM]. The same exponent (m = 0.943) is used in estimating the costs for Shell gasifiers.

NETL baseline report is used for reference cost cases. For non-CO2 capture cases, a radiant syngas cooler is used with to cool raw gas from the gasifier, in the process generating high pressure steam. For cases with CO2 capture, a quench cooling mechanism is used which helps in supplying a part of required water for the downstream water gas shift reactor. So, different cost models were developed for the non-capture and capture cases. Equation 1 shows the cost equation for the gasifier with radiant cooling section, used for non-capture cases. Equation 2 shows the cost equation for a gasifier with quench cooling, used to capture cases.

$$C_{gasifier,radiant} = 48,856 \times N_{T,G} \left(\frac{m_{coal}}{N_{O,G}} \right)^{0.943} (\$) \tag{1}$$

$$C_{gasifier,radiant} = 37,334 \times N_{T,G} \left(\frac{m_{coal}}{N_{O,G}} \right)^{0.943} (\$) \tag{2}$$

Where, N_T is the total number of trains, N_O is the number of operating trains and m_{coal} is the mass flow of as-received coal (tons per day).

7FB Gas Turbine

Cost models for gas turbine were also developed using NETL report as reference values. The determining variable is the number of turbines. Cost for one turbine is estimated as $47,431,000. For multiple turbines, this value is multiplied by the number of turbines.

Modifications to Existing Cost Equations

The cost models for other IGCC sections in the IECM were also updated to be in tune with recent values [2]. The same equations were used as in the earlier version but with an adjustment factor multiplied to the coefficient. The factors are shown in Table 15.

Table 15: Cost adjustment factors used to update the existing cost models to recent values

Process section	Cost adjustment factor
Air Separation Unit	1.471
Gasifier Area	
Coal Handling	4.337
Gasifier (non-capture)	1.096
Gasifier (capture)	0.946
Low Temperature Gas Cooling	0.591
Process Condensate Treatment	1.001
Activated Carbon Mercury Removal	0.002*gasification island cost
Sulfur Removal	
Sulfur Removal System-Hydrolyzer	7.539
Sulfur Removal System-Sulfinol	4.161
Sulfur Removal System-Selexol	1.25
Sulfur Removal System-Claus	3.026
CO2 Capture-Selexol	1.25
Power Block	
Gas Turbine	0.634
Heat Recovery Steam Generator	1.221
Steam Turbine	0.528
HRSG Feedwater System	3.584

Case Studies of IGCC Plants

The use of IECM is demonstrated by applying it to a few case studies. The first case is a replication of cases 5 and 6 of the NETL baseline study – Shell based IGCC without and with CO_2 capture, respectively. The other case studies show the ability of IECM in application to different input parameters and test the sensitivity of performance and cost behavior to those changes.

Case Study 1: NETL Baseline Report IGCC Cases

Case 5 of the NETL baseline report deals with an IGCC power plant using the Shell gasification system with radiant syngas cooling, without CO_2 capture. The plant uses Illinois#6 coal. Sulfinol process is used for H_2S removal. The net power output from the plant is 632 MW, produced using a GE 7FB combined cycle power plant. The plant uses dilution of syngas before entering the gas turbine combustor, to reduce its lower heating value to about 4.6 MJ/Nm^3.

Case 6 of the NETL baseline report utilizes the Shell gasification system with quench raw gas cooling. After shifting the syngas to convert almost all of the CO to CO2, co-capture of H2S and CO2 takes place in a dual stage Selexol process. Syngas entering the gas turbine combustor is diluted with both N2 from the ASU and humidification steam to reduce its heating value.

For this case study, performance and cost assumptions from the NETL cases 5 and 6 were given to IECM IGCC models, wherever possible. Efforts were made to match all the inputs but the possibility of missing out some parameters cannot be ruled out. The current IECM does not include N_2-integration capability. Lowering of heating value is achieved by increasing the moisture content of the syngas before entering the gas turbine combustor. Owners' costs are not included in NETL cost estimations, whereas IECM defaults include owners' costs. Owners' costs were forced to be nearly zero by zeroing out certain factors.

The following are a few major changes that were made to the performance defaults in IECM, in order to replicate cases 5 and 6:
- Ambient Air Temperature (Avg.) (°F): 59.00 (default: 77.00)
- Auxiliary power requirements for different processes were changed to match the baseline values:
  - Total ASU Power Requirement (% MWg): 7.080
  - Gasifier Area Power Requirement (% MWg): 0.6400
  - Sulfur Removal COS to H2S Conversion Efficiency (%): 99.50 (default: 98.50)
  - H_2S Removal Efficiency (%): 99.00
  - H_2S Removal Power Requirement (% MWg): 0.12
  - Power Block Power Requirement (% MWg): 5.460
- Power Block Fuel Gas Moisture Content (vol %): 48.53 for non-capture and 50% for capture cases. NETL case assumed N_2-injection into the gas turbine combustor which adds to the power generation capacity. Since N_2-injection is not used in IECM, the fuel gas moisture content value was modified to match the gas turbine output to 464 MW.

Important changes to the cost factors are:
- Capacity factor was changed to 80% (default: 75%)
- Discount Rate (Before Taxes) (fraction): 1.000e-4. Discount rate effectively set to zero as made near 0 because NETL report does not include owner's costs or interest during construction in the cost estimating methodology.
- Fixed Charge Factor (FCF) (fraction): 0.1750. NETL uses a fixed charge factor of 17.5%, considering IGCC as a high-risk technology.

Table 16 and Table 17 show the comparison of performance and cost results between IECM estimation and those reported in the baseline report for cases 5 and 6 respectively. It can be seen that most of the values match within +/- 2% of the reported values. The cost of electricity is slightly different because the NETL Baseline Study assumes small real escalation of coal prices, which is not modeled in the IECM.

Table 16: Comparison of results from IECM and NETL (case 5) for a Shell based IGCC plant without CO_2 capture

Parameter	IECM	NETL
Net power output (MW)	635.6	635.9
Net plant heat rate (BTU/kWh)	8,194	8,306
Net plant efficiency (%, HHV)	41.6	41.1
Total capital required (M$)	1,280	1,257
Total capital required ($/kW-net)	2,014	1,977
Cost of electricity ($/MWh)	80.61	80.5

Table 17: Comparison of results from IECM and NETL (case 6) for a Shell based IGCC plant with CO_2 capture

Parameter	IECM	NETL
Net power output (MW)	517.3	517.1
Net plant heat rate (BTU/kWh)	10,550	10,674
Net plant efficiency (%, HHV)	32.3	32.0
Total capital required (M$)	1,363	1,379
Total capital required ($/kW-net)	2,635	2,668
Cost of electricity ($/MWh)	106.8	110.4

Conclusion

This case study demonstrates the capability of IECM in obtaining similar results to the NETL study by varying the relevant inputs correspondingly.

Case Study 2: Effect of Plant Capacity on Capital Cost and Cost of Electricity

In this case study, the effect of changing plant size on the capital cost and cost of electricity is analyzed. In IECM, plant size can be changed by varying the number of gas turbines used in the plant. IGCC power plants with 1, 2 and 3 gas turbines are compared here. Performance and cost parameter assumptions are the same as in case study 1.

Figure 18 shows the results for capital cost as a function of net plant size, for both non-capture and CO2-capture cases. Economy of scale for an IGCC power plant can be seen in this figure. As the net power output increases, the specific capital cost decreases. However, the rate of decrease is lower as the plant size increases. The economy of scale of capital cost can also be seen by its effect on the cost of electricity, as shown in Figure 19. The cost of electricity also decreases with increasing plant size.
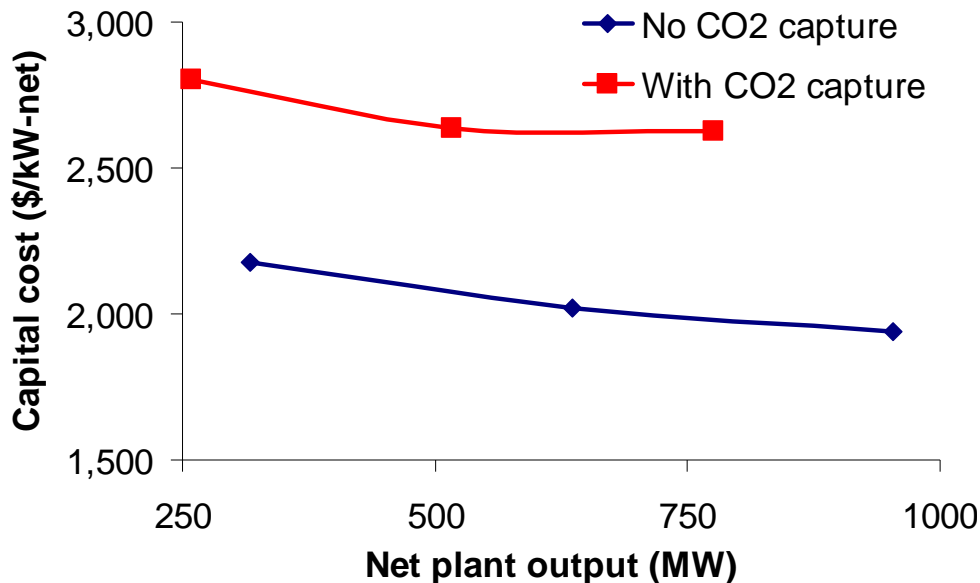
Figure 18: Sensitivity of capital cost to net plant output, with and without CO2 capture. As the plant size increases, specific capital cost decreases. CO2 capture increases the capital cost by more than 30%
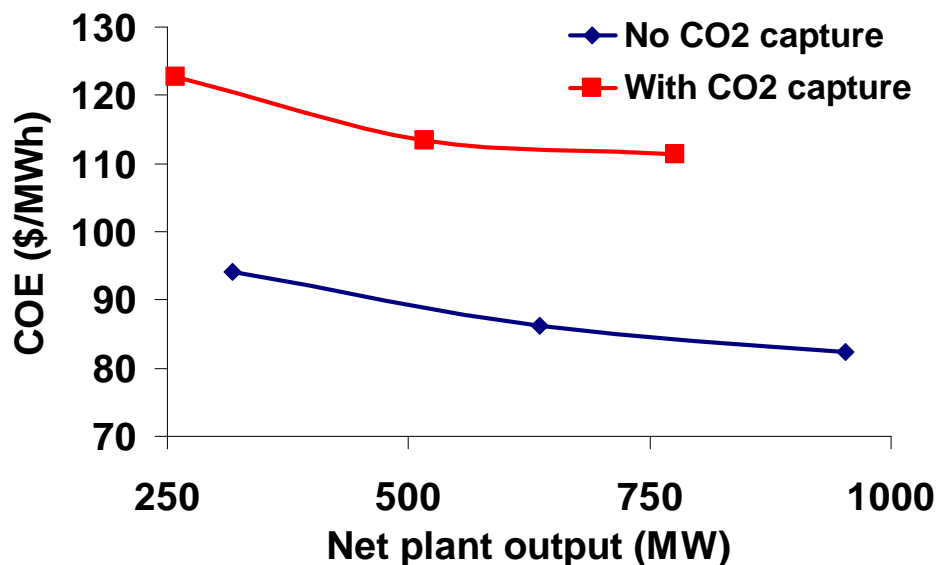
Figure 19: Sensitivity of cost of electricity to net plant output, with and without CO2 capture. As the plant size increases, specific capital cost decreases. CO_2 capture increases the COE by about 30%

Case Study 3: Effect of Type of Coal on Performance and Cost

Different types of coals have different effects on the performance and cost of a power plant. Here, IECM is applied to IGCC power plants using three different types of coal
- Appalachian Medium Sulfur bituminous coal (also called as Pittsburgh#8)
- Illinois#6 bituminous coal
- Wyoming PRB sub-bituminous coal

The properties and cost of coals used in this analysis are shown in Table 18. The default performance and cost assumptions of IECM are used for this analysis. The ambient temperature is 77 ^{o}F, and pressure is 14.7 psia. All the owners' costs are included. General facilities capital of 15%, engineering and home office fees of 10%, project contingency cost of 15%, and royalty fees of 0.5% of plant facilities cost was applied to all the process sections. The process contingency cost varies from process to process.

Table 18: Properties of coals used in this analysis

Coal	Appalachian medium sulfur	Illinois#6	Wyoming PRB
Rank	Bituminous	Bituminous	Sub-bituminous
Ash	7.24	11	5.32
C	73.81	61.2	48.18
H2	4.88	4.2	3.31
N2	1.42	1.16	0.7
Cl	6.00E-02	0.17	1.00E-02
S	2.13	3.25	0.37
O2	5.41	6.02	11.87
Moisture	5.05	13	30.24
HHV(BTU/lb)	13,260	11,670	8,340
Cost ($/ton)	45.24	42	8.75

Figure 20 shows the effect of coal type on the net plant efficiency, both for non-capture and CO_2 capture cases. The plant efficiency decreases with decreasing quality of coal and CO_2-capture has an efficiency penalty of roughly 9 – 10 percentage points. The CO2 emission intensities of different kinds of coal are shown in Figure 21. CO_2 emissions per unit output increase with decreasing coal quality, either with or without CO_2 capture.
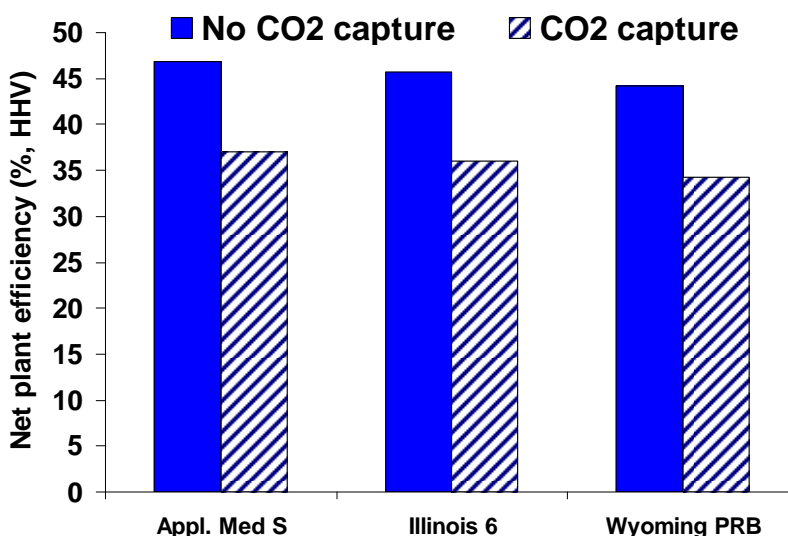
Figure 20: Effect of coal type on net plant efficiency of an IGCC power plant, with and without CO2 capture
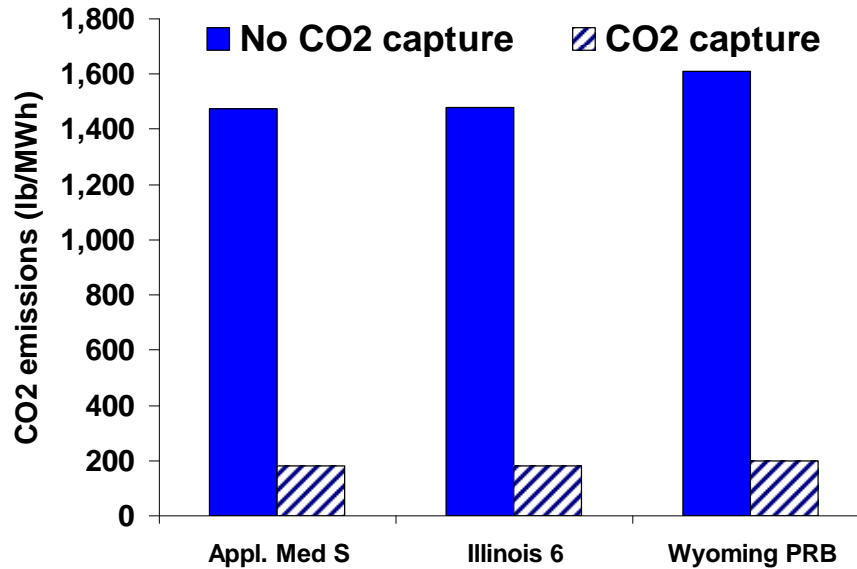
Figure 21: CO2 emission intensity of an IGCC power plant using different coal types

Figure 22 and Figure 23 show the effect of coal type on capital cost and cost of electricity, respectively. Capital cost of a plant using the lowest quality coal (Wyoming PRB) is about 12% higher than the one using the highest quality coal (Appalachian medium S). However, without CO2-capture, cost of electricity of the plant using Wyoming PRB is the lowest of all three. This is because of the lower price of sub-bituminous coal than that of bituminous coals. CO2-capture involves a capital cost increase of 20% for bituminous coals to 27% for sub-bituminous coals.
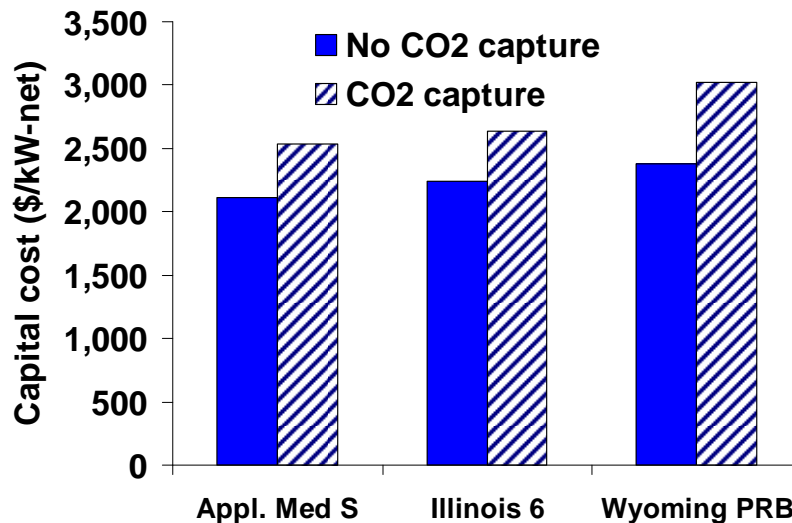
Figure 22: Effect of type of coal on capital cost of the plant, with and without CO2 capture
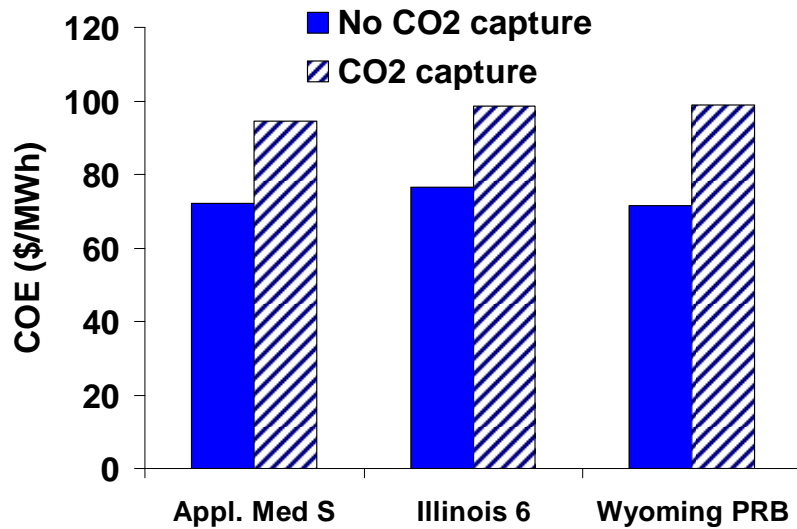
Figure 23: Effect of coal type on cost of electricity for an IGCC plant, with and without CO2 capture

Conclusion

Updates to the IGCC models of IECM user-interface were presented and the reasons and methodology of modifications were explained. Through the application of IECM to NETL case studies, the validity of IECM was demonstrated. The capability of IECM to do sensitivity analyses for various kinds of input parameters was also shown.

Appendix: Shell Gasification Model Development using Aspen Plus

Background and Objectives

In this report, results from a technical model of a Shell gasification process using 6 different types of coal are described. A process performance model was developed using Aspen Plus simulation software [6] that calculates the product gas compositions from a Shell gasifier operating on six different coals, including bituminous, sub-bituminous and lignite ranks. Gasification temperature and the amount of carbon lost in the slag were used as variables for sensitivity analysis. The results will eventually go into IECM software [8].

The objectives of this study are:
1. to build a process model for a Shell gasification process used for IGCC applications
2. to analyze the sensitivity of gas composition to variations in gasification temperature and carbon lost in slag

Introduction

Gasification of coal is essentially a reaction of carbon in coal with a source of hydrogen (usually steam) and/or oxygen to yield a gas containing predominantly carbon monoxide (CO), hydrogen (H2), carbon dioxide (CO_2) and methane (CH_4). Coal can be gasified to produce medium calorific value (10 – 16 MJ/m^3) synthesis gas (or syngas), consisting primarily of a mixture of CO and H_2. Synthetic natural gas whose main component is CH_4 can also be produced from coal. Since syngas is the reactant in FT reactions, only those gasifier technologies used to produce syngas are considered here.

Gasifiers that produce syngas generally involve reaction of coal with steam and oxygen in the presence of heat [2]. The main reactions occurring in these gasifiers are:

$$C + H_2O \rightarrow CO + H_2 \qquad \qquad \Delta H_{1000K}^{o} = 135 \text{ kJ/mol} \qquad \qquad (1)$$

$$C + \frac{1}{2} O_2 \rightarrow CO \qquad \qquad \Delta H_{1000K}^{o} = -112 \text{ kJ/mol} \qquad \qquad (2)$$

$$C + O_2 \rightarrow CO_2 \qquad \qquad \Delta H_{1000K}^{o} = -395 \text{ kJ/mol} \qquad \qquad (3)$$
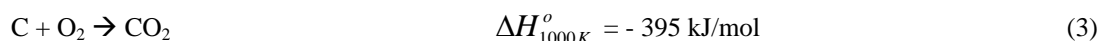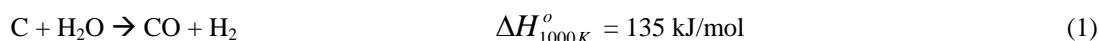
A gasifier is fundamentally a chemical reactor. Based on the reactor type, gasifiers are classified as fixed/moving bed, fluidized bed or entrained flow gasifiers. Selection of gasifier depends on a number of factors including the coal characteristics, quality requirements of syngas, operating parameters, site-specific requirements and so on. Of the above-mentioned gasifier types, entrained flow design is the most widely used. These gasifiers operate at high temperatures and are characterized by very low residence time of coal (of the order of seconds). High temperatures limit the formation of methane. The advantage of entrained flow gasifiers is the flexibility of using any type of coal. Coal has to be pulverized to help in its rapid gasification. Within the entrained gasifier design, there is variability in the method in which coal is fed into the gasifier. Coal can be fed either dry or in the form of water slurry. GE/Texaco entrained flow gasifiers are the most commonly used design followed by Shell gasifiers.

Shell Gasification

A Shell gasifier is a dry-feed entrained flow pressurized gasifier [9] [11]. Unlike the slurry-feed gasifiers in which slurry is used as the medium of coal transport to the gasifier, Shell gasifier uses nitrogen gas (N_2) as the transport medium. Oxygen and a small amount of steam are also fed to the gasifier in which coal reacts with oxygen at temperatures in excess of 1370 ^{o}C and a pressure of 4.3 MPa. Gasification at such high temperatures maximizes the production of CO and H_2 and minimizes the production of CO_2 and hydrocarbon gases and liquids. Ash is removed

at the bottom of the gasifier in the form of slag. The raw gas leaves the gasifier at 1600 ^{o}C and is cooled to about 900 ^{o}C by quenching with cooled recycle gas. Further cooling is achieved in a waste heat boiler which produces steam. The gas is then sent to gas-cleaning and scrubbing units.

For plants with CCS, NETL baseline report [**Error! Reference source not found.**] uses a water quench method to cool the raw syngas instead of a waste heat boiler. However, this does not affect the performance of the gasifier.
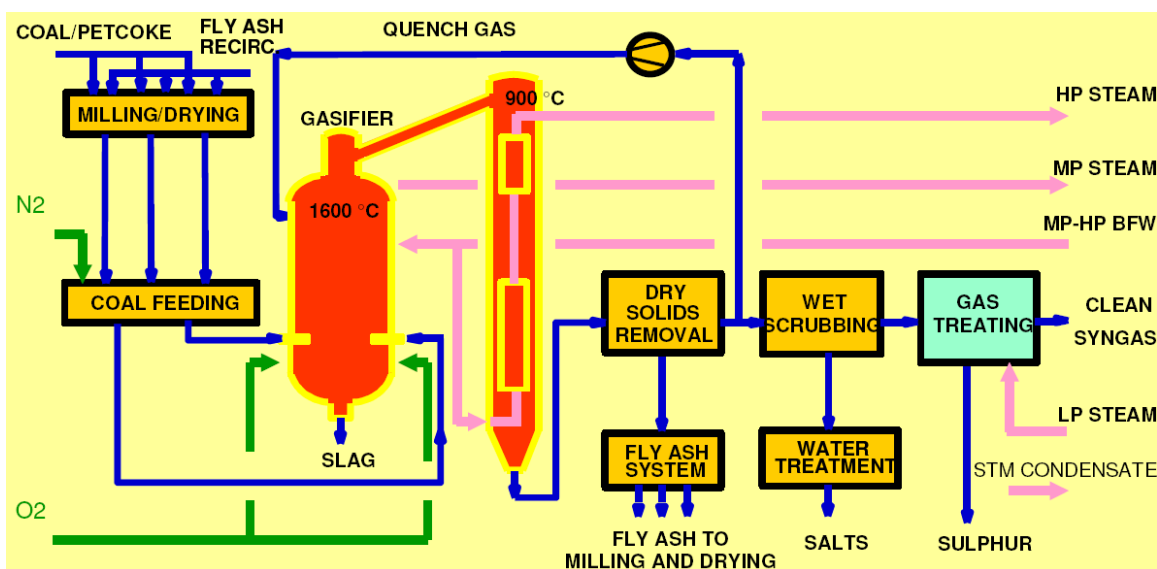
Figure 24: Shell gasification process [10]

Performance Model in Aspen Plus

A mathematical model for gasification should duplicate the reactions between carbon and other components in coal with oxygen and steam fed into the gasifier. Different gasifiers inject steam in different ways. In slurry-based gasifiers such as GE and E-Gas, steam comes in the form of water in the slurry used to transport coal into the gasifier. There are non-slurry based gasifiers (Shell) in which coal is transported into the gasifier using a nitrogen medium. Steam for such systems is fed directly into the gasifier. The other input is oxygen, which is fed into the gasifier from an Air Separation Unit (ASU). Thus, though the methods of injecting all the inputs into the gasifier may differ, gasification process is essentially a reaction of coal with water/steam and oxygen to produce syngas, as shown in Figure 25.
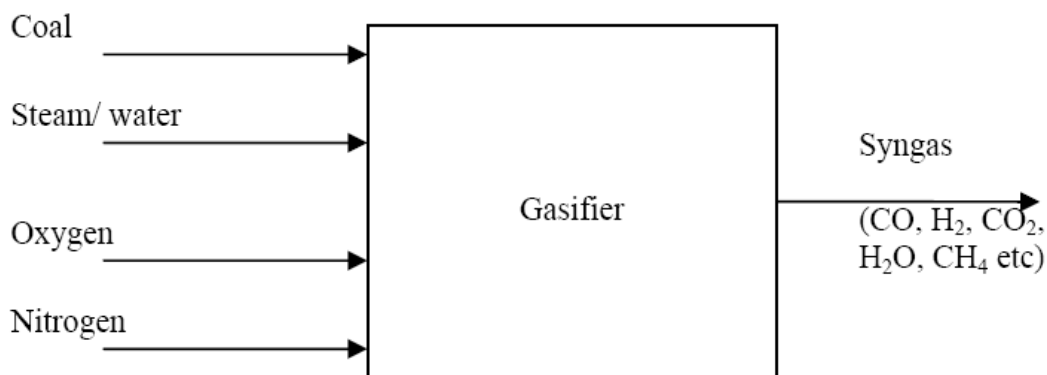
Figure 25: Block flow diagram of a gasifier

Coal Preparation

Six different types of coals are modeled here, whose ultimate analyses are given in Table 19. For the purpose of modeling using Aspen Plus, coal is a non-conventional solid, in the sense that it is composed of different component elements and cannot be represented as a single chemical species. This non-conventional material has to be decomposed into conventional components which will then react in the gasifier. The elemental composition of coal is given by its ultimate analysis. The amount of moisture in coal is given by its proximate analysis.

This non-conventional material is then 'decomposed' into different conventional components using a RYIELD reactor, which calculates the composition of the products based on a given yield distribution. The distribution is input in the form of a calculator block which uses the data from ultimate and proximate analyses to calculate the mass fractions of carbon (C), hydrogen (H_2), nitrogen (N_2), chlorine (Cl_2), sulfur (S), water (H_2O), oxygen (O_2) and ash. The procedure for this calculation is shown below.

Mass fraction of every component is given by,

$$y_{component} = Component_{coal} \times (1 - Moisture_{coal})$$

The mass fraction of each component in coal, $Component_{coal}$, is obtained from the ultimate analysis and $Moisture_{coal}$ is obtained from the proximate analysis data.

Heat released in the decomposition process is fed into the gasifier block since this process is not separate from the gasification process for practical purposes. However, since temperature is specified as an input variable to the gasifier model, this heat input does not affect the product gas composition.

Table 19: Ultimate analyses of different coals

Coal	Appalachian low sulfur	Appalachian medium sulfur	Illinois#6	WPC Utah	Wyoming PRB	ND lignite
Rank	Bituminous	Bituminous	Bituminous	Bituminous	Sub-bituminous	Lignite
Ash	9.79	7.24	11	11.59	5.32	15.92
C	71.74	73.81	61.2	67.66	48.18	35.04
H2	4.62	4.88	4.2	4.85	3.31	2.68
N2	1.42	1.42	1.16	1.22	0.7	0.77
Cl	7.00E-02	6.00E-02	0.17	1.00E-02	1.00E-02	9.00E-02
S	0.64	2.13	3.25	0.61	0.37	1.16
O2	6.09	5.41	6.02	6.11	11.87	11.31
Moisture	5.63	5.05	13	7.95	30.24	33.03
HHV(MJ/kg)	30.36	30.78	25.30	26.09	19.36	13.97

Coal Drying, Slag Removal and Carbon-Loss

Since Shell gasification is a dry process, feed coal needs to be dried before injecting into the gasifier. For bituminous coals, coal is dried to 5% moisture by weight. For sub-bituminous and lignite, the moisture content in the dried coal is 6% and 12% by weight, respectively [11].

Though in the actual process, slag is removed at the bottom of the gasifier, for the ease of modeling, here the non-conventional component "ash" can be removed from the decomposed coal stream before the gasifier block.

Some amount of carbon in coal is lost in slag. For modeling purposes, this "carbon-loss" is accounted for before the gasifier block.

All the three processes discussed above – coal drying, slag removal and carbon loss – are modeled using a single separator block (SEP in Aspen Plus). The split fraction of water is specified using a design specification fortran block (DesignSpec) which fixes the weight fraction of water in the gasifier feed depending on the type of coal. Split fraction of carbon is specified using a sensitivity block which varies the carbon loss between 0 and 2% with an interval of 0.5%. Ash is also removed completely in this block.

Mass flow rate of dried coal (gasifier feed) as compared to the wet coal is given by the following equation:

$$\overset{\square}{m}_{dried\ coal} = \overset{\square}{m}_{wet\ coal} \times \frac{\left(1 - Moisture_{wet\ coal}\right)}{\left(1 - Moisture_{dried\ coal}\right)}$$

Oxygen and Steam Feeds

Most of the entrained flow gasifiers use oxygen as the oxidation agent. Oxygen is separated from air typically in a cryogenic air separation unit (ASU) and the 95% pure oxygen is fed into the gasifier. For this Aspen Plus model, ASU is not modeled explicitly. The gasifier is directly fed with 95% pure oxygen which is compressed from atmospheric pressure to the gasification pressure. The energy required for ASU and oxygen compression is modeled using equations developed for IECM.

The flow rate of oxygen is specified using DesignSpec such that the ratio of oxygen to carbon is 0.442 mol/mol, as calculated from the values in NETL baseline report. Some amount of steam is also injected as a separate stream directly into the gasifier block. The mass flow rate is of steam is specified as 9.65% of wet coal mass flow rate using DesignSpec [**Error! Reference source not found.**]. These values are assumed to be the same for all coals.

Gasifier Block

In Aspen Plus, the reactor unit RGIBBS is used to model the gasification reactions. This can be used when the possible products are known but the exact reactions that take place to produce those components are not well-known. This reactor unit calculates the composition of the products based on the minimization of Gibbs' free energy. Apart from the material flow inputs to the reactor, the pressure at which reactions take place and either the reactor temperature or the heat duty has to be specified. It is assumed that all the reactions reach chemical equilibrium.

Considering the products in a typical gasifier product gas, apart from reactions 1 – 3 the following reactions are likely to take place in the gasifier [7]:

$C + 2\,H_2 \rightarrow CH_4$	(4)
$CO + H_2O \rightarrow CO_2 + H_2$	(5)
$2CO + O_2 \rightarrow 2CO_2$	(6)
$CH_4 + H_2O \rightarrow CO + 3H_2$	(7)
$S + H_2 \rightarrow H_2S$	(8)
$N_2 + 3H_2 \rightarrow 2NH_3$	(9)
$CO + H_2S \rightarrow COS + H_2$	(10)

To see the effect of temperature on the products, gasification temperatures of 1371 ^{o}C (2500 ^{o}F), 1427 ^{o}C (2600 ^{o}F) and 1482 ^{o}C (2700 ^{o}F) are modeled.

Results

The syngas compositions obtained from Aspen Plus modeling are given in the following tables. Results are shown for all the coals at different gasification temperatures and carbon loss values. The following general observations can be made:

- as the carbon content in the fuel increases, the CO fraction in the product gas increases and CO_2 fraction decreases

- for a given carbon loss fraction, an increase in temperature increases the production of CO and decreases methane formation
- for a given temperature, CO formation decreases with increasing carbon loss

Table 20: Syngas composition for Illinois#6 bituminous coal at 1371 ^{o}C

Illinois # 6, dried to 5% moisture by weight, temperature 1371 ^{o}C					
Carbon in slag (%)	0	0.5	1	1.5	2
CO	0.574	0.571	0.569	0.567	0.565
H_2	0.302	0.301	0.300	0.299	0.298
CH_4	0.001	0.001	0.001	0.001	0.001
H_2S	0.008	0.008	0.008	0.008	0.008
COS	0.001	0.001	0.001	0.001	0.001
NH_3	0.000	0.000	0.000	0.000	0.000
CO_2	0.017	0.018	0.019	0.021	0.022
H_2O	0.029	0.031	0.033	0.034	0.036
N_2	0.058	0.059	0.059	0.059	0.059
O_2	0.000	0.000	0.000	0.000	0.000

Table 20: Syngas composition for Illinois#6 bituminous coal at 1427 ^{o}C

Illinois # 6, dried to 5% moisture by weight, temperature 1427 ^{o}C					
Carbon in slag (%)	0	0.5	1	1.5	2
CO	0.574	0.572	0.570	0.568	0.565
H_2	0.302	0.301	0.300	0.299	0.298
CH_4	0.000	0.000	0.000	0.000	0.000
H_2S	0.008	0.008	0.008	0.008	0.008
COS	0.001	0.001	0.001	0.001	0.001
NH_3	0.000	0.000	0.000	0.000	0.000
CO_2	0.016	0.017	0.019	0.020	0.021
H_2O	0.029	0.031	0.033	0.035	0.037
N_2	0.058	0.059	0.059	0.059	0.059
O_2	0.000	0.000	0.000	0.000	0.000

Table 21: Syngas composition for Illinois#6 bituminous coal at 1482 ^{o}C

Illinois # 6, dried to 5% moisture by weight, temperature 1482 ^{o}C					
Carbon in slag (%)	0	0.5	1	1.5	2
CO	0.575	0.573	0.571	0.568	0.566
H_2	0.302	0.301	0.300	0.299	0.298
CH_4	0.000	0.000	0.000	0.000	0.000
H_2S	0.008	0.008	0.008	0.008	0.008
COS	0.001	0.001	0.001	0.001	0.001
NH_3	0.000	0.000	0.000	0.000	0.000
CO_2	0.016	0.017	0.018	0.019	0.020
H_2O	0.030	0.032	0.034	0.036	0.038
N_2	0.058	0.059	0.059	0.059	0.059
O_2	0.000	0.000	0.000	0.000	0.000

Table 21: Syngas composition for Appalachian low sulfur bituminous coal at 1371 ^{o}C

Appalachian low sulfur, dried to 5% moisture by weight, temperature 1371 ^{o}C					
Carbon in slag (%)	0	0.5	1	1.5	2
CO	0.594	0.592	0.590	0.587	0.585
H_2	0.301	0.301	0.300	0.299	0.298
CH_4	0.001	0.001	0.001	0.001	0.001
H_2S	0.002	0.002	0.002	0.002	0.002
COS	0.000	0.000	0.000	0.000	0.000
NH_3	0.000	0.000	0.000	0.000	0.000
CO_2	0.014	0.015	0.016	0.017	0.019
H_2O	0.023	0.025	0.026	0.028	0.030
N_2	0.054	0.055	0.055	0.055	0.055
O_2	0.000	0.000	0.000	0.000	0.000

Table 21: Syngas composition for Appalachian low sulfur bituminous coal at 1427 ^{o}C

Appalachian low sulfur, dried to 5% moisture by weight, temperature 1427 ^{o}C					
Carbon in slag (%)	0	0.5	1	1.5	2
CO	0.595	0.593	0.590	0.588	0.586
H_2	0.302	0.301	0.300	0.299	0.298
CH_4	0.001	0.001	0.001	0.000	0.000
H_2S	0.002	0.002	0.002	0.002	0.002
COS	0.000	0.000	0.000	0.000	0.000
NH_3	0.000	0.000	0.000	0.000	0.000
CO_2	0.013	0.014	0.015	0.017	0.018
H_2O	0.023	0.025	0.027	0.029	0.031
N_2	0.054	0.055	0.055	0.055	0.055
O_2	0.000	0.000	0.000	0.000	0.000

Table 22: Syngas composition for Appalachian low sulfur bituminous coal at 1482 ^{o}C

Appalachian low sulfur, dried to 5% moisture by weight, temperature 1482 ^{o}C					
Carbon in slag (%)	0	0.5	1	1.5	2
CO	0.595	0.593	0.591	0.589	0.587
H_2	0.302	0.301	0.300	0.299	0.298
CH_4	0.000	0.000	0.000	0.000	0.000
H_2S	0.002	0.002	0.002	0.002	0.002
COS	0.000	0.000	0.000	0.000	0.000
NH_3	0.000	0.000	0.000	0.000	0.000
CO_2	0.013	0.014	0.015	0.016	0.017
H_2O	0.023	0.025	0.027	0.029	0.031
N_2	0.054	0.054	0.055	0.055	0.055
O_2	0.000	0.000	0.000	0.000	0.000

Table 22: Syngas composition for Appalachian medium sulfur bituminous coal at 1371 ^{o}C

Appalachian medium sulfur, dried to 5% moisture by weight, temperature 1371 ^{o}C					
Carbon in slag (%)	0	0.5	1	1.5	2
CO	0.594	0.592	0.589	0.587	0.585
H_2	0.305	0.304	0.303	0.302	0.301
CH_4	0.001	0.001	0.001	0.001	0.001
H_2S	0.006	0.006	0.006	0.006	0.006
COS	0.001	0.001	0.001	0.001	0.001
NH_3	0.000	0.000	0.000	0.000	0.000
CO_2	0.012	0.013	0.014	0.015	0.016
H_2O	0.019	0.021	0.023	0.025	0.026
N_2	0.053	0.053	0.053	0.053	0.053
O_2	0.000	0.000	0.000	0.000	0.000

Table 23: Syngas composition for Appalachian medium sulfur bituminous coal at 1427 oC

Appalachian medium sulfur, dried to 5% moisture by weight, temperature 1427 ^{o}C					
Carbon in slag (%)	0	0.5	1	1.5	2
CO	0.595	0.592	0.590	0.588	0.586
H_2	0.305	0.304	0.303	0.303	0.302
CH_4	0.001	0.001	0.001	0.001	0.001
H_2S	0.006	0.006	0.006	0.006	0.006
COS	0.001	0.001	0.001	0.001	0.001
NH_3	0.000	0.000	0.000	0.000	0.000
CO_2	0.011	0.012	0.013	0.014	0.015
H_2O	0.019	0.021	0.023	0.025	0.027
N_2	0.053	0.053	0.053	0.053	0.053
O_2	0.000	0.000	0.000	0.000	0.000

Table 24: Syngas composition for Appalachian medium sulfur bituminous coal at 1482 oC

Appalachian medium sulfur, dried to 5% moisture by weight, temperature 1482 ^{o}C					
Carbon in slag (%)	0	0.5	1	1.5	2
CO	0.595	0.593	0.591	0.588	0.586
H_2	0.305	0.304	0.303	0.302	0.301
CH_4	0.000	0.000	0.000	0.000	0.000
H_2S	0.006	0.006	0.006	0.006	0.006
COS	0.001	0.001	0.001	0.001	0.001
NH_3	0.000	0.000	0.000	0.000	0.000
CO_2	0.010	0.011	0.013	0.014	0.015
H_2O	0.019	0.021	0.023	0.025	0.027
N_2	0.053	0.053	0.053	0.053	0.053
O_2	0.000	0.000	0.000	0.000	0.000

Table 25: Syngas composition for WPC Utah bituminous coal at 1371 ^{o}C

WPC Utah, dried to 5% moisture by weight, temperature 1371 ^{o}C					
Carbon in slag (%)	0	0.5	1	1.5	2
CO	0.577	0.575	0.572	0.570	0.568
H_2	0.316	0.316	0.315	0.314	0.313
CH_4	0.001	0.001	0.001	0.001	0.001
H_2S	0.002	0.002	0.002	0.002	0.002
COS	0.000	0.000	0.000	0.000	0.000
NH_3	0.000	0.000	0.000	0.000	0.000
CO_2	0.014	0.015	0.016	0.017	0.018
H_2O	0.025	0.027	0.028	0.030	0.032
N_2	0.055	0.055	0.055	0.056	0.056
O_2	0.000	0.000	0.000	0.000	0.000

Table 26: Syngas composition for WPC Utah bituminous coal at 1427 oC

WPC Utah, dried to 5% moisture by weight, temperature 1427 ^{o}C					
Carbon in slag (%)	0	0.5	1	1.5	2
CO	0.578	0.575	0.573	0.571	0.569
H_2	0.317	0.316	0.315	0.314	0.313
CH_4	0.001	0.001	0.001	0.001	0.000
H_2S	0.002	0.002	0.002	0.002	0.002
COS	0.000	0.000	0.000	0.000	0.000
NH_3	0.000	0.000	0.000	0.000	0.000
CO_2	0.013	0.014	0.015	0.016	0.017
H_2O	0.025	0.027	0.029	0.031	0.033
N_2	0.055	0.055	0.055	0.056	0.056
O_2	0.000	0.000	0.000	0.000	0.000

Table 27: Syngas composition for WPC Utah bituminous coal at 1482 oC

WPC Utah, dried to 5% moisture by weight, temperature 1482 ^{o}C					
Carbon in slag (%)	0	0.5	1	1.5	2
CO	0.578	0.576	0.574	0.572	0.569
H_2	0.317	0.316	0.315	0.314	0.313
CH_4	0.000	0.000	0.000	0.000	0.000
H_2S	0.002	0.002	0.002	0.002	0.002
COS	0.000	0.000	0.000	0.000	0.000
NH_3	0.000	0.000	0.000	0.000	0.000
CO_2	0.013	0.014	0.015	0.016	0.017
H_2O	0.025	0.027	0.029	0.031	0.033
N_2	0.055	0.055	0.055	0.056	0.056
O_2	0.000	0.000	0.000	0.000	0.000

Table 28: Syngas composition for Wyoming PRB sub-bituminous coal at 1371 ^{o}C

Wyoming PRB, dried to 6% moisture by weight, temperature 1371 ^{o}C					
Carbon in slag (%)	0	0.5	1	1.5	2
CO	0.545	0.543	0.541	0.538	0.536
H_2	0.265	0.264	0.263	0.262	0.261
CH_4	0.000	0.000	0.000	0.000	0.000
H_2S	0.002	0.002	0.002	0.002	0.002
COS	0.000	0.000	0.000	0.000	0.000
NH_3	0.000	0.000	0.000	0.000	0.000
CO_2	0.042	0.043	0.044	0.045	0.047
H_2O	0.064	0.066	0.068	0.070	0.072
N_2	0.073	0.073	0.073	0.073	0.073
O_2	0.000	0.000	0.000	0.000	0.000

Table 29: Syngas composition for Wyoming PRB sub-bituminous coal at 1427 oC

Wyoming PRB, dried to 6% moisture by weight, temperature 1427 ^{o}C					
Carbon in slag (%)	0	0.5	1	1.5	2
CO	0.547	0.545	0.542	0.540	0.538
H_2	0.263	0.262	0.261	0.260	0.259
CH_4	0.000	0.000	0.000	0.000	0.000
H_2S	0.002	0.002	0.002	0.002	0.002
COS	0.000	0.000	0.000	0.000	0.000
NH_3	0.000	0.000	0.000	0.000	0.000
CO_2	0.040	0.041	0.042	0.044	0.045
H_2O	0.066	0.068	0.070	0.072	0.074
N_2	0.073	0.073	0.073	0.073	0.073
O_2	0.000	0.000	0.000	0.000	0.000

Table 30: Syngas composition for Wyoming PRB sub-bituminous coal at 1482 oC

Wyoming PRB, dried to 6% moisture by weight, temperature 1482 ^{o}C					
Carbon in slag (%)	0	0.5	1	1.5	2
CO	0.548	0.546	0.544	0.542	0.539
H_2	0.262	0.261	0.260	0.259	0.258
CH_4	0.000	0.000	0.000	0.000	0.000
H_2S	0.002	0.002	0.002	0.002	0.002
COS	0.000	0.000	0.000	0.000	0.000
NH_3	0.000	0.000	0.000	0.000	0.000
CO_2	0.039	0.040	0.041	0.042	0.043
H_2O	0.067	0.069	0.071	0.073	0.075
N_2	0.073	0.073	0.073	0.073	0.073
O_2	0.000	0.000	0.000	0.000	0.000

Table 31: Syngas composition for North Dakota lignite at 1371 ^{o}C

ND Lignite, dried to 12% moisture by weight, temperature 1371 ^{o}C					
Carbon in slag (%)	0	0.5	1	1.5	2
CO	0.496	0.494	0.492	0.490	0.487
H_2	0.253	0.252	0.251	0.250	0.249
CH_4	0.000	0.000	0.000	0.000	0.000
H_2S	0.006	0.006	0.006	0.006	0.006
COS	0.001	0.001	0.001	0.001	0.001
NH_3	0.000	0.000	0.000	0.000	0.000
CO_2	0.054	0.055	0.056	0.058	0.059
H_2O	0.088	0.089	0.091	0.093	0.095
N_2	0.093	0.093	0.093	0.094	0.094
O_2	0.000	0.000	0.000	0.000	0.000

Table 32: Syngas composition for North Dakota lignite at 1427 oC

ND Lignite, dried to 12% moisture by weight, temperature 1427 ^{o}C					
Carbon in slag (%)	0	0.5	1	1.5	2
CO	0.498	0.496	0.494	0.492	0.489
H_2	0.251	0.250	0.249	0.248	0.247
CH_4	0.000	0.000	0.000	0.000	0.000
H_2S	0.006	0.006	0.006	0.006	0.006
COS	0.001	0.001	0.001	0.001	0.001
NH_3	0.000	0.000	0.000	0.000	0.000
CO_2	0.052	0.053	0.054	0.055	0.057
H_2O	0.090	0.091	0.093	0.095	0.097
N_2	0.093	0.093	0.093	0.094	0.094
O_2	0.000	0.000	0.000	0.000	0.000

Table 33: Syngas composition for North Dakota lignite at 1482 oC

ND Lignite, dried to 12% moisture by weight, temperature 1482 ^{o}C					
Carbon in slag (%)	0	0.5	1	1.5	2
CO	0.500	0.498	0.496	0.493	0.491
H_2	0.249	0.248	0.247	0.246	0.245
CH_4	0.000	0.000	0.000	0.000	0.000
H_2S	0.006	0.006	0.006	0.006	0.006
COS	0.001	0.001	0.001	0.001	0.001
NH_3	0.000	0.000	0.000	0.000	0.000
CO_2	0.050	0.052	0.053	0.054	0.055
H_2O	0.091	0.093	0.095	0.097	0.099
N_2	0.093	0.093	0.093	0.094	0.094
O_2	0.000	0.000	0.000	0.000	0.000

Conclusions

This report explains the performance and cost updates to PC and IGGC models in the IECM. For the PC plants, updates were made to the Base Plant, Steam and the CO_2 Capture system. For the IGCC plants, Aspen Plus simulation software was used to predict the product syngas compositions obtained by gasifying six different types of coals using a Shell gasifier at different operating conditions.

References

1. EPRI, "Advanced Coal Power Systems with CO2 Capture: EPRI's CoalFleet for Tomorrow Vision" Report #1016877, Electric Power Research Institute, Palo Alto, CA, September 2008.
2.   DOE/NETL, "Cost and Performance Baseline for Fossil Energy Plants. Volume 1: Bituminous Coal and Natural Gas to Electricity Final Report", August 2007.
3. C. A. Roberts, J. Gibbins, R. Panesar, G. Kelsall "Potential for Improvement in Power Generation with Post Combustion Capture of CO2" White Paper, http://uregina.ca/ghgt7/PDF/papers/peer/510.pdf.
4. DOE/NETL "Carbon Dioxide Capture from Existing Coal-Fired Power Plants" November 2007.
5. Steam, It's Generation and Use. Babcock and Wilcox. Barberton, Ohio. 2005
6. Aspen Technology, Inc., 2007, Ten Canal Park, Cambridge, MA 02141-2201.
7. Holt N.A.H and Alpert S.B, 2001, Integrated Gasification Combined-Cycle Power Plants, Encyclopedia of Physical Science and Technology, 897 – 924
8. IECM-cs, 2007, Integrated Env. Control Model Carbon Sequestration Edition, Carnegie Mellon Univ. Center for Energy and Env. Studies, http://www.iecm-online.com
9. Probstein R. F and Hicks R. E, 1985, Synthetic Fuels, Intl Student Edition, McGraw Hill, Singapore.
10. Steynberg A and Dry M., 2004, Fischer-Tropsch Technology, Studies in Surface Science and Catalysis, 152, Elsevier, Amsterdam.
11. Zuideveld P.L, 2005, Shell coal gasification using low-rank coals, Gasification Technologies Conference, San Francisco, Oct 9 -12.
12. Eldrid R, Kaufman L and Marks P., 2004, The 7FB: the next evolution of the F gas turbine, GE Power Systems, Schenectady, NY.

IECM Technical Documentation: Volume V
Carbon Dioxide Transport and Storage Models

November 2009

Disclaimer

IECM Technical Documentation: Volume V
Carbon Dioxide Transport and Storage Models

_____

DE-AC26-04NT41917

RDS Subtask 404.01.03:
Development and Application of the Integrated Environmental Control Model

Prepared for:

Office of Systems, Analyses and Planning
National Energy Technology Laboratory
Department of Energy
Pittsburgh, PA 15236
www.netl.doe.gov

Prepared by:
Sean McCoy
Edward S. Rubin
Carnegie Mellon University
Pittsburgh, PA 15213
www.iecm-online.com

November 2009

Contents

Oil Recovery Methods   127

Numerical Modeling of the Wellbore Environment   131

Arial Extent of CO_2 Plume Size in Aquifer Injection   139

CO_2 Price Conversion Table   143

Figures

Tables

Objectives and Organization

Large reductions in carbon dioxide (CO_2) emissions from fossil fuel use will be required to stabilize atmospheric concentrations of CO_2 [1-5]. One option to reduce CO_2 emissions to the atmosphere from large industrial sources—particularly fossil-fuel fired power plants—is carbon capture and storage (CCS); i.e., the capture of CO_2 directly from anthropogenic sources and disposal of it in geological sinks for significant periods of time [6]. CCS requires CO_2 to first be captured and compressed to high pressures, then transported to a storage site, where it is injected into a suitable geologic formation. Each of these steps—capture, transport, and storage—is capital and energy intensive, and will have a significant impact on the cost of production for electricity or other industrial commodities produced using CCS. However, with appropriate policy incentives, CCS could act as a potential "bridging technology" that would achieve significant CO_2 emission reductions while allowing fossil fuels to be used until alternative energy sources are more widely deployed.

This chapter is intended to be an overview of how CCS fits into a portfolio of advanced technologies that could, if implemented, lead to reduced emissions from the electric power sector. The chapter draws on the findings of the Intergovernmental Panel on Climate Change (IPCC) Fourth Assessment Report (AR4) [5] to review the magnitude of global emissions reductions required to meet various atmospheric stabilization targets. The chapter then reviews the importance of emissions from the electric sector; available means of mitigating these emissions, including CCS; and the challenges to CCS as an accepted method of reducing emissions. This provides the context for a concluding presentation of the objectives and overview of this report.

The Climate Change Challenge

Atmospheric concentrations of CO_2 have increased from a pre-industrial concentration of 278 ppm to a current concentration of 379 ppm. Approximately 60% of the nearly 50 Gt per year of greenhouse gas emissions are CO_2 from fossil fuel combustion [5]. Figure 1, reproduced from IPCC AR4, shows not only that CO_2 emissions from fossil fuel emissions have been growing steadily, but that the largest single contributor to CO_2 emissions is electricity generation.

Given past growth in CO_2 emissions, future growth in global population, and increasing global average income per capita, it is almost certain that total CO_2 emissions will continue to grow in the absence of a rapid decrease in the carbon intensity of the worlds primary energy supply [1].
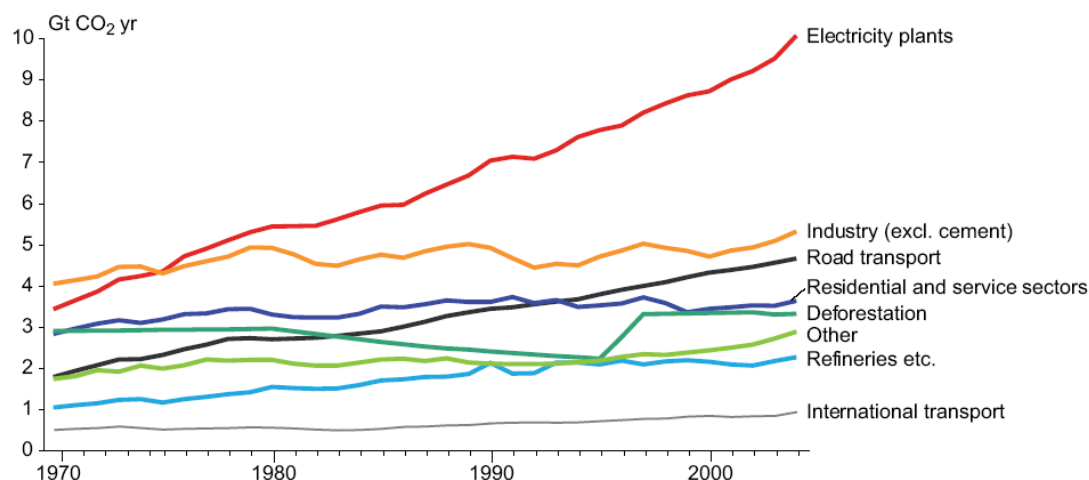
Figure 1.   Sources of global CO_2 emissions between 1970 to 2004 by sector adapted from the IPCC AR4 [7].

Table 1, adapted from the IPCC AR4 [5], shows the required emissions reductions to stabilize CO_2 concentrations at various levels, the long-term (i.e., equilibrium) global mean temperature increases associated with these concentrations, and the range of years in which CO_2 emissions peak. In this table, the temperature rise is based on the IPCC "best-estimate" climate sensitivity of 3^oC, which is "likely" to lie in the range of 2^oC to 4.5^oC. The emissions reduction trajectory varies between scenarios examined in the IPCC AR4, which explains the ranges of peaking years and changes in emissions in 2050 presented in Table 1.

Table 1.   A summary of emissions stabilizations scenarios showing required emissions reductions (adapted from the IPCC AR4 [5]).

Global Mean Temperature Rise (^oC)[*]	CO_2-eq Concentration (ppm)	2050 Change Global Emissions (% of 2000)	Peaking year for CO_2 Emissions
2.0 - 2.5	445 - 490	-85 to -50	2000-2015
2.5 - 2.8	490 - 535	-60 to -30	2000-2020
2.8 - 3.3	535 - 590	-30 to +5	2010-2030
3.3 - 4.1	590 - 710	+10 to +60	2020-2060
4.1 - 4.9	710 – 855	+25 to +85	2050-2080
4.9 - 6.1	855 - 1130	+90 to +140	2060-2090
[*] Temperature rise above pre-industrial global mean, based on AR4 "best-estimate" climate sensitivity of 3^oC			

Based on this IPCC summary, achieving the European Union (EU) target of no more than a 2^oC temperature increase would require an emissions reduction of between 85% and 50% from 2000 levels by 2050. Achieving long term stabilization at a doubling of pre-industrial levels (approximately 550 ppm CO_2), would require emissions to be approximately the same as in 2000 or lower despite any growth that would otherwise occur and would result in a warming of 2.8 to 3.3 ^oC.

The appropriate stabilization target for atmospheric concentration of CO_2 is uncertain. From the perspective of the United Nations Framework Convention on Climate Change, a stabilization target should prevent "dangerous anthropogenic interference" (DAI) with the climate system. However, what constitutes DAI and the atmospheric concentration of CO_2 at which DAI would be avoided, is unclear [7-9]. Nonetheless, achieving any significant levels of emissions reductions—or even restraining emissions growth—is a daunting task, thus will require a broad portfolio of advanced energy technologies and changes in energy consumption patterns [2-4]. Including CCS in this portfolio of technologies will allow emissions reductions targets to be met at lower costs than if CCS were not an option [10].

Mitigating Emissions from the Electricity Sector

As Figure 1 shows, emissions from electricity generation make up approximately one-third of global CO_2 emissions. In the US, electricity generation contributes 39% of all CO_2 emissions (i.e. approximately 2.4 Gt CO_2) [11], the majority of which come from coal combustion at large power plants. Thus, the potential exists for large CO_2 emissions reductions if the carbon intensity of electricity generation can be reduced.

There are a number of advanced technologies that can mitigate emissions from the electric sector. These advanced technologies can be generalized as efficiency improvements (both generation and end-use), decarbonization and sequestration (e.g., fuel switching and CCS), use of renewables (e.g. wind, solar, and biomass), and use of nuclear energy [2]. At the present time some of these technologies may be more desirable than others; however, the emissions reduction challenge will require more than one technology (e.g., see Pacala and Socolow [12]).

The CCS Option—Capturing CO_2

Capture of CO_2 can be accomplished via three general routes: pre-combustion CO_2 capture, where carbon is removed from the fuel prior to oxidization; post-combustion CO_2 capture, where fuel is combusted normally in a boiler or turbine, and CO_2 is removed from the exiting flue gas stream; and oxyfuel combustion, where the fuel is combusted with nearly stoichiometric amounts of oxygen in an atmosphere of CO_2. Figure 2 summarizes the major flows and processes in the three categories of capture processes.
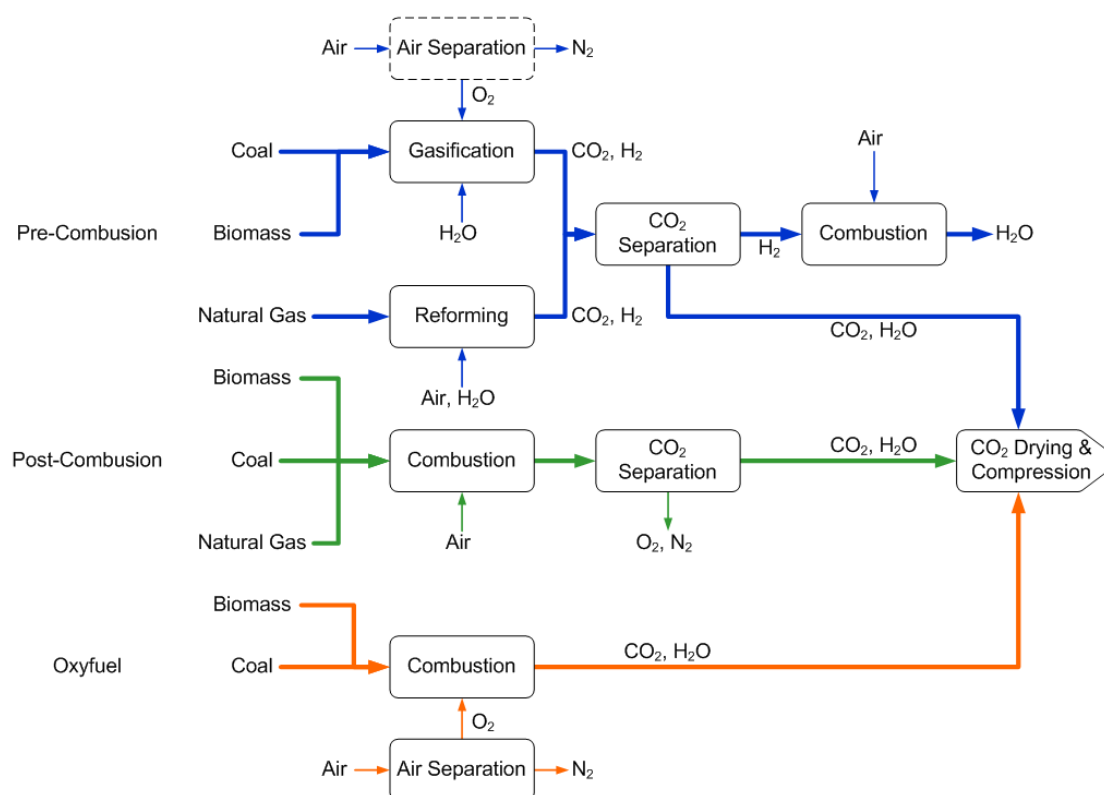
Figure 2. CO_2 capture processes summarized by major process steps, adapted from the IPCC Special Report on CCS [13].

All of these types of capture systems currently consume large amounts of energy, resulting in decreased plant efficiencies and reduced net power outputs when compared against the same plants without capture systems. As a result, power plants with capture systems will consume more fuel and water while producing more waste products (e.g. ash, slag, and sulfur) per unit of electricity generated [14]. The decrease in energy output coupled with the increased operating cost and increased capital cost (resulting from the capture system) results in a higher cost of electricity (COE) for capture plants versus those without capture. Figure 3, adapted from the IPCC Special Report on CCS [13],

summarizes the difference in COE and emissions rates between plants with and without capture (including compression, but not transport or storage) for three power plant technologies: pulverized coal (PC), integrated gasification combined cycle (IGCC), and natural gas combined cycle (NGCC).
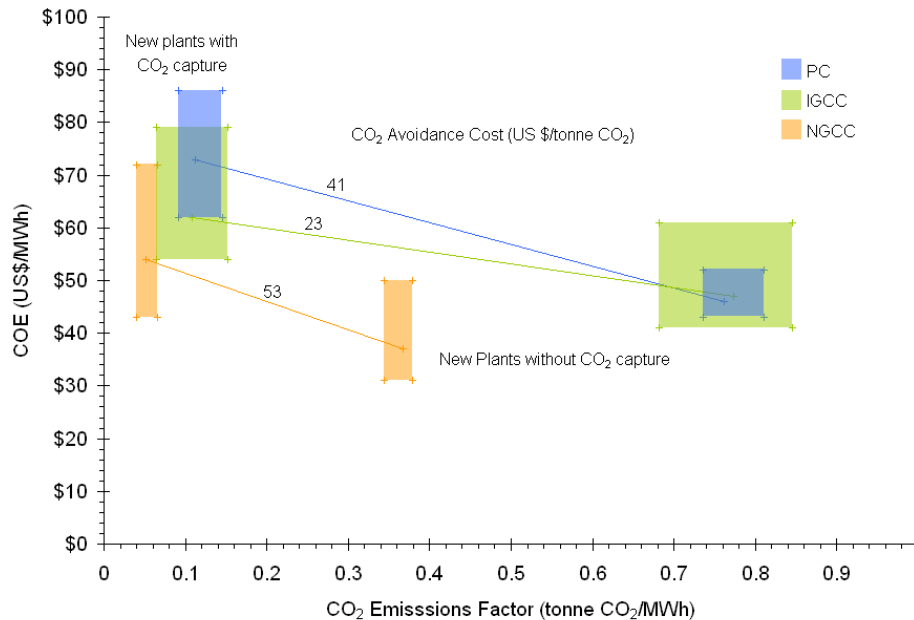
Figure 3.   Ranges for the COE and CO_2 emissions factor for different power plant technologies with and without capture based on current technologies. Coal plants use bituminous coals, PC plants use supercritical steam cycles, and all figures are for new plants. Lines connect the IPCC "representative values" [13], and indicate the CO_2 avoidance cost for the same type of plant.

There are several metrics for measuring the cost of carbon capture, including the incremental COE, cost of CO_2 avoided, and cost of CO_2 captured. Figure 3 shows the differences in COE between plants with and without capture and the cost of CO_2 avoided *for the same plant types1.*

The remainder of this report focuses on the costs of CO_2 transport and storage expressed as cost per metric tonne of CO_2 transported or stored. The appropriate metric for comparison with capture costs is the cost of CO_2 captured, which ranges from roughly $10 to $60 per tonne of CO_2 depending on plant type and other design and operating factors [13]. In general, the cost per tonne of CO_2 captured using current technologies is highest for NGCC plants, and approximately similar for PC and IGCC plants [13].

The technological maturity of CO_2 capture systems varies from technology to technology. The recent IPCC report concludes that the components of many capture systems are well understood from a technological standpoint, but there is a lack of experience in building and operating capture systems at scale [13].

The CCS Option—Transport of CO_2

There are multiple options for transporting compressed CO_2 from the source to the geological sink. Practical modes of overland transport include motor carrier, rail, and pipeline. The most economic method of transport depends on the locations of capture and storage, distance from source to sink, and the quantities of CO_2 to be transported. However, the quantity to be transported is the dominant factor—on the order of 2 to 3 million metric tonnes (Mt) per year of CO_2 would need to be transported from a single 500 MW coal-fired power plant. As a result, pipeline is the only viable option for overland transport [15, 16], and is the only method of transport considered in the report.

---

1 The cost of CO_2 avoided is highly sensitive to the context in which it is used and types of plants being compared. For example, in a situation where the alternative to building an IGCC plant with capture is to build an NGCC plant without capture, the relevant avoidance cost should be measured between these plant types.

There is considerable industrial experience in the transport of CO_2 by pipeline. Upwards of 50 Mt/y of CO_2 is transported over nearly 3100 km of pipelines primarily for use in EOR operations [17, 18]. For comparison, this would be the amount of CO_2 produced by about sixteen-500 MW coal fired power plants.

The CCS Option—Storage of CO_2

The theoretical capacity of geological sinks for CO_2 storage is uncertain, but likely very large [19]. Geological sinks suitable for storing captured CO_2 include: deep saline aquifers, depleted gas reservoirs, oil reservoirs, and coal beds. Storage of CO_2 in producing oil reservoirs and coal beds are referred to as enhanced oil recovery (EOR) and enhanced coal bed methane (ECBM) recovery, respectively. Table 2 shows the range of capacity estimates for deep saline formations, EOR, and ECBM reported by different authors [20-27].

Table 2.   Summary of CO_2 storage capacity estimates for deep saline formations, EOR, and ECBM reported by several authors.

Formation	United States (Gt CO_2)	Worldwide (Gt CO_2)
Deep Saline Aquifers	10^2	10^3-10^4
EOR & Depleted Oil and Gas Fields	10^2	10^3
ECBM	10^1	10^1-10^2

On a global scale, the estimated capacity of deep saline formations is largest, followed by oil and gas reservoirs (including depleted reservoirs) and ECBM, while mined salt caverns have an estimated global storage capacity that is insignificant in comparison.

Many difference approaches have been used to make estimates of the storage capacity in the subsurface on both regional and global levels, which explains the great variation in estimates of global capacity estimates shown in Table 2 [19, 27]. Asides from methodological issues, such as correlating surface area of sedimentary basins with storage capacity, the range in capacity estimates can be attributed to divergent assumptions used in the various assessments, and the level of the assessment (i.e., reserves vs. resources) [19, 28].

Even at the lower end of the range of capacity estimates in Table 2, there is still ample global capacity to sequester large amounts of CO_2. However, the availability of storage sites is highly variable. For example, sedimentary basins2 such as the Permian Basin (Southwest United States) and the Alberta Basin (Western Canada) will have large storage capacities in deep saline formations, and oil and gas reservoirs, whereas other areas, such as Central Canada, will have little capacity for storage owing to its location on the Precambrian Shield [29]. To effectively utilize regional storage capacities, CO_2 may have to be transported, potentially over large distances, since geological sinks further from the CO_2 source may be more suitable than nearby sinks. Suitability of geological formations for storage depends on the geological suitability of the particular sedimentary basin, the inventory of potential storage sites within the basin, the safety and long term fate of injected CO_2, and the capacity of the storage site [30].

Planned and Operating CO_2 Capture and Storage Projects

There are a number of planned CO_2 and operating storage projects. A number of these projects are relatively small-scale pilot projects (i.e., on the order of 10^5 tonnes CO_2 per year), such as the Phase III projects planned by the US Department of Energy (DOE) Carbon Sequestration Regional Partnerships [31]. However, there are also a growing number of large-scale commercial projects (i.e., 1 Mt CO_2 per year and larger). Large-scale projects currently operating or in an advanced stage of planning are summarized in Table 3 [27, 32, 33].

In addition to the projects listed in Table 3, there is a large number of operating EOR projects injecting natural CO_2 primarily for oil recovery. The Enhanced Oil Recovery (EOR) chapter contains an overview of operating EOR projects.

---

2 A sedimentary basin is a depression in the earth's crust formed by movement of tectonic plates where sediments have accumulated to form sedimentary rocks. Hydrocarbons commonly occur in sedimentary basins.

Processes analogous to those used in deep saline formation storage are used for acid gas3 disposal in Canada. Through 2005, over 4.5 Mt of acid gas have been injected into deep saline aquifers and depleted hydrocarbon reservoirs at 48 sites, produced by 42 separate gas plants [34, 35]. Both H_2S and CO_2 are disposed of simultaneously because co-capture of the two gases is less expensive than separate capture of H_2S and CO_2. Of the total amount of acid gas injected, approximately 2.5 Mt is CO_2.

Table 3.   A summary of operating commercial CO_2 storage projects

Project	Location	Operator	Storage Type	Injection Start Date	Annual Injection Rate	Total Planned Storage
Sleipner	North Sea	StatoilHydro	Aquifer	1996	1 Mt/y	20 Mt
Weyburn	Saskatchewan, Canada	EnCana	EOR	2000	1.2 Mt/y[*]	19 Mt
In Salah	Sahara, Algeria	Sonatrach, BP, StatoilHydro	Depleted Gas Reservoir	2004	1.2 Mt/y	17 Mt
Salt Creek	Wyoming, USA	Anadarko	EOR	2006	2.2 Mt/y[+]	27 Mt
Snohvit	Melkøya, Norway	StatoilHydro	Aquifer	2007	0.7 Mt/y	
Gorgon	Barrow Island, Australia	Chevron	Aquifer	2009[§]	3.2 Mt/y	>100 Mt
[*] Average annual delivery rate over 15 year CO_2 contract						
[+] Peak annual storage rate						
§ Planned date						

Many of these projects are being studied to better understand the processes occurring in storage, means of monitoring injected CO_2 and detecting leakage, and security of CO_2 storage in the long-term. The findings from these and other pilot projects can inform development of an integrated framework for CCS.

Challenges in CO_2 Transport and Storage

The challenges to the acceptance and widespread use of CCS as a technology to address the climate challenge are numerous. Perhaps one of the most critical is the public acceptance of CCS as a safe and effective means to reduce emissions. The issue of public perception is also tied to increasing scientific knowledge about the security of stored CO_2, its long-term fate, appropriate risk assessment, and development and implementation of an effective regulatory system. The following three sections give a brief overview of these issues.

Technical Challenges in CO_2 Transport and Storage

As Table 2 shows, there is a wide range of capacity estimates for both the US and the world, and as noted by Bradshaw et al. [19], there are capacity estimates in the literature that report US capacities larger than world capacities estimated by others. While efforts such as the US DOE Carbon Sequestration Regional Partnerships have made estimates of storage capacity at the national level, there is still a considerable range of uncertainty in their estimates [36]. Friedmann et al. [37] argue that it is prudent for governments to quickly undertake geological assessments of CO_2 storage capacity given their low cost relative to the benefit of having accurate capacity estimates for long-term planning.

A further challenge for geological storage is to improve understanding of potential leakage processes from storage formations. Potential leakage pathways can be both natural (e.g. open faults) and man-made (e.g. abandoned wells). Faults can be identified using seismic methods and characterized as either sealing or open. Abandoned wells can also be identified. However, in a mature sedimentary basin there may be hundreds of thousands of abandoned wells that can

---

3 Formally, an acid gas is any gas that can form acidic solutions when mixed with water. In this context, an acid gas is a mixture of hydrogen sulfide (H_2S) and CO_2 of varying proportions. In the petroleum industry, H_2S and CO_2 gases are obtained after a sweetening process is applied to a sour gas.

potentially serve as conduits to the surface (e.g., see Gasda [38]). A better understanding of the processes that could lead to leakage from wells and better tools to enable risk assessment would be beneficial.

Given the volumes of CO_2 to be stored and the locations in which storage is likely to occur, it is reasonable to assume that there will be leakage from some projects, even in cases where due diligence has been exercised. In such a situation, remediation will be required. Using natural gas storage facilities as analogs to CO_2 storage, Benson and Hepple [39] describe several pathways for leakage and possible remediation technologies. However, as both Benson and Hepple and the IPCC special report conclude [27], technologies to mitigate leakage should be further explored.

Regulatory Needs for CO_2 Transport and Storage

Despite the importance placed on CCS technologies by the US DOE, the US does not yet have a regulatory framework for CCS, nor does the US have a clear plan to develop an integrated regulatory framework. An integrated regulatory framework for CCS should encompass the entire lifecycle of a CSS project—from ensuring that storage sites are appropriate to verifying that CO_2 has been sequestered from the atmosphere to management of the long-term risks presented by the stored CO_2. Without an integrated regulatory framework or a clear plan forward—in addition to restrictions on CO_2 emissions—CCS will not be an option for commercial entities looking to reduce emissions.

In the US, the EPA has announced its intention to regulate geological storage of CO_2 under the Underground Injection Control (UIC) program and plans to propose draft regulations late in 2008. As pointed out by Wilson and others [40, 41], the UIC may not be an appropriate framework to regulate the lifecycle of a CCS project. An appropriate regulatory framework must balance the needs of a large number of stakeholders, accounting for the long-term liability resulting from injected CO_2 and incorporate lessons learnt from early pilot and commercial scale projects [42].

Pubic Perception of CO_2 Transport and Storage

Public acceptance of CCS as a safe and effective means of reducing CO_2 emissions is necessary for the technology to play a role in the future. Palmgren et al. [43] suggest that the initial public perception of CCS is not favorable in comparison with other energy technologies that could play a role in reducing emissions. In agreement, Reiner et al. [44] present survey results suggesting that the public are uncertain as to whether CCS should play a role in a portfolio of climate mitigation technologies. Of course, acceptance of CCS is also tied to acceptance of climate change as a pressing problem that requires prompt action [43, 44]. Further studies of public perception may be able to determine what aspects of CCS must be addressed, from a technological or regulatory standpoint, to improve its standing in the public arena.

Objectives and Organization of this Report

In addition to information on technical characteristics and risks, policy makers require methods to estimate the costs of CCS to evaluate proposed climate change mitigation strategies involving development of CCS projects. In addition, private actors also have an interest in examining the cost of CCS projects. In the last decade the understanding of CCS processes has increased greatly, as reflected by the recent IPCC Special Report [45]; however, there are still significant gaps in knowledge of the cost of integrated capture, transport, and storage processes. For example, many studies of carbon capture processes have been undertaken [13] and reasonable models linking process economics to key engineering parameters (i.e., engineering-economic models) have been developed [46], but they have not yet been linked with transport [47] and storage models to determine the economics of an integrated CCS process.

Current estimates of the costs of CO_2 transport and storage have by and large been based on rules-of-thumb adapted from petroleum engineering (e.g., see [48-52]). In storage, the uses of rules-of-thumb are appropriate for situations where there is limited knowledge of the geological properties of the reservoir at the scales of interest for cost calculations (i.e., over tens of km^2). For example, studies that have produced regional cost-curves for storage (i.e. the cost of storing a cumulative mass of CO_2) have typically applied these rules of thumb [51, 52]. However, when more specific geological information is available, cost estimates can be made that better reflect the specifics of the case (e.g., see [53]).

The goal of this report is to develop a suite of models that relate the specifics of CO_2 transport and storage projects—through both aquifer storage and EOR—to the cost of transport and geological storage. These models will: be flexible with respect to changing scenarios and assumptions; allow for probabilistic assessment; and, be relatively transparent and

easy to use. The models will be used in the report to assess the relative importance of the input parameters, the effects of variability in the input parameters, and the relative costs of CCS for illustrative cases.

The report is divided into several chapters, including this introductory chapter. These chapters describe the transport, EOR storage, and aquifer storage models, respectively, presenting deterministic results from application of each model to illustrative cases and results from Monte Carlo sensitivity studies using each model. A subsequent chapter ties together the findings from the illustrative cases, and makes recommendations on the types of problems the models can be applied to solve.

References

1. Hoffert, M.I., et al., *Energy implications of future stabilization of atmospheric CO_2 content.* Nature, 1998. **395**: p. 881-884.
2. Hoffert, M.I., et al., *Advanced Technology Paths to Global Climate Stability: Energy for a Greenhouse Planet.* Science, 2002. **298**: p. 981-987.
3. Caldeira, K., A.K. Jain, and M.I. Hoffert, *Climate Sensitivity Uncertainty and the Need for Energy Without CO_2 Emission.* 2003. **299**(5615): p. 2052-2054.
4. Green, C., S. Baksi, and M. Dilmaghani, *Challenges to a climate stabilizing energy future.* Energy Policy, 2007. **35**(1): p. 616-626.
5. Fisher, B.S., et al., *Issues related to mitigation in the long term context*, in *Climate Change 2007: Mitigation. Contribution of Working Group III to the Fourth Assessment Report of the Inter-governmental Panel on Climate Change*, B. Metz, et al., Editors. 2007, Cambridge University Press: Cambridge. p. 169-250.
6. Bachu, S., *Screening and ranking of sedimentary basins for sequestration of CO_2 in geological media in response to climate change.* Environmental Geology, 2003. **44**: p. 277-289.
7. Rogner, H.-H., et al., *Introduction*, in *Climate Change 2007: Mitigation. Contribution of Working Group III to the Fourth Assessment Report of the Inter-governmental Panel on Climate Change*, B. Metz, et al., Editors. 2007, Cambridge University Press: Cambridge. p. 95-116.
8. Mastrandrea, M.D. and S.H. Schneider, *Probabilistic integrated assessment of "dangerous" climate change.* Science, 2004. **304**(5670): p. 571-575.
9. Schneider, S.H. and M.D. Mastrandrea, *Probabilistic assessment "dangerous" climate change and emissions pathways.* Proceedings of the National Academy of Sciences of the United States of America, 2005. **102**(44): p. 15728-15735.
10. Herzog, H., et al., *Cost and Economic Potential*, in *IPCC Special Report on Carbon Dioxide Capture and Storage*, B. Metz, et al., Editors. 2005, Cambridge University Press: Cambridge, U.K.
11. Environmental Protection Agency, *Inventory of US Greenhouse Gas Emissions and Sinks: 1990-2005.* 2007, US Environmental Protection Agency: Washington, D.C.
12. Pacala, S. and R. Socolow, *Stabilization wedges: Solving the climate problem for the next 50 years with current technologies.* Science, 2004. **305**(5686): p. 968-972.
13. Thambimuthu, K., et al., *Capture of CO_2*, in *IPCC Special Report on Carbon Dioxide Capture and Storage*, B. Metz, et al., Editors. 2005, Cambridge University Press: Cambridge, U.K.
14. Rubin, E.S., A.B. Rao, and C. Chen. *Comparative Assessments of Fossil Fuel Plants with CO_2 Capture and Storage*. in *7th International Conference on Greenhouse Gas Control Technologies*. 2004. Vancouver, Canada: Elsevier Science.
15. Skovholt, O., *CO_2 Transportation System.* Energy Conversion & Management, 1993. **34**(9-11): p. 1095-1103.
16. Svensson, R., et al., *Transportation systems for CO_2-application to carbon capture and storage.* Energy Conversion & Management, 2004. **45**: p. 2343-2353.
17. Gale, J. and J. Davidson, *Transmission of CO_2- Safety and Economic Considerations.* Energy, 2004. **29**: p. 1319-1328.
18. Doctor, R., et al., *Transport of CO_2*, in *IPCC Special Report on Carbon Dioxide Capture and Storage*, B. Metz, et al., Editors. 2005, Cambridge University Press: Cambridge, U.K.
19. Bradshaw, J., et al., *CO_2 storage capacity estimation: Issues and development of standards.* International Journal of Greenhouse Gas Control, 2007. **1**(1): p. 62-68.
20. Koide, H., et al., *Subterranean Containment and Long-Term Storage of Carbon Dioxide in Unused Aquifers and in Depleted Natural Gas Reservoirs.* Energy Conversion & Management, 1992. **33**(5-8): p. 619-626.
21. Bachu, S., W.D. Gunter, and E.H. Perkins, *Aquifer Disposal of CO_2: Hydrodynamic and Mineral Trapping.* Energy Conversion & Management, 1994. **35**(4): p. 269-279.

22. Hendriks, C.A. and K. Blok, *Underground storage of carbon dioxide.* Energy Conversion & Management, 1995. **36**: p. 539-542.

23. Gunter, W.D., et al., *Large CO₂ sinks: Their role in the mitigation of greenhouse gases from an international, national (Canadian) and provincial (Alberta) perspective.* Applied Energy, 1998. **61**(4): p. 209-227.

24. Holloway, S., *Storage of Fossil Fuel-Derived Carbon Dioxide Beneath the Surface of the Earth.* Annual Review of Energy & Environment, 2001. **26**: p. 145-166.

25. Stevens, S.H., et al., *CO₂ Injection and Sequestration in Depleted Oil and Gas Fields and Deep Coal Seams: Worldwide Potential and Cost.* Environmental Geosciences, 2001. **8**(3): p. 200-209.

26. Shaw, J. and S. Bachu, *Screening, evaluation, and ranking of oil reservoirs suitable for CO₂-flood EOR and carbon dioxide sequestration.* Journal of Canadian Petroleum Technology, 2002. **41**(9): p. 51-61.

27. Benson, S., et al., *Underground geological storage*, in *IPCC Special Report on Carbon Dioxide Capture and Storage*, B. Metz, et al., Editors. 2005, Cambridge University Press: Cambridge, U.K.

28. Bachu, S., et al., *CO₂ storage capacity estimation: Methodology and gaps.* International Journal of Greenhouse Gas Control, 2007. **1**(4): p. 430-443.

29. Hitchon, B., et al., *Sedimentary basins and greenhouse gases: a serendipitous association.* Energy Conversion & Management, 1999. **40**: p. 825-843.

30. Bachu, S., *Sequestration of CO₂ in geological media in response to climate change: road map for site selection using the transform of the geological space into the CO₂ phase space.* Energy Conversion & Management, 2002. **43**: p. 87-102.

31. National Energy Technology Lab. *Regional Carbon Sequestration Partnerships*. 2007 [cited 2007 December 1]; Available from: http://www.netl.doe.gov/technologies/carbon_seq/partnerships/partnerships.html.

32. Torp, T.A. and J. Gale, *Demonstrating storage of CO₂ in geological reservoirs: The Sleipner and SACS projects.* Energy, 2004. **29**: p. 1361-1369.

33. Torp, T.A. and K.R. Brown. *CO₂ Underground Storage Costs as Experienced at Sleipner and Weyburn.* in *7th International Conference on Greenhouse Gas Control Technologies*. 2004. Vancouver, Canada: Elsevier Science.

34. Bachu, S. and W.D. Gunter. *Overview of Acid-Gas Injection Operations in Western Canada.* in *7th International Conference on Greenhouse Gas Control Technologies*. 2004. Vancouver, Canada: Elsevier Science.

35. Bachu, S. and K. Haug, *In-Situ Characteristics of Acid-Gas Injection Operations in the Alberta Basin, Western Canada: Demonstration of CO₂ Geological Storage*, in *The CO₂ Capture and Storage Project (CCP) for Carbon Dioxide Storage in Deep Geologic Formations for Climate Change Mitigation*, S. Benson, Editor. 2004, Elsevier Science.

36. National Energy Technology Lab, *Carbon Sequestration Atlas of the United States and Canada.* 2007, Pittsnburgh, PA: US Department of Energy. 86.

37. Friedmann, S.J., et al., *The low cost of geological assessment for underground CO₂ storage: Policy and economic implications.* Energy Conversion & Management, 2006. **47**: p. 1894-1901.

38. Gasda, S.E., S. Bachu, and M.A. Celia, *Spatial characterization of the location of potentially leaky wells penetrating a deep saline aquifer in a mature sedimentary basin.* Environmental Geology, 2004. **46**(6-7): p. 707-720.

39. Benson, S. and R. Hepple, *Prospects for Early Detection and Options for Remediation of Leakage from CO₂ Storage Projects*, in *The CO₂ Capture and Storage Project (CCP) for Carbon Dioxide Storage in Deep Geologic Formations for Climate Change Mitigation*, S. Benson, Editor. 2005, Elsevier Science.

40. Wilson, E.J., T.J. Johnson, and D.W. Keith, *Regulating the Ultimate Sink: Managing the Risks of Geologic CO₂ Storage.* Environmental Science & Technology, 2003. **37**: p. 3476-3483.

41. Keith, D.W., et al., *Regulating the Underground Injection of CO₂.* Environmental Science & Technology, 2005. **39**: p. 499A-505A.

42. Wilson, E.J., et al., *Regulating the Geological Sequestration of Carbon Dioxide.* Environmental Science & Technology. **In Press, Corrected Proof**.

43. Palmgren, C.R., et al., *Initial Public Perceptions of Deep Geological and Oceanic Disposal of Carbon Dioxide.* Environmental Science & Technology, 2004. **38**(24): p. 6441-6450.

44. Reiner, D.M., et al., *American exceptionalism? Similarities and differences in national attitudes toward energy policy and global warming.* Environmental Science & Technology, 2006. **40**(7): p. 2093-2098.

45. Metz, B., et al., eds. *IPCC Special Report on Carbon Dioxide Capture and Storage.* 2005, Cambridge University Press: Cambridge, U.K. 442.

46.   Rao, A.B. and E.S. Rubin, *A technical, economic, and environmental assessment of amine-based CO_2 capture technology for power plant greenhouse gas control.* Environmental Science & Technology, 2002. **36**(20): p. 4467-4475.
47.   McCoy, S.T. and E.S. Rubin, *An engineering-economic model of pipeline transport of CO_2 with application to carbon capture and storage.* International Journal of Greenhouse Gas Control. **In Press, Corrected Proof**.
48.   Hendriks, C.F., *Carbon dioxide removal from coal fired power plants.* 1 ed. 1994: Kluwer Academic Publishers.
49.   Smith, L., et al., *Carbon Dioxide Sequestration in Saline Formations- Engineering and Economic Assessment Final Technical Report.* 2001, Battelle Memorial Institute: Columbus, OH. p. 93.
50.   Hendriks, C., et al., *Building the Cost Curves for CO_2 Storage, Part 1: Sources of CO_2.* 2002, IEA Greenhouse Gas R&D Programme: Stoke Orchard, UK.
51.   Dahowski, R., et al., *A CO_2 Storage Supply Curve for North America.* 2004, IEA Greenhouse Gas R&D Programme: Stoke Orchard, UK.
52.   Wildenborg, T., et al. *Cost Curves for CO_2 Storage: European Sector.* in *7th International Conference on Greenhouse Gas Control Technologies.* 2004. Vancouver, Canada: Elsevier Science.
53.   Bock, B., et al., *Economic Evaluation of CO_2 Storage and Sink Enhancement Options.* 2003, TVA Public Power Institute: Muscle Shoals, AL.

Modeling CO$_2$ Transport by Pipeline[4]

There have been few studies that have addressed the cost of carbon dioxide (CO$_2$) transport in detail. However, earlier work by Svensson et al. [1] identified pipeline transport as the most practical method to move large volumes of CO$_2$ overland and other studies have affirmed this conclusion [2]. There is considerable experience in the transport of CO$_2$ by pipeline, as upwards of 50 million tonnes per year of CO$_2$ is transported over nearly 3100 km of pipelines primarily for use in enhanced oil recovery (EOR) operations [2, 3]. This chapter focuses on the cost of CO$_2$ transport via pipeline. In 1993, Skovholt [4] presented rules of thumb for sizing of CO$_2$ pipelines and estimated the capital cost of pipeline transport. In 2002, the International Energy Agency Greenhouse Gas Programme (IEA GHG) released a report that presented several correlations for the cost of CO$_2$ pipelines in Europe based on detailed case study designs [5]. More recently, an engineering-economic CO$_2$ pipeline model was developed at the Massachusetts Institute of Technology (MIT) [6]. Results from these and similar studies were summarized in the recent IPCC report [2]. However, none of these studies considered the unusual physical properties of CO$_2$ at high pressures [7], the realities of available pipeline diameters and costs, or regional differences in the cost of CO$_2$ transportation.

The objective of this chapter is to estimate the cost per tonne of transporting CO$_2$ for a range of CO$_2$ flow rates (e.g., reflecting different power plant sizes) over a range of distances, and to also incorporate regional cost differences within the continental US.

These cost estimates are embodied in an engineering-economic model that will be presented in this chapter. A probabilistic analysis is used to quantify the impact of uncertainty and variability in cost model parameters on CO$_2$ transport cost. This analysis also shows the range of costs associated with a given project and the probability of a given cost for a specific scenario.

Pipeline Transport Performance Model

The performance model takes as input engineering design parameters, such as pipeline length and design CO$_2$ mass flow and calculates the required pipe diameter. The transport performance model includes a comprehensive physical properties model for CO$_2$ and other fluids of interest (e.g., H$_2$S); accounts for the compressibility of CO$_2$ during transport; allows booster pumping stations and segment elevation changes; and, includes probabilistic assessment capabilities. Figure 4 shows the inputs and outputs from the performance model, and how the performance model interacts with the pipeline cost model (discussed in Pipeline Transport Capital Cost Model) and the CO$_2$ properties model (discussed in Estimation of Physical Properties).

---

[4] Based in part on McCoy, S.T. and E.S. Rubin, *An engineering-economic model of pipeline transport of CO$_2$ with application to carbon capture and storage.* International Journal of Greenhouse Gas Control. **In Press, Corrected Proof.**
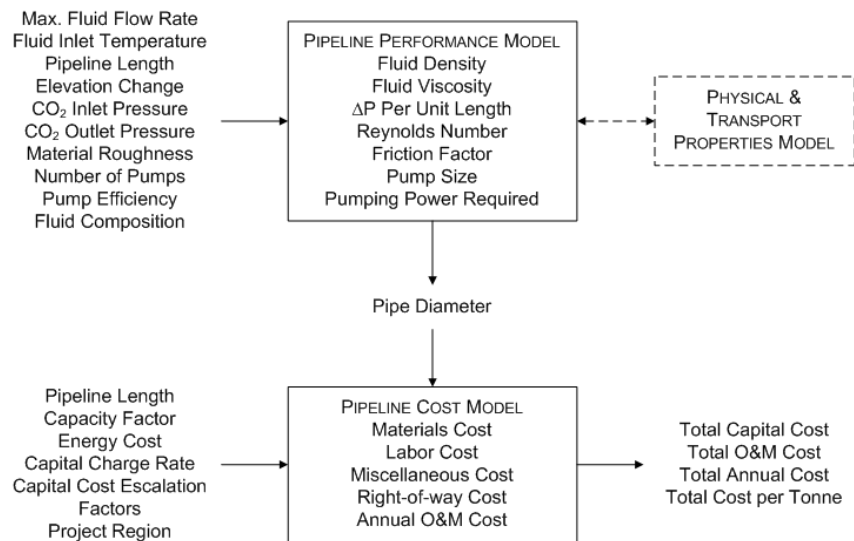
Figure 4.   The pipeline performance model takes a series of inputs defining the design of the pipeline project and calculates the required pipe diameter, which is input to the cost model.

Physical Properties of Carbon Dioxide

Efficient transport of CO_2 via pipeline requires that CO_2 be compressed and cooled to the liquid state [8]. Transport at lower densities (i.e., gaseous CO_2) is inefficient because of the low density of the CO_2 and relatively high pressure drop per unit length. Moreover, by operating the pipeline at pressures greater than the CO_2 critical pressure of 7.38 MPa, temperature fluctuations along the pipeline will not result in the formation of gaseous CO_2 and the difficulties encountered with two-phase flow [9], as the phase diagram in Figure 5 illustrates.
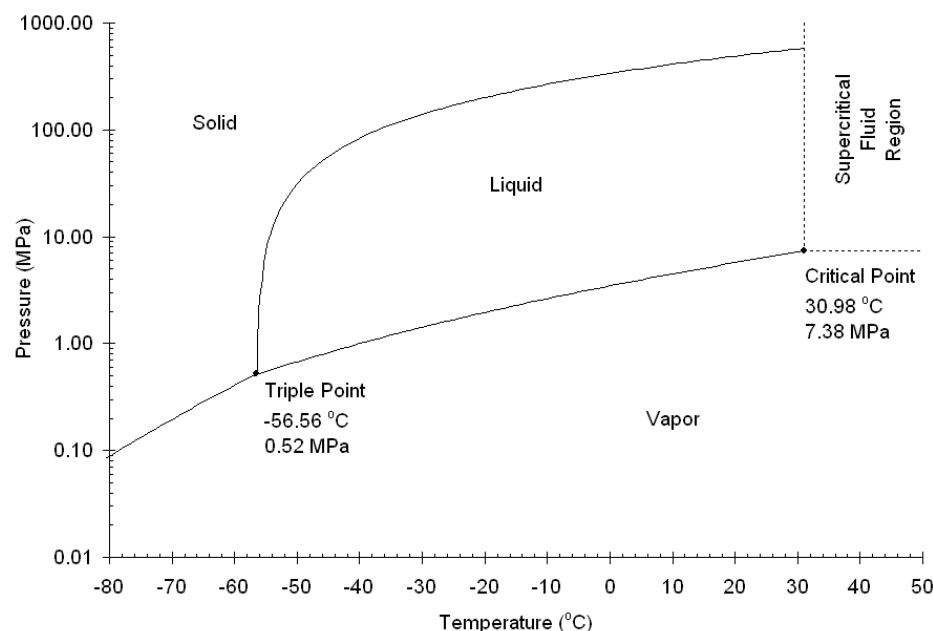
Figure 5.   A phase diagram for CO_2, showing the triple point, critical point, and the supercritical fluid region. Transport of CO_2 should occur in the liquid phase area at pressures greater than the critical pressure.

The properties of CO_2 are considerably different from other commonly transported fluids, such as natural gas. Thus, it is necessary to use accurate representations of the phase behavior, density, and viscosity of CO_2 and CO_2-containing mixtures in the design of the pipeline. The results presented here are based on the physical properties (i.e., density and phase behavior) of CO_2 and CO_2-containing mixtures predicted using a cubic equation of state with Peng-Robinson parameters, and mixing rules employing a binary interaction parameter [10]. The transport properties of CO_2 have been estimated using the Chung et al. method [11], extended to high pressures by Reid, Prausnitz, and Poling [12]. For more information on cubic equations of state, commonly used parameterizations, and estimation methods for transport properties, see Estimation of Physical Properties.

Figure 6 shows that the compressibility of CO_2 is non-linear in the range of pressures common for pipeline transport and is highly sensitive to any impurities, such as hydrogen sulfide (H_2S) or methane (CH_4). Figure 6 also shows that there is a significant difference between the compressibility of pure CO_2 and CO_2 with 10% H_2S (by volume). To reduce difficulties in design and operation, it is generally recommended that a CO_2 pipeline operate at pressures greater than 8.6 MPa where the sharp changes in compressibility of CO_2 can be avoided across a range of temperatures that may be encountered in the pipeline system [13]. Conversely, line-pipe with ASME-ANSI 900# flanges has a maximum allowable operating pressure of 15.3 MPa at 38°C [14]. Operating the pipeline at higher pressures would require flanges with a higher rating. Over the range of typical conditions shown in Figure 6, the density of CO_2 varies between approximately 800 kg/m^3 and 1000 kg/m^3.

Operating temperatures of CO_2 pipelines are generally dictated by the temperature of the surrounding soil. In northern latitudes, the soil temperature varies from a few degrees below zero in the winter to 6-8 ^{o}C in summer, while in tropical locations; the soil temperature may reach up to 20 ^{o}C [4]. However, at the discharge of compression stations after-cooling of compressed CO_2 may be required to ensure that the temperature of CO_2 does not exceed the allowable limits for either the pipeline coating or the flange temperature.
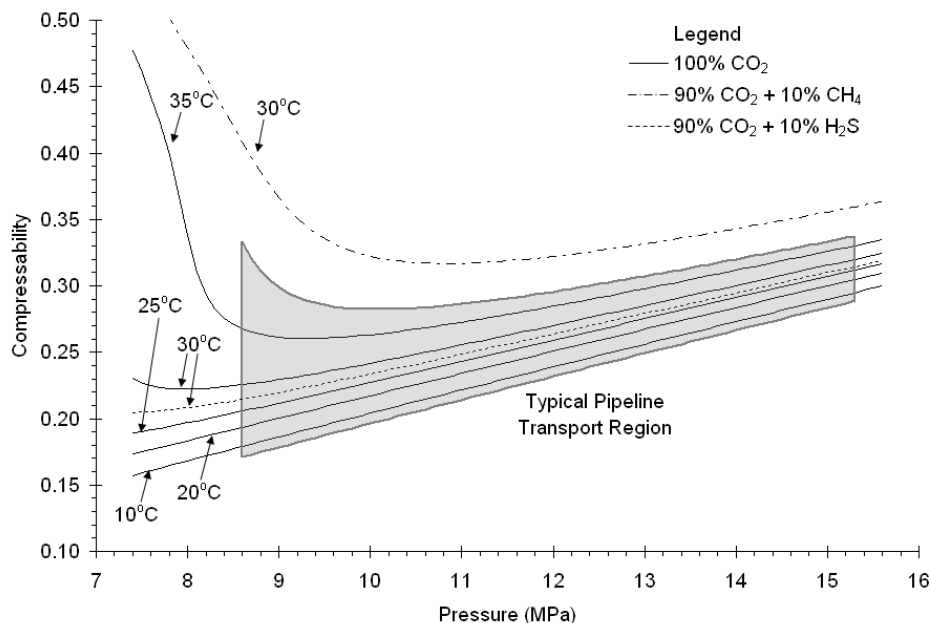
Figure 6.   The compressibility of CO_2 as predicted by the Peng-Robinson equation of state showing the nonlinearity in the transport region and the sensitivity of compressibility to impurities such as 10% H_2S or 10% CH_4.

Pipe Segment Engineering and Design

While there are proven flow equations available for use with high pressure gas pipelines (e.g. AGA fully turbulent equation), these equations can introduce error into the estimation of flow rates in liquid CO_2 due to the underlying assumptions made in their development [13]. The pipeline performance model used here is based on an energy balance on the flowing CO_2, where the required pipeline diameter for a pipeline segment is calculated while holding the upstream and downstream pressures constant. A pipeline segment is defined as a length of pipeline for which the inlet pressure and

minimum outlet pressure are specified (e.g., a length of pipeline lying between two compressor stations). The energy balance assumes that changes in kinetic energy of the flowing CO_2 are negligible, and that the compressibility of the CO_2 or CO_2 containing mixture can be averaged over the length of the pipeline segment. In addition, the typically long length of a CO_2 pipeline segment coupled with the lack of insulation on buried pipelines means that it can be treated as an isothermal system, where the CO_2 is at the temperature of the earth surrounding the pipeline.

Equation 1 shows the differential form of this energy balance, which is integrated in following steps by making several simplifying assumptions. Equation 1 accounts for changes in kinetic energy, pressure-volume work, changes in potential energy, and energy loss due to skin friction in a flow system.

$$\frac{c}{g_c v} du + \frac{1}{v} dp + \frac{g}{g_c v^2} dh + \frac{2 f_F c^2}{g_c D_i} dL = 0 \tag{1}$$

In Equation 1: c is a constant equal to the product of density, ρ, and fluid velocity, u; g is acceleration due to gravity; g_c is the conversion factor converting force units (in the SI system of units, this is equal to unity); v is the specific volume of fluid; p is pressure; h is height; f_F is the fanning friction factor; D_i is the pipeline diameter; and L is the length of the pipe segment.

Each term in Equation 1 has to be integrated over the length of the pipe segment between the upstream and downstream conditions, represented as points 1 and 2, respectively. The first term at left in Equation 1 is the kinetic energy term, which is integrated via the simple substitution:

$$\int_1^2 \frac{c}{g_c v} du = \frac{c^2}{g_c} \ln\left(\frac{u_2}{u_1}\right)$$

Integration of the pressure-volume work term in Equation 5 is somewhat more complex, and requires substitution of the compressibility for specific volume, and definition of average pressure and temperature conditions. For any fluid, compressibility is defined as:

$$Z = \frac{pvM}{RT}$$

where, R is the ideal gas constant, T is the absolute temperature of the fluid, and M is the molecular weight of the fluid. Thus, the specific volume can be rewritten in terms of the compressibility as:

$$v = \frac{ZRT}{pM}$$

Substituting the definition of specific volume above into the pressure-volume work term of Equation 1 results in:

$$\int_1^2 \frac{1}{v} dp = \int_1^2 \frac{pM}{ZRT} dp = \frac{M\left(p_2^2 - p_1^2\right)}{2 Z_{ave} R T_{ave}}$$

Fort the case of a CO_2 pipeline modeled here, the average temperature, T_{ave}, is assumed to be constant at ground temperature so that $T_{ave} = T_{ground}$. Because pressure varies non-linearly along the pipeline, the average pressure, P_{ave}, is calculated [14]:

$$P_{ave} = \frac{2}{3}\left(p_2 + p_1 - \frac{p_2 p_1}{p_2 + p_1}\right) \tag{2}$$

Integration of the potential energy term is relatively simple using the definitions of average temperature and pressure, the result being:

$$\int_1^2 \frac{g}{g_c v^2} dh = \frac{g p_{ave}^2 M^2}{g_c Z_{ave}^2 R^2 T_{ave}^2}\left(h_2 - h_1\right)$$

The friction loss term is integrated as follows:

$$\frac{2f_F c^2}{g_c D_i} \int_1^2 dL = \frac{2f_F c^2}{g_c D_i} L$$

Thus, the result of integrating Equation 1, is then given below:

$$\frac{c^2}{g_c}\ln\left(\frac{u_2}{u_1}\right) + \frac{M\left(p_2^2 - p_1^2\right)}{2Z_{ave}RT_{ave}} + \frac{gp_{ave}^2 M^2}{g_c Z_{ave}^2 R^2 T_{ave}^2}\left(h_2 - h_1\right) + \frac{2f_F c^2 L}{g_c D_i} = 0 \qquad (3)$$

where, for pipe with a circular cross section:

$$c = \frac{4\dot{m}}{\pi D_i^2}$$

Solving Equation 3 for the internal diameter results in the following equation:

$$D_i = \left\{\frac{-64Z_{ave}^2 R^2 T_{ave}^2 f_F \dot{m}^2 L}{\pi^2\left[MZ_{ave}RT_{ave}\left(p_2^2 - p_1^2\right) + 2gP_{ave}^2 M^2\left(h_2 - h_1\right)\right]}\right\}^{\frac{1}{5}} \qquad (4)$$

where, $\dot{m}$ is the design (i.e. maximum annual) mass flow rate of CO_2.

Thus, Equation 4 can be used to calculate the pipe diameter required for a given pressure drop. Complicating this, however, is the Fanning friction factor, which is a function of the pipe diameter. The Fanning friction factor can not be solved for analytically, thus an explicit approximation for Fanning friction factor is given as [15]:

$$\frac{1}{2\sqrt{f_F}} = -2.0\log\left\{\frac{\varepsilon/D_i}{3.7} - \frac{5.02}{Re}\log\left[\frac{\varepsilon/D_i}{3.7} - \frac{5.02}{Re}\log\left(\frac{\varepsilon/D_i}{3.7} + \frac{13}{Re}\right)\right]\right\} \qquad (5)$$

where ε is the roughness of the pipe, which is approximately 0.0457 mm for commercial steel pipe [16], and Re is the Reynolds number. The Reynolds number is given by Equation 18:

$$Re = \frac{4\dot{m}}{\mu\pi D_i} \qquad (6)$$

where μ is the viscosity of the fluid. As a result, Equations 4, 5, and 6 must be solved iteratively to determine the pipe diameter required for a particular application. In the iteration scheme shown in Figure 7, the Reynolds number, Equation 6, is first calculated using an initial estimate of pipe diameter based on a velocity of 1.36 m/s. This initial velocity is representative of CO_2 pipeline flows, and thus minimizes the number of iterations required over a range of model inputs for both design mass flow rate and pipeline length. The calculated Reynolds number is then used in Equation 5 to estimate the Fanning friction factor, which is then substituted into Equation 4. Reynolds numbers for CO_2 pipelines are well into the turbulent regime, typically on the order of 10^6. This leads to an updated diameter, which is compared with the value at the previous iteration. Values for the internal diameter usually converge to within 10^{-6} m in less than 5 iterations.
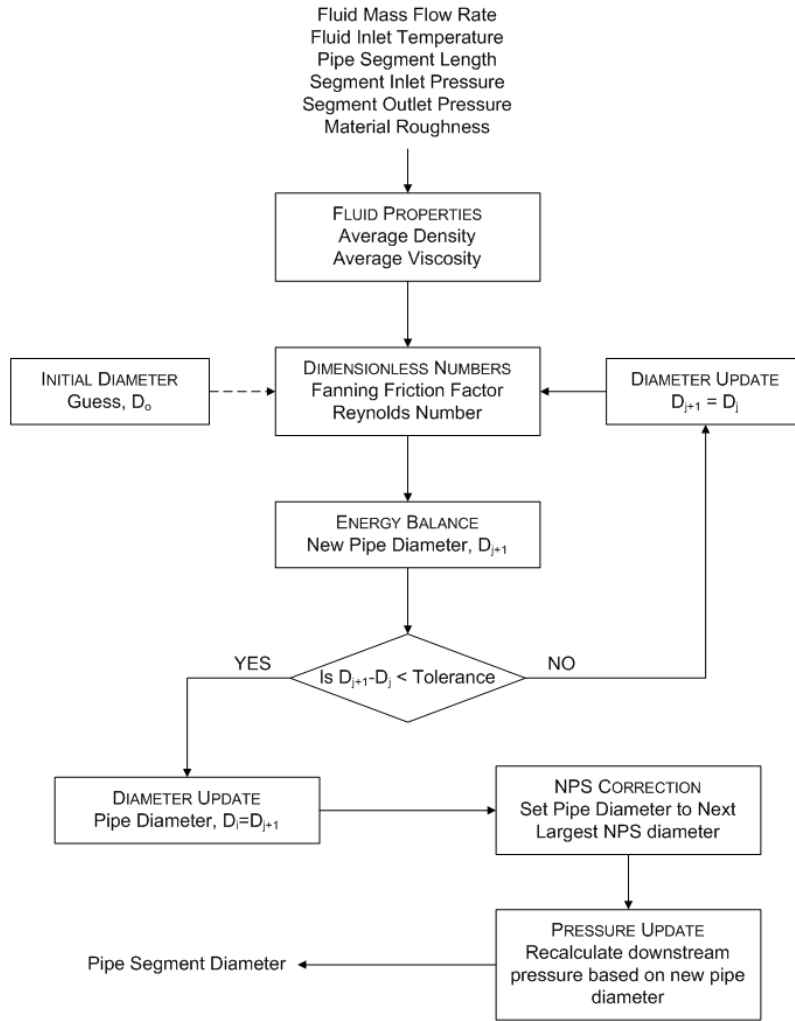
Figure 7.   Flowchart illustrating the method used to estimate the pipeline segment diameter.

Line pipe is not available in continuous diameters. Thus the internal pipe diameter calculated must be adjusted to account for both available pipe diameters and the pipe wall thickness. A discrete size of line pipe is frequently referred to by its Nominal Pipe Size (NPS), which corresponds approximately to the outside pipe diameter measured in inches. In the model presented here, eleven NPS values between 4 and 30 are available. To determine the inside diameter, the pipe wall thickness (also known as the pipe schedule) for each NPS is estimated using the method specified in the Code of Federal Regulations (CFR), which regulates the design, construction, and operation of CO_2 pipelines in the United States. The pipe wall thickness, t, in meters is given as [17]:

$$ t = \frac{p_{mop} D_o}{2 SEF} $$

where, p_{mop} is the maximum operating pressure of the pipeline (Pa), D_o is the outside pipe diameter (m), S is the specified minimum yield stress for the pipe material (Pa), E is the longitudinal joint factor (reflecting different types of longitudinal pipe welds), and F is the design factor (introduced to add a margin of safety to the wall thickness calculation). For the purposes of estimating the pipe wall thickness, the maximum operating pressure is assumed to be 15.3 MPa, the longitudinal joint factor is 1.0, and the design factor is 0.72 (as required in the CFR). The minimum yield stress is dependent on the specification and grade of line pipe selected for the pipeline. For CO_2 service, pipelines are generally constructed with materials meeting American Petroleum Institute (API) specification 5L [18]. In this case, the minimum yield stress has been specified as 483 MPa, which corresponds to API 5L X-70 line pipe.

The value of D_i calculated from Equation 4 is adjusted to the next larges value of D_i for an available NPS. Based on the adjusted D_i, the adjusted downstream pressure for the pipeline segment is calculated. This pressure will always be greater than the downstream pressure specified by the user since the adjusted diameter will always be greater than the optimum value calculated by Equation 7.

Booster Compression Engineering and Design

Booster compression stations may be required for longer pipeline distances, or for pipelines in mountainous or hilly regions with large increases in elevation. Additionally, in some cases the use of booster compression stations may allow a smaller pipe diameter to be used, resulting in a reduced cost of CO_2 transport.

The compression station size is developed from an energy balance on the flowing CO_2 in a manner similar to the calculation of the pipe segment diameter. If both elevation and velocity changes in the compressor are negligible, the energy balance is:

$$dH = Q + dW$$

where H is enthalpy, Q is heat, and W is work. Thus, if compression is assumed to be adiabatic and reversible (i.e., no heat is lost to the surroundings during compression and there are no losses), then:

$$Q = TdS = 0$$

where T is temperature and S is entropy. Therefore, the reversible work required is equal to the isentropic enthalpy change of the fluid being compressed:

$$W_{is} = \Delta H_{is}$$

The actual work required per unit of CO_2 compressed can then be calculated by dividing by the isentropic and mechanical efficiency:

$$W = \frac{\Delta H_{is}}{\eta_{is} \eta_{mech}} \tag{7}$$

The fluid enthalpy required in Equation 7 is determined by using thermodynamic departure functions based on the Peng-Robinson parameterization of the cubic equation of state [12] with ideal gas thermodynamic properties calculated using the method proposed by Aly and Lee [19]. Further details on the calculation of enthalpy using these methods are described in Estimation of Physical Properties.

In addition to calculating the work required for a compression stage, the compression algorithm calculates the outlet temperature from compression stage, which allows the required cooling duty to be determined. The general algorithm for calculating the energy requirement for a compressor station is shown in

Both the compressor size (i.e., brake horsepower) and pipeline diameter are calculated on the basis of the maximum design mass flow rate of CO_2, while the compression station annual power consumption is calculated on the basis of the nominal (i.e., annual average) mass flow rate of CO_2. The nominal mass flow rate of CO_2 is the product of the pipeline load factor and the design mass flow rate of CO_2. The compressor size is required to determine the capital cost of the compressor, while the compressor station annual power requirement is required to calculate operating cost.
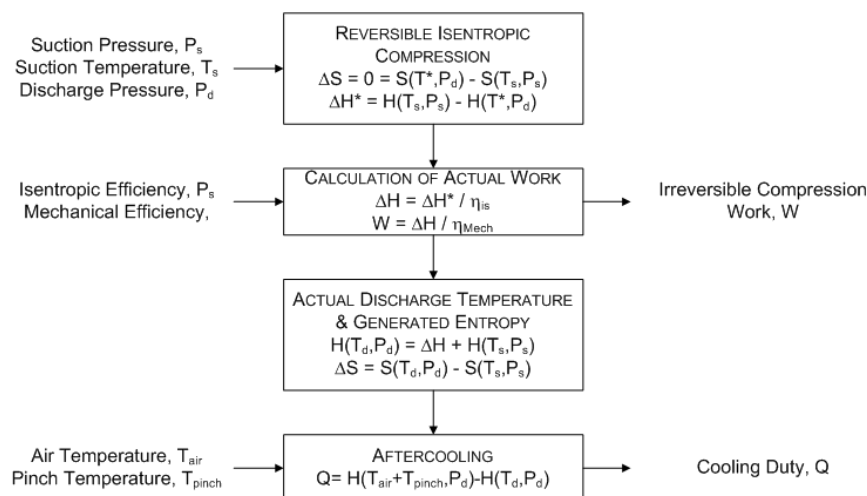
Figure 8.   The algorithm used to estimate the compressor size and energy requirements for compression of CO_2 at booster compression stations.

Illustrative Performance Model Results

Figure 9 shows the NPS of a pipeline carrying pure CO_2 as a function of the design CO_2 mass flow rate, as calculated by the iteration scheme shown in Figure 7. For fixed inlet pressure and minimum outlet pressure, the required pipe diameter increases with increasing design CO_2 flow rate and pipeline distance. Steps in pipeline diameter occur because of the discrete NPS available in the model. For example, the model estimates an internal diameter of 0.38 m for a pipeline spanning a distance of 100 km designed to carry 5 million tonnes per year of CO_2 at a pressure drop of 35 kPa per km. However, this is not a common line pipe size; thus, the next largest NPS is selected by the model, which has an internal diameter of about 0.39 m.
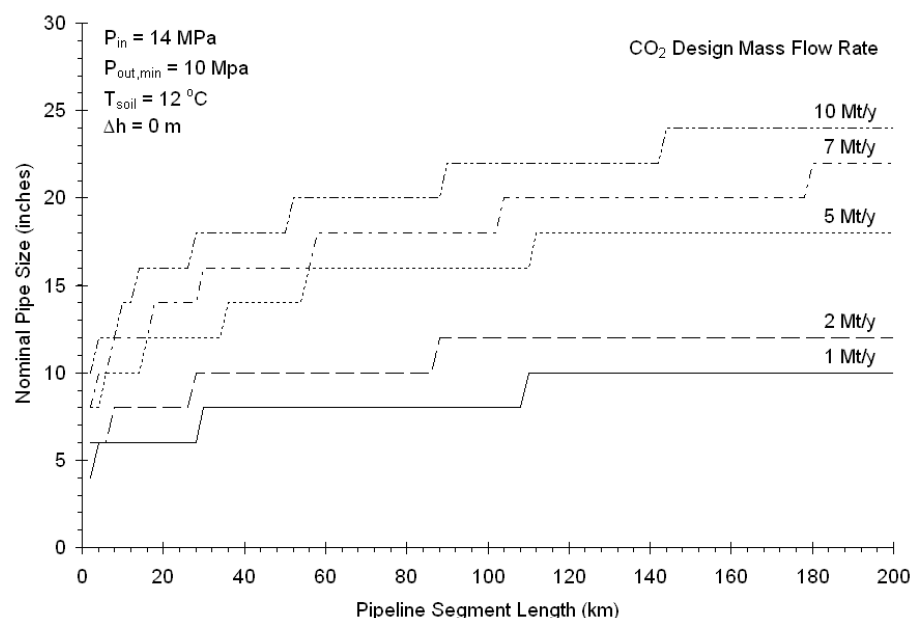
Figure 9.   Pipeline diameter as a function of length for several flow rates in Mt/y for isothermal flow at 12°C.

Figure 9 also shows the economies of scale inherent in the design of the pipeline. For a 100 km long pipeline designed to carry 1 million tonnes per year of CO_2, the model calculates a diameter of 8 inches. For a pipeline with the same design

parameter, except designed to handle 5 million tonnes per year, the calculated diameter is 16 inches; for 10 million tonnes per year, the diameter is 22 inches.

The illustrative results for the booster compression station are shown in Figure 10 show that the compressor power requirement increases linearly with mass flow rate and decreases more or less linearly with increasing isentropic efficiency. A single compressor station compressing pure CO_2 at 12 $^{\circ}$C from approximately 10 MPa to 14 MPa requires 1.43 kWh per tonne of CO_2 that, for a design capacity of 5 million tonnes per year, CO_2 requires an 817 kW compressor.
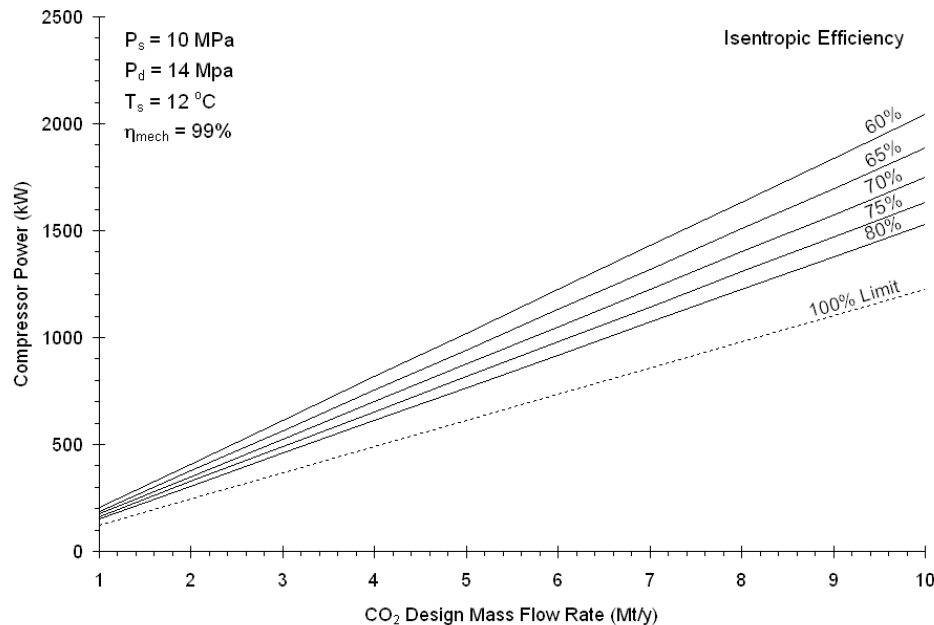
Figure 10. *Illustrative results from the booster compression station model showing the compressor size as a function of the design mass flow rate of pure CO_2 for several different isentropic efficiencies.*

Pipeline Transport Capital Cost Model

The pipeline transport economic models take output from the performance model (i.e., pipeline diameter) combined with a user-specified pipeline length and the pipeline project region to estimate the capital cost and annual operating costs of the pipeline, as shown in Figure 4.

Detailed construction cost data for actual CO_2 pipelines (i.e., as-built-cost including the length and diameter) are not readily available; nor have many such projects been constructed in the last decade [2]. For these reasons, the data set used to develop the pipeline capital cost models is based on natural gas pipelines. However, there are many similarities between transport of natural gas and CO_2. Both are transported at similar pressures, approximately 10 MPa and greater. Assuming the CO_2 is dry, which is a common requirement for CCS, both pipelines will require similar materials. Thus, a model based on natural gas pipelines offers a reasonable approximation for a preliminary design model used in the absence of more detailed project-specific costs.

Pipeline Data Set

The CO_2 pipeline capital cost model is based on regression analyses of natural gas pipeline project costs published between 1995 and 2005 [20-31]. These project costs are based on Federal Energy Regulatory Commission (FERC) filings from interstate gas transmission companies. The entire data set contains the "as-built" costs for 263 on-shore pipeline projects in the contiguous 48-states and excludes costs for pipelines with river or stream crossings as well as lateral pipeline projects (i.e., a pipeline of secondary significance to the mainline system, such as a tie-in between the mainline and a power plant). Costs from each year's projects have been adjusted to 2004 dollars using the Marshall and Swift equipment cost index [32].

The pipeline data set contains information on the year and location of the project and the length and diameter of the pipeline. Locations are listed by state in the data set; however, to develop the regression models presented here, the states have been grouped into six regions. The project regions used here are the same as those used by the Energy Information Administration for natural gas pipeline regions [36], and are shown in Figure 11.
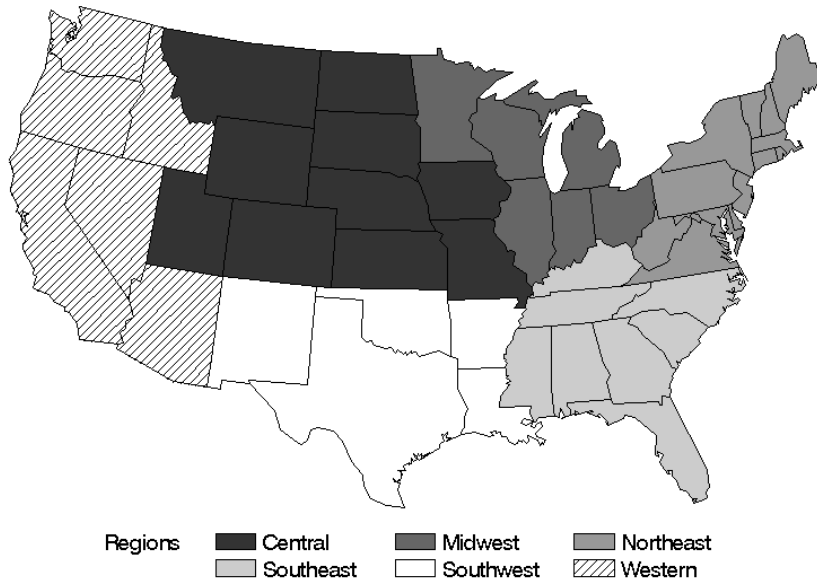
Figure 11.   The regions used in the pipeline transport cost model.

The total construction cost for each project is broken down into four categories: materials, labor, right-of-way (ROW), and miscellaneous charges. The materials category includes the cost of line pipe, pipe coatings, and cathodic protection. Labor is the cost of pipeline construction labor. ROW covers the cost of obtaining right-of-way for the pipeline and allowance for damages to landowners' property during construction. Miscellaneous includes the costs of surveying, engineering, supervision, contingencies, telecommunications equipment, freight, taxes, allowances for funds used during construction (AFUDC), administration and overheads, and regulatory filing fees.

Pipeline Capital Cost Models

Separate cost models have been developed for each of the cost categories. The capital cost models take this general form:

$$\log(C) = a_0 + a_1 NE + a_2 SE + a_3 C + a_4 SW + a_5 W + a_6 \log(L) + a_7 \log(D_{nps}) \qquad (8)$$

where *NE*, *SE*, *CL*, *SW*, and *W* are binary variables reflecting the five geographic regions besides Midwest (i.e., Northeast, Southeast, Central, Southwest, and West, respectively) that take a value of 1 or 0 depending on the region and increase or decrease the estimated cost relative to the Midwest value. *C* is the pipeline capital cost in 2004 US dollars. The variable *L* is the total pipeline length in kilometers, and the *D* is the pipeline NPS. Regional variables exist in the cost model only if they are statistically significant predictors of the cost; thus different cost-component models include different sets of regional variables.

If the intercept and regional variables in Equation 8 are collected into a single term and rearranged, the cost model can be rewritten in Cobb-Douglas[5] form:

$$C = bL^{a_6} D_{nps}^{a_7}$$
$$where \ \log(b) = a_0 + a_1 NE + a_2 SE + a_3 C + a_4 SW + a_5 W \qquad (9)$$

---

[5] In economic theory, a Cobb-Douglas production function has the form $f(K, L) = AK^a L^b$, where K and L traditionally refer to capital and labor.

There are several properties of Cobb-Douglas functions that are interesting in the context of the cost models. If the sum of a_6 and a_7 is equal to one, the total cost exhibits constant returns to scale (i.e., cost is linear with L and D). If the sum is less than one, there are decreasing returns to scale, and if the sum is greater than one, increasing returns to scale. Moreover, the values of a_6 and a_7 represent the elasticity of cost with respect to length and diameter, respectively.

Parameter estimates for the materials, labor, miscellaneous charges, and ROW cost components are given in Table 4. The generalized regression model given in Equation 8 accounts for a large proportion of the variation in the data set for each of the cost categories, as reflected by all of the cost component models having an adjusted-r^2 value greater than 0.81, with the exception of ROW, which has an adjusted-r^2 value of 0.67.

Table 4.   Parameter estimates for the pipeline cost model, Equation 8, where standard errors are indicated in parentheses.

Coefficient Estimate	Cost Component			
	Materials	Labor	ROW	Miscellaneous
a_0	3.112** (0.067)	4.487** (0.109)	3.950** (0.244)	4.390** (0.132)
a_1	-	0.075* (0.032)	-	0.145** (0.045)
a_2	0.074** (0.021)	-	-	0.132* (0.054)
a_3	-	-0.187** (0.048)	-0.382** (0.093)	-0.369** (0.061)
a_4	-	-0.216** (0.059)	-	-
a_5	-	-	-	-0.377** (0.066)
a_6	0.901** (0.012)	0.820** (0.023)	1.049** (0.048)	0.783** (0.027)
a_7	1.590** (0.045)	0.940** (0.077)	0.403* (0.167)	0.791** (0.091)
** Significant at the 1% level * Significant at the 5% level				

Based on the regression results shown in Table 4, several general observations can be made. The cost of all four components exhibit increasing returns to scale, which means that multiplying both the length and diameter by a constant n multiplies the materials cost by a factor greater than n. For example, doubling both pipeline length and diameter results in a nearly 6-fold (rather than 4-fold) increase in materials cost. For the materials, labor and miscellaneous costs, the elasticity of substitution for length is less than one; thus, a doubling in pipeline length results in less than a doubling of the cost for these components (often referred to as economies of scale). However, the elasticity of substitution for length in the ROW cost is approximately one, so that doubling the length results in a doubling of ROW cost (which is reasonable, as the ROW cost per unit of land should be approximately constant regardless of the pipeline length). The elasticity of substitution for pipeline diameter is less than one for labor, miscellaneous, and ROW costs, again indicating economies of scale; however, for materials cost it is approximately 1.6, so that doubling the pipeline diameter results in a three-fold materials cost increase. Note that this still reflects an economy of scale in the total cost of materials since doubling the diameter would quadruple the total mass of steel needed.

At least one regional variable was found to be statistically significant in all of the regression model cost categories, implying that for some regions, the cost of constructing a pipeline is higher or lower than the average for the Midwest region. For example, the labor cost regression results (Table 4) show that the cost intercept is approximately $6,000

greater in the Northeast than the Midwest and approximately \$10,000 lower in the Central and Southwest regions. There is no statistical difference (at the 5% level) between the Midwest and West or Southeast cost intercepts.

Cost differences between regions could be caused by a combination of two types of factors: differences between regions in the average cost of materials, labor, miscellaneous costs, and land (affecting ROW cost); and, differences in other geographic factors, such as population density and terrain. Regional variation in labor and materials cost for power plant construction have been documented by the Electric Power Research Institute (EPRI) [33]. However, because the routings of pipeline projects are not reported in the data set, it is not possible to identify how these individual factors contributed to overall cost of the projects. Thus, there are plausible circumstances where similar pipeline projects in different regions could have costs much closer to one another than to comparable projects within their respective regions (e.g. pipelines of similar length and design CO_2 mass flow in heavily populated versus unpopulated areas within the same state). Zhang et al. [34] have developed more data intensive tools to study least-cost routing of specific CO_2 pipelines which are complimentary to the use of the current screening level model.

Compressor Capital Cost Model

The total capital cost of a reciprocating compressor station has been estimated by the IEA for a European study involving the pipeline transmission of CO_2 [5]. This cost is given by the regression in Equation 27:

$$C = 8.35P + 0.49$$

where the result is in millions of US dollars (2004), and P is the installed booster station power in MW. This correlation yields a cost slope of \$8,346 per kW of installed capacity.

Illustrative Capital Cost Model Results

The behavior of the capital cost models is shown in Figure 12, where the category cost model results are stacked to indicate the total cost of a 16 inch diameter pipeline for distances from 10 mi to 60 mi located in the Midwest. For reference, a 16 inch pipeline could transport approximately 5 million metric tonnes of CO_2 per year over a 100 km distance, which would be approximately the maximum annual emissions of a 600 MW (net) pulverized coal fired plant with 90% CO_2 capture.

Figure 12 shows that the labor cost accounts for over 50% of the total cost of a 16 inch pipeline across all distances between 5 km and 100 km. The next largest cost category is engineering, overheads, and AFUDC (i.e., miscellaneous), followed by materials, and ROW. However, the size breakdown shown in Figure 12 is dependent on the pipeline diameter. For example, the material cost increases more rapidly with pipeline diameter than the miscellaneous cost, thus for a 36 in pipeline, the materials cost is much a much larger fraction of the total cost than the miscellaneous cost.

The regional dependence of the labor, miscellaneous, and ROW models means that the predicted cost of projects in some regions will be either higher or lower than the cost of equivalent projects in other regions. The difference in cost between the Midwest and the other five regions is summarized in Table 5 for a 16 inch diameter pipeline that is 100 km long. The results in this table show that, when compared to the Midwest, pipelines in the Northeast and Southeast are more expensive to construct, and pipelines in the Central and Southwest are less expensive to construct.
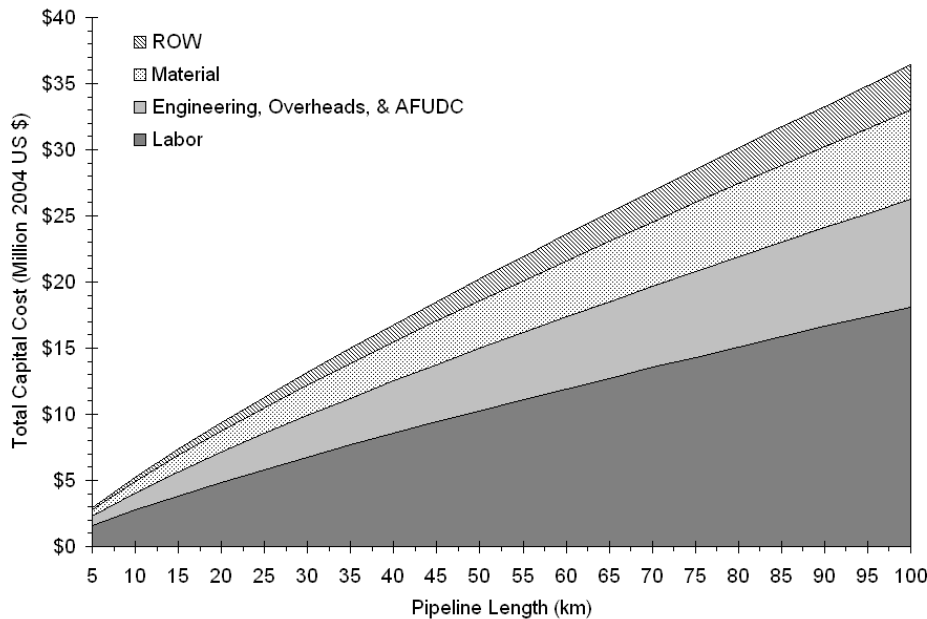
Figure 12. The capital cost (in millions of constant 2004 US dollars) of a 16 inch pipeline located in the Midwest over varying lengths.

Table 5. The cost of construction of a 100 km, 16 inch pipeline in the Midwest in millions of dollars (constant 2004 US dollars), and the regional differences relative to Midwest cost, where values in brackets are negative.

Capital Cost (Million $)	Midwest	Difference from Midwest				
		Northeast	Southeast	Southwest	West	Central
Material	6.746	0	1.244	0	0	0
Labor	18.129	3.430	0	(7.113)	0	(6.348)
Miscellaneous	8.110	3.226	2.890	0	(4.707)	(4.640)
ROW	3.417	0	0	0	0	(1.999)
Total	36.402	6.656	4.134	(7.113)	(4.707)	(12.988)

Pipeline Transport Operating & Maintenance Cost Model

In the United States, pipeline maintenance activities are regulated under Title 49 of the Code of Federal Regulations (CFR), Section 195, subsections 400 through 452. These regulations specify requirements for training, inspections, and repairs. Routine activities that fall under the category of maintenance activities include:

- ROW and facilities environmental protection
- ROW and site maintenance
- Pipeline depth of cover maintenance
- Aerial inspection/patrol and leak detection
- ROW erosion control and stabilization
- Cathodic protection monitoring and maintenance
- Pipeline integrity assessment

- Pipeline repair and modifications

- Pipeline encroachment assessment

- Equipment operational test and routine maintenance

- Aesthetics and landscaping

In addition to these activities, Title 49 of the CFR, Section 195, Subpart 452, requires the operator of a CO_2 pipeline to develop and maintain an integrity management program that addresses risks along each segment of their pipeline system. This program is particularly addressed to address risks in high consequence areas (i.e., a populated place or navigable waterway).

While operating and maintenance (O&M) costs are not large in comparison to the annualized capital cost of pipeline transport, they are nonetheless significant. Bock et al. [6] report that the O&M cost of operating a 480 km CO_2 pipeline is between \$40,000 and \$60,000 per month. On an annual basis, this amounts to approximately \$3,250 per kilometer of pipeline in 2004 dollars. Thus, for a 100 km long pipeline, transporting approximately 5 million tonnes per year of CO_2 with no booster pumping stations, the O&M cost would account for approximately 6% of the total cost per tonne of transportation.

Based on the EPRI Technical Assessment Guide [33], the O&M charges associated with the booster compression stations (in addition to energy cost) are assumed to be 1.5% of their original capital cost, annually.

Combining Performance and Cost

As Figure shows, the cost model is dependent on the diameter of the pipeline as calculated by the performance model. Thus, the model begins by calculating the pipeline diameter for each pipeline segment using the method described in Pipe Segment Engineering and Design.

The number of pipeline segments is determined by the number of compressor stations specified by the user—the number of pipeline segments being one greater than the number of booster stations. For example, for a 100 km pipeline if there are two compression stations specified there are then three pipe segments. The pipeline segment length, inlet pressure, and minimum outlet pressure are all specified by the user for each pipeline segment. Thus, the calculated pipeline diameter for each pipeline segment can be different.

The capital cost for the pipeline project is estimated by summing up the capital cost for each pipeline segment and booster station. However, because the elasticity of substitution for length is less than one for materials, labor and miscellaneous capita cost (as shown by the coefficients in Table 4), the cost for each segment is calculated as if the entire pipeline project length were of that particular diameter, then scaled to the length of the segment. For example, the materials capital cost of a 16 inch NPS, 100 km long pipeline, is \$67,459 per km; for a 100 km long pipeline with two 50 km long segments, one of which is 16 inch NPS, the materials capital cost for the shorter 16 inch NPS segment is still \$67,459. This approach is taken because it is assumed that the economies of scale for a long pipeline project with multiple segments of differing diameters would be equal to—or at least insignificantly different from—the economies of scale for a project of the same length of a single diameter.

The key results reported by the newly developed pipeline model include the total capital cost, annual O&M cost, total levelized cost, and the levelized cost per metric tonne of CO_2 transported (all in constant 2004 US dollars). The capital cost can be subject to capital cost escalation factors applied to individual categories of the capital cost (i.e., materials, labor, miscellaneous, and ROW). These escalation factors can be used to account for anticipated changes in capital cost components (e.g., in the cost of steel) or other project-specific factors that might affect capital costs relative to the regional averages discussed earlier (e.g., river crossings). Capital costs are annualized using a levelized fixed charge factor calculated for a user-specified discount rate and project life [35]. The cost per tonne CO_2 transported reflects the amount of CO_2 transported, which is the product of the design mass flow rate and the pipeline capacity factor.

Illustrative Case Study Results

Illustrative results from the pipeline model were developed using parameters representative of a typical coal-fired power plant in the Midwest region of the United States (Table 6). Several parameter values (e.g., capital recovery factor) are

default values from the IECM software [35]. Table 6 includes a nominal CO_2 mass flow rate and pipeline length, but these two parameters are varied parametrically in the case study results presented here.

Table 6.   Illustrative case study parameters for the pipeline transport model

Model Parameter	Deterministic Value	Uncertainty Distribution
Pipeline Performance Parameters		
Design Mass Flow (Mt/y)	5	Variable[§]
Pipeline Length (km)	100	Variable[§]
Elevation Change (m)	0	
Pipeline Capacity Factor (%)	100	Uniform (50, 100)
Ground Temperature (^{o}C)	12	
Inlet Pressure (MPa)	13.79	Uniform (12, 15)
Minimum Outlet Pressure (MPa)	10.3	
Pipe Roughness (mm)	0.0457	
Number of Booster Stations	0	
Economic and Financial Parameters		
Project Region	Midwest	
Capital Recovery Factor (%)	15[6]	Uniform (10, 20)
Annual O&M Cost ($/km/y)	3,250	Uniform (2,150, 4,350)
Escalation Factor for Materials Cost	1	Uniform (0.75, 1.25)
Escalation Factor for Labor Cost	1	Uniform (0.75, 1.25)
Escalation Factor for ROW Cost	1	Uniform (0.75, 1.25)
Escalation Factor for Miscellaneous Cost	1	Uniform (0.75, 1.25)
Escalation Factor for Compression Cost	1	

For the case study CO_2 pipeline in the Midwest, the total levelized cost of transport is estimated to be $1.16 per tonne of CO_2 transported. Table 7 shows the regional differences in CO_2 transport cost relative to the Midwest for a pipeline with the same parameters as in Table 6. In general, the model shows that the cost is greatest in the Northeast, followed (in descending order) by the Southeast, Midwest, West, Southwest, and Central U.S. This trend applies to all pipeline lengths and design mass flows. Overall, the cost category that accounts for the largest regional difference is the labor cost, which is lowest in the Southwest and highest in the Northeast.

Table 7. The cost of pipeline transport in the Midwest and regional differences relative to the Midwest, where bracketed values are negative (all costs in constant 2004 US dollars).

Transport Cost ($/tonne CO_2)	Midwest	Difference from Midwest				
		Northeast	Southeast	Southwest	West	Central
Materials	0.20	0	0.04	0	0	0
Labor	0.54	0.10	0	(0.21)	0	(0.19)
Miscellaneous	0.24	0.10	0.09	0	(0.14)	(0.14)
ROW	0.10	0	0	0	0	(0.06)
O&M	0.07	0	0	0	0	0
Total	1.16	0.20	0.12	(0.21)	(0.14)	(0.39)

---

[6] Corresponds to a 30-year plant lifetime with a 14.8% real interest rate (or, a 20-year life with 13.9% interest rate) [§] This parameter modeled as a discrete value for sensitivity analysis

Figure 13 shows results from the model as a function of pipeline distance for a project in the Midwest for four different design mass flow rates. In this example the pipeline capacity factor is assumed to be 100%, so the annual mass transported equals the design capacity of the pipeline. Figure 13 shows that the levelized transport cost increases with distance and decreases with increasing design capacity for a fixed distance. For a typical 500 MW power plant (emissions of approximately 2-3 million tonnes per year), transport costs could range from $0.15 per tonne for a 10 km pipeline to $4.06 per tonne for a 200 km pipeline. For an annual capacity factor of 75% (typical of existing coal-fired power plants), the levelized cost per tonne would increase to between $0.20 per tonne for the 10 km pipeline to $5.41 per tonne for 200 km pipeline. Figure 13 also illustrates the differences in cost between the pipelines constructed in the Northeast and Central regions. For all pipeline distances and all pipeline design capacities, the transport cost is lowest in the Central region and highest in the Northeast region.
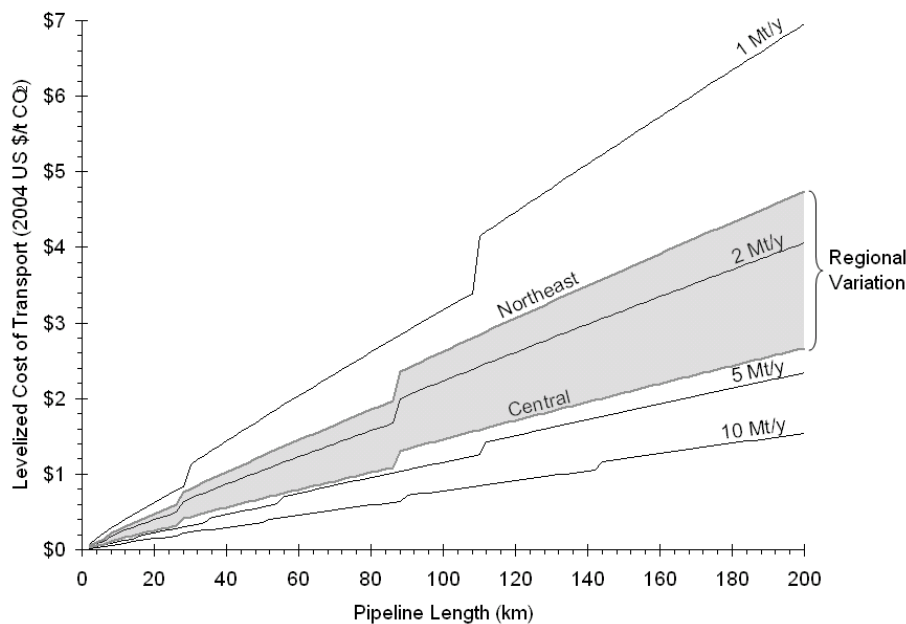
Figure 13.   Illustrative results from the transport model showing the transport cost (in constant 2004 US dollars) over a range of pipeline design capacities and pipeline distances

Model Sensitivity Analysis Results

To assess the sensitivity of the model to changes in multiple design and financial parameters, uniform distributions were assigned to several parameters of interest and a series of Monte Carlo trials were used to calculate the pipeline transport cost. The uniform distribution was selected to represent uncertainty or variability because there is no prior information that would suggest choosing a more complex distribution (such as a triangular or lognormal distribution). The design parameters of interest are the ground temperature, and pipeline inlet pressure, while financial parameters include pipeline capacity factor, capital recovery factor, and annual pipeline O&M cost. Values of the input parameters for the probabilistic analysis are also shown in Table 6.

For this analysis 1,000 trials were conducted for each region. From these trials a cumulative distribution function (CDF) for transport cost has been generated, shown in Figure 14. The CDF shows that for a Midwest pipeline project transporting 5 million tonnes of CO_2 annually over 100 km, a 90% probability interval (which reflects the selection of input parameters) yields levelized costs between approximately $1.03 and $2.63 per tonne of CO_2 transported. The minimum and maximum cost predicted by the model are $0.75 and $3.56 per tonne of CO_2 transported; however, these values are very sensitive to the number of Monte Carlo simulations performed. A less sensitive measure is the median cost of transport, which is $1.65 per tonne under these conditions.
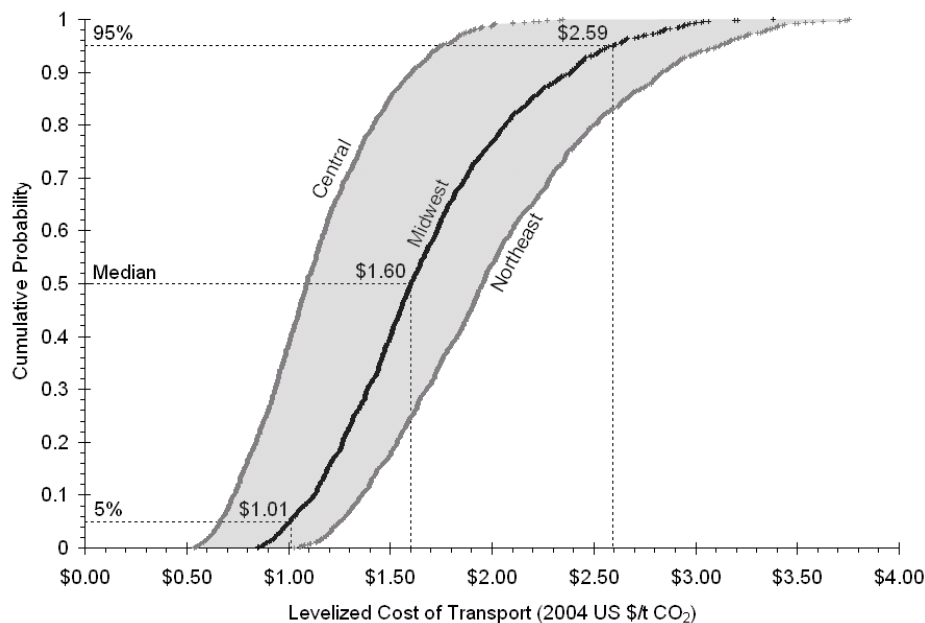
Figure 14.   Cumulative density function generated from the Monte Carlo sensitivity analysis on the transport model.

Using the cost models for different regions changes the results of the sensitivity analysis, also shown in Figure 14. Thus, a project in the Central US region will have costs less than a project in the Midwest or Northeast for all combinations of input parameters. The median cost of a project in the Central US transporting 5 million tonnes of CO_2 annually over 100 km is $1.09 per tonne, with 90% confidence interval between $0.66 and $1.74 per tonne. In the Northeast, the project cost could approach that of the Midwest for some combinations of input parameters. The median cost of this project in the Northeast is $1.95 per tonne, with a 90% confidence interval between $1.26 and $3.12 per tonne.

Results of the Monte Carlo trials can also be used to assess the sensitivity of transport cost to the model parameters having uniform distributions. The measure used to assess the sensitivity is the Spearman rank-order correlation (r_s) [36]. Similar to the commonly used Pearson product-moment correlation (i.e., r-value), which measures strength of a linear relationship between variables, rank-order correlation is a measure of direction and association between the statistical rank of variables. The value of the rank order correlation coefficient between the transport cost and the model parameters is shown in Figure 15. The dashed vertical lines to the left and the right of the axis in Figure 15 indicate the 5% significance level ($r_s = \pm0.07$); thus rank-order correlation coefficients smaller than this value are not statistically significant at the 5% level. Figure 15 shows the strongest correlation is between pipeline capacity factor ($r_s = -0.67$) and transport cost, followed by capital recovery factor ($r_s = 0.65$). Following these, significant rank-order correlation coefficients (by decreasing magnitude) are the inlet pressure, real materials escalation rate, and elevation change. This implies that the pipeline capacity factor and capital recovery factor are far stronger determinants of pipeline transport cost than any of the escalation factors. For example, to double the levelized cost of transport for the illustrative CO_2 pipeline (parameters presented in Table 6) the capital cost escalation factor for pipeline materials would have to be increased 400% to 800%, depending on the project region. By contrast, only a 50% reduction in the pipeline capacity factor is required to double the levelized cost.
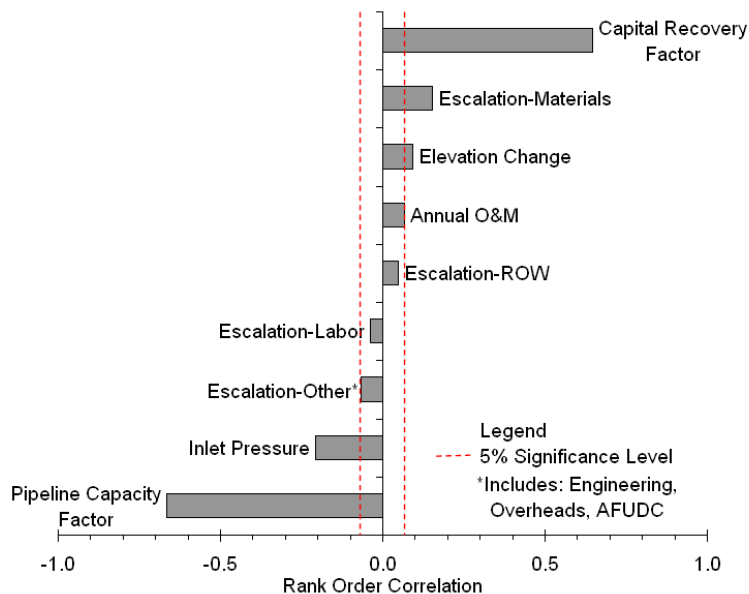
Figure 15. Rank-order correlation between the results of the Monte Carlo sensitivity analysis and the parameters assigned uniform distributions.

Optimization of Pipeline Parameters

While the results presented in this section are based on reasonable assumptions about design parameters (presented in Table 6), the parameters may not be the optimum parameters to minimize the cost of transport. For example, incorporating compressor stations into the design can result in reduced capital costs. Moreover, in many cases this will be necessary due to terrain features. Cost savings can occur with the installation of compressor stations if the decreased capital cost resulting from a smaller diameter pipeline offset the increased capital and operating costs from compressor stations.

Figure 16 shows the difference between the levelized cost of transport with and without the optimal number of compressor stations for different annual CO_2 flow rates and distances using the pipeline performance and design parameters listed in Table 6. The cost of energy is assumed to be $40 per MWh in this analysis. Regardless of the assumptions surrounding energy cost, however, cost savings achieved by adding booster stations decrease with increasing amounts of CO_2 handled, and increases with pipeline length. The optimum number of compressors in Figure 16 was arrived at through a "brute force" optimization method where the number of compressors for a given flow rate and distance is increased in integer steps from zero to find the number of compressors that minimizes cost.
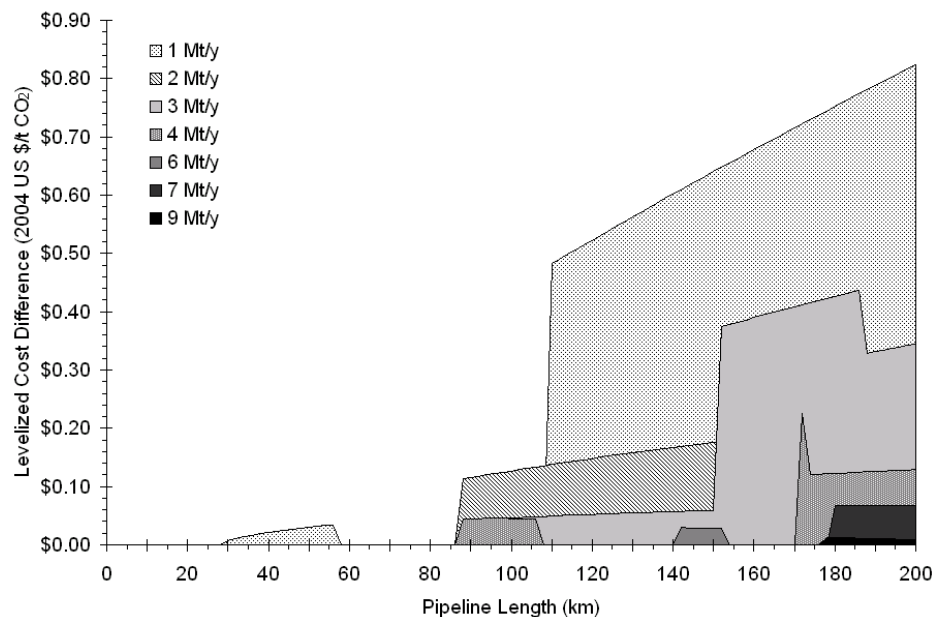
Figure 16.   The difference (in constant 2004 US dollars) between the levelized cost of transport without compression and with the cost-minimizing number of compressors.

Comparison with Other Models

Differences between the pipeline transport model developed in this report and other models stem from differences in the performance model (i.e., the way the required pipeline diameter is calculated), as well as in the cost model. To better explain differences between available models, differences in the performance model, cost model, and overall results will be discussed separately.

Performance Model Comparison

The pipeline transport model developed in this report (referred to as the CMU model) is compared in Figure 17 with a model developed by MIT [6]. The most significant differences between the MIT model and CMU model are that: the MIT model allows for continuous pipe sizes while the CMU model only allows discrete pipe sizes corresponding with commonly available NPS; the CMU model allows for discrete pipe segments with elevation changes, while the MIT model does not; and, the MIT model does not account for the compressible nature of the flowing CO_2, while the CMU model does.

Figure 17 shows that for the same conditions, the CMU model tends to predict a larger pipe diameter than the MIT model. Part of the explanation for this difference is that the pipeline diameter predicted by the CMU model is the NPS pipe size, while the MIT pipeline model predicts the required internal diameter. However, the difference between the predicted diameters is larger than can be explained by wall thickness for larger distances. The primary reason for the difference, particularly at longer distances, is that the CMU model accounts for compressibility of the CO_2, resulting in a larger pipe diameter. Moreover, the MIT model calculates the properties of the flowing CO_2 at the inlet of the pipeline, rather than averaged over the entire length of the pipeline as in the CMU model, resulting in a smaller calculated pipe diameter.
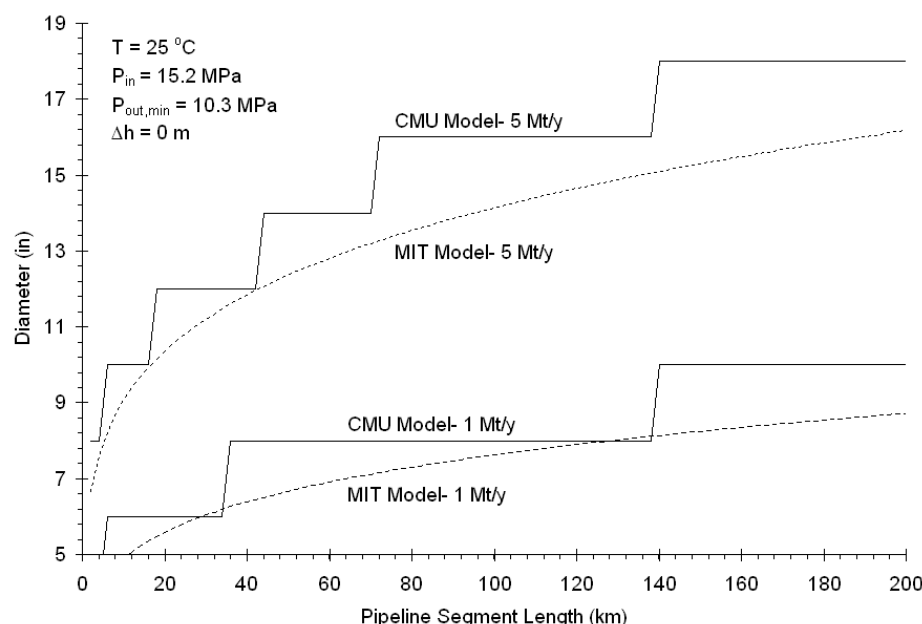
Figure 17.   A comparison between the MIT model and the CMU model, showing that the CMU model generally predicts a larger pipe diameter for a range of flow rates (1-5 Mt/y).

A further comparison can be made with the rules-of-thumb proposed by Skovholt [4] which are based on relatively low pressure compared to the pressures that would likely be used in a CO_2 pipeline constructed today. The parameters used by Skovholt are presented in Table 8.

Table 8.   Parameters used by Skovholt to determine rules-of-thumb for pipe diameter

Pipeline Parameter	Value
Segment Length (km)	250
Ground Temperature (oC)	6
Maximum Pressure (MPa)	11
Minimum Pressure (MPa)	9

Using these parameters, the diameters calculated by Skovholt are compared with diameters calculated by the CMU model for the same conditions in Table 9. In this case, the diameters calculated by the CMU model are consistently larger for all mass flow rates. Moreover, the CMU model can not accommodate the case of 110 million tonnes per year in one pipeline. The reasons for the difference between the diameters presented by Skovholt and those calculated by the CMU model are not clear, as Skovholt does not describe the methods used to calculate the rules-of-thumb.

Table 9.   Pipe diameters proposed by Skovholt compared with those calculated by the CMU model (all diameters in inches).

Design Mass Flow (Mt$_{CO2}$/y)	Skovholt	CMU Model
3	16	18
20	30	36
35	40	48
110	64	N/A

Cost Model Comparison

The CMU cost models can be compared with the cost model from the previously mentioned MIT study [6], cost models developed in a study for the IEA [5], and models developed for the Midwest Geological Carbon Sequestration (MGSC) Partnership [37]. This comparison is shown in Figure 18 for the case of a 16-inch pipeline.

Figure 18 shows the total capital cost of a 16 inch NPS pipeline for a range of distances as calculated by the MIT model, which uses a simple slope factor ($/in/km); the MGSC model, which uses discrete slope factors ($/km) for diameters between 4 and 24 inches, and; the IEA models, which depends on the operating pressure of the pipeline as well as length and diameter. The IEA ANSI Class #900 model is for pipelines with an operating pressure up to approximately 14 MPa, while the Class #1500 model is for pressures up to about 23 MPa. The figure shows that the CMU model predicts costs that are less than those predicted by the MIT model, on the low side of the MGSC model, and higher than either of the IEA models. Moreover, Figure 18 shows that the MIT, IEA, and MGSC models are linear in length, but the CMU model is slightly non-linear. In the CMU model, the cost per unit length decreases slightly with increasing pipeline length.
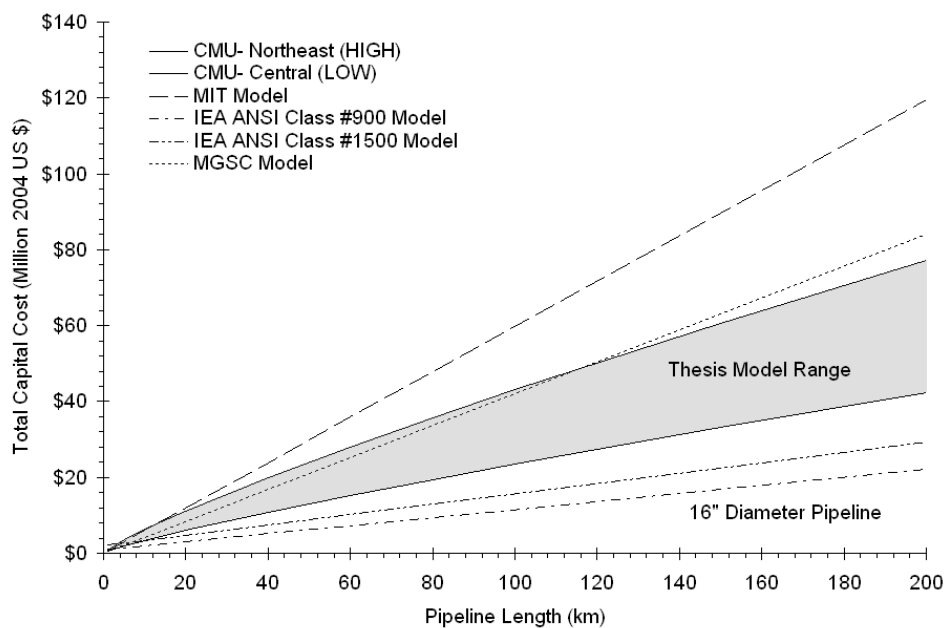
Figure 18.   The range of capital costs possible from the CMU cost models, depending on region, compared with the capital costs possible from the MIT, IEA, and MGSC models for a 16" NPS pipeline over a range of pipeline lengths.

The differences between the CMU, MIT, IEA, and MGSC models are likely due to the differing approaches taken in their development. Both the IEA and MGSC models are based on "bottom-up" cost estimates, developed from private design studies of pipeline projects. On the other hand, the MIT model is based on similar data to the CMU model, but with a smaller set of projects, no variation by region, and no accounting for the non-linear effects of length on cost.

Overall Model Comparison

Results from the MIT model and the CMU model can be compared over a range of lengths. Unfortunately, the overall results of the IEA and MGSC model can not be compared in the same way—the IEA model implementation is not amenable to sensitivity analysis, while the MGSC has not developed a design model. Figure 19 shows the results of the comparison between the MIT and CMU models for a fixed mass flow rate of 5 Mt/y, and a charge factor of approximately 16%.
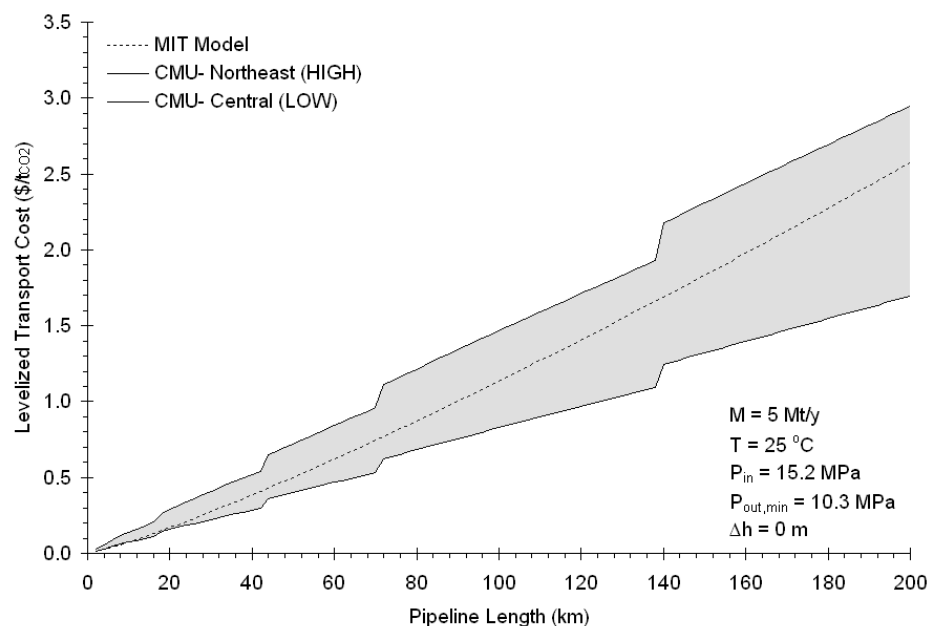
Figure 19.   A comparison of results from the CMU pipeline transport model and the MIT pipeline transport model for a design mass flow rate of 5 million tones of CO₂ per year over a range of distances.

Figure 19 shows that, depending on the region selected in the CMU model, the lower costs and the larger pipe diameters predicted by the CMU transport model compared to the MIT cost model cancel out. Nonetheless, there are significant differences between the costs predicted by the models, particularly at long lengths for pipelines in the Central, West, and Southwest, where the cost predicted by the CMU model is at least 20% less than the cost predicted by the MIT model.

The CMU model is also compared in Figure 20 against the results presented in the IPCC Special Report on Carbon dioxide Capture and Storage [2]. Levelized costs shown in Figure 20(a) generally agree with the results presented in the IPCC Special Report, repeated in Figure 20 (b). However, costs for projects in the central region are lower than the lower "onshore" bound in Figure 19. This may be because the results represented in the IPCC Special Report figure are not region specific. Moreover, the pipeline inlet pressure, outlet pressure, and temperature could be adjusted to change the required pipe diameter, altering the costs presented in Figure 20 (a).
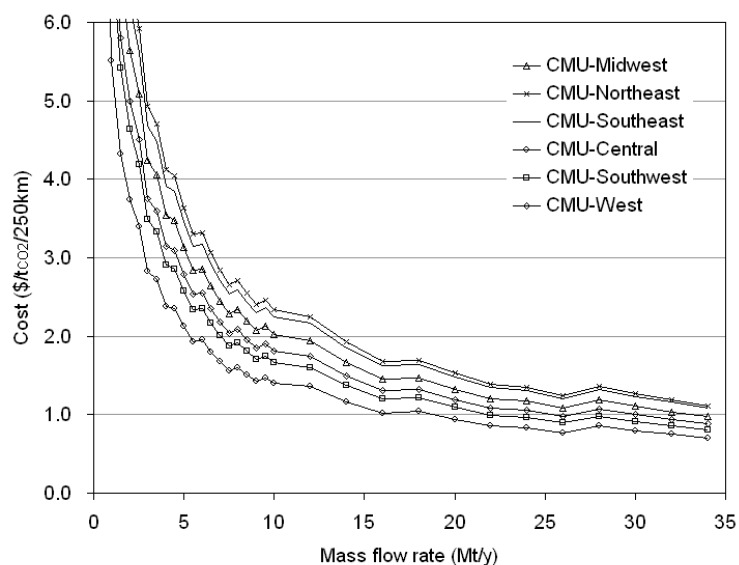
(a)
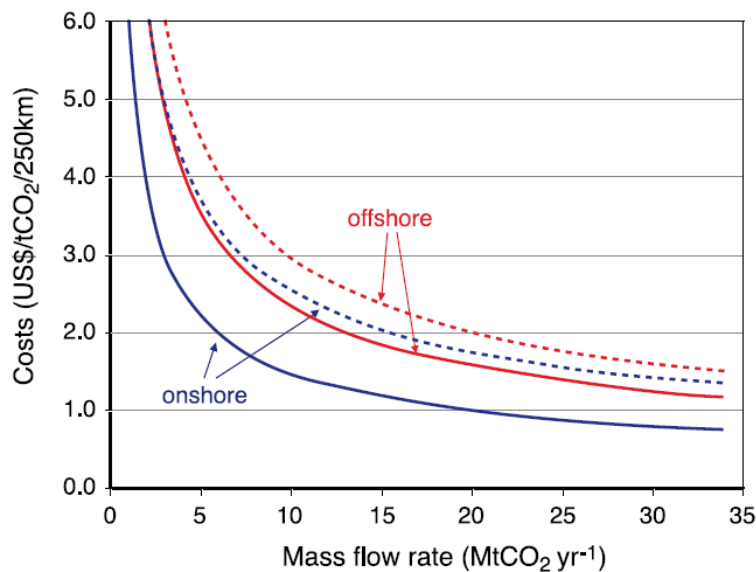
(b)

Figure 20. Comparison of results from the CMU model (a) and results reproduced from the IPCC Special Report [2] (b).

References

1. Svensson, R., et al., *Transportation systems for CO₂-application to carbon capture and storage.* Energy Conversion & Management, 2004. **45**: p. 2343-2353.
2. Doctor, R., et al., *Transport of CO₂*, in *IPCC Special Report on Carbon Dioxide Capture and Storage*, B. Metz, et al., Editors. 2005, Cambridge University Press: Cambridge, U.K.
3. Gale, J. and J. Davidson, *Transmission of CO₂- Safety and Economic Considerations.* Energy, 2004. **29**: p. 1319-1328.
4. Skovholt, O., *CO₂ Transportation System.* Energy Conversion & Management, 1993. **34**(9-11): p. 1095-1103.
5. Woodhill Engineering Consultants, *Pipeline Transmission of CO₂ and Energy: Transmission Study - Report.* 2002, IEA Greenhouse Gas R&D Programme: Stoke Orchard, UK.
6. Bock, B., et al., *Economic Evaluation of CO₂ Storage and Sink Enhancement Options.* 2003, TVA Public Power Institute: Muscle Shoals, AL.
7. Fesmire, C.J., *531 BCF of CO₂ Through the CRC System.* Energy Progress, 1983. **3**(4): p. 203-206.
8. Zhang, Z.X., et al., *Optimization of pipeline transport for CO₂ sequestration.* Energy Conversion & Management, 2006. **47**: p. 702-715.
9. Recht, D.L., *Design Considerations for Carbon-Dioxide Pipe Lines. 1.* Pipe Line Industry, 1984. **61**(3): p. 53-54.
10. Reid, R.C., J.M. Prausnitz, and B.E. Poling, *The Properties of Gases and Liquids.* 4th ed. 1987: McGraw-Hill Book Company.
11. Chung, T.H., et al., *Generalized Multiparameter Correlation for Nonpolar and Polar Fluid Transport Properties.* Industrial & Engineering Chemistry Research, 1988. **27**: p. 671-679.
12. Poling, B.E., J.M. Prausnitz, and J.P. O'Connell, *The Properties of Gases and Liquids.* 5 ed. 2001: McGraw-Hill Book Company.
13. Farris, C.B., *Unusual Design Factors for Supercritical CO₂ Pipelines.* Energy Progress, 1983. **3**(3): p. 150-158.
14. Mohitpour, M., H. Golshan, and A. Murray, *Pipeline Design & Construction.* 1st ed. 2003, New York, NY: ASME Press.
15. Zigrang, D.J. and N.D. Sylvester, *Explicit Approximations to the Solution of Colebrook Friction Factor Equation.* AICHE Journal, 1982. **28**(3): p. 514-515.

---

16.   Boyce, M.P., *Transport and Storage of Fluids*, in *Perry's chemical engineers' handbook*, R.H. Perry, D.W. Green, and J.O. Maloney, Editors. 1997, McGraw-Hill: New York, NY.

17.   "Transportation." Title 49 <u>Code of Federal Regulations</u>, Pt. 195. 2005 ed., 170-171.

18.   American Petroleum Institute, *Spec 5L- Specification for Line Pipe*. 43rd ed. 2004, Washington, D.C.: American Petroleum Institute. 155.

19.   Aly, F.A. and L.L. Lee, *Self-consistent equations for calculating the ideal gas heat capacity, enthalpy, and entropy.* Fluid Phase Equilibria, 1981. **6**(3-4): p. 169-179.

20.   Smith, C.E., W.R. True, and J. Stell, *US gas carriers see 2004 net jump; construction plans rebound.* Oil & Gas Journal, 2005. **103**(34): p. 50-54.

21.   True, W.R., *Special Report: Pipeline Economics.* Oil & Gas Journal, 2000. **98**(36): p. 68-86.

22.   True, W.R., *Special Report: Pipeline Economics.* Oil & Gas Journal, 2003. **101**(34): p. 60-90.

23.   True, W.R., *Profitable 2000, higher demand push US natural gas construction plans.* Oil & Gas Journal, 2001. **99**(36): p. 66-80.

24.   True, W.R., *More construction, higher costs in store for US pipelines.* Oil & Gas Journal, 2000. **98**(36): p. 68-70.

25.   True, W.R., *U.S. pipelines experience another tight year, reflect merger frenzy.* Oil & Gas Journal, 1999. **97**(34): p. 13.

26.   True, W.R., *US pipeline companies solidly profitable in 2002, scale back construction plans.* Oil & Gas Journal, 2003. **101**(34): p. 60-90.

27.   True, W.R., *Fed data show solid 2001 for US pipeline companies, more gas capacity planned.* Oil & Gas Journal, 2002. **100**(38): p. 52.

28.   True, W.R., *Construction plans jump; operations skid in 1996.* Oil & Gas Journal, 1997. **95**(31): p. 37.

29.   True, W.R., *U.S. pipelines continue gains into 1996.* Oil & Gas Journal, 1996. **94**(48): p. 39.

30.   True, W.R., *U.S. interstate pipelines ran more efficiently in 1994.* Oil & Gas Journal, 1995. **93**(48): p. 39.

31.   True, W.R. and J. Stell, *US construction plans slide; pipeline companies experience flat 2003, continue mergers.* Oil & Gas Journal, 2004. **102**(32): p. 52.

32.   Chemical Engineering. *Plant Cost Index.* 2006 [cited 2006 1 June 2006]; Available from: http://www.che.com/pindex/.

33.   Electric Power Research Institute, *TAG-Technical Assessment Guide Volume 1: Electricity Supply.* 1993, Electric Power Research Institute: Palo Alto, California.

34.   Zhang, H., W. Li, and H. Herzog, *MIT CO_2 Pipeline Transport and Cost Model.* 2007, Massachusetts Institute of Technology: Carbon Capture and Sequestration Technologies Program: Boston, Massachusetts.

35.   Berkenpas, M.B., et al., *User Manual: Integrated Environmental Control Model.* 2004, Carnegie Mellon University: Pittsburgh, PA. p. 371.

36.   Morgan, M.G., M. Henrion, and M. Small, *Uncertainty : a guide to dealing with uncertainty in quantitative risk and policy analysis.* 1990, Cambridge: Cambridge University Press. 332.

37.   Nyman, D.J., J.S. Dracos, and R. Varagani, *Carbon Dioxide Capture and Transportation Options in the Illinois Basin--Task 3: Assess Carbon Dioxide Transportation Options in the Illinois Basin.* 2004, Midwest Geological Sequestration Partnership: Champaign, IL. p. 82.

Enhanced Oil Recovery (EOR)

The first Enhanced Oil Recovery (EOR) pilot projects employing miscible CO_2-flooding[7] began in the late 1970's. Since then, the number of these projects in the US has increased to 80 in 2006 producing close to 250,000 barrels of oil per day (BOPD), as shown in Figure 21. While there are CO_2-flood EOR projects operating in Turkey and Trinidad, these are immiscible CO_2-flooding projects in which oil displacement happens through a different—generally less efficient—mechanism. Production from miscible CO_2-floods accounts for slightly more than a third of the total domestic US oil production from EOR methods [1]. The large number of operating CO_2 floods has greatly contributed to understanding of the processes involved.
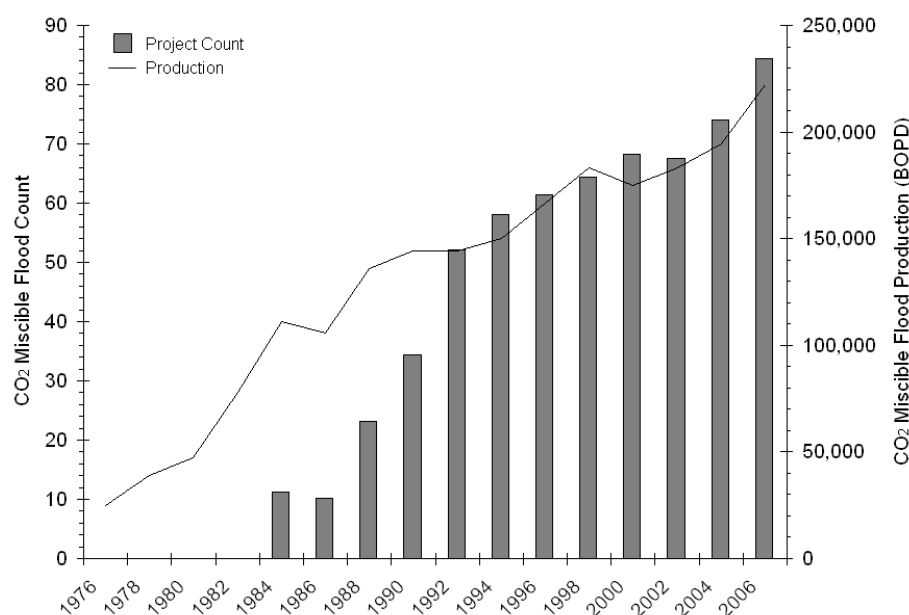
Figure 21.   Counts of domestic US miscible CO_2 flood EOR projects and production in barrels of oil per day (BOPD) between the late 1970's and 2006 [1, 8].

There are a number of methods used to model oil recovery in secondary (i.e., waterflooding) and enhanced production (i.e., CO_2-flooding, polymer injection, etc.) [2]. These methods, in order of both increasing complexity and data requirements, are: rule-of-thumb estimates [3, 4]; semi-analytical fractional-flow models [5, 6]; and, stream-tube [7] and finite difference models (e.g. ECLIPSE, GEM/STARS, UTCOMP, etc.). Investment decisions on CO_2-flooding projects are usually rely on predictions from numerical simulations performed only after a full model of the particular field has been developed and verified through a history match (i.e., matching modeled and actual production of the field over

---

[7] CO_2-flooding processes can be categorized as miscible or immiscible; this chapter concerns the former type of CO_2-flood. The Oil Recovery Methods chapter contains a brief primer on oil recovery processes which discusses the differences in between these processes.

time). Without access to a history-matched model, predictions about the response of the field to enhanced recovery methods are limited to rule-of-thumb and semi-analytical results.

A number of studies have examined the potential for production from miscible CO_2-flooding in US domestic oil reservoirs [9-11] using semi-analytical screening models relating oil production rates to CO_2 injection rates, geological properties, and assumptions on the development of an oil field. These studies, performed for Congress or a government agency, have approached the assessment from the perspective of increasing domestic oil production, but none of them examined the economics of miscible CO_2-flooding in the context of a geologic storage process.

More recently, several studies have also attempted to evaluate the economics of CO_2 storage through miscible CO_2-flooding [3, 12]. These studies have applied rules-of-thumb to estimate oil production and the cost of CO_2 storage via EOR. The Holtz et al. study [12] used these rules of thumb to estimate incremental oil production and the resulting cost of storage for specific cases in West Texas. Similarly, the study by Massachusetts Institute of Technology (MIT) [3] used three hypothetical scenarios to illustrate a possible range of cost. There have been no studies performed to date that use a semi-analytical model to estimate the economics of CO_2-flood EOR for CO_2 storage.

The objective of this chapter is to develop and apply a semi-analytical model that can be applied to estimate the cost of geological storage of CO_2 via miscible CO_2-flood EOR[8] based on limited amount of site-specific data. The engineering-economic model will be used to assess the sensitivity of storage cost to changes in geological settings and assumptions regarding the development of the EOR. It will also show the potential range of costs that could occur and the probability associated with these costs for a given scenario.

The CO$_2$ Miscible-Flood Enhanced Oil Recovery Process

The CO_2 flood EOR process can be broken down into several steps, as shown in Figure 22. In the CO_2-flood process, CO_2 is injected through an injection well (i.e., injector) into the target reservoir; the CO_2 extracts oil from the reservoir; and, the CO_2-oil mixture, along with reservoir brine, is brought to the surface at a well (i.e. producer). These three process steps happen at the level of a well pattern (i.e., a cluster of injection and production wells) undergoing CO_2-flooding in an oil field. Depending on the size of the oil field, there may be hundreds of patterns. For example, at the SACROC field in Texas, the largest CO_2 flood (by production), there are 414 injection wells and 354 production wells [1].

---

[8] Herein the term CO_2-flooding will refer to the miscible process
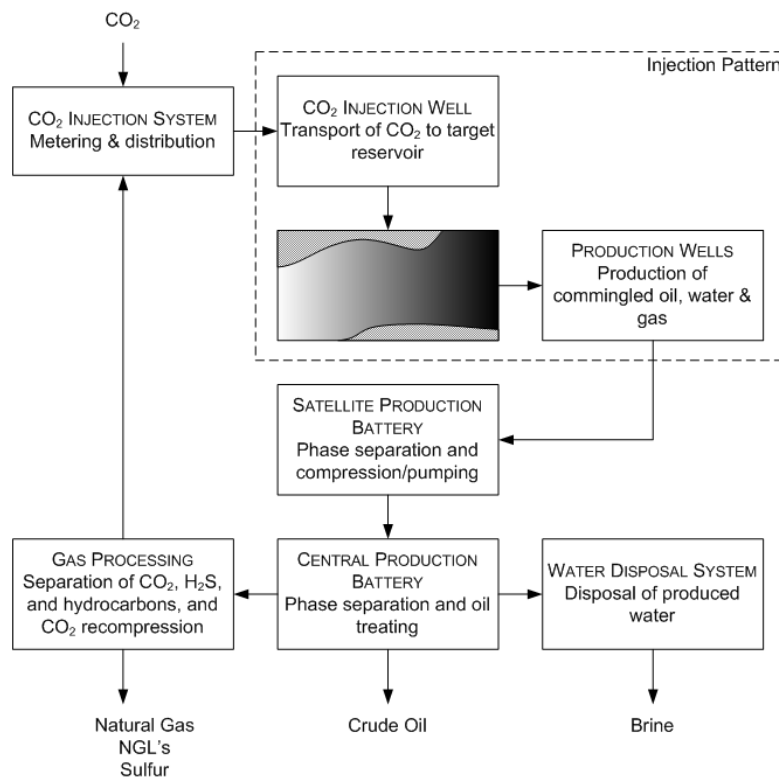
Figure 22. Material flows and process steps in CO_2-flooding

At the surface, the produced fluid mixture from a number of well patterns is collected, separated by phase, and the crude oil treated through the addition of chemicals such as emulsifiers to prepare it for sale. These steps happen at production batteries, and depending on the field design, may be distributed between satellite production batteries, handling fluids from a small number of patterns, and a central production battery, handling fluids from the entire field.

Traditional CO_2-flood projects are designed to minimize the amount of CO_2 that must be purchased; thus, CO_2 separated from the produced oil is compressed and recycled to the injector. The gaseous stream separated from the produced oil typically also contains hydrogen sulfide gas (H_2S), methane, ethane, and natural gas liquids[9] (NGLs), which may be separated from the CO_2 recycle, depending on purity requirements for the injected CO_2, safety requirements for dealing with H_2S, and process economics.

CO_2-flood projects explicitly intended to be operated as CO_2 storage operations may be designed somewhat differently than traditional CO_2 floods. For example, with an economic incentive to store as much CO_2 as possible, it may be desirable to eliminate CO_2 recycle (and potentially H_2S separation) from the CO_2-flood operation, and integrate the CO_2 flood with acid-gas injection,[10] maximizing the amount of CO_2 stored by the project while recovering a comparable amount of oil to a traditional EOR project [13, 14]. In addition, it may be possible to optimize operation and design of injection patterns to maximize both oil recovery and CO_2 storage. For example, design of well completions to create "favorable" CO_2 injection profiles, changes in the composition of the injected solvent stream over time, and shut-in of production wells to minimize the ratio of gas-to-oil (GOR) produced can all increase the amount of CO_2 that remains trapped in the subsurface while increasing oil recovery rates [15, 16].

---

[9] NGLs are natural gas components that are liquids under ambient conditions, such as propane and butane.

[10] Formally, an acid gas is any gas that can form acidic solutions when mixed with water. In the petroleum industry, acid gas refers to a mixture of H_2S and CO_2.

Enhanced Oil Recovery Performance Model

The model of the EOR process developed here can be separated into two parts: a performance model, and a economics model. As shown in Figure 23, the performance model takes inputs that describe reservoir and oil properties, and the operating strategy (field properties). From these inputs the model estimates the oil recovery rate as a function of the amount of CO_2 injected, the required wellhead pressure to achieve the desired injection rate, and the total amount of oil recovered from the project at the end of its economic life.
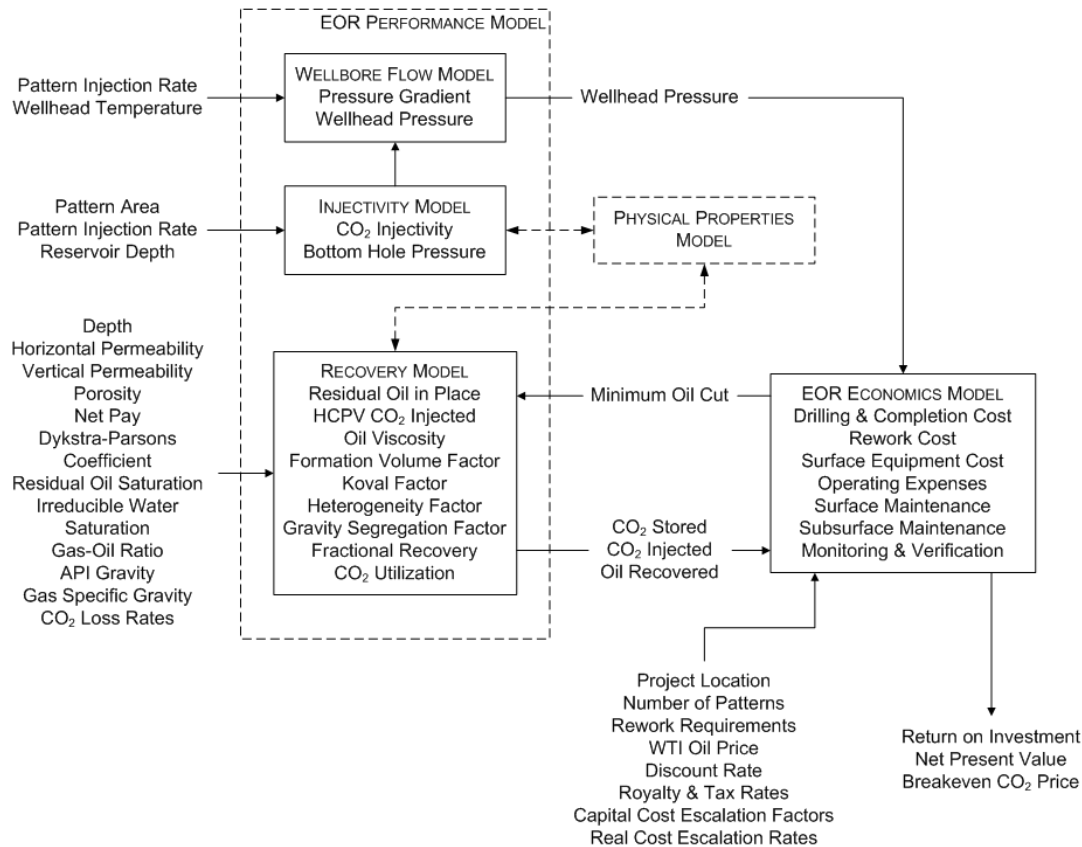
Figure 23. The CO_2-flood EOR engineering-economic model developed here.

Establishing the Bottom Hole Injection Pressure—Modeling Injectivity

The rate at which CO_2 can be injected into the oil reservoir is determined by the injectivity of the system. Injectivity is defined as the injection rate divided by the excess pressure above reservoir equilibrium pressure driving injection [17]:

$$I = \frac{q}{p_{wb} - p_e} \tag{10}$$

Thus, given an injection rate, q, and reservoir equilibrium pressure, p_e, the pressure at the well bottom, p_{wb}, can be calculated if the injectivity is known.

For an isolated injection pattern, the injectivity can be calculated analytically. Figure 24 shows the geometry of a typical isolated inverted 5-spot injection pattern and the nomenclature used in the derivation.
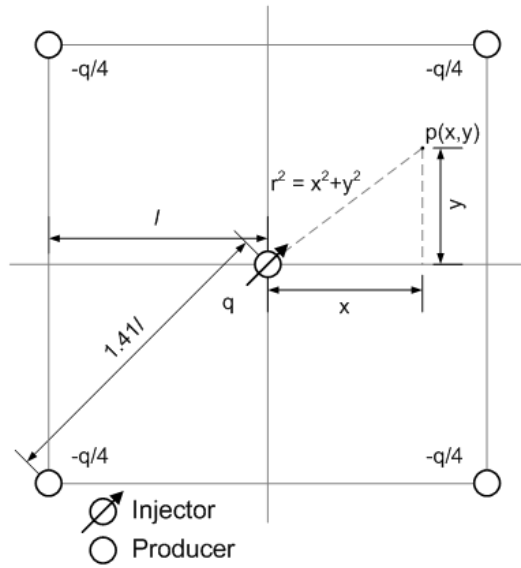
Figure 24.   An inverted 5-spot pattern, where CO_2 is injected through the well at center, and fluid is produced at the four surrounding wells, showing nomenclature used in derivation of the injectivity equation.

An analytical solution for pressure at any point in the system can be written if several assumptions are made, which are: the system is at steady state; the reservoir fluid and injected fluids are the same and incompressible; the reservoir permeability is homogeneous and isotropic; and, full completion of all five wells through the net pay. The solution is derived by superposition of the effects of each of the individual wells as [18]:

$$\frac{4\pi kh[p(x,y) - p_e]}{q\mu} = \ln\left\{ \frac{\left[\left((l+x)^2 + (l-y)^2\right)\left((l-x)^2 + (l-y)^2\right)\left((l-x)^2 + (l+y)^2\right)\left((l+x)^2 + (l+y)^2\right) \right]^{1/4}}{\left(x^2 + y^2\right)} \right\}$$

where, k is permeability, h is reservoir thickness (i.e., net pay), q is the CO_2 injection rate, μ is viscosity of the CO_2, and l is the producer-injector spacing.

Solving the above equation for pressure at x equals the wellbore radius, r_w, where r_w is small (i.e., $r_w << l$), and y is equal to zero, then rearranging for injectivity results in Equation 11.

$$I = \frac{q}{p_{wb} - p_e} = \frac{4\pi kh}{\mu \ln\left\{ \frac{\left[(l+r_w)^2 + l^2\right]^{1/2}\left[(l-r_w)^2 + l^2\right]^{1/2}}{r_w^2} \right\}} \tag{11}$$

Equation 11 will likely overestimate the injectivity of CO_2 in a tertiary-flooding situation (i.e., where CO_2 flooding is occurring after waterflooding) as it is derived on the basis of a single flowing fluid. In such a situation, the effects of multi-phase flow, fluid mixing, and permeability heterogeneity will result in reduced injectivity compared to the value predicted by Equation 11 [19, 20]. Other analytical models for 5-spot injectivity, such as that for a 5-spot flooding network [21], are derived based on similar assumptions and also overestimate injectivity.

Equation 11 is thus used in the model to estimate the required well bottom pressure (bottomhole injection pressure or BHIP) for the injection rate supplied to the model. In addition to the injection rate, the pattern area and reservoir equilibrium pressure are required. The producer-injector distance, l, is calculated on the basis of pattern area, where (as can be seen from Figure 24) one-half the square-root of pattern area is equal to the producer-injector distance. The reservoir equilibrium pressure can be calculated from the hydrostatic pressure gradient and depth [22]:

$$p_e = Gd \tag{12}$$

where G is the pressure gradient, typically ranging from 10.5 kPa/m to 12.4 kPa/m [23].

It is undesirable to cause uncontrolled fractures in a reservoir undergoing CO_2 flooding, thus the upper limit on injection pressure is the fracture pressure of the reservoir rock. In absence of field data, this can be estimated from a correlation presented by Heller and Taber [24]:

$$G_f = \gamma - \beta e^{-\alpha d}$$
$$p_f = G_f d$$

(13)

where, P_f is the fracture pressure at depth (Pa), G_f is the fracture gradient (Pa/m), and α, β and γ are coefficients with the values: 4.36×10^{-4} m^{-1}, 9.24 kPa/m, and 22.62 kPa/m.

From the Surface to the Reservoir—Modeling the Wellbore Environment

As shown by Equation 10, injectivity is proportional to the difference between the reservoir pressure and the pressure at the well bottom (BHIP). Thus, estimating the injection rate for a given wellhead pressure (or vice versa) requires estimation of the pressure change through the well.

BHIP is frequently estimated by assuming it is equal to the hydrostatic pressure exerted by a static column of fluid (e.g., Hendriks [23]). However, this is only an approximation valid at low flow rates, as the loss of pressure due to friction between the flowing fluid and the surrounding rock counteracts the pressure increase due to hydrostatic pressure. For a high capacity well, such as that found in the Norwegian Sleipner project, pressure losses due to friction will not be negligible. Moreover, heat transfer between the surrounding rock and the wellbore also affects the pressure and temperature distribution in the well [25, 26].
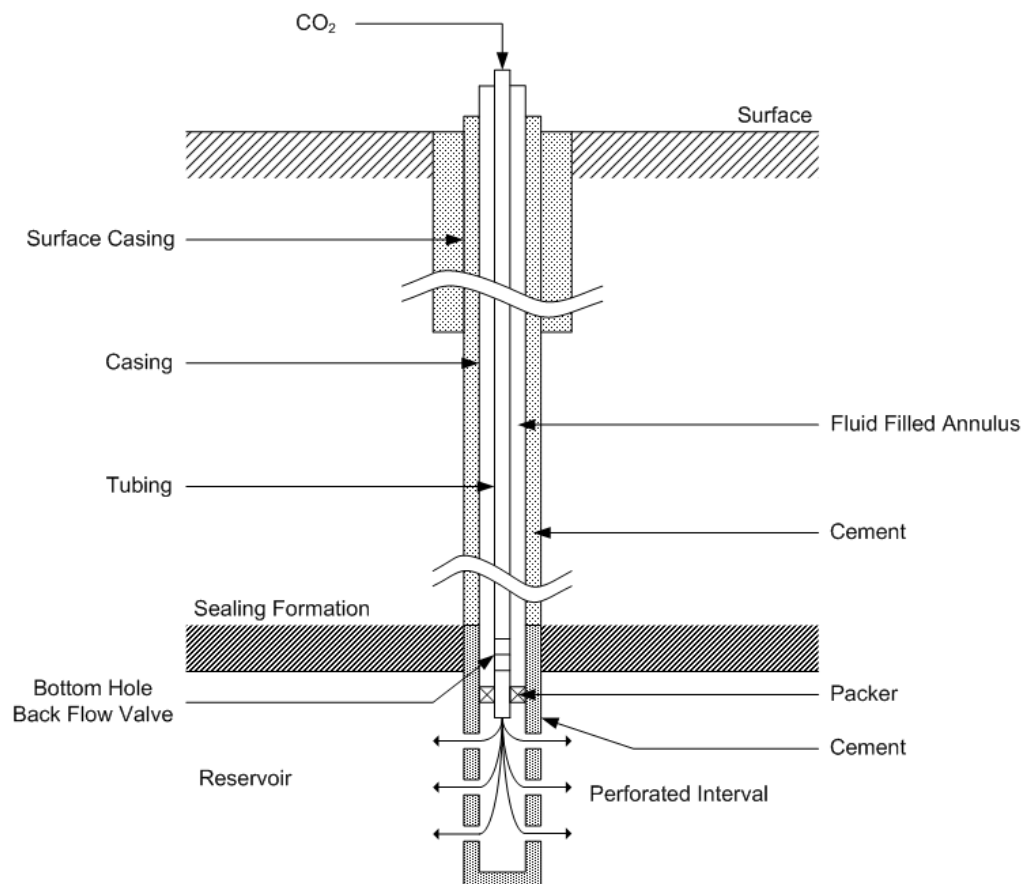
Figure 25.   A typical well completion, showing components relevant to modeling flow in the wellbore.

Figure 25 shows a typical vertical injection well completion. For simplicity, this figure does not show the conductor pipe or differentiate between the intermediate and production casing strings. The annulus between the production casing and the production tubing is generally filled with a fluid, such as a brine or hydrocarbon. The injectant flows from the surface to the reservoir through the production tubing and enters the reservoir through perforations in the production tubing.

A full numerical model of the wellbore allows sensitivity of BHIP and bottomhole temperature to changes in a variety of input parameters to be estimated. The Numerical Modeling of the Wellbore Environment chapter describes a numerical model that can be used to calculate the pressure gradient in a CO_2 injection well considering pressure changes due to hydrostatic head, friction losses, and heat transfer. However, the complexity of such a model is unnecessary in the context of the EOR performance model. Thus, a response surface model based on the full numerical model (described in the Numerical Modeling of the Wellbore Environment chapter) is used to estimate BHIP in the EOR performance model.

The response surface model assumes that the pressure gradient in the wellbore is a linear function of depth and, thus, that the BHIP can be written as:

$$p_{wb} = \frac{\Delta P}{\Delta L} L + p_{wh} \tag{14}$$

where, p_{wb} is the BHIP pressure, p_{wh} is the wellhead pressure, and L is the wellbore length.

Results from the numerical model show that the pressure gradient in the well becomes non-linear at high flow rates. Because Equation 14 can only represent pressure gradients linear in depth, it is valid only for flow rates below approximately 1 Mt CO_2 per year at temperatures less than 30°C and wellhead pressures greater than 8 MPa for the 3-inch (0.076 m) inside diameter tubing modeled (see Numerical Modeling of the Wellbore Environment chapter for a description of the other parameters used in the numerical model). The form of the regression equation for pressure gradient is:

$$\frac{\Delta P}{\Delta L} = a_1 q^2 + a_2 \log(p_{wh})^2 \tag{15}$$

where, P_{wh} is the wellhead pressure (Pa), and q is the volumetric flow rate (m^3/d) at wellhead conditions.

Parameter estimates for the regression coefficients are given in Table 10. The regression model given in Equation 15 accounts for a large proportion of the variation in the set of 2895 data points generated by the numerical model, reflected by an adjusted-r^2 value of 0.99.

Table 10.   Regression coefficient estimates for the pressure drop correlation, Equation 15, where standard errors are reported in parentheses.

Coefficient	Value
a_1	-7.008×10^{-4} ** (3.100×10^{-6})
a_2	1.812×10^{2} ** (2.692×10^{-1})
** Significant at the 1% level	

The regression coefficients in Table 10 show that the wellbore pressure gradient is negatively correlated with the volumetric flow rate, and positively correlated with the square of the base-ten logarithm of pressure. In addition, wellhead temperature influences the pressure gradient predicted by Equation 15 through its effect on volumetric flow rate. Figure 26 shows the pressure gradient predicted by Equation 15 using the coefficients listed in Table 10.

The difference between the lines of constant mass flow at 25 $^{\circ}$C and 0 $^{\circ}$C in Figure 26 shows that the pressure gradient is negatively correlated with wellhead temperature. However, in the limit as volumetric flow rate approaches zero, Equation 15 reduces to a strictly pressure dependent function, shown by the single dashed line in Figure 26. Nonetheless, Equation 15 can be used to estimate the hydrostatic pressure gradient for a static column of CO_2 within the limits of the regression equation.
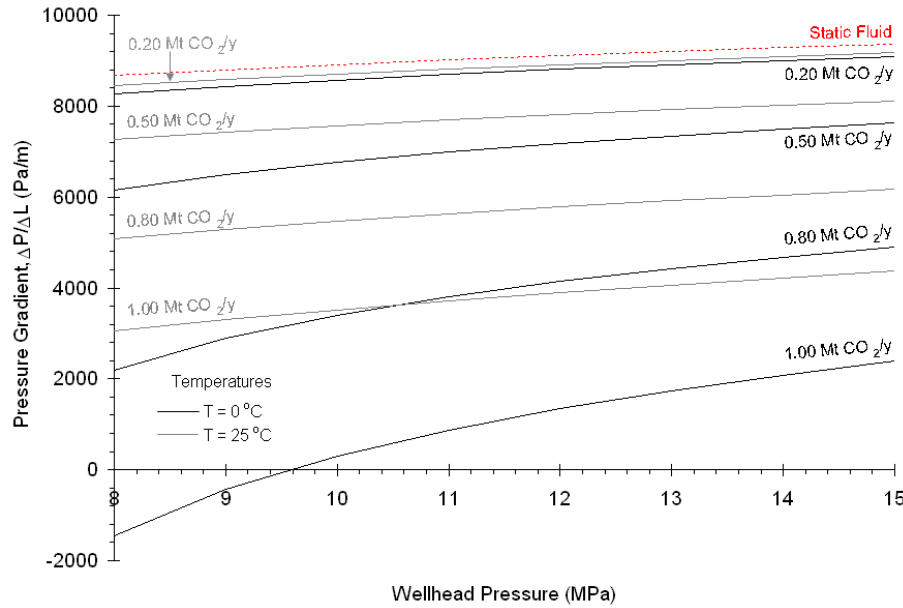
Figure 26. Pressure gradients predicted by the reduced form wellbore pressure model for mass flow rates between 0.2 and 1.0 Mt CO_2 per year at two different wellhead temperatures and for a static column of CO_2.

Estimating Recovery of Oil

Recovery of oil and gas in miscible CO_2-flooding (or any other EOR process) can be characterized by the overall recovery efficiency, E_r. The overall recovery efficiency is the product of a number of factors:

$$E_r = E_m \cdot E_d \cdot E_a \cdot E_v \qquad (16)$$

where, E_m is the mobilization efficiency, E_d is (linear) displacement efficiency, E_a is areal (horizontal) sweep efficiency, and E_v is vertical sweep efficiency [27, 28]. The product of the overall recovery efficiency and the volume of oil in place prior to the commencement of the recovery operation, V_{pd}, is the volume of oil produced.

Mobilization efficiency is the ultimate fraction of oil that can be recovered at the microscopic level from a differential volume of reservoir rock [27]. This is written as:

$$E_m = \frac{S_{oi} - S_{or}}{S_{oi}} \qquad (17)$$

Where, S_{oi} and S_{or} are the phase saturation for the oil phase initially (before CO_2-flooding) and residual to the CO_2 flood, respectively. The residual oil saturation reflects the effects of interfacial tension between the fluids in the rock and ratios of viscous to capillary forces [28].

In miscible displacement, the injected solvent (CO_2 or otherwise) becomes completely miscible with the reservoir oil. For a given solvent-oil pair, miscibility is a function of reservoir temperature and pressure, and is characterized by the minimum miscibility pressure (MMP)[11]. At pressures greater than MMP, CO_2 in contact with reservoir oil extracts low and intermediate molecular weight hydrocarbons from the oil, and after multiple contacts with the crude oil, this CO_2-rich phase becomes completely miscible with the reservoir oil [29-31]. This is described in the EOR literature as multi-contact miscibility (MCM) [28].

Under miscible conditions, interfacial tension between the oil and CO_2 is effectively zero. Consequently, S_{or} is assumed to be zero, and Equation 17 reduces to 100% mobilization efficiency.

---

[11] See the Oil Recovery Methods chapter for a brief discussion of MMP and miscible CO_2-flood screening criteria

Displacement efficiency is a measure of the fraction of the oil swept from the reservoir in a linear displacement, and is a function of the volume of CO_2 injected, V_{pi}. Displacement efficiency is defined as [27]:

$$E_d = \frac{S_{oi} - S_o(V_{pi})}{S_{oi} - S_{or}}$$

In this equation, the initial and residual oil saturation are assumed to be known parameters; however, oil saturation as a function of the injected volume of CO_2 must be calculated.

Saturation of fluid at a point in the reservoir as a function of the volume of injected solvent can be estimated from a fractional-flow based model. In a reservoir undergoing CO_2-flooding, there are at least three flowing phases: a water phase, CO_2-rich phase, and an oil-rich phase. Moreover, because of the differences in viscosity between the flowing phases, each phase travels at a different velocity, resulting in viscous fingering (illustrated in Figure 27).

This figure is copyrighted and cannot be reproduced here. The figure can be found in the doctoral thesis "The Economics of CO_2 Transport by Pipeline and Storage in Saline Aquifers and Oil Reservoirs" by Sean McCoy, Carnegie Mellon University, January, 2008.

Figure 27. Displacement fronts in a quarter of an inverted five-spot pattern, for different mobility ratios, showing the effect of viscous fingering reproduced from Habermann (© 1960 Society of Petroleum Engineers) [32].

While there have been great improvements made in analyzing multiphase miscible systems with viscous fingering [33, 34], it is still difficult to solve the system of equations analytically for fractional flow. Consequently, the model presented here is a two-phase, semi-empirical model of unstable displacement, similar to other models used at the screening level to estimate oil recovery in CO_2-flooding [5, 10, 35, 36].

The equations used to estimate displacement efficiency in the CO_2-flooding case are based on the analogous case of immiscible displacement [6]. In an immiscible displacement (e.g. a waterflood), where one phase is displacing another immiscible phase, neglecting capillary pressure in a horizontal reservoir, the fractional flow of the displacing fluid, f_d, can be written [27]:

$$f_d = \frac{1}{1 + \left(\dfrac{\mu_d k_{ro}}{\mu_o k_{rd}}\right)} \tag{18}$$

where: μ refers to the viscosity of the displacing fluid, d, and oil o; and k_r is the relative permeability of the rock with respect to oil, o, and the displacing fluid, d.

Assuming that the relative permeability of the rock to the flowing phases is a linear function of the displacing fluid saturation, S_d, we can write:

$$\frac{k_{ro}}{k_{rd}} = \frac{1-S_d}{S_d}$$

Then, if the mobility ratio is defined as,

$$M = \frac{\mu_o}{\mu_d} \tag{19}$$

Equation 18 can be written:

$$f_d = \frac{1}{1+\left(\dfrac{1-S_d}{S_d}\right)\left(\dfrac{1}{M}\right)} \tag{20}$$

This derivation only applies for a stable displacement, where the mobility ratio is less than or equal to one. In this situation, the oil is capable of traveling at the same velocity as the displacing fluid under an imposed pressure gradient. When the mobility ratio is greater than one, the displacing fluid will bypass the oil, leaving regions of the reservoir unswept by the displacing fluid, and thus reducing oil recovery.

In the CO_2-flooding process, the displacing fluid, CO_2, is miscible with oil and the mobility ratio is on the order of 10-100; thus, without modification Equation 20 is unsuitable for determining fractional flow. Koval [6] suggested, however, that this immiscible displacement equation can be used to model miscible displacement if the mobility ratio, M, is replaced with an effective mobility ratio, K. Koval originally intended that this factor would account for mixing between CO_2 and oil, viscous fingering, and effects of reservoir heterogeneity. Further development of the Koval model has extended it to account for vertical sweep.

Vertical sweep efficiency is the fraction of the reservoir that has been swept by the displacing fluid [27]. In the CO_2 flooding process, the injected CO_2 tends to be less dense than the reservoir oil; thus, CO_2 tends to migrate towards the top of the reservoir leaving lower portions of the reservoir unswept.

Paul and Lake [36] recognized that Koval's definition of K could be adjusted for vertical sweep, by including a gravity segregation factor. Thus, as used here K is defined as [36]:

$$K = EHG \tag{21}$$

where: E is effective mobility, accounting for miscibility of CO_2 and oil, and viscous fingering [6]; H is the heterogeneity factor, accounting for effects of dispersion and channeling [37]; and, G is the gravity segregation factor [36].

The factors in Equation 21 are defined as:

$$E = \left(0.78 + 0.22M^{1/4}\right)^4 \tag{22}$$

$$\log H = \left[\frac{V_{DP}}{\left(1-V_{Dp}\right)^{0.2}}\right] \tag{23}$$

$$G = 0.565\log\left(\frac{t_h}{t_v}\right) + 0.870, \text{ where } \frac{t_h}{t_v} = 2.5271 k_v A \frac{\Delta\rho}{q\mu_s} \tag{24}$$

In Equation 23, V_{DP} is the Dykstra-Parsons coefficient, which is a measure characterizing the permeability distribution of the reservoir. In Equation 24, k_v is the reservoir permeability in the vertical direction (md), A is the pattern area (acres), q is the gross injection rate of CO_2 (RB/day), and $\Delta\rho$ is the density difference between CO_2 and oil (kg/m^3).

Determining the relationship between fractional flow and fluid saturation requires the equation of Buckley and Leverett [6]. The Buckley-Leverett equation describes displacement of one immiscible fluid by another, relating the velocity of the displacing-fluid front in the reservoir to the derivative of the fractional flow equation [38]. Thus, the integrated form of the Buckley-Leverett equation, relates the distance of a plane of fluid saturation to distance in the reservoir:

$$x(S_d) = \frac{V_i}{A\phi} \frac{df_d}{dS_d}\bigg|_{S_d}$$

where: x is the distance in the reservoir, V_i is the volume of injected fluid, A is the cross sectional area of the reservoir, and φ is reservoir porosity.

At the production well, where x equals L, the Buckley-Leverett equation can be solved to yield:

$$V_{i,pv} = \frac{V_i}{LA\phi} = \frac{1}{\dfrac{df_d}{dS_d}\bigg|_{S_d}} \qquad (25)$$

In Equation 25, $V_{i,pv}$ refers to the dimensionless pore volume of fluid injected into the reservoir. The denominator of Equation 1.16 is shown for simplicity as the product of length, area, and porosity; however, the pore volume available for flow is reduced by the presence of immobile water (i.e., $1-S_w$).

Substituting for K and taking the derivative of Equation 20 yields the expression for the derivative of fractional flow required in Equation 25:

$$\frac{df_d}{dS_d} = \frac{K}{[1 + S_d(K-1)]^2} \qquad (26)$$

Thus, substituting Equation 26 into 25, and solving for f_d we arrive at an equation for the fractional flow of the displacing fluid (CO_2) at the producing well in the linear system after breakthrough (i.e., the time at which CO_2 reaches the production well):

$$f_d = \frac{K - \sqrt{K/V_{i,PV}}}{(K-1)} \qquad (27)$$

where, f_d is referred to as the "cut" of the displacing fluid (e.g., f_c is referred to as the CO_2 cut). Breakthrough occurs after the injection of $1/K$ pore volumes of CO_2 based on the solution of Equation 27 with f_d equal to zero.

To arrive at the pore volume of oil produced from the linear reservoir, equivalent to $E_d E_v$, Equation 27 must be integrated and added to the pore volumes produced prior to breakthrough.

$$\begin{aligned}
E_d E_v &= V_{i,PV}\big|_{bt} + \int_{V_{i,PV}|_{bt}}^{V_{i,PV}} \left[1 - \frac{K - \sqrt{K/V_{i,PV}}}{(K-1)}\right] dV_{i,PV} \\
&= \frac{1}{K} + \int_{V_{i,PV}|_{bt}}^{V_{i,PV}} \left[1 - \frac{K - \sqrt{K/V_{i,PV}}}{(K-1)}\right] dV_{i,PV} \qquad (28) \\
&= \frac{2\sqrt{KV_{i,PV}} - V_{i,PV} - 1}{(K-1)}
\end{aligned}$$

Thus, after CO_2 breakthrough, the product of displacement efficiency and vertical sweep efficiency in a linear flood is given by Equation 28.

Areal sweep, E_a in Equation 16, is the fraction of the well pattern swept by the displacing fluid. To estimate areal sweep, the model uses Claridge's modification of Koval's method [5]. Claridge's method estimates the areal sweep for a 5-spot well pattern (or inverted 5-spot, shown in Figure) and is based on the concept of apparent pore volumes injected. Claridge defines apparent pore volumes injected, $V_{a,PV}$, as:

$$V_{a,PV} = \frac{V_{i,PV}}{E_d E_v} \qquad (29)$$

Where the product, $E_v E_d$, is calculated using Equation 28, using the pore volumes of fluid injected relative to the volume fraction swept by the injected fluid, $V_{d,PV}$, in place of $V_{i,PV}$:

$$V_{d,PV} = \frac{V_{i,PV}}{E_A} = \left(\frac{E_v E_d}{E_A} \right) V_{a,PV} \qquad (30)$$
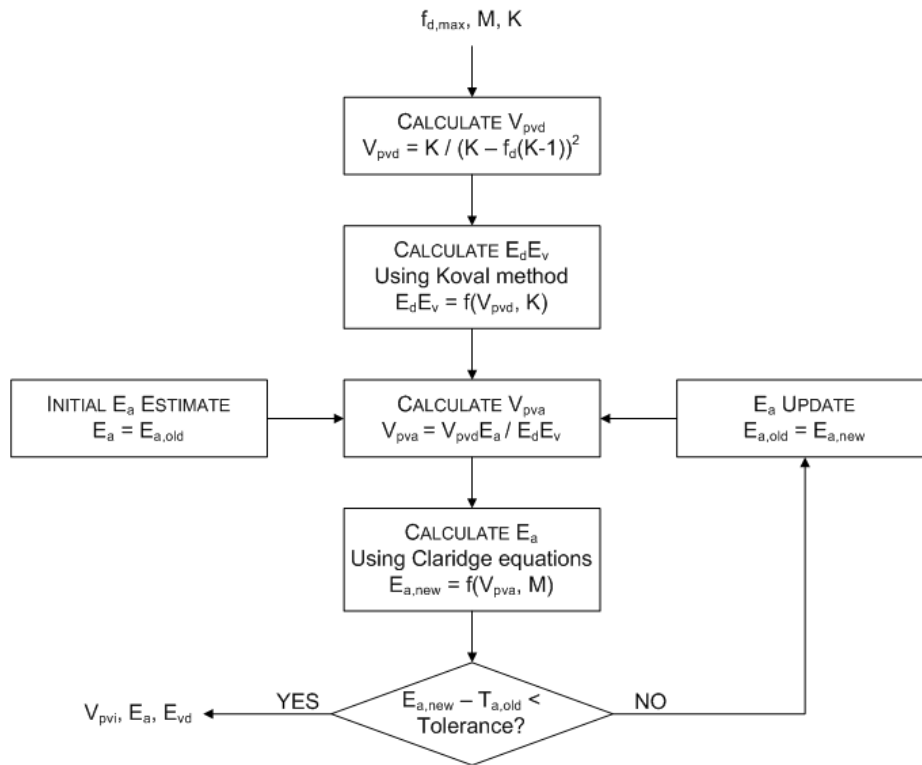
Figure 28.   The iteration scheme used to calculate E_a and $E_v E_d$

Areal sweep in Equation 30 is calculated based on the set of equations given below as Equation 31.

Equations 28, 29, 30 and 31, can be used to estimate the fraction of total oil recovered, i.e., E_r, as a function of the fraction of CO_2 in the produced fluid, f_d. Unfortunately, there is no analytical solution to calculate E_a and $E_v E_d$ as a function of f_d (or V_{pvi}) using these equations. Thus, the model uses the iteration scheme presented in Figure 28 to arrive at the values of $E_v E_d$, E_a, and V_{pvi}.

$$E_{a,bt} = \begin{cases} V_{a,PV}, & V_{a,PV} \leq 1 \\ 1.0, & V_{a,PV} > 1 \end{cases}$$

$$M_{bt} = \frac{1 - E_{a,bt}}{E_{a,bt} - 0.4}$$

$$E_a = \frac{E_{a,bt} + 0.4M'}{1 + M''} \qquad (31)$$

$$M' = 25 \frac{M_{bt}^{5/6} + 0.3 + 2.3(V_{a,PV} - 1)}{V_{a,PV} + 1}$$

$$M'' = \frac{M - M_{bt}}{(M' - M_{bt})^{(0.85 - 0.55E_{a,bt} + 0.25V_{a,PV})}}$$

Estimating Net CO_2 Injected—The CO_2 Mass Balance

The amount of CO_2 injected (i.e., gross CO_2 injected) in traditional CO_2-flooding is many times greater than the actual amount of CO_2 stored (i.e., net CO_2 injected minus any leakage to the atmosphere) because CO_2 produced with oil is traditionally recycled and re-injected. The amount of CO_2 stored at the end of the economic life of the field must be estimated from a mass balance on CO_2 in the system. In this case, we consider pressure and temperatures to be constant, thus the mass balance can be written in terms of volume. Figure 29 shows the process streams required for a volumetric balance.

All of the volumetric flow rates in the following equations are written in terms of volumes at reservoir conditions (e.g., reservoir barrels, denoted RB). Conversions between reservoir volumes and surface volumes (e.g., stock-tank barrels, denoted STB) can be made by using the formation volume factor, defined for fluid x (i.e. oil or CO_2) as:

$$B_x = \frac{\rho_x(T_{res}, p_{res})}{\rho_x(T_{std}, p_{std})} \qquad (32)$$

where the density is measured at petroleum industry standard conditions, which are 60 °F (289 K) and 1 atm (101 kPa).
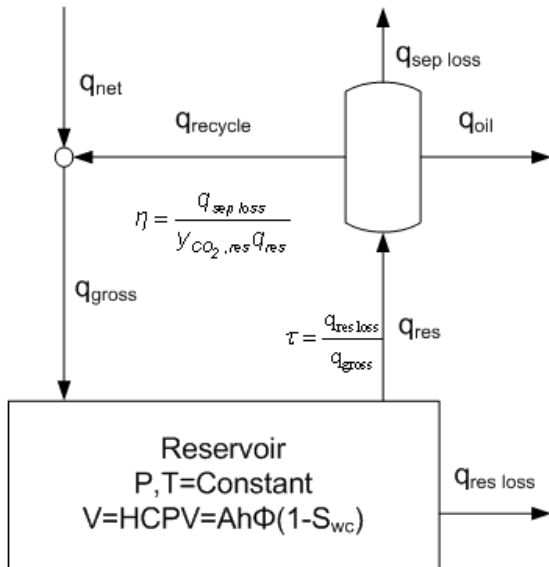
Figure 29.   *The process streams required for the mass balance, where q indicates the cumulative volume.*

The EOR performance model requires the gross injection rate, q_{gross}, be specified. Thus from Figure 29 flow rates for the process streams of interest can be written:

$$q_{prod} = q_{gross}(1-\tau)$$
$$q_{rcy} = q_{gross} f_d (1-\tau)(1-\eta)$$
$$q_{net} = q_{gross}\left[1 - f_d (1-\tau)(1-\eta)\right]$$

(33)

where τ specifies the rate of CO_2 escaping from the pattern, and η specifies the rate with which CO_2 is lost to the atmosphere from the separator.

Note that both loss rates imply that CO_2 leaves the process through some mechanism; however, only the loss rate to the atmosphere reduces the greenhouse gas mitigation efficiency of CO_2-flooding. Losses of CO_2 in the reservoir may result from poor injection well conformance, i.e., where injected fluids, in this case CO_2, that do not enter the intended zone in the reservoir [39]. In addition, some of the injected CO_2 will dissolve in residual water and oil, or escape into adjacent non-productive zones of the reservoir. This lost CO_2, the flow rate of which is represented by q_{loss}, is assumed to remain in the reservoir and not reach the atmosphere.

The fraction of CO_2 produced at the surface that escapes from processing facilities (the stream q_{atm}) is specified by η—the efficiency of surface processing. Emissions in this stream are fugitive emissions from the surface processing steps, occurring due to leaks in valves and flanges and the imperfect separation of CO_2 from produced oil and water.

To estimate the net CO_2 stored, the mass balance equations (33) must be rewritten in terms of cumulative volumes of CO_2. Following the nomenclature established in Figure 29, the gross volume of CO_2 injected is:

$$V_{gross} = \frac{V_{prod}}{(1-l)}$$

(34)

The produced volume, V_{prod}, is the sum of the volumes of oil produced and CO_2 produced, V_{CO2}:

$$V_{prod} = V_{pvi} Ah\phi(1-S_w) = E_a E_v E_d Ah\phi(1-S_w) + V_{CO2}$$

where, A is the pattern area, h is net pay, φ is the reservoir porosity, and S_w is the average water saturation in the reservoir (i.e. the fraction of the pore space saturated with water).

The displaceable pore volumes[12] of CO_2 produced after breakthrough, V_{pvd}, is calculated by integrating Equation 27:

$$V_{pvd,CO2} = \int_{V_{pvd,bt}}^{V_{pvd}} \frac{K - \sqrt{K/V_{i,PV}}}{(K-1)} dV_{i,PV}$$
$$= \frac{KV_{pvd} - 2\sqrt{KV_{pvd}} + 1}{K-1}$$

Thus, the actual pore volumes of CO_2 injected can be written (via Equation 30) as:

$$V_{CO2} = E_a Ah\phi(1-S_w)V_{pvd,CO2}$$

Now the remaining equations required for the mass balance can be written:

$$V_{rcy} = V_{CO2}(1-\eta)$$
$$V_{net} = \frac{V_{prod}}{(1-l)} - V_{CO2}(1-\eta)$$

(35)

---

[12] The displaceable pore volume is the fraction of the total hydrocarbon pore volume (HCPV) that can be displaced by CO_2-flooding. The actual pore volume is just that, i.e. the hydrocarbon pore volume.

Recovery of CO_2—Surface Facility Engineering

The prior production history of an oil field significantly influences all aspects of a CO_2 flood, including changes to surface facilities. The equipment already in place at the field determines what new equipment will be needed and generally depends on whether CO_2-flooding is being used as a secondary or tertiary recovery method. Equipment already in place and adopted for use in CO_2-flooding will have performance that is different from that which is new. Table 11Table 11, modified from Jarrell et al. [39], summarizes the categories of surface facilities required for a CO_2 flood and whether equipment already in place is required and can be used as is, or modified for use in CO_2-flooding, or if new equipment is required.

Table 11.   Surface facility categories and changes required for CO_2-flooding depending on production stage, where "NC" indicates no change, and "NR" indicates not required.

Equipment Category	Secondary Recovery	Tertiary Recovery
Gas Processing Plant		
Dehydration/compression	New	New
CO2 removal	New	New
H2S removal	New	New
NGL separation	New	New
Production Facilities		
Central tank battery	NC	Upsize
Satellite batteries	Upsize	Upsize
Fluid gathering	NC	Upsize
Gas gathering	Upsize	Upsize
Water Injection Facilities		
Makeup water	NR	Downsize
Disposal	NC	New
Distribution system	NC	NC*
CO2 Injection System		
Injection skids	New	NR*
Distribution lines	New	NR*
Production Wells		
Wellhead	Upsize/NC	Upsize/NC
Lift equipment	NC+	Downsize§
Injection Wells		
Wellhead	New	Upsize/NC
Downhole equipment	New	Upsize/NC
* Assumes existing water distribution system and water injection wells can be converted to CO_2 injectors		
+ Gas production increase		
§ Water production decrease—gas production increase		

The most significant differences between CO_2-flooding (and specifically continuous CO_2-injection) applied as secondary and tertiary recovery methods are changes in water production and requirements for well workover[13]. In secondary production, produced water rates should not significantly increase; thus, changes to water disposal facilities are not required. Conversely, in tertiary CO_2 flooding, produced water that would otherwise have been re-injected in the

---

[13] A workover is maintenance on a well where the tubing string may be pulled and replaced.

waterflood must now be disposed. Additionally, because water injection wells have already been drilled and completed during waterflooding, they will likely only require minor modifications, such as a new wellhead, for CO_2 injection [39].

Regardless of the previous history of the field, gas processing facilities will be required. Moreover, these are the most costly facilities in the CO_2 flood [39]. The gas processing facilities must, at a bare minimum dehydrate and compress the produced CO_2 for re-injection; however, there are many other processes that can be incorporated, such as removal of H_2S and separation of NGLs prior to re-injection [39, 40]. The design of the gas processing plant depends on purity requirements for the injected gas (based on the effect of impurities on MMP), regulatory requirements, and markets for byproducts (e.g. sulfur and NGLs).

Ideally a performance model would estimate sizes of separator vessels, absorption columns, pumps, and compressors, allowing both capital and operating costs (as well as energy requirements and the associated CO_2 emissions) to be estimated. However, the dependence of surface facilities requirements on the prior production history of the field, and the variety and complexity of options for surface facilities means that it is difficult to develop a generic performance model for surface facilities. For example, in the case of the gas processing facilities, there are at least two broad classes of processes for gas dehydration in use, three for H_2S removal, and four for NGL separation [40].

The EOR performance model must, however, estimate the energy requirements for CO_2 compression, as this is an energy intensive process common to all CO_2 floods. The compression energy requirement is based on compressing the recycle stream of CO_2 from atmospheric pressure to the required wellhead pressure. The energy requirement is calculated based on the method discussed in the Modeling CO_2 Transport by Pipeline chapter.

Illustrative Performance Model Results

Performance model results have been generated for four illustrative case study reservoirs, selected from successful projects that currently are (or were) operating and have published reservoir descriptions [41-46]. These four reservoirs cover a range of performance parameter values—*kh* from 1,500 to 5200 md·ft and pattern areas from 40 acres to 160 acres—and two lithologies—sandstone and limestone. The model performance inputs and other pertinent data are shown in Table 12.
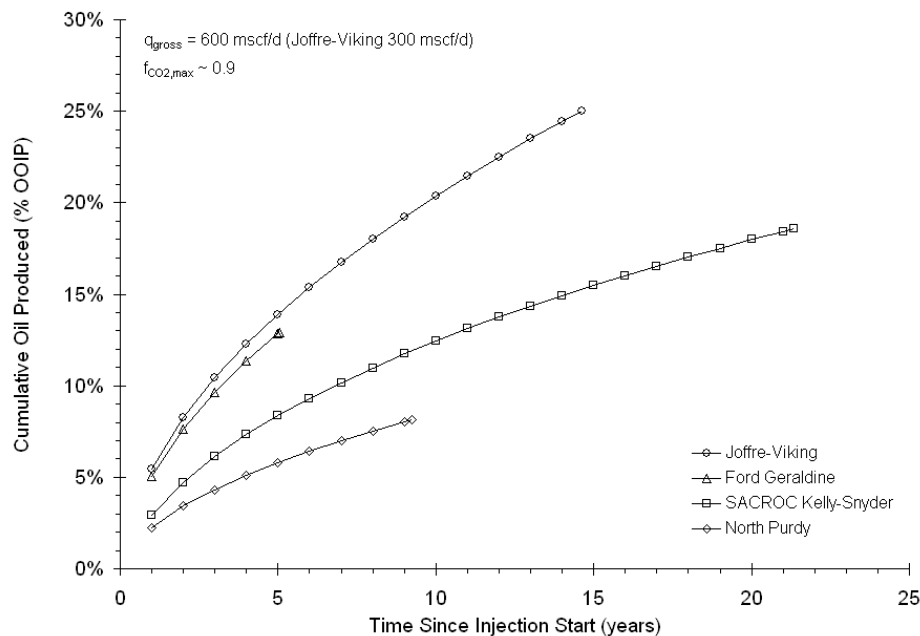
Figure 30.   Cumulative oil recovery as a fraction of OOIP for a typical pattern in the four illustrative case studies listed in Table 12.

Each of the case studies was evaluated at a constant injection rate of 600 mscf (thousand standard cubic feet) per CO_2 per day per pattern (32 tonnes CO_2 per day) with the exception of the Joffre-Viking, where injection was modeled at a constant 300 mscf CO_2 per day (16 tonnes per day) due to the extremely high permeability of the Viking pool. Injection rates on the order of hundreds of mscf per day per pattern are typical of current practice [1] and, for comparison, are 200

times smaller than the amount of CO_2 captured from a 500 MW pulverized coal power plant. The cumulative oil production as a percent of the original oil in place (OOIP) over time for a single typical pattern in each of the four CO_2 floods is shown in Figure 30.

Table 12. Key performance model parameters for the four case study reservoirs as well as residual oil in place (ROIP) prior to CO_2-flooding and the original oil in place (OOIP) at discovery [41-46].

Parameter	Northeast Purdy Unit	SACROC Unit, Kelly-Snyder Field	Ford Geraldine Unit	Joffre Viking Unit
Location	Oklahoma	Texas	Texas	Alberta
Reservoir	Purdy Springer A	Canyon Reef	Ramsey	Viking
Lithology	Sandstone	Limestone	Sandstone	Sandstone
Previous Recovery	Primary & Waterflood	Primary & Waterflood	Primary & Waterflood	Primary & Waterflood
Productive Area (acres)	9,177	49,900	5,280	16,611
Number of Patterns	229	1,248	132	208
Pattern Area (acres)	80	40	40	80
Depth (m)	2,499	2,042	2,680	1,500
p_{res} (MPa)	20.7	18.6	9.7	14.0
MMP (MPa)	14.5	11.0	6.2	
T_{res} (K)	338	328	301	329
Net Pay (m)	12.2	81.7	7.6	3.0
k_h (md)	44	19	60	507
k_v/k_h	0.18	0.40	0.10*	0.10
ϕ (%)	13.0	3.9	23.3	13.0
V_{DP}	0.80	0.68	0.70*	0.70*
S_{orw} (%)	47	42	41	35
γ_{API} (^{o}API)	35	41	40	42
μ_o (cp)	1.4	0.4	1.4	1.0
B_o (RB/STB)	1.2	1.5	1.3	1.2
R_s (scf/STB)	400	1,000	575	264
p_b (MPa)	19.3	12.8	9.5	-
γ_g (air = 1)	-	1.03	-	-
ROIP (MMSTB)	146	1,163	76	47
OOIP (MMSTB)	220	2,163	97	93
* Estimated parameter value				

Figure 30 shows that, of the four illustrative cases, a typical pattern in the Joffre-Viking field could be expected to have the highest incremental recovery under CO_2-flooding, followed by Ford Geraldine, SACROC Kelly-Snyder, and North Purdy cases. In addition, the life of a typical pattern in each case was set by specifying a maximum CO_2 cut, $f_{c,\,max}$, of approximately 0.9 (see Equation 27). The CO_2 cut over time is given in Figure 31.
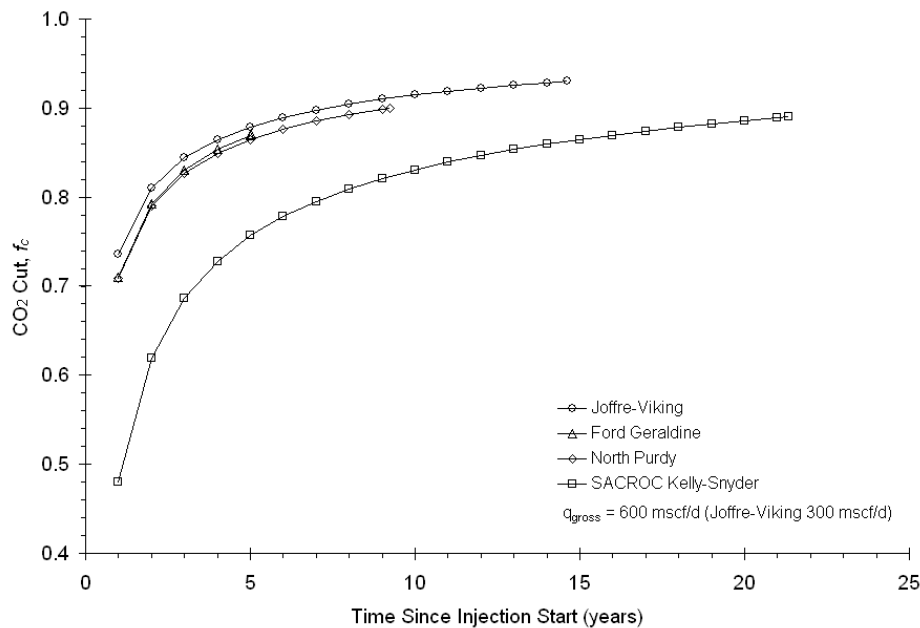
Figure 31.   The CO_2 cut for a typical pattern in the four illustrative case studies listed in Table 12.

Summary results for typical patterns in each of the four case studies are shown in Table 21. The results from the four case studies are considerably different from one another. In general, the gross utilization of CO_2 is somewhat higher than the typical rule-of-thumb for West-Texas (i.e., 7-10 mscf/STB [47]); however, the estimated net CO_2 utilization does agree with numbers predicted for operating CO_2 floods, summarized in Table 14 [46-48]. Note that changing the CO_2 cut will change both oil recovery and CO_2 utilization; thus, reported CO_2 utilizations are a function of the expected life the field. Because of this, caution must be exercised in comparing the model results in Table 13 and predicted values in Table 14 as *they are not be directly comparable.*

Table 13.   End-of-life summary results from the EOR performance model for a typical pattern in the four illustrative case studies listed in Table 12.

Parameter	Northeast Purdy Unit	SACROC Unit, Kelly-Snyder Field	Ford Geraldine Unit	Joffre Viking Unit
Pattern Life (years)	9.24	21.35	5.04	14.62
Oil Recovery (10^3 STB)	157	322	95	112
Recovery (% OOIP)	8	19	13	25
Gross Utilization (mscf/STB)	13	15	12	14
Net Utilization (mscf/STB)	3	4	4	3
CO_2 Stored (kt)	25	67	17	16
CO_2 Storage Rate (tonne/STB)	0.16	0.21	0.18	0.14

The sensitivity of the cumulative oil recovery at the pattern end-of-life to changes in model parameters using the SACROC Kelly-Snyder case is illustrated in Figure 32. The parameters varied in this single-parameter sensitivity analysis are the reservoir temperature, pressure, permeability, Dystra-Parsons coefficient, oil viscosity, and oil API gravity. Because the pattern area, reservoir net pay, porosity, initial oil saturation and formation volume factor were not changed, the ROIP at the beginning of the CO_2 flood remains constant. Thus, changes in the cumulative oil produced shown in Figure 32 are directly proportional to changes in displacement efficiency.

Table 14.   Predicted ultimate net utilization and gross utilization of CO_2 and the incremental oil recovery reported in the literature for the four case study fields and eight other projects [46-48].

Field Name	Net Utilization (mscf/STB)	Gross Utilization (mscf/STB)	Incremental Oil (% OOIP)
Case Studies			
Northeast Purdy Unit	4.6	6.5	7.5
SACROC-4PA & 17PA	3.2-6.5	9.5-9.7	7.5
Ford Geraldine	5	9	17
Joffre Viking	5.4-6.9		14-18
Other Reported Values			
Dollarhide Devonian	2.4		14
East Vacuum Grayburg-San Andres	6.3	11.1	
Means San Andres		15	9.2
North Cross	7-8	18	22
Rangely Weber	4-6	9.2	7.5
Twofreds	8		15.6
Wertz		13-15	
Wasson-Denver	5.3		16.6
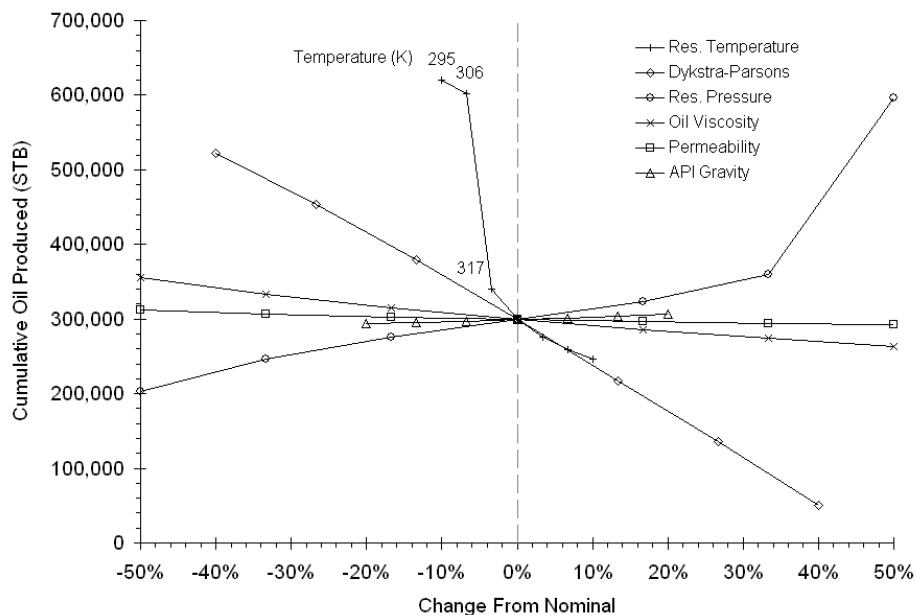
Figure 32.   Sensitivity of cumulative oil recovery at the pattern end-of-life using the SACROC Kelly-Snyder parameter values as defined in Table 12, highlighting the temperatures over which oil production changes rapidly.

The strong sensitivity of the cumulative oil production to decreases in reservoir temperature is because CO_2 density and viscosity undergo rapid changes in the vicinity of the critical temperature of CO_2 (304 K). The net CO_2 utilization also exhibits the same strong sensitivity to small changes in temperature, as shown in Figure 33; however, unlike oil recovery, net CO_2 utilization is insensitive to changes in reservoir permeability, Dykstra-Parsons coefficient, oil viscosity, and API gravity.
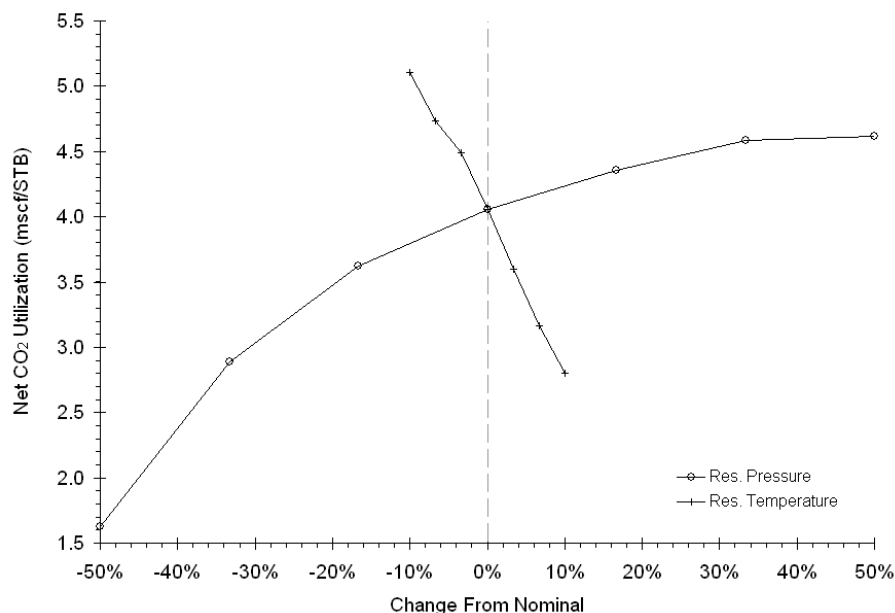
Figure 33.   Sensitivity of net CO₂ utilization at the pattern end-of-life using the SACROC Kelly-Snyder parameter values as defined in Table 12

Enhanced Oil Recovery Economics Model

The economics model developed for EOR storage of CO_2 takes a number of inputs (shown in Figure 23), along with the performance model results, to estimate the profitability of the CO_2 flood, measured by net present value (NPV) and return on investment (ROI). The model estimates NPV and ROI by performing a discounted cash flow analysis using the oil production rates and CO_2 consumption rates from the performance model.

The model estimates the annual revenues and costs from the field from both oil production and (if applicable) CO_2 storage. The revenues from oil production are subject to royalties, severance taxes, and *ad valorem* taxes specified by the user. Expenses are incurred for normal field operating and maintenance costs, as well as fluid lifting, and processing of recycled CO_2.

The capital cost of the project is estimated based on the requirements for field production equipment, field CO_2 processing equipment, new pattern injection and production equipment, drilling and completion costs for new wells, and workovers for existing wells. These capital costs are amortized over the life of the field using the project discount rate.

The following sections describe how capital, O&M, fluid lifting, and CO_2 processing costs are estimated. In addition, the relationship used to estimate the first purchase price of crude oil based on market standard oil prices (e.g., the West Texas Intermediate) is described.

Lease Equipment Capital Cost

Converting a producing lease[14] to CO_2-flooding requires a number of changes to existing equipment, as shown in Table 11. Lewin & Associates developed a regression equation to estimate the costs of lease equipment for 12 regions of the United States in 1981 [49]. The lease equipment category covers the costs of adding or modifying production equipment for CO_2 service. When updated to 2004 dollars using the EIA Oil and Gas Lease Equipment and Operating Cost index [50], cost predicted by the Lewin & Associates regressions compare well with cost estimates in more recent reports (e.g., see [51]).

---

[14] In this context, a parcel of land—including underlying mineral rights—that the operator leases for oil production, usually consisting of more than one pattern.

Region	States	a_1	a_2
1	AK	50362	3×10^{-5}
2	CA, OR, WA	50362	3×10^{-5}
2A	Pacific Coast-Offshore, ID, NV, UT	50362	3×10^{-5}
3	CO, AZ, NM-West	34774	3×10^{-5}
4	WY, MT, ND, SD	34774	3×10^{-5}
5	TX-West, NM-East	29211	4×10^{-5}
6	TX-East, AR, LA, MS, AL	29211	4×10^{-5}
6A	Gulf Cost-Offshore	29211	4×10^{-5}
7	OK, KS, NE, MO, IA, MN	29211	4×10^{-5}
8	MI, WI	29211	4×10^{-5}
9	IL, IN, KY, TN	29211	4×10^{-5}
10	OH, PA, WV, NY, VA, NC	29211	4×10^{-5}
11A	SC, GA, FL	29211	4×10^{-5}

The Lewin & Associates cost regressions take the form:

$$C = a_1 e^{a_2 d} \tag{36}$$

where C represents cost and d is depth in ft. The regression coefficients (where the a_1 parameter values have been updated to 2004 dollars) are listed by region in Table 15.

The costs for CO_2 processing equipment—also considered as lease equipment, but not included in the Lewin & Associates regression—vary widely depending on the type of processing required. The capital cost is generally lower for simple compression and dehydration equipment than for more complex facilities incorporating NGL separation. For simple compression and dehydration systems, a regression has been developed based on 12 point estimates presented in the literature [3, 10, 27, 39, 51]. The regression equation takes the form:

$$\log(C_{CPE}) = a_0 + a_1 \log(N_p q_{rcy,\max}) \tag{37}$$

where C_{CPE} is the capital cost of CO_2 processing equipment, N_p is the number of patterns, and $q_{rcy,max}$ is the pattern recycle rate (at the maximum CO_2 cut) in mmscf (million standard cubic feet) per day. If construction is staggered (e.g., 10 patterns in year zero, 12 patterns in year 1), N_p would in this case be equal to the maximum number of patterns constructed in a given year (i.e., 12).

Parameter estimates for the coefficients in the CO_2 processing equipment cost correlation are given in Table 16. The generalized regression model given in Equation 37 accounts for a large proportion of the variation in the data set as reflected by an adjusted-r^2 value of 0.72.

Table 16.   Regression coefficient estimates for the CO_2 processing equipment cost correlation, Equation 37, where standard errors are reported in parentheses.

Coefficient	Value
a_0	9.374×10^{-1} ** (1.855×10^{-1})
a_1	5.851×10^{0} ** (3.109×10^{-1})
** Significant at the 1% level	

Use of the regression coefficients presented in Table 16 in Equation 37 results in costs ranging from \$6,187,000 for compression and dehydration train handling 10 mmscf per day to \$53,570,000 for a train handling 100 mmscf per day.

Pattern Equipment Capital Cost

Pattern equipment includes both production related-equipment (e.g., rods, pumps, wellheads, etc.) and injection-related equipment (e.g., injection skids, wellheads, etc.). This category does not include the drilling and completion (i.e., installation of tubing and downhole equipment) of new injection or production wells, which is treated in Drilling and Completion Capital Cost.

The cost models for production equipment and injection equipment associated with new wells are taken from the Lewin & Associates [49], and updated to 2004 dollars using the EIA Oil and Gas Lease Equipment and Operating Cost index [50]. The form of the Lewin & Associates cost model is presented in Equation 36, and the regression coefficients are listed by region in Table 17 (where the a_1 parameter values have been updated to 2004 dollars).

Table 17.   Regression coefficients for production equipment and injection equipment from Lewin and Associates [49] updated to 2004 dollars for use in Equation 36.

Region	States	Production Equipment		Injection Equipment	
		a_1	a_2	a_1	a_2
1	AK	48328	1.1×10^{-4}	33132	9.0×10^{-5}
2	CA, OR, WA	48328	1.1×10^{-4}	33132	9.0×10^{-5}
2A	Pacific Coast-Offshore, ID, NV, UT	48328	1.1×10^{-4}	33132	9.0×10^{-5}
3	CO, AZ, NM-West	31130	1.5×10^{-4}	33132	9.0×10^{-5}
4	WY, MT, ND, SD	31130	1.5×10^{-4}	33132	9.0×10^{-5}
5	TX-West, NM-East	36049	1.5×10^{-4}	33132	9.0×10^{-5}
6	TX-East, AR, LA, MS, AL	36049	1.4×10^{-4}	33132	9.0×10^{-5}
6A	Gulf Cost-Offshore	36049	1.4×10^{-4}	33132	9.0×10^{-5}
7	OK, KS, NE, MO, IA, MN	36049	1.4×10^{-4}	33132	9.0×10^{-5}
8	MI, WI	36049	1.4×10^{-4}	33132	9.0×10^{-5}
9	IL, IN, KY, TN	36049	1.4×10^{-4}	33132	9.0×10^{-5}
10	OH, PA, WV, NY, VA, NC	36049	1.4×10^{-4}	33132	9.0×10^{-5}
11A	SC, GA, FL	36049	1.4×10^{-4}	33132	9.0×10^{-5}

For wells that are already in place and only require a well workover (i.e., tubing and downhole equipment replacement) prior to CO_2-flooding, the cost is expressed as a sum of a fraction of the production or injection equipment cost (depending on whether the well is a producer or injector) and Drilling and Completion Capital Cost (next section). The expression for workover cost is [49]:

$$C_{WO} = 0.48 C_{D\&C} + 0.50 C_{PE} \tag{38}$$

where $C_{D\&C}$ are the drilling and completion capital cost (discussed in the following section) and C_{PE} is the cost of production equipment.

Drilling and Completion Capital Cost

Drilling and completion (D&C) costs include the cost of physically drilling an injection well, running casing, hanging tubing, and installing any downhole equipment (e.g., chokes and packers). D&C costs are well documented by the annual Joint Association Survey (JAS) on Well Drilling Costs [52], which lists the average cost of wells drilled and completed each year by depth interval and state. A regression based on these costs was also developed by Lewin & Associates [49] in 1981, and has been updated to 2004 dollars using the using the EIA Oil and Gas Lease Equipment and Operating Cost

index [50]. The form of the Lewin & Associates cost model is presented in Equation 36, and the regression coefficients are listed by region in Table 18 (with the a_1 parameter values updated to 2004 dollars).

Note that recent increases oil price have spurred a large increase in drilling activity. Thus, similar to increases in lease, production, and injection equipment costs (driven by materials cost increases), D&C costs in years after 2004 can be expected to be considerably higher. The EIA Oil and Gas Lease Equipment and Operating Cost index [50] can be used to update these costs for future periods.

Table 18.   Regression coefficients for well drilling and completion from Lewin and Associates [49] updated to 2004 dollars for use in Equation 36.

Region	States	a_1	a_2
1	AK		
2	CA, OR, WA	70123	3.2×10^{-4}
2A	Pacific Coast-Offshore, ID, NV, UT	185819	3.2×10^{-4}
3	CO, AZ, NM-West	80086	2.7×10^{-4}
4	WY, MT, ND, SD	74808	2.8×10^{-4}
5	TX-West, NM-East	43986	3.4×10^{-4}
6	TX-East, AR, LA, MS, AL	44041	3.5×10^{-4}
6A	Gulf Cost-Offshore	996487	1.1×10^{-4}
7	OK, KS, NE, MO, IA, MN	42493	3.5×10^{-4}
8	MI, WI	65370	3.8×10^{-4}
9	IL, IN, KY, TN	34362	3.9×10^{-4}
10	OH, PA, WV, NY, VA, NC	23529	5.1×10^{-4}
11A	SC, GA, FL	216124	3.0×10^{-4}

Operating & Maintenance Cost Model

Operating and maintenance (O&M) costs for CO_2-flooding includes operating expenses for labor, consumables, surface equipment maintenance, and subsurface equipment maintenance, including periodic well workovers. Lewin & Associates [49] have estimated O&M costs as a function of well depth and region and these costs have been updated to 2004 dollars using the EIA Oil and Gas Lease Equipment and Operating Cost index [50]. The form of the Lewin & Associates cost model is presented in Equation 36, and the regression coefficients are listed by region in Table 19 (with the a_1 parameter values updated to 2004 dollars).

Table 19.   Regression coefficients for O&M costs from Lewin and Associates [49] updated to 2004 dollars for use in Equation 36.

Region	States	a_1	a_2
1	AK	28577	1.3×10^{-4}
2	CA, OR, WA	28577	1.3×10^{-4}
2A	Pacific Coast-Offshore, ID, NV, UT	28577	1.3×10^{-4}
3	CO, AZ, NM-West	26847	1.1×10^{-4}
4	WY, MT, ND, SD	26847	1.1×10^{-4}
5	TX-West, NM-East	26878	1.1×10^{-4}
6	TX-East, AR, LA, MS, AL	26878	1.1×10^{-4}
6A	Gulf Cost-Offshore	26878	1.1×10^{-4}

7	OK, KS, NE, MO, IA, MN	26878	1.1×10^{-4}
8	MI, WI	26878	1.1×10^{-4}
9	IL, IN, KY, TN	26878	1.1×10^{-4}
10	OH, PA, WV, NY, VA, NC	26878	1.1×10^{-4}
11A	SC, GA, FL	26878	1.1×10^{-4}

Fluid Pumping and CO_2 Processing Cost

The unit cost of lifting liquids to the surface and processing recycled CO_2 (i.e. dehydration and compression) are model parameters provided by the user. Default values are Advanced Resources International estimates, which are $0.25 per STB of fluid for lifting and 1% of the oil price [51] per mscf CO_2 for processing.

Illustrative Economics Model Capital and O&M Cost Results

Results from the economics model for the capital cost of an inverted 5-sport injection pattern are illustrated in Figure 34. This figure shows the capital cost of pattern equipment for a project in West Texas or Eastern New Mexico (i.e., model region 5) for three separate cases: no new wells required to convert a pattern to a CO_2-flood; four new producers drilled and completed to develop a flooding-pattern; and, four new producers and a new injector drilled and completed. As indicated by Equation 36, the cost is an exponential function of depth.
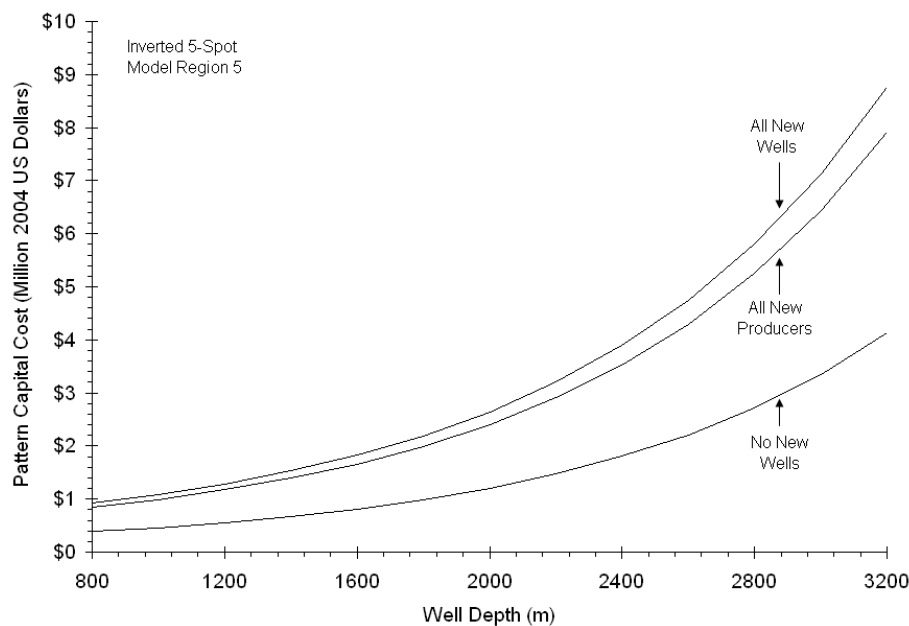
Figure 34. Cost of completing one inverted five-spot pattern in West Texas or Eastern New Mexico for three different cases.

The lease equipment cost for a field in West Texas or Eastern New Mexico (i.e., model region 5) as a function of the maximum CO_2 recycle rate and number of injection patterns is shown in Figure 35. The lease equipment cost is not highly sensitive to reservoir depth because the depth-dependent capital cost of production equipment is only a small fraction of the non-depth dependent lease equipment cost. The majority of the lease equipment cost is the cost of CO_2 processing equipment, which a function of the maximum CO_2 recycle rate.
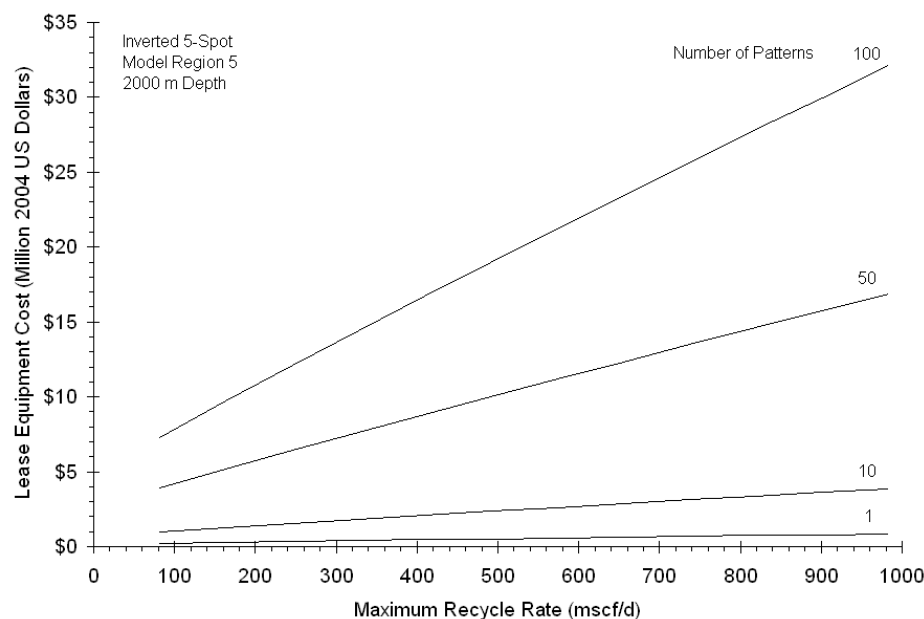
Figure 35. Lease equipment capital cost in West Texas or Eastern New Mexico as a function of CO_2 recycle rate for differing numbers of patterns.

Similar to pattern cost, O&M cost is an exponential function of depth, as shown in Figure 36 for a field in West Texas or Eastern New Mexico (i.e., model region 5).
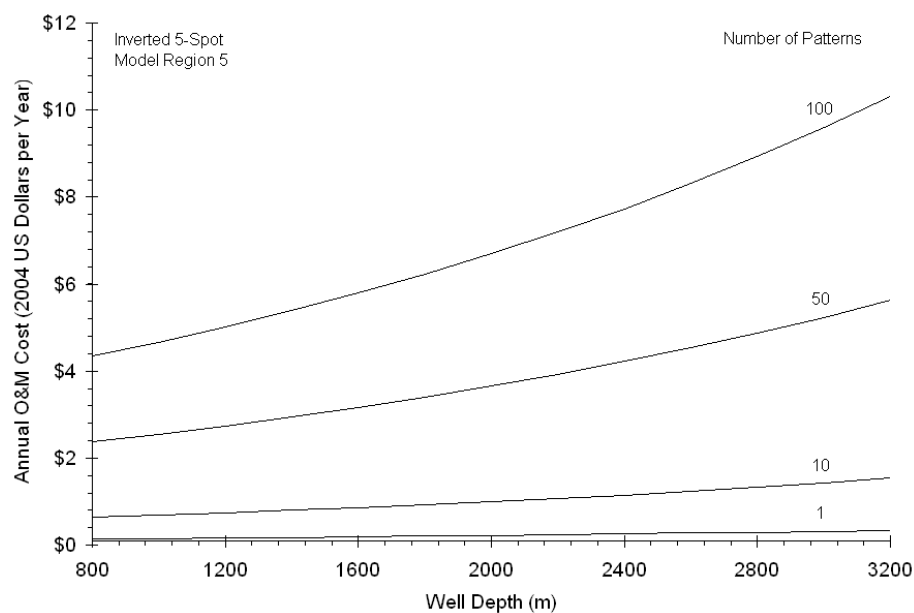
Figure 36. Field O&M cost in West Texas or Eastern New Mexico as a function of well depth for differing numbers of patterns.

The total pattern capital cost is the cost for one pattern (shown in Figure 34) multiplied by the number of patterns; thus, it scales linearly with number of patterns. The annual O&M cost also scales linearly with the number of patterns. Conversely, the lease capital cost does not scale linearly with the number of patterns because the dominant component of the lease capital cost is the CO_2 processing equipment cost (Equation 37), which is a non-linear function of the maximum CO_2 recycle rate. In addition, the maximum recycle rate for the project can be decreased by spreading pattern construction out over a number of years. Table 20 shows the breakdown of capital costs associated with the development

of a 50 pattern CO_2 flood, with a maximum recycle rate of 500 mscf per pattern and a 2000 m deep reservoir for two extreme cases: no wells initially present, and all required wells (and associated production equipment) present.

Table 20. The capital and O&M cost in 2004 US dollars for a lease with 50 injection patterns where all wells are new— corresponding to a greenfield development—and all wells are already in place—corresponding to tertiary recovery.

Cost Item	All New Wells	No New Wells
Pattern Capital Cost		
Well Drilling & Completion ($)	$47,000,000	$0
Production Well Equipment ($)	$9,000,000	$0
Injection Well Equipment ($)	$3,000,000	$0
Production Well Workovers ($)	$0	$16,000,000
Injection Well Workovers ($)	$0	$11,000,000
Producer-Injector Conversions ($)	$0	$0
Subtotal ($)	$59,000,000	$27,000,000
Lease Equipment		
Production Lease Equipment ($)	$3,000,000	$0
CO_2 Processing Equipment ($)	$8,000,000	$8,000,000
Subtotal ($)	$10,000,000	$8,000,000
Total Cost		
O&M Cost		
Annual O&M Cost ($/year)	$4,000,000	$4,000,000

Oil Purchase Price Adjustment

The price in dollars per barrel a lease owner receives for the crude oil produced from their lease, including CO_2-flooding projects, is known as the "first purchase price." This price is a function of the oil stream (i.e., the type of oil categorized by reservoir or general area) and is corrected for oil gravity, where heavier oils (i.e. those with lower API gravities) have correspondingly lower first purchase prices. Generally, gravity corrections only apply to oils below 40.0° API.

Estimating revenues from crude oil production requires a relationship between a commonly used benchmark oil price and the first purchase price. This relationship has been developed using a dataset containing the first purchase price of domestic crude oil, binned by API gravity, between January 1993 and November 2006 and a second dataset containing the West Texas Intermediate (WTI) price over the same period. West Texas Intermediate is a 39.6° API oil, with 0.24% sulfur, priced free on board at Cushing, Oklahoma. Both of these datasets were collected and published by the Energy Information Administration (EIA). The fitted correlation takes the form:

$$P_{FPP} = a_o + a_1 P_{WTI} + a_2 G_{20} + a_3 G_{25} + a_4 G_{30} + a_5 G_{35} + a_6 G_{40} \qquad (39)$$

where: P_{FPP} is the first purchase price of crude oil, P_{WTI} is the WTI price, and G_{20} through G_{40} are binary variables indicating API gravity. The binary variables take the value of one for oil with API gravities in the ranges shown in Table 21. The binary variables take the value of one for oil with API gravities in the ranges shown in Table 21, and zero otherwise. For example, for a 32.0° API oil, the variable G_{35} takes the value of one, while all the other binary variables take the value of zero.

Parameter estimates for the coefficients in the first purchase price correlation are given in Table 22. The regression model given in Equation 39 accounts for a large proportion of the variation in the data set as reflected by having an adjusted-r^2 value greater than 0.99.

Table 21.   API gravity ranges corresponding to the binary variables in Equation 39

Binary Variable	API Gravity (γ_{API}) Range
G_{20}	$\gamma_{API} \leq 20.0$
G_{25}	$20.0 < \gamma_{API} \leq 25.0$
G_{30}	$25.0 < \gamma_{API} \leq 30.0$
G_{35}	$30.0 < \gamma_{API} \leq 35.0$
G_{40}	$40.0 \leq \gamma_{API}$

Table 22.   Regression coefficient estimates for the first purchase price correlation, Equation 39, where standard errors are reported in parentheses.

Coefficient	Value
a_0	-4.754×10^{-1} ** (9.756×10^{-2})
a_1	0.954×10^{-1} ** (2.190×10^{-3})
a_2	-4.842×10^{0} ** (1.007×10^{-1})
a_3	-3.643×10^{0} ** (1.003×10^{-1})
a_4	-5.986×10^{0} ** (9.921×10^{-2})
a_5	-1.152×10^{0} ** (9.856×10^{-2})
a_6	-6.309×10^{-1} ** (9.824×10^{-2})
** Significant at the 1% level	

The results of the first purchase price correlation for a range of WTI prices and API gravity ranges is shown in Figure 37. For example, for a WTI price of 75$ per barrel, a lease owner can expect to receive $70/bbl for the 37° API oil produced from their lease, while an owner with a lease producing 66° API oil can expect to receive $65/bbl.
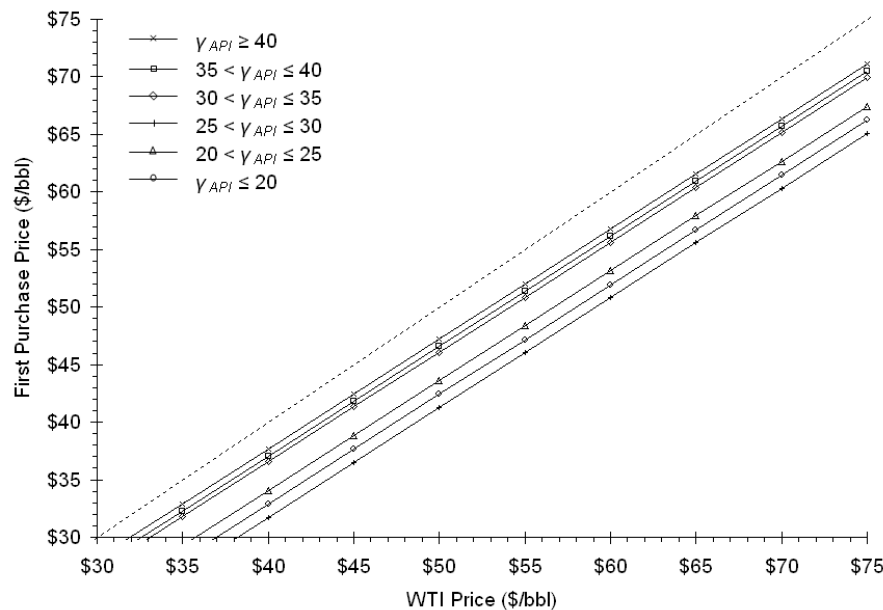
Figure 37.   The first purchase price for crude oil as a function of the WTI price and the API gravity range.

Combining Performance and Cost

As shown in Figure 23, the maximum CO_2 cut, $f_{CO2,max}$, is specified in the economics model. The performance model uses this CO_2 cut to determine the pattern life, which defines the ultimate amount of oil recovered and CO_2 stored for a pattern. The performance of a single pattern is then multiplied by the total number of patterns completed and operating (allowing for staged construction) to arrive at the overall field performance.

The annual cash flow (in real dollars) is estimated by subtracting costs from annual oil revenues, which are calculated as the annual oil production estimated by the performance model multiplied by the real first purchase price (inflated using the real cost escalation rate for the oil price specified by the user). This real cash flow is discounted using the project discount rate to arrive at the NPV and ROI for the project. The costs considered by the model are:

- royalties and taxes, the rates for both of which are user specified and subject to escalation rates;

- the annual cost of purchasing CO_2, calculated by multiplying the annual CO_2 requirement calculated by the performance model and the specified CO_2 price (subject to the real cost escalation rate for CO_2);

- the O&M cost, calculated by the methods discussed in Operating & Maintenance Cost Model, and subject to a real cost escalation rate;

- CO_2 processing cost and fluid lifting cost, calculated as discussed in Fluid Pumping and CO_2 Processing Cost, and subject to real cost escalation rates;

- M&V cost, which is a user supplied value in real dollars and subject to real escalation rates;

- Capital costs as discussed in Lease Equipment Capital Cost, Pattern Equipment Capital Cost and Drilling and Completion Capital Cost, and are subject to capital cost escalation factors that can be used to scale the capital costs predicted by the model; and,

- Debt service on capital expenditures, calculated based on the project discount rate.

Illustrative Case Studies

The performance model parameters for the four illustrative cases were given in Table 12 and were previously used to illustrate the behavior of the performance model. Economics model parameter values used in the case studies are listed in Table 23 and are the same for each case, making comparisons among the four cases simpler. The WTI oil price is varied parametrically in the estimation of the breakeven cost for CO_2. The breakeven cost for CO_2 is the CO_2 purchase price at which the project net present value (NPV) equals zero.

Table 23.   Economics model parameter values used in the four case studies

Project Parameter	Deterministic Value
WTI Oil Price ($/STB)	50.00
CO_2 Purchase Price ($/mscf)[†]	2.00
Real Discount Rate (%)	12
CO_2 Processing O&M Cost ($/mscf)[†]	0.50
Lifting O&M Cost ($/STB)	0.60
Operating Monitoring & Verification ($/y)	0
Closure Cost ($)	0
Taxes & Royalties	
Royalty Rate (%)	12.5
Severance Tax Rate (%)	5.0
Ad Valorium Tax Rate (%)	2.0
CO_2 Tax ($/tonne)	0.00
Real Escalation Rates	
Oil Price (%/year)	1
CO_2 Tax (%/year)	1
CO_2 Cost (%/year)	1
CO_2 Processing O&M Cost (%/year)	1
Lifting O&M Cost (%/year)	1
M&V Cost (%/year)	1
Lease O&M Cost (%/year)	1
Capital Cost Escalation Factors	
Drilling & Completion	1
Production Well Equipment	1
Injection Well Equipment	1
Production Lease Equipment	1
CO_2 Processing Equipment	1
Producer Breakdown	
Existing Producers	n[‡]
New Producers	0
Producer Workovers	n[‡]
Injector Breakdown	
Existing Injectors	$n + \left\lfloor \sqrt{4n-3} \right\rfloor + 2$ [*]
Producer-Injector Conversions	0
New Injectors	0
Injector Workovers	$n + \left\lfloor \sqrt{4n-3} \right\rfloor + 2$ [*]

[†] The CO_2 Price Conversion Table chapter lists price conversions from $/mscf to $/tonne
[‡] n is the number of patterns, thus there is one injector per pattern
[*] Number of production wells in a five-spot flooding network

The pattern construction schedule used for all of the cases assumes 50% of the patterns built in the year prior to the start of injection (year zero); 30% of the patterns built in the first year; and, 20% of the patterns built in the second year. Using this pattern schedule, the performance parameters in Table 12, and economics parameter values in Table 23, results in the CO_2-flood performance summarized in Table 24.

Table 24.   Results for the four illustrative cases described in Table 12

Parameter	Northeast Purdy Unit	SACROC Unit, Kelly-Snyder Field	Ford/Geraldine Unit	Joffre Viking Pool
$f_{c,max}$	0.90	0.88	0.87	0.93
Oil Produced (MMSTB)	36	402	13	23
CO_2 Stored (Mt)	5.8	83.3	2.3	3.3
Capital Cost (million 2004 US Dollars)	$231	$787	$155	$80
NPV (million 2004 US Dollars)	$175	$3,247	-$7	$162
ROI	53%	162%	7%	110%

As previously noted, the $f_{c,max}$ values shown in Table 22 maximize the NPV for each project and were isolated using parabolic interpolation and refined with bisection [53]. Increasing the value of the maximum CO_2-cut increases the project life, increasing the payback time for the project capital; however, this may also result in negative cash-flows towards the end of the project. The effect of changing the maximum CO_2 cut on NPV is shown for the Northeast Purdy and Ford Geraldine Units in Figure 38. This figure shows that values of f_c of approximately 0.90 and 0.88 maximize the NPV of the respective projects, correspond to project lifetimes of 12 years and 8 years, respectively, under the case study assumptions.
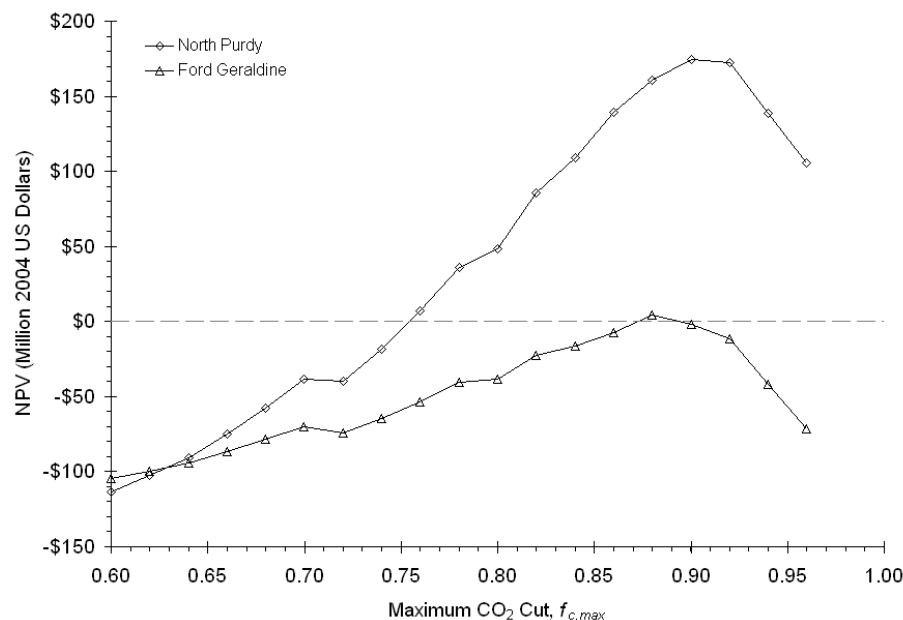
Figure 38.   NPV as a function of changing maximum CO_2 cut for the Northeast Purdy Unit and the Ford Geraldine Units

The results in Table 24 show that, from the standpoint of large-scale CO_2 sequestration, projects similar to Northeast Purdy, Ford Geraldine or Joffre Viking would be of limited value as stand-alone projects, as they store small amounts of CO_2 relative to the amount of CO_2 produced from a large point source such as a power plant over its lifetime of operation

(e.g. 500 MW coal fired plant over 30 years produces emissions of 90 Mt). Moreover, the rate at which these three projects store CO_2 is much lower than the rate that a large point source produces CO_2 (e.g. 500 MW coal fired plant produces emissions of 2-3 Mt per year), as illustrated in Figure 39. Conversely, a large field similar to the SACROC Kelly-Snyder field in Texas (developed rapidly, as in the case study) could sequester large amounts of CO_2 at rates compatible with a large point source.
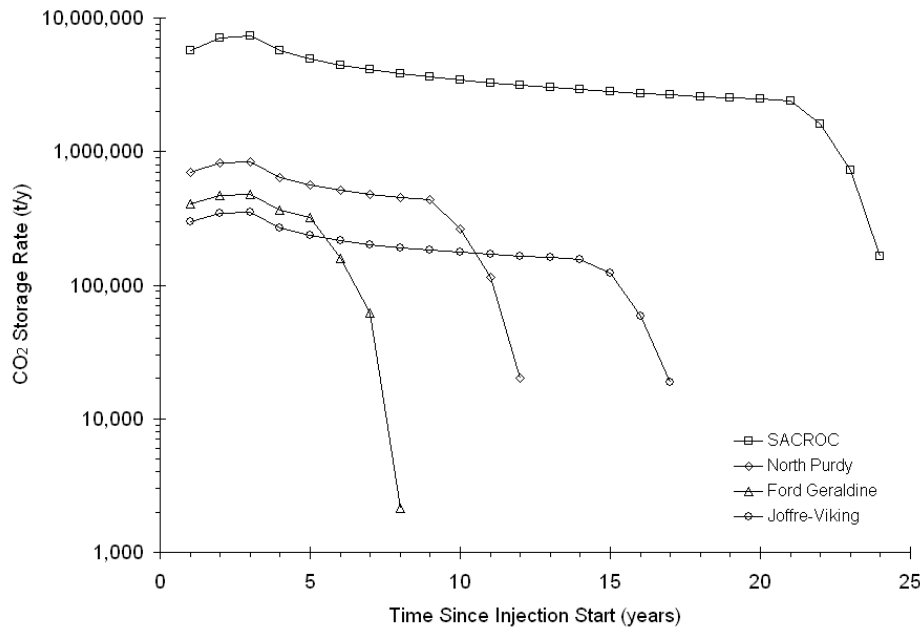
Figure 39. CO_2 storage rates for the four illustrative cases.
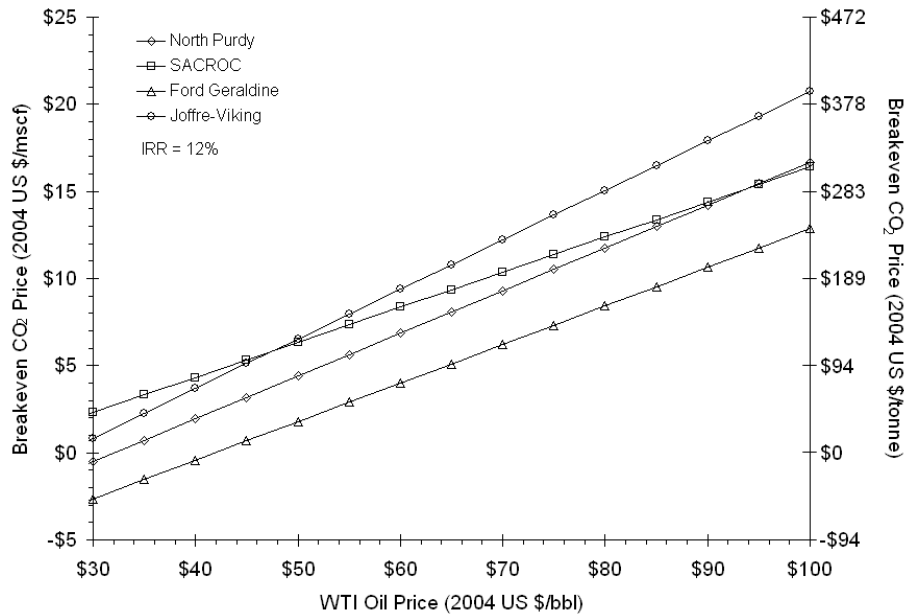
Figure 40.   The breakeven CO_2 price for the four illustrative cases.

The breakeven CO_2 price can also be calculated by the model, as shown in Figure 40. The breakeven CO_2 price can be interpreted as the highest price a CO_2-flood developer would be willing to pay for CO_2 delivered to the site, based on the assumed benchmark oil price (and numerous other factors).

As would be expected based on pattern performance, there is considerable variation between breakeven costs for each case. However, at recent oil prices (i.e., greater than \$50/bbl) all of the case study projects would be able to breakeven paying at least \$1 per mscf CO_2 (\$19 per tonne CO_2). The breakeven costs shown in Figure 40 are somewhat more pessimistic than those estimated in the literature [54] for generic sandstone and carbonate west-Texas reservoirs, but this may be the result of a number of factors: the model here uses higher capital costs compared to earlier studies; operation of the field can increase recovery (and the amount of CO_2 stored [55]) for example, by "shutting-in" patterns, drilling additional wells, and inverting injection patterns; and, improved mobility control in traditional water alternating gas (WAG) CO_2-floods results in lower CO_2 utilization rates. Both the addition of a third mobile phase to the reservoir (as occurs in WAG CO_2-floods) and the effects of operational decisions can not modeled analytically.

Model Sensitivity Analysis Results

To assess the sensitivity of the model to changes in multiple performance and economic parameters, uniform distributions were assigned to a number of parameters and the model was used to estimate the breakeven price for CO_2 over a series of Monte Carlo trials for the SACROC Kelly-Snyder case. The uniform distribution was selected to represent uncertainty or variability because there is no prior information that would suggest choosing a more complex distribution (such as a triangular or lognormal distribution). Twelve performance model parameters and seven economic model parameters were assigned distributions; both the parameters and the distributions for the parameter values are listed in Table 25.

Of all the performance parameters in the model, those in Table 25 were selected because they are parameters that are likely to vary over a large reservoir such as the Kelly-Snyder Canyon Reef. Parameters that directly affect the amount of oil in place at the beginning of the project were assumed to vary less from their deterministic values than those that vary considerably over the life of the project (e.g. reservoir pressure), or those that are largely speculative (i.e., loss fractions), because the amount of oil in place would likely be quite well known at the beginning of a tertiary CO_2-flood. All performance and economic model parameters not listed in Table 25 were treated as constants (with the values listed in Table 12 and Table 23) and the optimum NPV-maximizing CO_2 cut of 0.89 for the SACROC Kelly-Snyder deterministic case was used. For this analysis, 1,000 trials were conducted. From these trials, three cumulative distribution functions (CDF) were generated showing the breakeven CO_2 price, the net CO_2 utilization, and the cumulative mass of CO_2 stored.

Table 25.   Assumed uncertainty distributions for parameters considered in the sensitivity analysis of the SACROC Kelly-Snyder case.

Model Parameter	Uncertainty Distribution
Performance Model Parameters	
Gross CO_2 Injection Rate, q_{gross} (mscf/d)	Uniform (450, 750)[a]
Reservoir Pressure, p_{res} (MPa)	Uniform (14, 23.3)[a]
Reservoir Temperature, T_{res} (K)	Uniform (320, 335)[b]
Net Pay, h (m)	Uniform (74, 90)[b]
Horizontal Permeability, k_h (md)	Uniform (17, 21)[b]
Permeability Anisotropy, k_v/k_h	Uniform (0.3, 0.5)[a]
Porosity, ϕ (%)	Uniform (3.5, 4.3)[b]
Dykstra-Parsons Coefficient, V_{DP}	Uniform (0.61, 0.75)[b]
Initial Oil Saturation, S_{orw} (%)	Uniform (38, 46)[b]
Oil Viscosity, μ_o (cp)	Uniform (0.32, 0.39)[b]
Reservoir Loss Fraction, η (%)	Uniform (0, 10)[c]
Surface Processing Loss Fraction, τ (%)	Uniform (0, 4)[c]
Economics Model Parameters	
CO_2 Processing O&M Cost (\$/mscf)	Uniform (0.40, 0.60)[e]
Real Discount Rate (%)	Uniform (10, 15)

Lifting O&M Cost ($/STB)	Uniform (0.50, 0.70)
Oil Price Real Escalation Rate (%/year)	Uniform (-1, 2)[e]
Capital Cost Escalation Factors	
Production Well Equipment	Uniform (0.75, 1.00)
Injection Well Equipment	Uniform (0.75, 1.00)
Production Lease Equipment	Uniform (0.75, 1.00)
CO_2 Processing Equipment	Uniform (0.75, 1.00)

[a] Distribution bounds 25% above and below deterministic value (see Table 12)

[b] Distribution bounds 10% above and below deterministic value (see Table 12)

[c] Distribution bounds 100% above and below deterministic value (see Table 12)

[d] Distribution bounds 20% above and below deterministic value (see Table 23)

[e] Starting with an oil price of $50/bbl in 2006, real escalation rates between -1% and 2% per year result in 2004 constant dollar oil prices between $40/bbl and $80/bbl in 2030. For reference, the most recent EIA Annual Energy Outlook projects oil prices of approximately $30/bbl (low price case) and $90/bbl (high price case) in 2030 (2004 constant dollars) [56].

Figure 41 shows the CDF for the breakeven CO_2 price based on an oil price of $50/bbl with the uncertain real price escalation rate given in Table 25. The median breakeven price of CO_2 from the sensitivity analysis is $6.39 per mscf CO_2 ($121 per tonne CO_2), with a 90% confidence interval of $4.78 to $8.60 per mscf CO_2 ($90 to $163 per tonne CO_2, respectively).
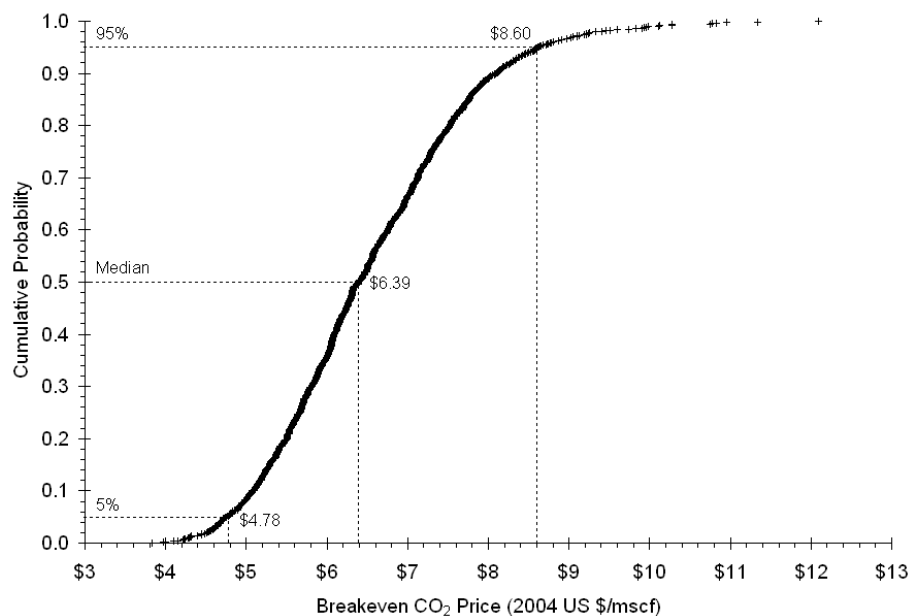
Figure 41.   CDF for the breakeven CO_2 price for the SACROC Kelly-Snyder case

Results of the Monte Carlo trials can also be used to assess the sensitivity of breakeven cost to the model parameters having uniform distributions. The measure used to assess the sensitivity is the Spearman rank-order correlation (r_s) [57]. The value of the rank order correlation coefficient between the breakeven CO_2 price and the model parameters assigned distributions is shown in Figure 43. The dashed vertical lines to the left and the right of the axis in Figure 43 indicate the 5% significance level (rs = ±0.07); thus rank-order correlation coefficients smaller than this value are not statistically significant at the 5% level. Figure 43 shows the strongest correlation is between the oil price escalation rate (r_s = 0.57)— a proxy for oil price—and breakeven CO_2 price, followed by reservoir loss fraction (r_s = -0.53) and reservoir pressure (r_s = -0.41). Following these, significant rank-order correlation coefficients (by decreasing magnitude) are the: reservoir temperature, Dykstra-Parsons coefficient (representing permeability heterogeneity), surface loss rate, gross injection rate, initial oil saturation, porosity, CO_2 processing O&M cost, and escalation in drilling and completion cost.
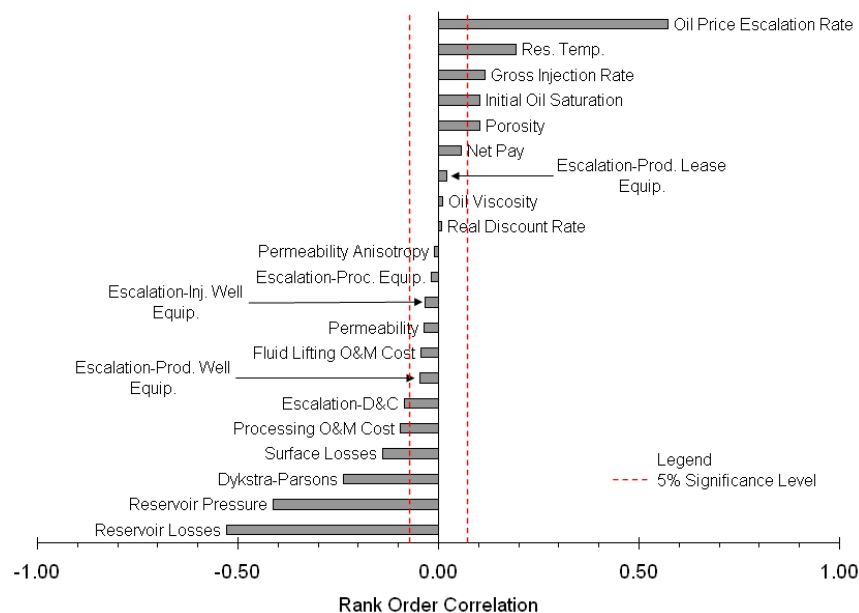
Figure 42.   Rank-order correlation between the results of the Monte Carlo sensitivity analysis and the parameters assigned uniform distributions.

These results show that the breakeven CO_2 price is highly sensitive to a number of factors. In practice, however, the uncertainty around these parameters should be relatively small. While factors such as reservoir pressure, temperature, and initial oil saturation (i.e., residual to waterflooding) may vary from area to area within the field, they will be well characterized by the time tertiary CO_2 flooding is being planned. Moreover, reservoir pressure and reservoir loss rates can be controlled to some extent. In contrast, the uncertainty associated surrounding future oil prices over the operating life of the field is far and away the most difficult parameter to estimate. In this analysis the real oil price at the start of the CO_2-flood has been assumed to be well known compared to the nominal oil price in some future year of operation; thus, the real oil price escalation rate has been assigned uncertainty.

The CDF for net CO_2 utilization for the SACROC Kelly-Snyder case is shown in Figure 43. The median value is 4 mscf CO_2 per STB (0.21 tonnes CO_2 per STB), with a 90% confidence interval between 3 and 5 mscf CO_2 per STB (0.16 and 0.26 tonnes CO_2 per STB). The CO_2 utilization is most sensitive to the reservoir loss rate ($r_s = 0.77$), reservoir pressure ($r_s = 0.54$), reservoir temperature ($r_s = -0.27$), and the surface loss rate ($r_s = 0.21$). The net CO_2 utilization is strictly a function of the performance model and is unaffected by factors such as oil price (at a constant maximum CO_2 cut).
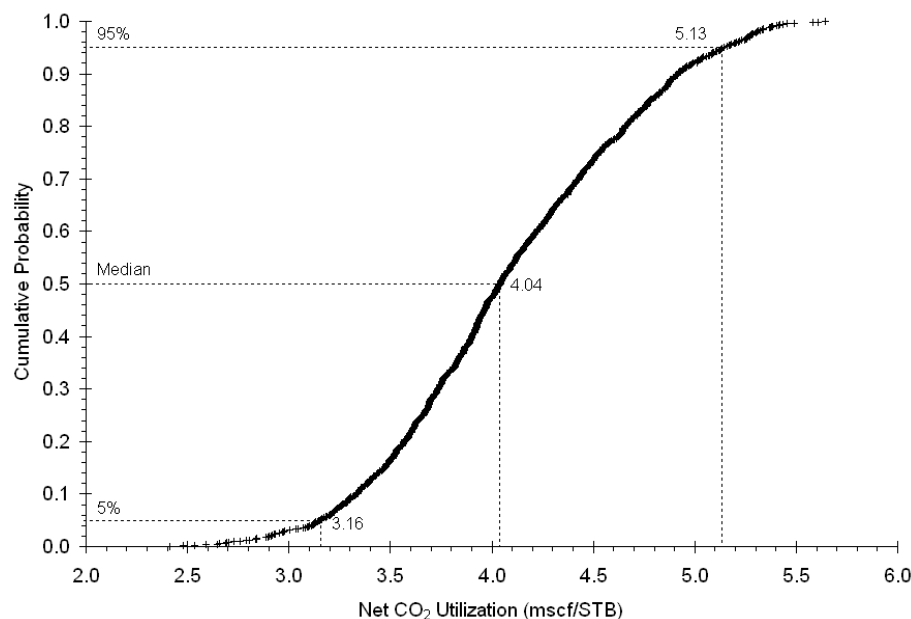
Figure 43. CDF for net CO$_2$ utilization

The CDF for the net CO$_2$ stored (i.e. the net mass CO$_2$ injected minus losses to the atmosphere) resulting from the sensitivity analysis is shown in Figure 44. The median amount of CO$_2$ stored is 81 Mt of CO$_2$, with a 90% confidence interval between 54 and 126 Mt of CO$_2$ stored. For a fixed maximum CO$_2$ cut, the amount of CO$_2$ stored is most sensitive to reservoir pressure (r_s = 0.57), reservoir loss rate (r_s = 0.45), Dykstra-Parsons coefficient (r_s = -0.39), reservoir temperature (r_s = -0.32), and reservoir porosity (r_s = 0.21).
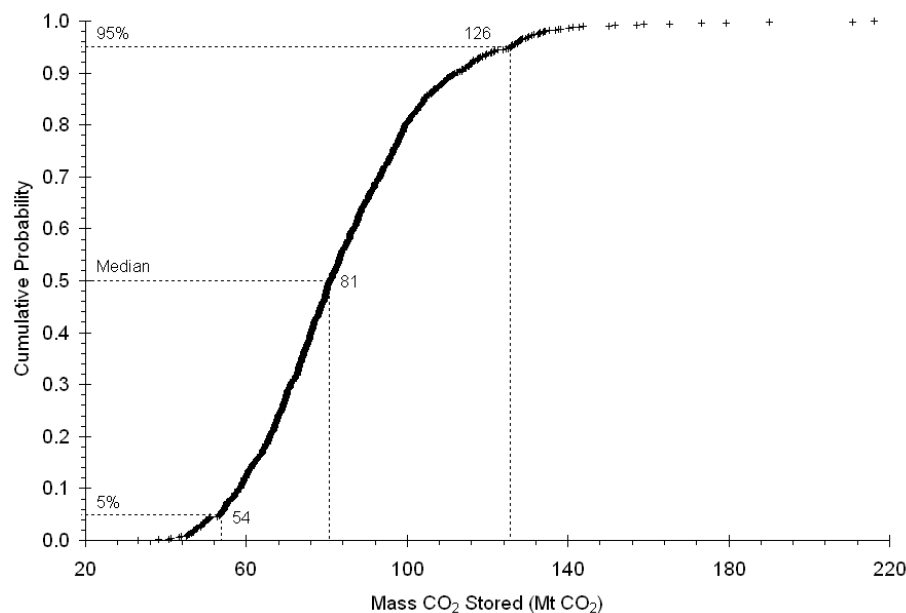
Figure 44. CDF for the net mass of CO$_2$ stored at the field end-of-life

The rank-order correlation results show (for this case) that the reservoir pressure, reservoir temperature and the reservoir loss rate are consistently have a strong impact on the breakeven CO$_2$ price, the net CO$_2$ utilization, and the amount of CO$_2$ stored. In addition, the results appear to be more sensitive to permeability variations than absolute permeability. Both the breakeven CO$_2$ price and the amount of CO$_2$ stored are also impacted by CO$_2$ losses from surface processing. Unlike the reservoir parameters, which are to a large extent unchangeable for a given reservoir, losses from surface

processing equipment could be minimized though design decisions and maintenance. However, because CO_2 has traditionally been a commodity in EOR, it would stand to reason that losses to the atmosphere are currently monitored. Unfortunately this data is not reported in the literature.

Comparison with Other Models

It is difficult to quantitatively compare the model developed here with other EOR screening models discussed earlier such as the DOE sponsored CO_2-PM [36] or CO_2-Prophet [7] models for a number of reasons. While both of these models are designed to be "screening" models, they take different approaches, require different sets of input parameters, have been presented in the literature using different cases, and are meant for different groups of users (i.e. reservoir engineers versus strategic planners) than the model developed here.

The CO_2-PM model is based on the same correlations for vertical and aerial sweep efficiency as used here; however the CO_2-PM displacement efficiency calculations account for three flowing phases (oil, water, and CO_2) and thus requires input characterizing the relative permeability curves for each of the flowing phases which at a screening level would likely be unavailable to the user. The CO_2-Prophet model is a stream tube model, allowing the model to account for irregular injection patterns and varying production rates from each well in the pattern but does not perform any economic analysis. Like CO_2-PM, CO_2-Prophet requires inputs for the relative permeability curves for each of the flowing phases (i.e., for CO_2-Prophet, this is a set of 14 parameters [7]) that would likely be unavailable to the user.

Despite the differences in the level of detail (e.g., the model presented here doesn't treat water as a mobile phase), the relative shape of the oil recovery curves generated by the model presented here and the CO_2-PM and CO_2-Prophet models are similar. Moreover, they reach similar endpoint recoveries at roughly similar pore volumes (see Paul et al. [36] for CO_2-PM example results and Dobitz and Preiditis [7] for CO_2-Prophet example results).

Kinder Morgan (KM) has also developed a public CO_2-flood scoping model based on typical WAG CO_2-flooding performance from the San Andres formation in the Permian Basin (see [39]). The core of the KM model is a set of dimensionless curves that are scaled based on user inputs to provide results for a specific case. As illustrated by the sensitivity analysis shown earlier, and acknowledged by KM[15], this approach does not consider a number of important factors that are reservoir specific. Nonetheless, the KM dimensionless curves are compared to results for both dimensionless oil production and CO_2 production generated by the model presented here in Figure 45 and Figure 46.

Figure 45 shows that compared to the KM-WAG curve, the model developed here reaches similar oil recoveries at similar volumes of CO_2 injected for the Joffre-Viking and Ford Geraldine cases. The smaller area under the KM-WAG curve than the illustrative case curves in Figure 46 implies that the KM-WAG model recycles less CO_2 of the life of the project compared to the model developed here. Thus, the KM-WAG model would predict lower gross CO_2 utilizations, which translates into lower operating costs over the life of the field. However, as both figures show, the KM-WAG curves end at 0.75 HCPV of CO_2 injected while two of the illustrative cases inject almost twice as much.

---

[15] The KM model is provided with the disclaimer that "the data and processes contained hereon are intended to provide example results for data only and should not be relied on for any specific case or application. Results may vary depending on numerous variables."
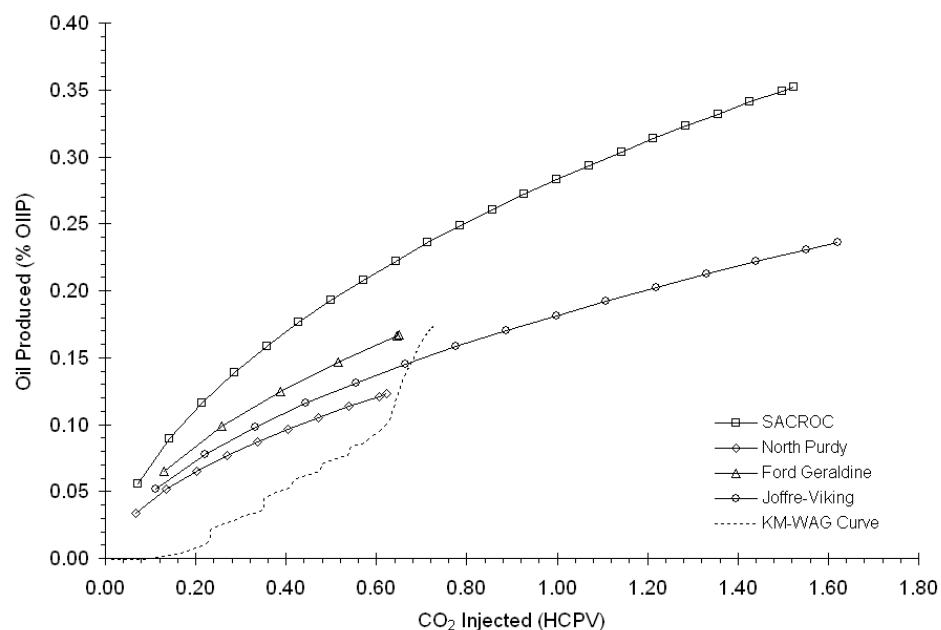
Figure 45. A comparison of dimensionless results for oil production obtained from the four cases presented here and the KM-WAG curve.
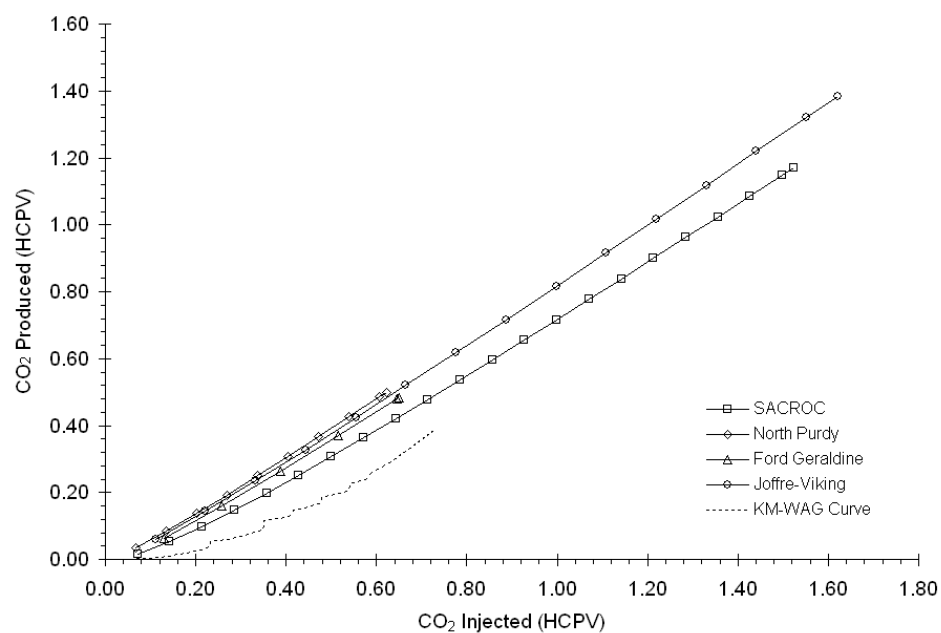
Figure 46. A comparison of dimensionless results for CO_2 production obtained from the four cases presented here and the KM-WAG curve.

References

1.   Moritis, G., *CO_2 injection gains momentum.* Oil & Gas Journal, 2006. **104**(15): p. 37-41.
2.   Gerritsen, M.G. and L.J. Durlofsky, *Modeling fluid flow in oil reservoirs.* Annual Review of Fluid Mechanics, 2005. **37**: p. 211-238.

3.   Bock, B., et al., *Economic Evaluation of CO_2 Storage and Sink Enhancement Options*. 2003, TVA Public Power Institute: Muscle Shoals, AL.

4.   Amyx, J.W. and D.M. Bass, *Estimating Secondary Reserves*, in *Petroleum Economics and Valuation Symposium*. 1962, Society of Petroleum Engineers: Dallas, TX.

5.   Claridge, E.L., *Prediction of Recovery in Unstable Miscible Flooding*. SPE Journal, 1972. **12**(2): p. 143-155.

6.   Koval, E.J., *A Method for Predicting the Performance of Unstable Miscible Displacement in Hetrogeneous Media*. SPE Journal, 1963. **3**(6): p. 145-154.

7.   Dobitz, J.K. and J. Prieditis, *A Stream Tube Model for the PC*, in *SPE/DOE Ninth Symposium on Improved Oil Recovery*. 1994, Society of Petroleum Engineers: Tulsa, OK.

8.   Moritis, G., *EOR oil production up slightly*. Oil & Gas Journal, 1998. **96**(16): p. 49-50.

9.   Office of Technical Assessment, *Enhanced Oil Recovery Potential in the United States*. 1978, Office of Technical Assessment: Washington, DC. p. 238.

10.   National Petroleum Council, *Enhanced Oil Recovery*. 1984.

11.   Interstate Oil and Gas Compact Commission, *An Evaluation of Known Remaining Oil Resources in the United States: Project on Advanced Oil Recovery and the States*. 1993, Interstate Oil & Gas Compact Comission: Oklahoma City, OK.

12.   Holtz, M.H., P.K. Nance, and R.J. Finley, *Reduction of Greenhouse Gas Emissions through CO_2 EOR in Texas*. Environmental Geosciences, 2000. **8**(3): p. 187-199.

13.   Bachu, S. and W.D. Gunter. *Overview of Acid-Gas Injection Operations in Western Canada*. in *7th International Conference on Greenhouse Gas Control Technologies*. 2004. Vancouver, Canada: Elsevier Science.

14.   Bachu, S. and K. Haug, *In-Situ Characteristics of Acid-Gas Injection Operations in the Alberta Basin, Western Canada: Demonstration of CO_2 Geological Storage*, in *The CO_2 Capture and Storage Project (CCP) for Carbon Dioxide Storage in Deep Geologic Formations for Climate Change Mitigation*, S. Benson, Editor. 2004, Elsevier Science.

15.   Kovscek, A.R. and Y. Wang, *Geologic storage of carbon dioxide and enhanced oil recovery. I. Uncertainty quantification employing a streamline based proxy for reservoir flow simulation*. Energy Conversion & Management, 2005. **46**: p. 1920-1940.

16.   Kovscek, A.R. and M.D. Cakici, *Geologic storage of carbon dioxide and enhanced oil recovery. II. Cooptmization of storage and recovery*. Energy Conversion & Management, 2005. **46**: p. 1941-1956.

17.   Craft, B. and M. Hawkins, *Applied Petroleum Reservoir Engineering*. 1st ed. Prentice-Hall Chemical Engineering Series. 1959, Englewood Cliffs, NJ: Prentice-Hall. 437.

18.   Brigham, W., *Doublets and Other Allied Well Patterns*. 2000, Stanford University Petroleum Research Institute: Stanford, CA.

19.   Roper Jr., M.K., K. Sepehrnoori, and G.A. Pope, *Analysis of Teritary Injectivity of Carbon Dioxide*, in *SPE Permian Basin Oil and Gas Recovery Conference*. 1992, Society of Petroleum Engineers: Midland, TX.

20.   Pizarro, J.O.S. and L.W. Lake, *Understanding Injectivity in Heterogeneous Reservoirs*, in *SPE/DOE Improved Oil Recovery Symposium*. 1998, Society of Petroleum Engineers: Tulsa, OK.

21.   Muscat, M., *Flow of Homogeneous Fluids*. 1st ed. 1937, New York: McGraw-Hill. 763.

22.   Bachu, S., *Sequestration of CO_2 in geological media in response to climate change: road map for site selection using the transform of the geological space into the CO_2 phase space*. Energy Conversion & Management, 2002. **43**: p. 87-102.

23.   Hendriks, C.F., *Carbon dioxide removal from coal fired power plants*. 1 ed. 1994: Kluwer Academic Publishers.

24.   Heller, J.P. and J.J. Taber, *Influence of Reservoir Depth on Enhanced Oil Recovery by CO_2 Flooding*, in *Permian Basin Oil & Gas Recovery Conference of the Society of Petroleum Engineers*. 1986, Society of Petroleum Engineers: Midland. TX.

25.   Tek, R.M. and D.L. Katz, *Temperature and Pressure Gradients in Gas Wells*, in *53rd Annual Fall Technical Conference and Exhibition of the Society of Petroleum Engineers of AIME*. 1978, Society of Petroleum Engineers: Houston, TX.

26.   Ramey, H.J., *Wellbore Heat Transmission*. Journal of Petroleum Technology, 1962(April): p. 427-435.

27.   Klins, M.A., *Carbon Dioxide Flooding-Basic Mechanisms and Project Design*. 1984, Boston: International Human Resources Development Corporation. 267.

28.   Green, D.W. and G.P. Willhite, *Enhanced Oil Recovery*. SPE Textbook Series. 1998, Richardson, TX: Society of Petroleum Engineers. 545.

29. Holm, L.W. and V.A. Josendal, *Mechanisms of Oil Displacement by Carbon Dioxide*. Journal of Petroleum Technology, 1974(December): p. 1427-1438.

30. Stalkup Jr., F.I., *Miscible Displacement*. 1983, Dallas: Society of Petroleum Engineers. 204.

31. Orr, F.M., B. Dindoruk, and R.T. Johns, *Theory of Multicomponent Gas/Oil Displacements*. Industrial & Engineering Chemistry Research, 1995. **34**: p. 2661-2669.

32. Habermann, B., *The Efficiency of Miscible Displacement as a Function of Mobility Ratio*. Transactions of AIME, 1960. **219**: p. 264-272.

33. Jessen, K., et al., *Fast, approximate solutions for 1D multicomponent gas-injection problems*. SPE Journal, 2001. **6**(4): p. 442-451.

34. Juanes, R. and M.J. Blunt, *Analytical solutions to multiphase first-contact miscible models with viscous fingering*. Transport in Porous Media, 2006. **64**(3): p. 339-373.

35. Shaw, J. and S. Bachu, *Screening, evaluation, and ranking of oil reservoirs suitable for CO_2-flood EOR and carbon dioxide sequestration*. Journal of Canadian Petroleum Technology, 2002. **41**(9): p. 51-61.

36. Paul, G.W., L.W. Lake, and T.L. Gould, *A Simplified Predictive Model for CO2 Miscible Flooding*, in *59th Annual Technical Conference and Exhibition of the Society of Petroleum Engineers*. 1984, Society of Petroleum Engineers: Houston, TX.

37. Lake, L.W., *Enhanced Oil Recovery*. 1996, Upper Saddle River, NJ: Prentice Hall.

38. Dake, L.P., *Fundamentals of reservoir engineering*. 1 ed. 1978: Elsevier.

39. Jarrell, P.M., et al., *Practical Aspects of CO_2 Flooding*. SPE Monograph Series. 2002, Richardson, TX: Society of Petroleum Engineers. 220.

40. Ormiston, R.M. and M.C. Luce, *Surface Processing of Carbon Dioxide*. Journal of Petroleum Technology, 1986(August): p. 823-828.

41. Simlote, V.N. and E.M. Withjack, *Estimation of Tertiary Recovery by CO_2 Injection--Springer A Sand, Northeast Purdy Unit*. Journal of Petroleum Technology, 1981(May): p. 808-818.

42. Dicharry, R.M., T.L. Perryman, and J.D. Ronquille, *Evaluation and Design of a CO_2 Miscible Flood Project-SACROC Unit, Kelly-Snyder Field*. Journal of Petroleum Technology, 1973(November): p. 1309-1318.

43. Langston, M.V., S.F. Hoadley, and D.N. Young, *Definitive CO_2 Flooding Response in the SACROC Unit*, in *SPE/DOE Enhanced Oil Recovery Symposium*. 1988, Society of Petroleum Engineers: Tulsa, OK.

44. Kane, A.V., *Performance Review of a Large-Scale CO_2-WAG Enhanced Recovery Project, SACROC Unit--Kelly-Snyder Field*. Journal of Petroleum Technology, 1979(February): p. 217-231.

45. Phillips, L.A., J.L. McPherson, and R.J. Leibrecht, *CO_2 Flood: Design and Initial Operations, Ford Geraldine (Delaware Sand) Unit*, in *58th Annual Technical Conference and Exhibition*. 1983, Society of Petroleum Engineers: San Francisco, CA.

46. Stephenson, D.J., A.G. Graham, and R.W. Luhning, *Mobility Control Experience in the Joffre Viking Miscible CO_2 Flood*. SPE Reservoir Engineering, 1993(August): p. 183-188.

47. EPRI, *Enhanced Oil Recovery Scoping Study*. 1999, Electric Power Research Institute: Palo Alto, CA. p. 148.

48. Brock, W.R. and L.A. Bryan, *Summary Results of CO_2 EOR Field Tests, 1972-1987*, in *SPE Joint Rocy Mountain Regional\Low Permeability Reservoirs Symposium and Exhibition*. 1989, Society of Petroleum Engineers: Denver, CO.

49. Lewin & Associates Inc., *Economics of Enhanced Oil Recovery*. 1981, Department of Energy: Washington, DC. p. 123.

50. Energy Information Administration. *Oil and Gas Lease Equipment and Operating Costs 1988 Through 2006*. 18 June 2007 [cited 26 September 2007]; Available from: http://www.eia.doe.gov/pub/oil_gas/natural_gas/data_publications/cost_indices_equipment_production/current/coststudy.html.

51. Advanced Resources International, *Basin Oriented Strategies for CO_2 Enhanced Oil Recovery: Permian Basin*. 2006, US Department of Energy: Arlington, VA. p. 117.

52. American Petroleum Institute, *Joint Association Survey on Drilling Costs*. 2002, American Petroleum Institute: Washington, DC. p. 111.

53. Press, W.H., *Numerical recipes in C : the art of scientific computing*. 2nd ed. 1992, Cambridge; New York: Cambridge University Press. xxvi, 994 p.

54. Wolsky, A.M. and D.J. Jankowski, *The Value of CO_2: Framework and Results*. Journal of Petroleum Technology, 1986(September): p. 987-994.

55. Jessen, K., A.R. Kovscek, and F.M. Orr, *Increasing CO_2 Storage in Oil Recovery*. Energy Conversion & Management, 2005. **46**: p. 293-311.

56. Energy Information Administration, *Annual Energy Outlook 2007*. 2007, US Department of Energy: Washington, D.C. p. 229.

57. Morgan, M.G., M. Henrion, and M. Small, *Uncertainty : a guide to dealing with uncertainty in quantitative risk and policy analysis*. 1990, Cambridge: Cambridge University Press. 332.

Saline Aquifers

A saline aquifer is a geologic formation with sufficient porosity and permeability to transmit significant quantities of water with a dissolved solids content that makes the water unfit for consumption, agricultural, or industrial uses, and is referred to as "brine" or "formation water". Moreover, this formation should be of sufficient depth to ensure that injected CO_2 remains in the supercritical phase [1]. As of late 2007, there are three planned or operating projects injecting CO_2 into saline aquifers and one other project injecting CO_2 into the water leg of a hydrocarbon reservoir for the purpose of CO_2 storage (see Table 1.3).

While there are many analogues to CO_2 storage, such as acid gas injection [2, 3], natural gas storage [4, 5], disposal of treated wastewater [5, 6], and disposal of hazardous waste [5], there are still many gaps in our understanding of CO_2 storage processes, including the cost of storage [7]. The objective of this chapter is to present the development of a model that will allow the cost of CO_2 storage to be estimated given the specifics of a storage site.

A limited number of studies have examined the cost of aquifer storage [8-10]. None of these studies have developed a comprehensive model that estimates performance of a storage project from wellhead to subsurface and bases cost on the project performance. The earliest study by Hendriks [8] estimated costs based on petroleum engineering rules-of-thumb for a hypothetical aquifer and performed single parameter sensitivity analysis on the depth. Bock et al. [9] performed a cost analysis on three hypothetical cases using a correlation for single-well injectivity developed by Law [11] and costs based on data from secondary oil production. The work by Bock et al. also contained a sensitivity analysis on four parameters [9]. Studies have also been performed for the IEA Greenhouse Gas Programme (e.g., see [12]) that have applied relatively crude rules-of-thumb to estimate costs for a large number of aquifers.

In this chapter, an analytical model is developed to estimate the cost of geological storage of CO_2 in aquifers for a range of geological settings and CO_2 injection rates. The cost estimates for CO_2 storage are embodied in an engineering-economic that is used to assess the sensitivity of storage cost to changes in geological settings and other assumptions. This analysis will also show the potential range of costs that could occur and the probability associated with these costs for a given scenario.

The Aquifer Storage Process

The aquifer storage process, the steps of which are shown in Figure 47, is considerably simpler than the EOR process modeled in the Enhanced Oil Recovery (EOR) chapter. In the aquifer storage process, CO_2 is received at the storage site and compressed if the pressure is not high enough for injection. Following recompression (if necessary), CO_2 is distributed to the injection wells which transport it to the target formation.
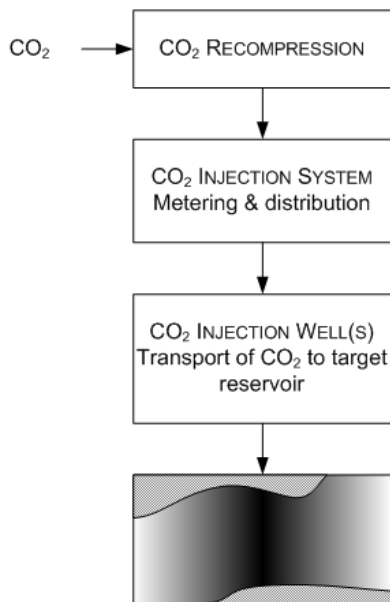
Figure 47.   Material flows and process steps in aquifer storage of CO_2

In the aquifer injected CO_2 will spread radially away from the wellbore under the imposed pressure gradient. The rate at which CO_2 moves away from the wellbore is given by Darcy's law [13, 14], in which the fluid flux is proportional to the permeability of the formation to CO_2, k. On a larger scale (both spatially and temporally), to avoid the release of CO_2 to the atmosphere, the injected fluid must be trapped in the formation. Trapping mechanisms can be either physical, where CO_2 remains as a separate phase, or chemical, in which CO_2 dissolves into the formation water and may react with minerals present in the formation to become immobilized—processes typically occurring on a scale of decades to centuries [7, 15]. Thus, in the short term, the rate at which CO_2 can be injected as well as the storage site capacity are functions of the imposed pressure gradient and aquifer permeability. Conversely, the security of CO_2 storage with respect to leakage and the long term capacity of the aquifer are functions of fluid trapping mechanisms.
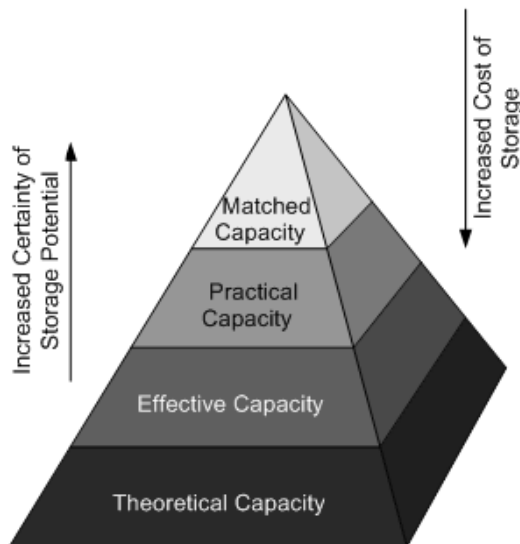
Figure 48.   The resource-reserve pyramid for geological storage of CO_2 developed by the CSLF [15].

The aquifer storage model developed here can be applied to any aquifer; however, the capacity of that aquifer to accept CO_2 may be less than implied by the model should the aquifer not meet certain technical constraints, such as caprock integrity or continuity. Figure 48 shows the reserve-resource pyramid developed by the Carbon Sequestration Leadership

Forum (CSLF) [15], where the available storage capacity decreases as constraints are applied to the physical storage capacity of the geological system (i.e. theoretical capacity). Following this nomenclature, the model developed here is a tool that can be used to estimate the practical, or economic, capacity of a system [15].

Aquifer Storage Performance Model

The model of the aquifer storage process presented here can be separated into two parts: a performance model, and a cost model. As shown in Figure 49, the performance model takes inputs that describe reservoir and brine properties, the development of the storage field, and the time horizon of interest. From these inputs the model estimates the number of wells required to achieve the desired injection over the planning horizon, the required wellhead pressure to achieve this rate, and the additional compression energy required (if any) to meet this wellhead pressure.
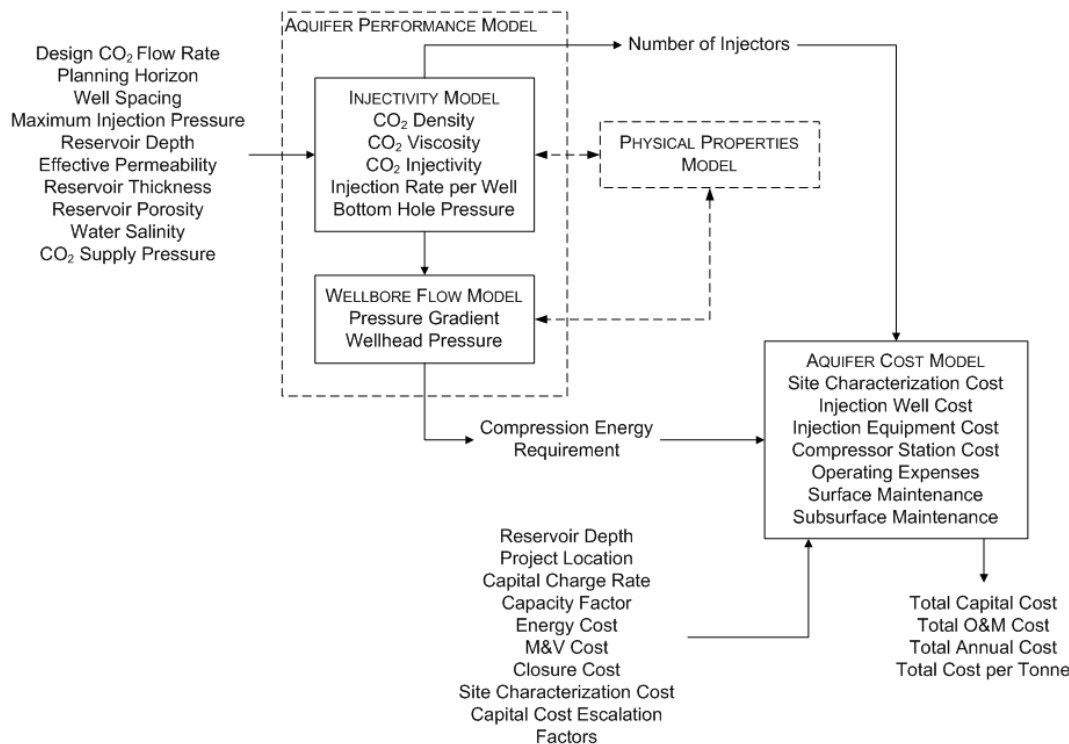
Figure 49. Schematic of the Aquifer storage engineering-economic model parameters.

In the first four sections (see Approximate Solution to Injectivity of a Doublet System through Injectivity and Sensitivity to Boundary Conditions) the approximate solution to injectivity for a doublet system is developed, extended to a multi-well system, and sensitivity of the multi-well system to boundary conditions is examined. This analysis is followed by development of a wellbore flow model for CO_2 (see Establishing the BHIP – Flow in the Wellbore), treatment of reservoir heterogeneity (see Describing Reservoir Heterogeneity), generation of a generic multi-well geometry (see Generating the System Geometry for Multi-Well Scenarios), and concludes with illustrative results (see Illustrative Performance Model Results).

Approximate Solution to Injectivity of a Doublet System

Injection of millions of tonnes per year of CO_2 into an aquifer will require multiple injection wells in many cases. For example, the developers of the Australian Gorgon project (which is summarized in Table 1.3) estimate that seven injection wells will be required to handle a cumulative injection rate of more than 3 million metric tonnes (Mt) per year CO_2 [16]. A scenario with multiple injection wells (i.e. injectors) is more complex than a similar scenario with only one injector because the pressure field generated by any well will interact with the pressure field of every other injector.

Thus, the interactions between multiple injection wells injecting CO_2 into the same confined aquifer must be considered when estimating the injectivity of the injection well system. Injectivity, I, is the injection rate of fluid normalized to the difference between the bottom-hole injection pressure (BHIP) and a reference pressure—usually the initial aquifer pressure. The behavior of a multi-well system can be derived from the behavior of a two-well system, referred to as a doublet [17].

For a single injection well, the governing equation is given as Equation 40, written in terms of radial coordinates and pressure (as opposed to fluid head) [14]:

$$\frac{\partial^2 p}{\partial r^2} + \frac{1}{r}\frac{\partial p}{\partial r} = \frac{c\mu}{k_{h,eff}\, b}\frac{\partial p}{\partial t} \tag{40}$$

where, p refers to pressure (Pa), r refers to radial distance from the injection well (m), c is compressibility of the rock-fluid system $(1/Pa)$[16], μ is viscosity (Pa·s), $k_{h,eff}$ is effective permeability in the horizontal direction (m^2), b is thickness of the aquifer (m), and t is time (s).

For a confined homogeneous aquifer—an aquifer confined between two aquitards (i.e., formations that do not permit flow of water) with spatially invariant permeability—Equation 40 was solved by Thies (see, for example [14]) to give:

$$p(X,t) - p_i = \frac{q\mu}{4\pi k_{h,eff}\, b} W(u) \tag{41}$$

where $W(u)$ is the well function evaluated at u for a confined aquifer and $p(X, t)$ is the pressure at time t, and point $X(x,y)$. The well function is the exponential integral, and is tabulated in many textbooks (e.g., [14], [13]) or can be calculated from the evaluation of a power series expansion [18]. The variable u is defined in Equation 42, where r refers to the distance between X and the injector:

$$u = \frac{r^2 c\mu}{4 k_{h,eff}\, t} \tag{42}$$

Using Equation 41 the pressure at any point in the system can be estimated as a function of time. Moreover, the applicability of Equation 41 can be expanded to a multi-well system by writing:

$$\frac{4\pi k_{h,eff}\, b}{\mu}\left[p(X,t) - p_i\right] = \sum_{i=1}^{n} q_i W(u_i) \tag{43}$$

where the right hand side of Equation 43 is the superposition of the well effects from n wells on the pressure at point X.

However, for the purpose of the performance model, the steady state solution for injection rates as a function of system geometry, well pressure, and reservoir pressure is desirable. To arrive at a steady state solution for Equation 40, terms from the power series expansion for $W(u)$ can be used. The first few terms from the expansion are [19]:

$$W(u) = -0.5772 - \ln u + u - \frac{1}{4}u^2 + \frac{1}{18}u^3 - \frac{1}{96}u^4 + \frac{1}{600}u^5 + ... \tag{44}$$

The values of the well function corresponding to the truncated power series using the first two (i.e., $-0.5772 - \ln u$) to six terms is given in Figure 50.

Given typical ranges for permeability (10^{-14} to 10^{-16} m^2), compressibility (10^{-9} to 10^{-10} Pa^{-1}), and viscosity (10^{-3} to 10^{-5} cP), the values for u of practical interest for the CO_2 injection problem (i.e., where t is on the order of years and r on the order of kilometers) will usually be less than 0.1. Only at very large distances and short times will the values of u be on the order of 1. Thus, use of only the first two terms of the power series expansion are adequate for this analysis and will result in a steady state solution for the incompressible system on a finite but expanding spatial domain, as described by Nordbotten et al. [20] (for an analogous problem).

---

[16] Note that this compressibility, c, is different from the unitless compressibility factor, z. In this context, c equals $1/v \cdot \partial v/\partial p$, where v is specific volume.
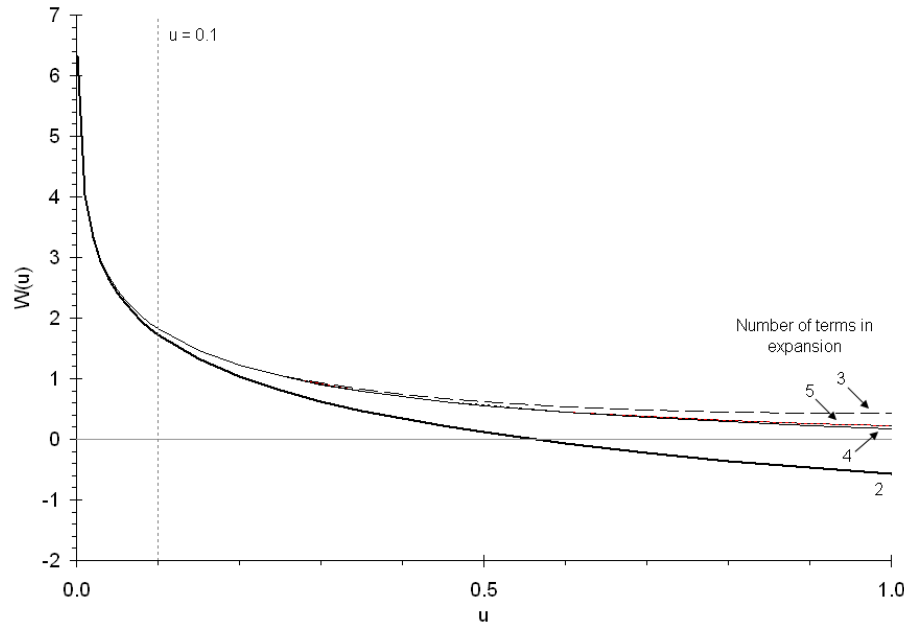
Figure 50.   Values of the well function, W(u), corresponding to different numbers of terms used in the power series expansion.

Using this approximation in Equation 43 for a two well system ($n = 2$) results in:

$$\frac{4\pi k_{h,eff} b}{\mu}\left[p(X,t) - p_i\right] = q_1\left[-0.5772 - \ln\left(\frac{r_{X,1}^2 c\mu}{4k_{h,eff} t}\right)\right] + q_2\left[-0.5772 - \ln\left(\frac{r_{X,2}^2 c\mu}{4k_{h,eff} t}\right)\right]$$

To arrive at a steady state solution for this equation, one well must be an injector and the other must be a producer, and the flow rates in the two wells must be equal. This generic type of two well system is referred to as a doublet system [17]. With these conditions met, the equation for the system can be reduced to:

$$\frac{4\pi k_{h,eff} b}{q\mu}\left[p(X,t) - p_i\right] = \ln\left(\frac{r_{X,2}^2}{r_{X,1}^2}\right) = \ln(K) \tag{45}$$

Thus, Equation 45 is the steady state solution for the pressure at any point X in the doublet system. The logarithmic term on the right hand side is a constant, K, and thus the locus of points where $p = p(X, t)$ form circles of constant pressure [17].

Extending the Doublet Solution to a Two Injector System

The solution presented in Equation 45 is only for a doublet system—one producer and one injector—not a system of multiple injectors. To arrive at a solution for a system with multiple wells where the pressure is defined as a constant at a given radius, several additional steps must be taken. These steps are summarized following the approach taken by Brigham [17].

The first step in the solution is to define the relationship for a single well near a constant pressure boundary, shown in Figure 51.
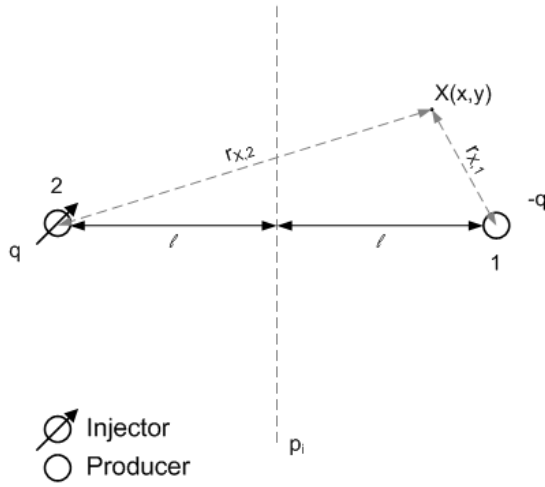
Figure 51.   The doublet system used to derive the pressure-flow relationship for pressure at an injection or production well near a constant pressure boundary, where p = p$_e$, modified from Brigham [17].

Writing the equations in terms of the pressure at well 1, the distance from well 1 to X is r_w (i.e., the radius of the wells) while the distance from well 2 to X is $2l$ (assuming that $l \gg r_w$). Thus, the equation for well 1 (or well 2, if signs are flipped) is:

$$\frac{4\pi k_{h,eff} b}{q\mu}\left(p_{wb,1} - p_i\right) = \ln\left(\frac{r_w}{2l}\right)^2 \tag{46}$$

Equation 46 does not contain any reference to parameters at well 2 and, in fact, well 2 serves only as an "image" well and need not exist in the system [13]. Equation 46 forms the basis for the second step in the multi-well solution, which is the equation for the pressure of a well off-center in a constant-pressure circle. The geometry of this system is shown in Figure 52.
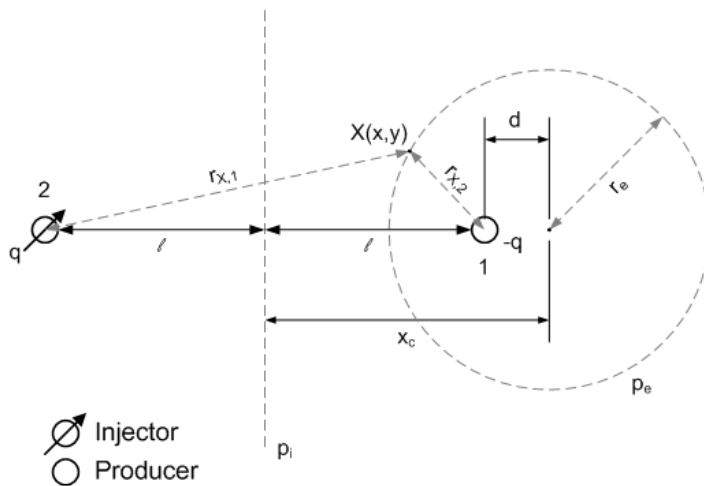
Figure 52.   The doublet system used to define the pressure-flow relationship for a well located d units off center in the constant pressure circle defined by r$_e$, modified from Brigham [17].

To derive the equation for pressure at well 1 in terms of the pressure at r_e, the difference in pressure between the constant pressure circle (at p_e) and the constant pressure line (at p_i) must be derived. This result is then subtracted from the equation for the difference in pressure between the well and the constant pressure line (Equation 46).

The solution for the pressure difference between any point on the constant pressure circle and the constant pressure line is in the form of Equation 45:

$$\frac{2\pi k_{h,eff} b}{q\mu}\left(p_e - p_i\right) = \ln\left(\sqrt{K}\right) \tag{47}$$

Subtracting the equation for the constant pressure line (Equation 46) from Equation 47 and simplifying, we arrive at:

$$\frac{2\pi k_{h,eff} b}{q\mu}\left(p_e - p_{wb,1}\right) = \ln\left(\frac{2l\sqrt{K}}{r_w}\right) \tag{48}$$

K must be eliminated from the above equation by writing the equation of the constant pressure circle of Figure 52 in terms of l and K. As defined in Equation 45, K can be written as the ratio of the square distances between point X (on the constant pressure circle) and the two wells:

$$K = \frac{\left(l - x\right)^2 + y^2}{\left(l + x\right)^2 + y^2}$$

This can then be manipulated to give the equation for the circle with radius r_e:

$$\left[x - \frac{l\left(1 + K\right)}{\left(1 - K\right)}\right]^2 + y^2 = \frac{4l^2 K}{\left(1 - K\right)^2}$$

Therefore, the radius of the circle is:

$$r_e = \frac{2l\sqrt{K}}{1 - K}$$

Writing d in terms of l and K, we get:

$$d = \frac{2lK}{1 - K}$$

Taking the ratio of of r_e and d we can solve for K:

$$K = \frac{d^2}{r_e^2}$$

and, from the previous three equations:

$$\sqrt{K} = \frac{r_e}{2l}\left(1 - \frac{d^2}{r_e^2}\right)$$

Therefore, the equation for a well producing (or injecting, with a change of sign) off-center in a constant pressure circle is:

$$\frac{2\pi k_{h,eff} b}{q\mu}\left(p_e - p_{wb,1}\right) = \ln\left[\frac{r_e}{r_w}\left(1 - \frac{d^2}{r_e^2}\right)\right] \tag{49}$$

If $d = 0$, Equation 49 reduces to the commonly applied equation for a well on center in a constant pressure circle [13, 21]. This on-center equation can also be derived from the integration of the radial form of Darcy's law. A number of studies have used the on-center solution (Equation 49) to estimate aquifer injectivity in CO_2 storage [8, 9, 11, 22], and this solution will be used in the following sections as a comparison to the multi-well solution derived here.

The final step involves the extension of the single well off-center result to a multi-well system injecting into a constant pressure circle. This requires the estimation of the pressure effect of one well in the constant pressure circle on another. The geometry of the system is defined in Figure 53.
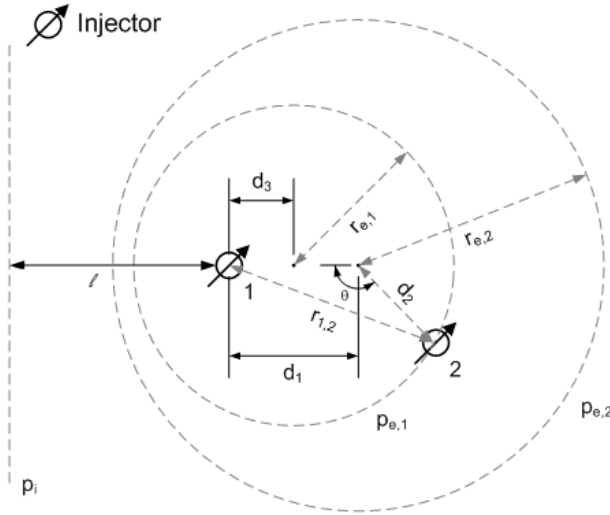
Figure 53.   The geometry of the system used to develop the relationship pressure-flow relationship for multiple wells injecting into a constant pressure circle, modified from Brigham [17].

The equation for the effect of one well on another (i.e., well 2 on well 1) injecting in a constant pressure circle is derived by writing the pressure drop between the two constant pressure circles defined by $r_{e,1}$ and $r_{e,2}$, via two different approaches and solving for the logarithmic terms. From the geometry of the system in Figure 53 it is clear that well 2 can be anywhere on the circle defined by $r_{e,1}$.

The first two equations are for well 1, off center by d_3 in the circle formed by $r_{e,1}$ and off center by d_1 in the circle formed by $r_{e,2}$. These equations are written using the off-center result presented in Equation 49 (note that the sign of the left hand side has been flipped because well 1 is an injector):

$$\frac{2\pi k_{h,eff} b}{q\mu}\left(p_{wb,1} - p_{e,1}\right) = \ln\left[\frac{r_{e,1}}{r_w}\left(1 - \frac{d_3^2}{r_{e,1}^2}\right)\right]$$

$$\frac{2\pi k_{h,eff} b}{q\mu}\left(p_{wb,1} - p_{e,2}\right) = \ln\left[\frac{r_{e,2}}{r_w}\left(1 - \frac{d_1^2}{r_{e,2}^2}\right)\right]$$

The result of subtracting the second equation from the first is:

$$\frac{2\pi k_{h,eff} b}{q\mu}\left(p_{e,2} - p_{e,1}\right) = \ln\left[\frac{r_{e,2}\left(r_{e,1}^2 - d_3^2\right)}{r_{e,1}\left(r_{e,2}^2 - d_1^2\right)}\right] \qquad (50)$$

The second set of equations is for the pressure difference between the line of constant pressure at the center of the system and each of the circles (Equation 47), as:

$$\frac{2\pi k_{h,eff}\, b}{q\mu}\left(p_{e,1}-p_i\right)=\ln\!\left(\frac{r_{e,1}}{d_3}\right)$$

$$\frac{2\pi k_{h,eff}\, b}{q\mu}\left(p_{e,2}-p_i\right)=\ln\!\left(\frac{r_{e,2}}{d_1}\right)$$

Subtracting the second equation from the first results in a statement of the pressure effect of well 2 on well 1 (or vice versa):

$$\frac{2\pi k_{h,eff}\, b}{q\mu}\left(p_{e,1}-p_{e,2}\right)=\ln\!\left(\frac{r_{e,1}}{d_3}\frac{d_1}{r_{e,2}}\right) \tag{51}$$

Since neither $r_{e,1}$ or d_3 should appear in the solution, we would like to eliminate these terms from Equation 51. The left hand side of Equations 50 and 51 are equal, thus we can set the logarithmic terms equal, and isolate the ratio of $r_{e,1}$ to d_3:

$$\left(\frac{r_{e,1}}{d_3}\right)^2=\frac{r_{e,2}+d_3 d_1 - d_1^2}{d_3 d_1}$$

The ratio $r_{e,1}$ to d_3 can also be written from the system geometry using the cosine law:

$$\left(\frac{r_{e,1}}{d_3}\right)^2=\frac{d_1 d_2^2 + d_1\left(d_1-d_3\right)^2 - \left(d_1-d_3\right)\!\left(d_2^2 + d_1^2 - r_{1,2}\right)}{d_1 d_3^2}$$

Setting the two previous equations equal, solving for $d_1 d_2$, and back substituting results in:

$$\left(\frac{r_{e,1}}{d_3}\right)^2=\frac{d_2^2 d_1^2 + r_{e,2}^2\left(r_{e,2}^2 - d_2^2 - d_1^2 + r_{1,2}^2\right)}{r_{1,2}^2 d_1^2}$$

Substituting this relationship back into Equation 51, where the logarithmic terms are squared and the logarithm is multiplied by ½ yields:

$$\frac{2\pi k_{h,eff}\, b}{q\mu}\left(p_{e,1}-p_{e,2}\right)=\frac{1}{2}\ln\!\left[\frac{d_2^2 d_1^2 + r_{e,2}^2\left(r_{e,2}^2 - d_2^2 - d_1^2 + r_{1,2}^2\right)}{r_{1,2}^2 r_{e,2}^2}\right] \tag{52}$$

This is final expression for the effect of well 2 on well 1 (or vice versa). Thus, for well 1 the sum of the effects of injecting off-center into a constant pressure circle and of well 2 on well 1 is:

$$\frac{2\pi k_{h,eff}\, b}{\mu}\left(p_{wb,1}-p_e\right)=q_1\ln\!\left[\frac{r_e}{r_w}\left(1-\frac{d_1^{\,2}}{r_e^2}\right)\right]+\frac{q_2}{2}\ln\!\left[\frac{d_2^2 d_1^2 + r_e^2\left(r_e^2 - d_2^2 - d_1^2 + r_{1,2}^2\right)}{r_{1,2}^2 r_e^2}\right] \tag{53}$$

Similarly for well 2, the above equation can be written:

$$\frac{2\pi k_{h,eff}\, b}{\mu}\left(p_{wb,2}-p_e\right)=q_2\ln\!\left[\frac{r_e}{r_w}\left(1-\frac{d_2^{\,2}}{r_e^2}\right)\right]+\frac{q_1}{2}\ln\!\left[\frac{d_2^2 d_1^2 + r_e^2\left(r_e^2 - d_2^2 - d_1^2 + r_{1,2}^2\right)}{r_{1,2}^2 r_e^2}\right] \tag{54}$$

where, in both of the above equations, $r_{e,i}$ and $p_{e,i}$ have been replaced with r_e and p_e, respectively.

A General Multi-Well Model

Equations 53 and 54 form a linear system that allows the BHIP to be related to the system geometry, aquifer properties, and injection rates for the two-well example. This linear system can be extended to a generic system of n wells by writing the equation $\overline{A} \cdot \vec{x} = \vec{b}$, where:

$$\overline{A} = \begin{bmatrix} \alpha_1 & \beta_{1,2} & \cdots & \beta_{1,n} \\ \beta_{2,1} & \alpha_2 & \cdots & \beta_{2,n} \\ \vdots & \vdots & & \vdots \\ \beta_{n,1} & \beta_{n,2} & \cdots & \alpha_n \end{bmatrix} \tag{55}$$

$$\vec{x} = \begin{bmatrix} q_1 \\ q_2 \\ \vdots \\ q_n \end{bmatrix} \tag{56}$$

$$\vec{b} = \begin{bmatrix} \dfrac{2\pi kb}{\mu}\left(p_{wb,1} - p_e\right) \\ \dfrac{2\pi kb}{\mu}\left(p_{wb,2} - p_e\right) \\ \vdots \\ \dfrac{2\pi kb}{\mu}\left(p_{wb,n} - p_e\right) \end{bmatrix} \tag{57}$$

In equation 55, α_n is the off-center logarithm term written for well n (i.e. the term multiplied by q_1 in Equation 53 is α_1) and $\beta_{n,k}$ is the pressure effect of well k on well n (i.e., the term multiplied by q_2 in Equation 53 is $\beta_{1,2}$). It is clear from the two well system that $\beta_{n,k}$ is equal to $\beta_{k,n}$. Therefore, for a specified geometry, BHIP for each of n-wells, and aquifer properties, the injection rate for each of n-wells can be calculated by inversion of $\overline{A}$ followed by multiplication by $\vec{b}$ or a number of alternative methods, such as Gauss-Jordan elimination or LU-factorization with substitution [18].

The injectivity of the linear system as a function of the number of wells and system geometry can be generalized to any set of aquifer properties by using the dimensionless injectivity, i_d. For well n, the dimensionless injectivity is defined as [23]:

$$i_{d,n} = \frac{q_n \mu}{2\pi k_{h,eff} b (p_{wb,n} - p_e)} \tag{58}$$

If it is assumed that the BHIP, $p_{wb,n}$, at each injection well is equal—which appears to be the configuration that maximizes the sum of the $i_{d,n}$ for the n-well system—the dimensionless injectivity for each well can easily be calculated by setting each element of $\vec{b}$ (Equation 57) to 1 and solving for $\vec{x}$ (Equation 56), which now contains $i_{d,n}$. Figure 54 shows the average, minimum, and maximum dimensionless well injectivity in systems with 1 to 100 wells with 40-acre well spacing.
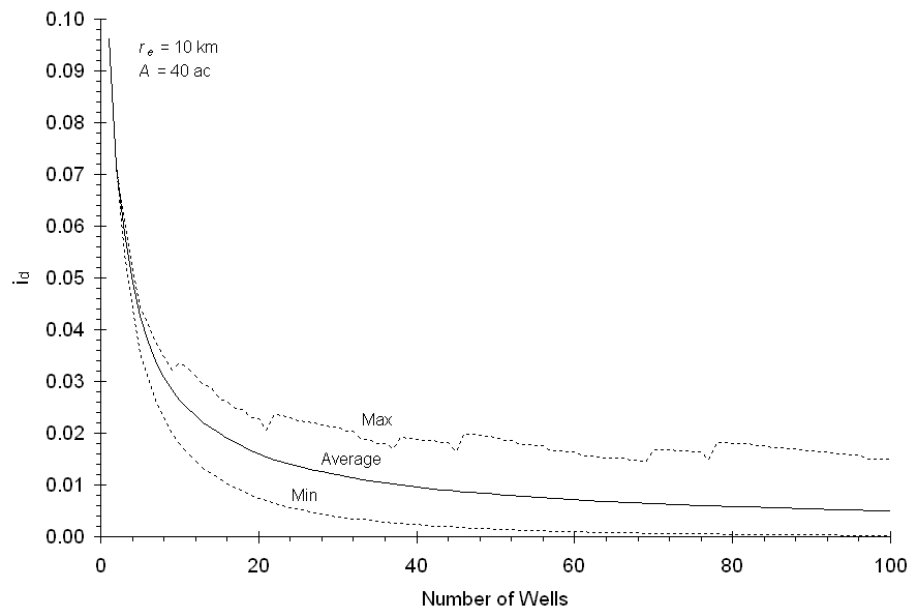
Figure 54.   The average, minimum, and maximum injectivity for systems with 1 to 100 wells on 40 acre spacing, and a constant pressure radius where $p_e = p_i$ at 10 km.

This figure clearly shows that the addition of wells to the system decreases the average, minimum, and maximum well injectivity in the system. The well with the minimum injectivity is always the well at the center of the system, while the well with the maximum is always on the perimeter of the system. The decrease in the average injectivity of individual wells with the addition of more wells (Figure 54) means that the there are diminishing returns from adding wells to a system. Figure 55 shows the total (cumulative) injectivity of systems with 1 to 100 wells for three different well spacings.
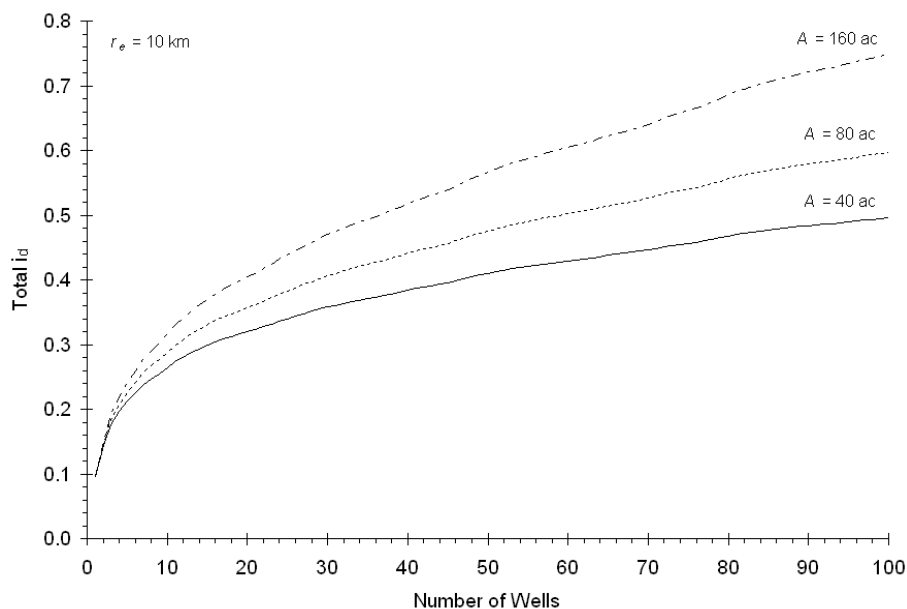
Figure 55.   The total injectivity for systems with 1 to 100 wells on 40, 80, and 160 acre spacing with a constant pressure radius where $p_e = p_i$ at 10 km

The results shown in both Figure 54 and Figure 55 are based on a constant pressure radius, r_e, of 10 km. The selection of an appropriate value for r_e and the sensitivity of the injectivity to r_e are discussed in the following section.

Injectivity and Sensitivity to Boundary Conditions

Describing the behavior of a well injecting to a constant pressure circle containing other injectors requires that the pressure (p_e) at radius (r_e) is known, as shown in Equation 53. Typically, the pressure, p_e, is assumed to be the initial reservoir pressure, p_i, prior to injection, in which case r_e is referred to as the drainage radius of the system. However, this radius will increase with time [20] and the transient behavior of the system cannot be derived from the steady-state solution presented in Approximate Solution to Injectivity of a Doublet System. Thus, Equation 43 must be solved numerically to arrive at a solution. A five-well system shown in Figure 56 is used to illustrate the numerical solution.
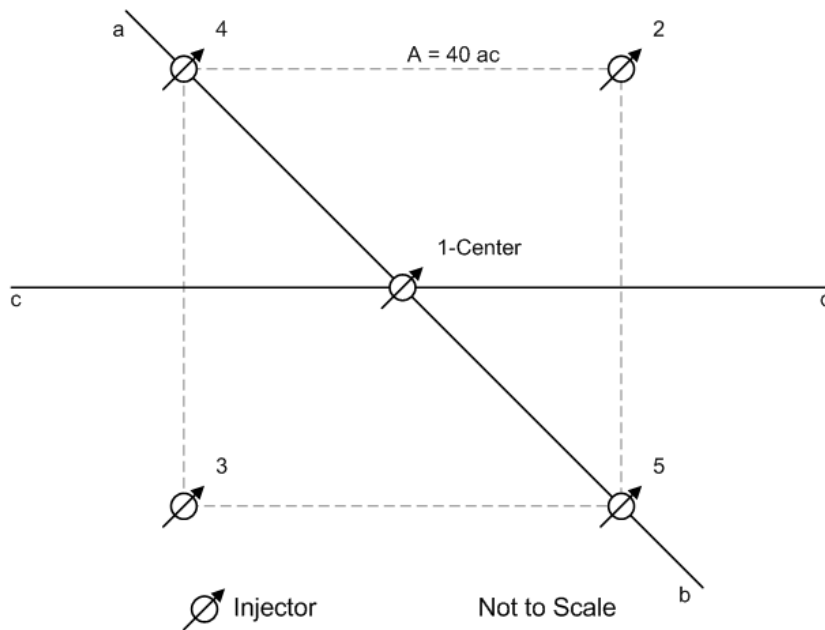
Figure 56.   An illustrative 40-acre, 5-well injection pattern used to calculate the change in pressure field with time.

The resulting pressure distribution is shown in Figure 57 for cuts a-b, and Figure 58 for cut c-d based on injection of 1 million tonnes of CO_2 per year. The aquifer parameters are representative of a medium-permeability aquifer ($k_h = 50$ md), at a depth of approximately 1000 m.
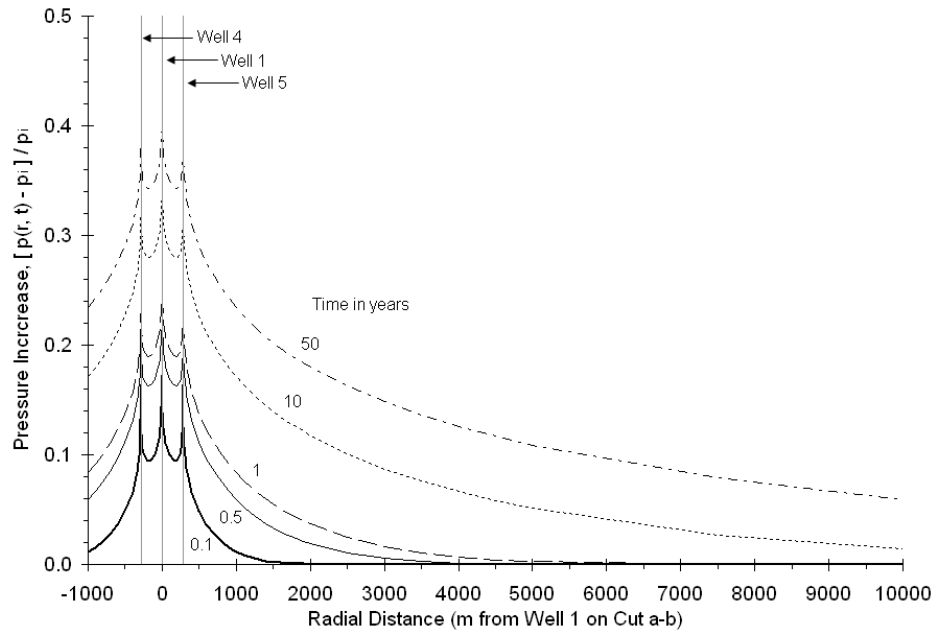
Figure 57.   Pressure distribution in a confined aquifer for an illustrative set of parameters along cut a-b (shown in Figure 56) at times ranging from 0.1 years (i.e., 30 days) to 50 years.
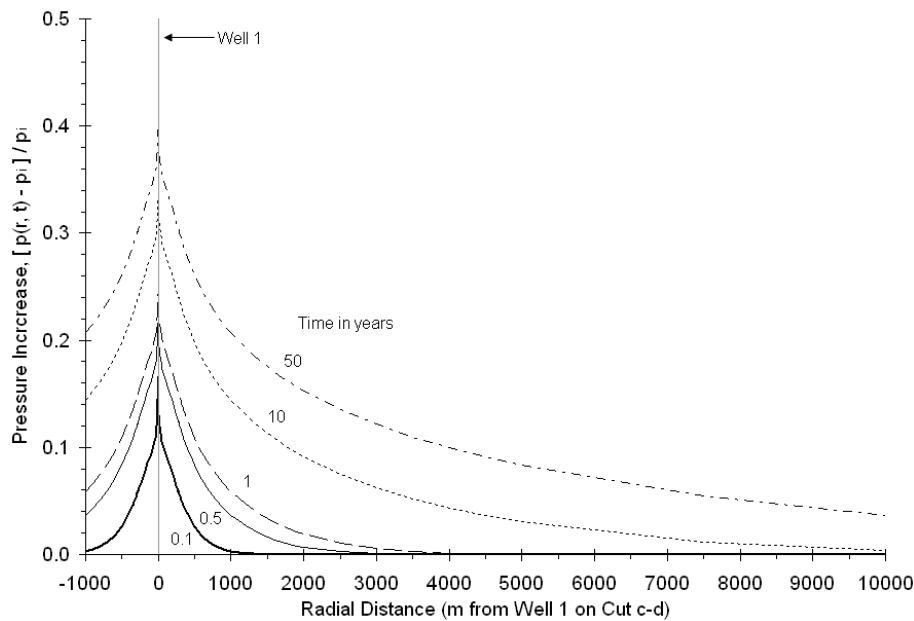
Figure 58.   Pressure distribution in a confined aquifer for an illustrative set of parameters along cut c-d (shown in Figure 1.5) at times ranging from 0.1 years (i.e., 30 days) to 50 years.

Figure 57 and Figure 58 both show that over time the pressure at any given radius in the system increases over time for a case with a fixed injection rate. Note that over time the BHIP required to maintain the fixed injection rate increases. In this example, at 0.1 years (i.e., 30 days) the aquifer pressure is equal to the initial pressure at a radial distance of approximately 1,000 m (1 km). As time passes, the pressure transient moves further outwards, and the radial distance at which the current pressure equals the initial pressure increases.

The rate at which the pressure transient moves outwards will vary from system to system but the general behavior of every system will be the same, i.e., the pressure transient will move radially away from the well(s) over time. Nordbotten et al. [20] have shown that the rate at which the pressure transient moves outwards is proportional to the square root of

time. Following Nordbotten et al. [20], the definition of u (Equation 42) can be rearranged to calculate the radius at which the pressure is approximately equal to the initial pressure:

$$r_e = \sqrt{t\left(\frac{4k_{h,eff}\,u_c}{c\mu}\right)} \qquad (59)$$

where u_c is the cut-off value of u chosen such that the value of $W(u)$ is acceptably close to zero. If a truncated power series expansion with an even number of terms is used to approximate $W(u)$, as done here, the value for u_c at which $W(u) = 0$ can be calculated (see Figure 50). For the two-term expansion, this value of u_c is 0.5615. Thus, for a specified set of aquifer parameters the value of r_e can be calculated, as illustrated in Figure 59.

$k = 50$ md
$\mu = 57\ \mu$Pa s
$c = 7.9 \times 10^{-9}\ Pa^{-1}$
$u_c = 0.5615$
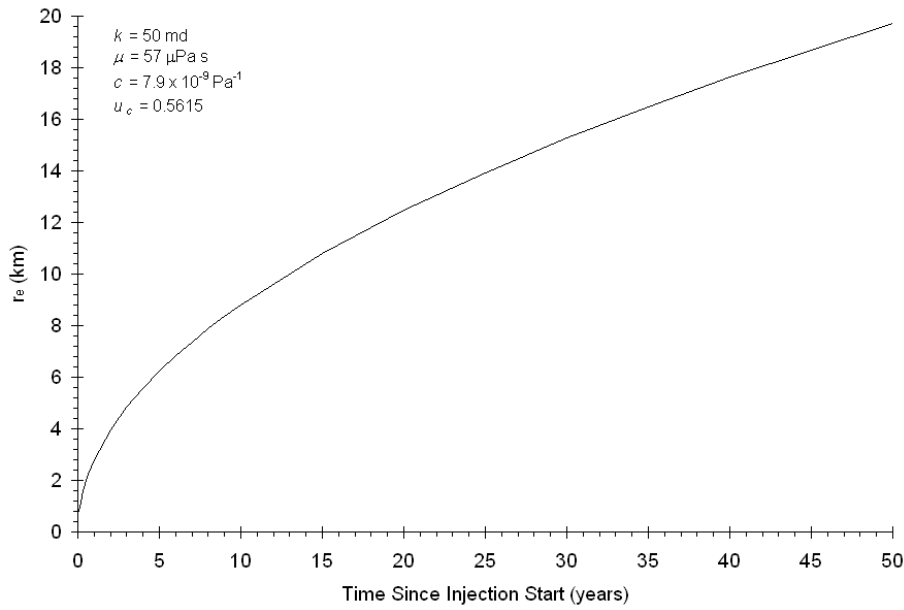
Figure 59. The radius at which $p = p_i$ for the example system above calculated using Equation 59

Based on these results, if the solution for injectivity were desired for a time of approximately 10 years, the appropriate value of r_e (where $p = p_i$) would be approximately 10 km. While these results suggest the magnitude of r_e, its exact value will depend on parameter values for the aquifer of interest. Thus, it is of interest to determine whether a general result for r_e will suffice by examining the sensitivity of the simplified system (Equation 53) to r_e.

The sensitivity of $i_{d,n}$ is its derivative with respect to r_e, which is solved for via:

$$\vec{x}' = \overline{A}^{-1}\left(-\overline{A}'\vec{x}\right)$$

where $\overline{A}'$ represents $\dfrac{\partial}{\partial r_e}\overline{A}$ and $\vec{x}'$ represents $\dfrac{\partial}{\partial r_e}\vec{x}$.

For a five-well system with geometry corresponding to that show in Figure 56, Figure 60 shows clearly that the sensitivity of dimensionless injectivity to changes in r_e falls non-linearly with r_e. For example, an increase in r_e from 10 km to 11 km would result in a decrease to the dimensionless injectivity of approximately 2%, whereas the same increase at 20 km would result in an injectivity decrease of less than 1%.

Comparing the illustrative results shown in Figure 59 and the general results from Figure 60 suggest that for a planning horizon of 10 to 20 years in a CO_2 storage project, the appropriate drainage radius is between 10 and 20 km; and, the injectivity calculated with this assumptions will be relatively insensitive to r_e.
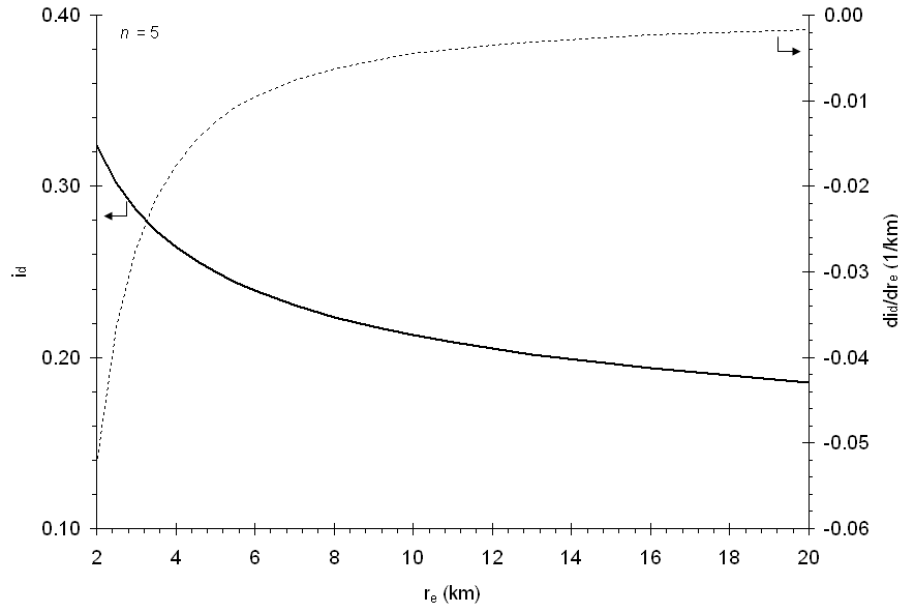
Figure 60. Dimensionless injectivity and its derivative with respect to the pressure boundary radius, r_e, for a 40 ac, five-well system of injectors.

Establishing the BHIP—Flow in the Wellbore

Equation 53 shows that the injection rates in the system are a function of the wellbore pressure. Thus, knowledge of the BHIP is necessary to estimate the number of wells required for a specified injection rate.

The BHIP will be limited to some fraction of the reservoir fracture pressure, as it would be undesirable to fracture the wellbore environment in a CO_2 storage operation. In the absence of field data, the fracture pressure can be estimated from a correlation presented by Heller and Taber [24]:

$$G_f = \gamma - \beta e^{-\alpha d}$$
$$p_f = G_f d \tag{60}$$

where, G_f is the fracture gradient (Pa/m); α, β and γ are coefficients with the values 4.36×10^{-4} m^{-1}, 9.24 kPa/m, and 22.62 kPa/m, respectively; and, p_f is the fracture pressure at depth (Pa).

Once the BHIP is known, the wellhead pressure needed to generate the BHIP can be calculated. The design of CO_2 injection wells for aquifer storage will likely be nearly identical to those designed for EOR, shown in Figure 3.5. The Numerical Modeling of the Wellbore Environment chapter describes a numerical model that can be used to calculate the pressure gradient in a CO_2 injection well considering pressure changes due to hydrostatic head, friction losses, and heat transfer. However, as in the EOR performance model, the complexity introduced by such a model is undesirable in the context of an aquifer storage performance model. Thus, a response surface model (the same as that used for the EOR performance model) based on the full numerical model described in the Numerical Modeling of the Wellbore Environment chapter is used to estimate the wellhead pressure in the aquifer storage performance model. The description in this section mirrors that in From the Surface to the Reservoir – Modeling the Wellbore section in the Enhanced Oil Recovery (EOR) chapter.

The response surface model assumes that the pressure gradient in the wellbore is a linear function of depth and, thus, that the BHIP can be written as:

$$p_{wb} = \frac{\Delta p}{\Delta L} L + p_{wh} \tag{61}$$

where, p_{wb} is the BHIP pressure, p_{wh} is the wellhead pressure, and L is the wellbore length.

Because Equation 61 can represent only pressure gradients linear with depth, it is valid only for flow rates below approximately 1 Mt CO_2 per year per well at temperatures less than $30^{\circ}C$ and wellhead pressures greater than 8 MPa for the 3-inch (0.076 m) inside diameter tubing modeled. The form of the regression equation for pressure gradient is:

$$\frac{\Delta p}{\Delta L} = a_1 q^2 + a_2 \log(p_{wh})^2 \qquad (62)$$

where, p_{wh} is the wellhead pressure (Pa), and q is the volumetric flow rate (m³/d) at wellhead conditions.

Parameter estimates for the regression coefficients are given in Table 26. The complete set of parameters used to generate the dataset upon which the regression is based are listed in the Numerical Modeling of the Wellbore Environment chapter. The regression model given in Equation 62 accounts for a large proportion of the variation in the set of 2895 data points generated by the numerical model, reflected by an adjusted-r^2 value of 0.99.

Table 26. Regression coefficient estimates for the pressure drop correlation, Equation 62, where standard errors are reported in parentheses.

Coefficient	Value
a_1	-7.008 × 10⁻⁴ ** (3.100 × 10⁻⁶)
a_2	1.812 × 10² ** (2.692 × 10⁻¹)
** Significant at the 1% level	

The regression coefficients in Table 26 show that the wellbore pressure gradient is negatively correlated with the volumetric flow rate, and positively correlated with the square of the base-ten logarithm of pressure. In addition, wellhead temperature influences the pressure gradient predicted by Equation 62 through its effect on volumetric flow rate. Figure 3.6 shows the pressure gradient predicted by Equation 61 using the coefficients listed in Table 26.

Describing Reservoir Heterogeneity

Equation 43 and the approximate solution for the multi-well system (e.g., for the two-well case, Equations 53 and 54) were derived for a reservoir with homogeneous permeability. This means that the permeability in the direction of flow--primarily horizontal—is spatially invariant. However, this is rarely the case in a real aquifer. The variation in permeability can be described by the Dykstra-Parsons coefficient, V_{DP}, which is defined as [25]:

$$V_{DP} = \frac{k_{0.5} - k_{0.16}}{k_{0.5}} \qquad (63)$$

where $k_{0.5}$ is the median permeability and $k_{0.16}$ is the 16th percentile permeability based on the distribution of measured permeability values. A V_{DP} value of zero corresponds to a homogeneous reservoir and values approaching 1.0 correspond to increasingly heterogeneous reservoirs. Willhite concludes that the value of V_{DP} falls between 0.5 and 0.9 for most oil reservoirs [26].

Because V_{DP} describes the variation in the underlying distribution of permeability, if the mean permeability, k_{avg}, and distribution of permeability measurements are known, a number of reservoirs can be generated that have an equal prior probability of representing the actual aquifer. The definition of V_{DP} (Equation 63), however, does not imply any specific permeability distribution for k. Jensen et al. [27] conclude that permeability measurements tend to follow a power-normal distribution [28] and, in practice it is commonly assumed that permeability measurements are log-normally distributed, which is a limiting case of the power-normal distribution.

The aquifer storage model developed here assumes that permeabilities are drawn from a log-normal distribution and that the aquifer can be represented by a series of horizontal layers, each with uniform permeability, k_i, and thickness, h_i (see Figure 61). Thus, given k_{avg}, V_{DP}, the aquifer net thickness (i.e. the thickness that available for fluid flow), b, and the number of layers in the formation, the model will generate the effective permeability, $k_{h,avg}$, that characterizes the aquifer. Figure 61 shows the generic layered aquifer generated by the model.
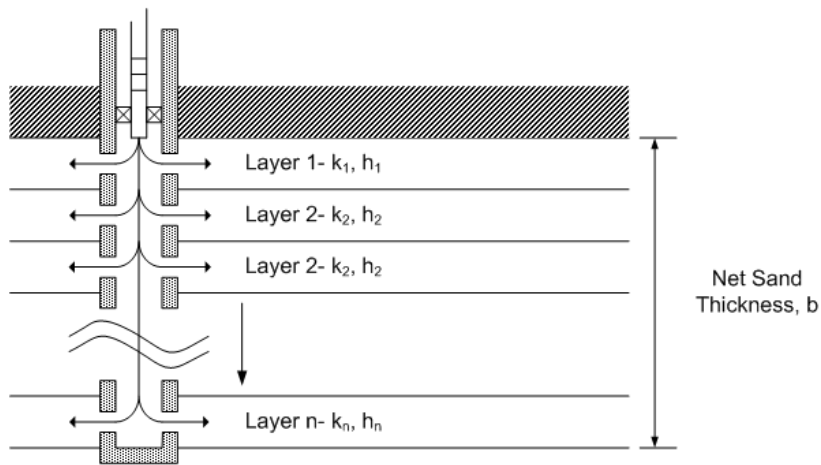
Figure 61.   Generic layered aquifer model.

The effective permeability characterizing the formation shown in Figure 61 is given by [13]:

$$k_{h,eff} = \frac{\sum_{i=1}^{n} k_i h_i}{b} \tag{64}$$

where k_i and h_i are the permeability and thickness of layer i, and n is the number of layers in the system.
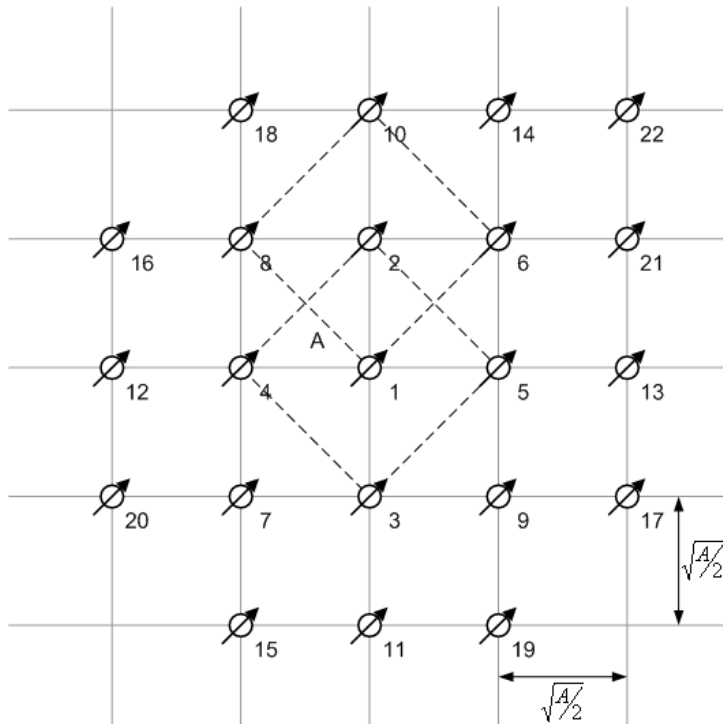
Figure 62.   The arrangement of wells in an n-well system used by the model

Generating the System Geometry for Multi-Well Scenarios

When more than two injection wells are required, the arrangement of these wells inside the constant pressure circle must be specified. Unfortunately, Equation 53 shows that the positioning of these wells relative to one another and to the drainage radius influences the injectivity of the system. To make the problem of positioning the wells manageable, the model assumes that the wells are located at the vertices of a square lattice. The lengths of the edges in the lattice are a function of the area associated with each injection well, referred to as the pattern spacing. Figure 62 shows the typical arrangement of wells in an *n*-well system.

Wells are added to the system at unoccupied lattice points in order of increasing radial distance from the center of the system, thus minimizing the surface area required for an *n*-well system.

Illustrative Performance Model Results

Results from the performance model have been generated for four illustrative cases. The Oklahoma North Purdy, Springer A and Alberta Joffre-Viking cases were used in the Enhanced Oil Recovery (EOR) chapter to illustrate the behavior of the CO_2-flood EOR model. These two oil fields are treated as aquifers with equivalent petrophysical properties for this case study. The Texas South Liberty-Frio and Alberta Lake Wabamun-Manniville cases have been identified as potential targets for large-scale geological sequestration [11, 29-31]. These four aquifers are all sandstone bodies, with depths greater than 1 km and *kh* values (i.e. the product of permeability and net sand thickness) from 4,500 to 940,000 md·ft. The performance inputs and other pertinent data have been collected from a number of sources [32-38], and are shown in Table 27. The parameters for the Mannville Aquifer were derived from an analysis of the datasets provided by the Alberta Geological Survey as part of their "Test Case for Comparative Modeling of CO_2 Injection, Migration and Possible Leakage—Wabamun Lake Area, Alberta, Canada" [38].

Table 27.   Key performance model parameters for the four case study reservoirs

Parameter	Northeast Purdy Unit	Joffre Viking Pool	South Liberty	Lake Wabamun Area
Location	Oklahoma	Alberta	Texas	Alberta
Unit	Springer "A" Sandstone	Viking Aquifer	Frio Formation	Mannville Aquifer
Lithology	Sandstone	Sandstone	Sandstone	Sandstone
Well Spacing (acres)	80	80	80	80
CO_2 supply pressure (MPa)	10.3	10.3	10.3	10.3
$P_{wb,max}$ (% of p_{frac})	90%	90%	90%	90%
r_w (m)	0.15	0.15	0.15	0.15
Depth (m)	2,499	1,500	1,850	1,514
p_{res} (MPa)	21.0	7.8	15.2	14.4
T_{res} (K)	338	329	329	327
k_h (md)	44	507	944	23
Net Sand (m)	91	30	300	59
ϕ (%)	13.0%	13.0%	27%	11.2%
x_{brine} (ppm$_w$)	100,000	40,000	100,000	68,074
S_{wc}	0.20	0.30	0.30	0.66
$k_{rw,c}'$	1.00	1.00	1.00	0.80
$k_{rc,w}'$	1.00	1.00	1.00	0.12
V_{DP}	0.82	0.70	0.67	0.92

Each of the cases was evaluated with a project capacity factor (i.e. the percentage of the design capacity actually used on an annual basis) of 100% across a range of injection rates—3 Mt CO_2 per year being roughly equivalent to the amount of CO_2 captured from a 500 GW coal-fired power plant—with a time horizon of 10 years used to calculate the drainage

radius as described in Injectivity and Sensitivity to Boundary Conditions. The number of wells required for each of the illustrative cases is shown in Figure 63.
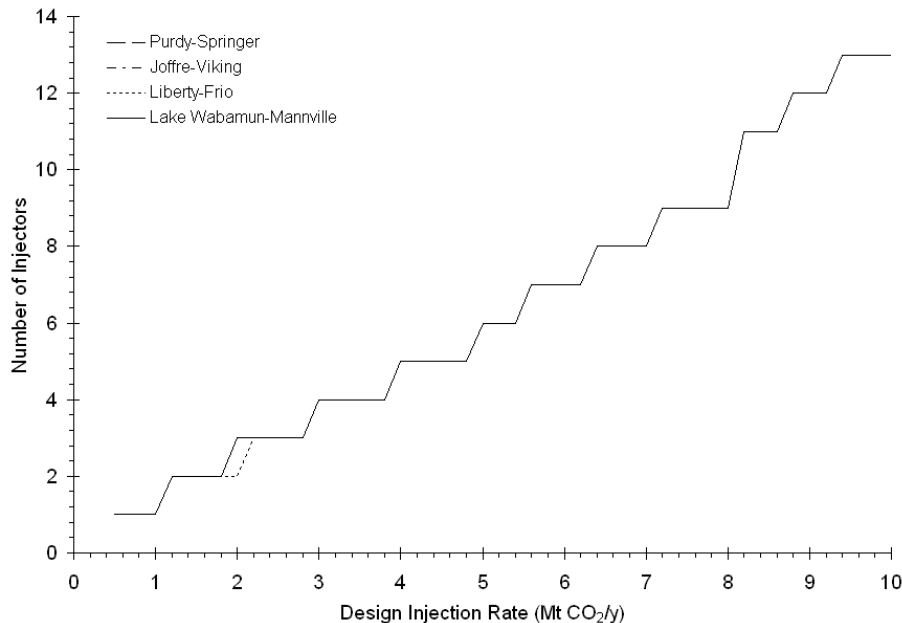
Figure 63.   Number of wells required for each of the cases described in Table 27; note that the same number of wells is required across almost the entire range of injection rates for all four cases.

The number of injection wells predicted for each of the cases is the same despite the differing reservoir descriptions across the range of injection rates shown in Figure 63. This is not indicative of a broad trend that applies to all aquifers, as other sets of realistic aquifer parameters results in different numbers of wells being required than presented in Figure 63. However, at larger injection rates, the number of wells required for each of the sites begins to diverge. For example, for over 11 Mt CO_2 per year—comparable to the emissions from 2500 GW of pulverized coal capacity—the Lake Wabamun-Mannville site requires more injection wells than the other three sites. Nonlinearities in the number of injection wells are difficult to discern because of the 1 Mt CO_2 per year per well limit imposed by the wellbore model. Nonetheless, a second-order polynomial is the best fit curve to the data points in Figure 63.

The four cases are better differentiated by the required difference between the BHIP, p_{wb}, and initial aquifer pressure, p_i, required to match the specified injection rates, as shown in Figure 64. These results clearly show that to obtain the same injection rate, the pressure rise around the wellbore is highest for the Lake Wabamun-Mannville case—the aquifer with the lowest value of kh—and lowest for the Liberty-Frio case—the aquifer with the highest kh. In addition, the data points clearly show the non-linear interplay of pressure and injection rates in a multi-well system.

Figure 65 shows the required wellhead pressure estimated by the model for each of the cases across a range of injection rates. The wellhead pressure required by the Joffre-Viking case is lower than the minimum pressure allowable by the wellbore model, thus it is not shown in Figure 65. The relative order of the data points for a given flow rate reflect the required BHIP for each of the cases that were shown in the previous figure. The discontinuous "saw tooth" curves shown in both Figure 64 and Figure 65 are the result of the model being able to add only integer number of wells. Only a small range of flow rates can be handled by a given number of wells and, within this range, the required BHIP and corresponding wellhead pressure increase with increasing flow rates until the maximum BHIP is reached, at which point the number of wells increases.
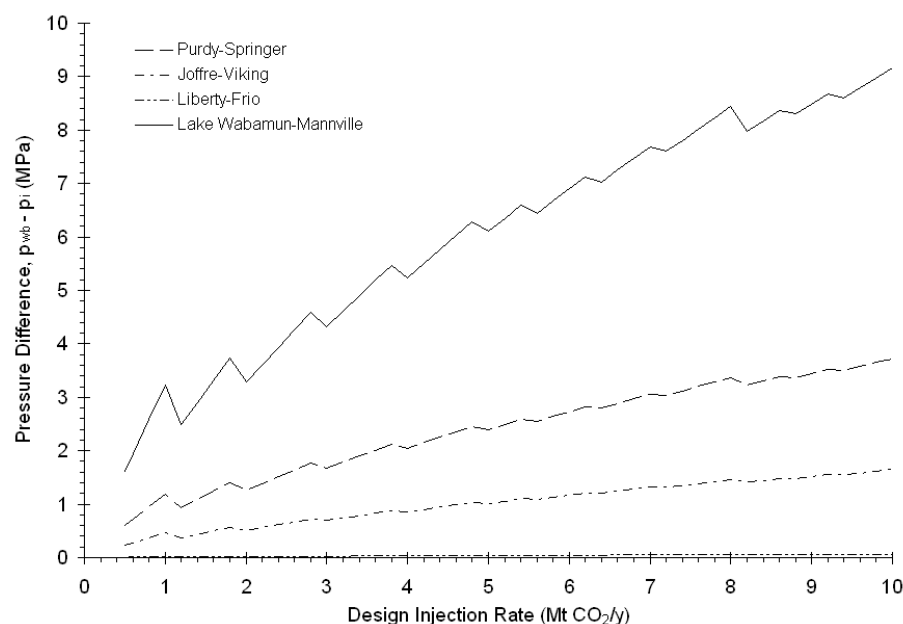
Figure 64.   The difference between the BHIP, p_{wb}, and the initial aquifer pressure, p_i, for each of the cases across a range of design injection rates.
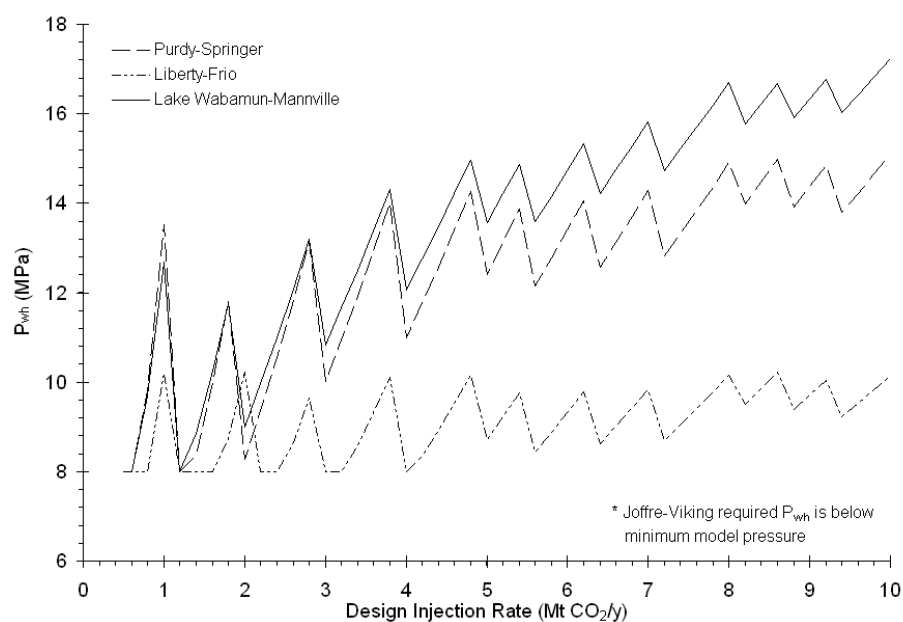
Figure 65.   Wellhead pressure required to inject the CO_2 as a function of the design injection rate for each of the cases. Note that the wellhead pressure required for the Joffre-Viking case is not shown because it is below the minimum pressure of 8 MPa allowable in the wellbore model.

Saline Aquifer Storage Cost Model

The capital costs for saline aquifer storage consist of four elements: site characterization costs; project capital costs; operating and maintenance (O&M) cost; and, monitoring, verification, and closure costs.

The capital cost model structure, shown earlier in Figure 49, combines results from the performance model with specified cost factors to estimate the total capital cost of an aquifer storage project reported as a levelized cost in 2004

US dollars per tonne CO_2. The capital cost of a storage project include the cost of any additional CO_2 compression (where necessary to increase the pressure of CO_2 prior to injection), the cost of surface equipment required for each well (e.g. the wellhead, CO_2 metering equipment, etc.), and the cost of drilling and completion of injection wells. The capital cost also includes a one-time cost of site characterization. Annual expenses include the costs of normal field operation and maintenance (including periodic well workovers), and compression of CO_2 prior to injection. The following sections describe how the costs associated with each of these categories were estimated.

Site Characterization Cost

The cost of site characterization is highly dependent on the requirements of the regulatory regime to which the project is subject. However, given that CO_2 should be isolated from the atmosphere for long timescales, it would be prudent to characterize the subsurface over the area which the injected CO_2 is likely to spread over a set time horizon to ensure that conduits to the surface, natural or otherwise, do not exist. Thus, the main factor affecting the cost of site characterization will be the area of review. Nordbotten et al. have proposed a method to estimate the aerial extent of plume spread in CO_2 storage [39] and, this method, described in the CO_2 Price Conversion Table chapter, is used to estimate the required area of review for a storage project over the specified planning horizon. Tombari suggests the approximate costs associated with characterizing this area to be: \$100,000 per square mile (mi^2, \$38,610 per km^2) for geophysical characterization (3-D seismic); \$3,000,000 to drill and log a well; and an additional 30% of these total costs for data processing, modeling, and other services [40]. One well would be required for every 25 mi^2 (65 km^2) of the review area [40].

Project Capital Costs—Drilling and Completion

The capital cost of an aquifer storage project can be classified into three main areas: well drilling and completion (D&C); injection equipment costs (e.g., wellhead, flow and control equipment, distribution piping, etc.); and, compression equipment costs. D&C costs are discussed in this section, while injection and compression equipment costs are described in the Project Capital Costs – Injection Well Equipment and Project Capital Costs – Compression Equipment sections, respectively.

D&C costs include the cost of physically drilling an injection well, running casing, hanging tubing, and installing any downhole equipment (e.g., chokes and packers, as shown in the figure earlier in From the Surface to the Reservoir—Modeling the Wellbore Environment section). D&C costs are well documented by the annual Joint Association Survey (JAS) on Well Drilling Costs [41], which lists the average cost of oil and gas wells drilled and completed each year by depth interval and state. A regression model based on these costs was developed by Lewin & Associates [42], and updated to 2004 dollars in this research using the using the EIA Oil and Gas Lease Equipment and Operating Cost index [43]. This is the same regression model used to estimate D&C cost in the EOR model (see Drilling and Completion Capital Cost in the Enhanced Oil Recovery (EOR) chapter), except that the regions have been aggregated to be consistent with those used in the injection equipment cost model by taking the highest state-level cost as representative of the region. The form of the Lewin & Associates cost model is:

$$C = a_1 e^{a_2 d} \qquad (65)$$

where C is cost in 2004 US dollars per well, a_1 and a_2 are regression coefficients and d is the well depth in feet. The value of the regression coefficients (where the a_1 parameter values have been updated to 2004 dollars) are listed by region in Table 28.

The recent increase in oil prices has spurred a large increase in drilling activity. Thus,as with recent increases in injection equipment costs (driven by materials cost increases), D&C costs in years after 2004 can be expected to be considerably higher. D&C costs for future periods can be estimated using the EIA in the Oil and Gas Lease Equipment and Operating Cost [43].

Table 28.   Regression coefficients for use in Equation 65 for well drilling and completion (D&C) adapted from Lewin and Associates [42] and updated to 2004 US dollars.

Region	States	a_1	a_2
1	West Texas	43986	3.4×10^{-4}
2	South Texas	44041	3.5×10^{-4}
3	South Louisiana	44041	3.5×10^{-4}
4	Mid-Continent Region	42493	3.5×10^{-4}
5	Rocky-Mountain Region	80086	2.7×10^{-4}
6	California	70123	3.2×10^{-4}

Project Capital Costs—Injection Well Equipment

The cost of equipping injection wells for CO_2 for aquifer storage is assumed to be comparable to the cost of equipping wells for water injection. This assumption is consistent with those made by Bock et al. [9] to assess the cost of aquifer storage and by Advanced Resources International for the cost of CO_2-flood EOR [44]. The incremental cost of water injection equipment associated with adding new wells to a producing oil field in West Texas is estimated annually by the EIA for 2,000 ft (610 m), 4,000 ft (1219 m) and 8,000 ft (2438 m) deep wells [43]. A regression equation developed in this research has the same form as Equation 65, with coefficients values described in Table 29.

The EIA cost for water injection wells has been extended to other regions by scaling the West Texas incremental cost using the ratio of primary production equipment cost in the region of interest to the cost in West Texas. The EIA estimates the cost of primary production equipment for oil fields located in six regions: West Texas, South Texas, South Louisiana, the Mid-Continent Region (i.e., Oklahoma, Kansas, Nebraska, Iowa, Missouri), the Rocky-Mountain Region (i.e., Western New Mexico, Colorado, Wyoming, Montana), and California [43]. The regression coefficients for the cost (in 2004 US dollars) of equipping an incremental injection well in each of these regions is presented in Table 29.

Table 29.   Regression coefficients for use in Equation 65 for the incremental cost of equipping an injection well for CO_2 storage in 2004 US dollars.

Region	States	Injection Equipment	
		a_1	a_2
1	West Texas	31226	8.57×10^{-5}
2	South Texas	37040	3.54×10^{-5}
3	South Louisiana	39876	3.45×10^{-5}
4	Mid-Continent Region	39876	3.45×10^{-5}
5	Rocky-Mountain Region	29611	7.92×10^{-5}
6	California	38931	6.39×10^{-5}

The costs predicted by using the above regression are the cost of equipping an injection well in a developed field. The EIA cost estimates are for the addition of eleven water injection wells to a field with ten production wells. Thus, the costs derived from this data should be scaled to represent the cost associated with projects where some infrastructure already exists. In the case of a new aquifer storage project, no prior infrastructure would exist. Thus, the average cost per well of installing *n* injection wells would be somewhat higher than the unit cost of installing *n+1* injection wells. The scaling equation used in the aquifer model is based on a power-law scaling rule [45], where the exponent of 0.5 is from Bock et al. [9]:

$$C_{IE,n} = \begin{cases} C_{IE}\left(\dfrac{21}{n}\right)^{0.5}, n \leq 21 \\ C_{IE}, n > 21 \end{cases} \qquad (66)$$

where C_{IE} is the scaled average cost of injection well equipment cost for n-wells ($ per well) and C_{IE} is the un-scaled average cost calculated from Equation 65 with coefficients from Table 29 ($ per well). Equation 66 shows that maximum economies of scale are assumed to be reached by 21 wells—the total number of wells in the EIA cost estimate—after which it is assumed that the cost no longer scales with the number of wells.

Project Capital Costs—Compression Equipment

In the case where the pipeline pressure is insufficient for CO_2 injection, a compressor must be added at the storage site. The total capital cost of a reciprocating compressor station has been estimated by the International Energy Agency (IEA) in a European study of the pipeline transmission of CO_2 [46]. That compressor cost model was also used in earlier in the pipeline transport model (see the Compressor Capital Cost Model section found in the Modeling CO_2 Transport by Pipeline chapter), and is given by Equation 67:

$$C = 8.35P + 0.49 \qquad (67)$$

where, C is the compressor capital cost in millions of US dollars (2004) and P is the installed booster station power in MW. This correlation yields a unit cost of $8,346 per kW of installed capacity.

Operating and Maintenance Costs

Operating and maintenance (O&M) costs for an aquifer storage project include expenses for labor, chemicals, and other consumables, plus expenses for surface equipment and subsurface equipment maintenance, including periodic well workovers. If CO_2 recompression is required, the cost of energy to operate the compressors is also and O&M cost.

O&M costs for CO_2 injection are assumed to be comparable to the costs of water injection for secondary oil recovery. This is consistent with the assumption made by Bock et al. [9] to assess the cost of aquifer storage and by Advanced Resources International for the cost of CO_2-flood EOR [44]. The O&M cost of water injection in secondary oil recovery at a field in West Texas is estimated annually by the EIA for 2,000 ft (610 m), 4,000 ft (1219 m) and 8,000 ft (2438 m) deep wells [43]. The form of the equation developed in this research to fit these data points again is given by Equation 65, shown earlier, with coefficient values given in Table 30.

The EIA O&M cost for water injection has been extended to other regions by scaling the West Texas O&M cost using the ratio of primary production O&M cost in the region of interest to the cost in West Texas. The EIA estimates the O&M cost of primary production for oil fields located in six regions: West Texas, South Texas, South Louisiana, the Mid-Continent Region (i.e., Oklahoma, Kansas, Nebraska, Iowa, Missouri), and the Rocky-Mountain Region (i.e., Western New Mexico, Colorado, Wyoming, Montana) [43]. The regression coefficients for the O&M cost (in 2004 US dollars) in each of these regions is presented in Table 30.

Table 30.   Regression coefficients for use in Equation 65 for O&M cost in 2004 US dollars per well.

Region	States	a_1	a_2
1	West Texas	26873	1.03×10^{-4}
2	South Texas	38954	9.60×10^{-5}
3	South Louisiana	38853	1.03×10^{-4}
4	Mid-Continent Region	26790	1.34×10^{-4}
5	Rocky-Mountain Region	32893	8.78×10^{-5}
6	California	29537	1.67×10^{-4}

Monitoring, Verification and Closure Costs

Like the cost of site characterization, the costs of monitoring and verification (M&V) and site closure will be highly dependent on the requirements of a regulatory regime, which has yet to be developed (e.g., see Wilson et al. [47]). Benson et al. [48] have estimated the cost of M&V for two hypothetical scenarios. In both cases it was assumed that 258 million tonnes of CO_2 was injected into an aquifer over a 30 year period, and seismic surveys are performed in the each

of the first two years, the fifth-year, and every fifth year thereafter for 80 years. One scenario assumed a low residual gas saturation, leading to a large CO_2 plume; the second scenario, a high residual gas saturation, leading to a small plume size. From these two scenarios Benson et al. [48] estimate the levelized cost of site characterization, operational M&V, and post-closure M&V to be between $0.05 and $0.08 per tonne of CO_2 injected. If the effects of discounting are ignored, the prorated share of the total cost estimated by Benson et al. [48] attributable to operating M&V is approximately $0.02 per tonne CO_2.

Additional cost of site closure to the operator could range from zero— for example, if the site performs as predicted and responsibility is transferred to the government—to many times the original capital cost—for example, if the site does not perform as predicted and responsibility for the stored CO_2 remains with the site owner or operator for an extended period of time. The analysis by Benson et al. [48] implicitly assumed that the site operator would be responsible for the cost of post-closure monitoring, and based on the total levelized of $0.05 to $0.08 per tonne, the levelized cost of post-closure M&V is very small. This suggests that a one-time charge (in real dollars) associated with closure could be very small, particularly considering that the charge occurs at the end of the project life, although there are no empirical basis for such estimates. Given these uncertainties, for purposes of cost estimation the model allows for either a lump-sum (real dollar) charge for the closure or a fee to be levied on each tonne of CO_2 injected that could be paid into a fund over the operating life of the project to cover the closure cost. Default values for both of these parameters are zero, but can be adjusted to explore other assumptions.

Illustrative Cost Model Results

Model Results for the cost of well drilling, completion and equipping for a project in West Texas with up to 40 injection wells are illustrated in Figure 66 for depths between 1000 and 3000 m. As shown earlier by the illustrative performance model results, the wellhead pressure (and thus the compressor power requirement) depends on depth and other performance model results. Thus, the cost shown in Figure 66 does not include the capital cost of compression equipment, which is shown in Figure 67, as a function of the compressor power requirement, which is determined from the performance model.
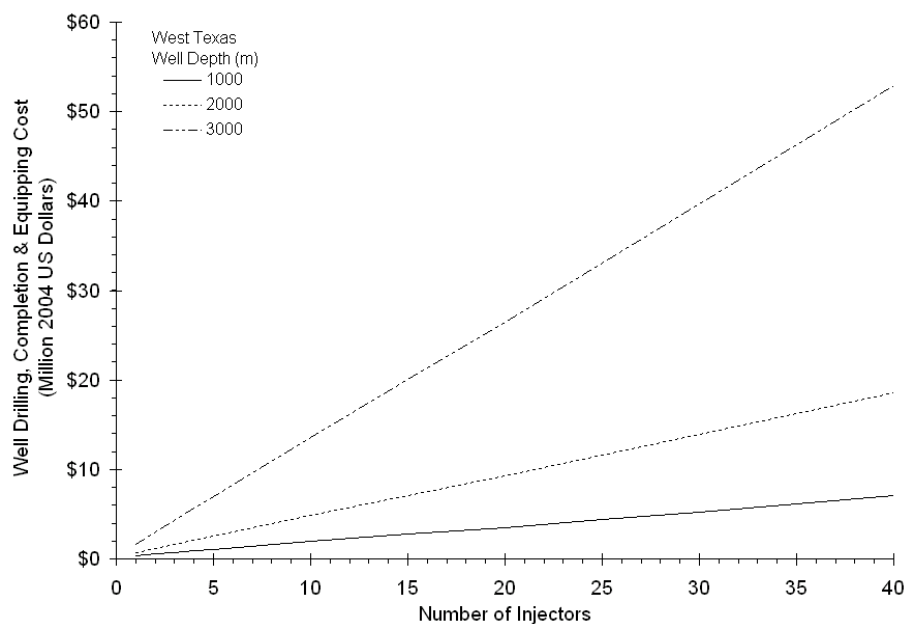
Figure 66.   Capital cost of well drilling, completion, and equipping for a project located in West Texas with up to 40 injection wells for depths of 1000, 2000, and 3000 m.
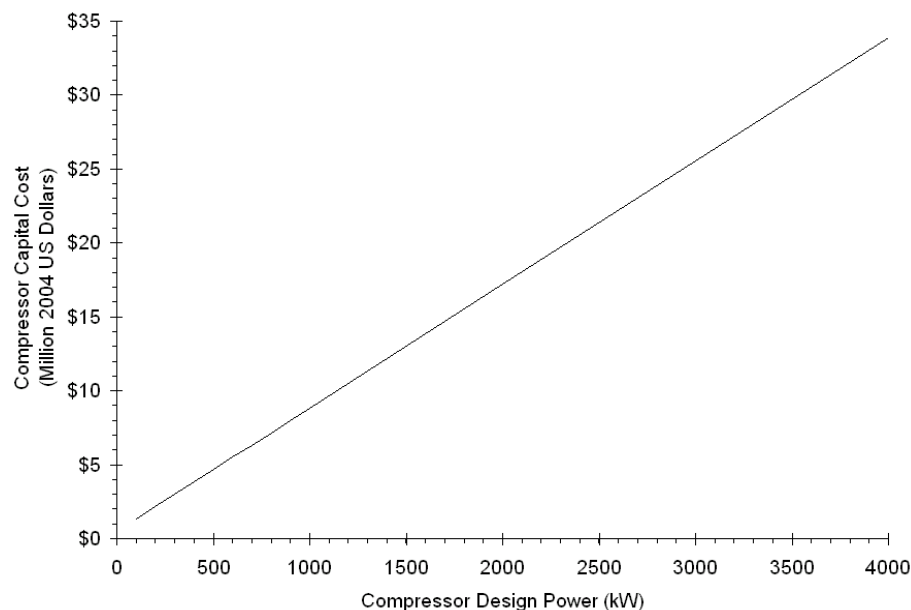
Figure 67.   The capital cost of compression equipment as a function of the compressor power requirement.

The cost of site characterization is shown in Figure 68. The steps in cost at radii of approximately 4.5 and 6.5 km are caused by the addition of a well to the characterization requirements.
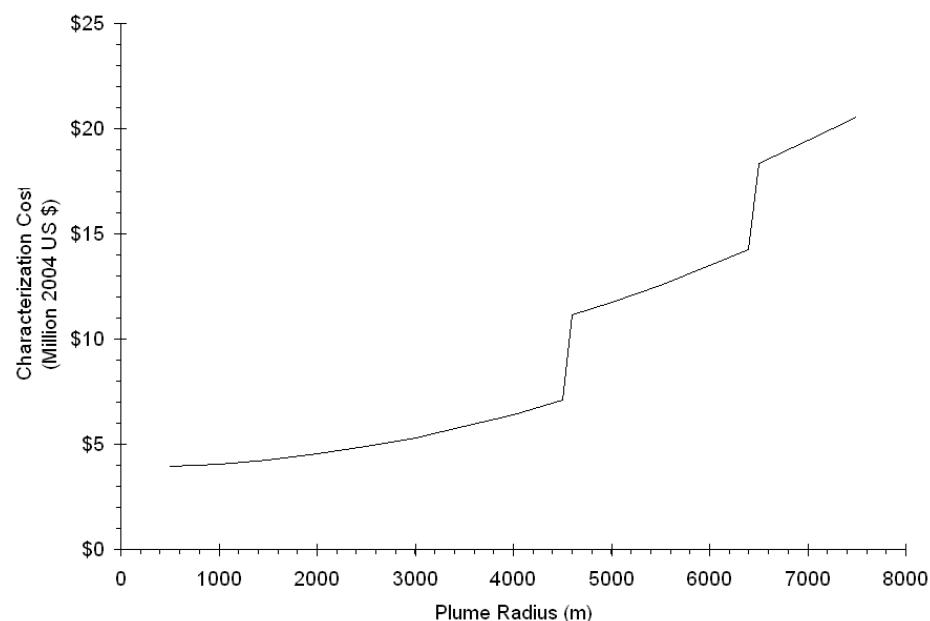
Figure 68.   The cost of site characterization used in the model for plume radii between 0.5 and 8.0 km.

The site characterization cost found here are considerably larger than that of some prior estimates for aquifer storage, where the cost was only $1.7 million (2003) dollars [49], and applied without consideration of project size [9, 50]. However, the costs in Figure 68 are similar to a more recent estimate by Benson et al. [48].

The operating and maintenance cost for a West Texas project, excluding the cost of any additional energy associated with compression and any M&V costs, are shown in Figure 69. The additional annual cost of M&V and site closure would depend on the CO_2 injection rate, much as the site characterization cost depends on injection rate, as well as the unit cost of monitoring activities. Assuming an injection rate of 3 Mt CO_2 per year—roughly equivalent to emissions

from a 500 MW coal fired power plant—and a combined cost of $0.03 per tonne CO_2 for M&V and site closure, the additional O&M cost would be approximately $0.1 million per year.
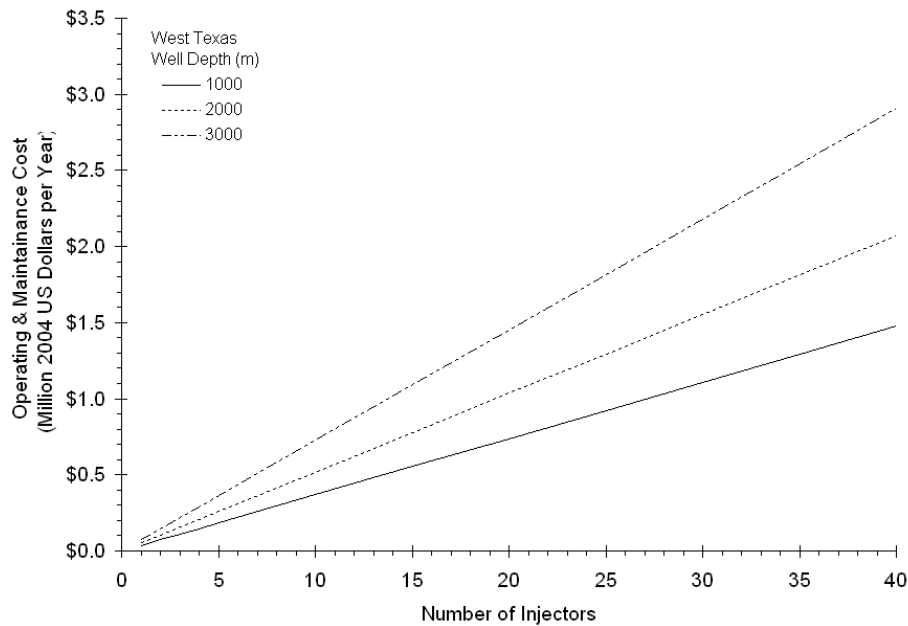
Figure 69. O&M cost for a West Texas project, excluding the cost of any required compression energy and any M&V costs

Combining Performance and Cost

The performance model takes inputs from the user, as shown in Figure 49, and calculates the number of wells required for the specified geology, injection rate, and limits on the BHIP via the methods discussed in Approximate Solution to Injectivity of a Doublet System. The number of wells is then adjusted upwards if the resulting injection rate for any single well is greater than 1 million tonnes CO_2 per year, which is the limit for the wellbore flow model (see Establishing the BHIP – Flow in the Wellbore). The adjusted number of wells, compressor power requirement (calculated via the method discussed in the Modeling CO_2 Transport by Pipeline chapter), and user inputs are used to estimate the capital cost of the project, as well as the O&M costs. Both capital and O&M costs are subject to capital cost escalation factors (i.e., multipliers) that can be adjusted to change the capital costs estimated by the model. The levelized cost of CO_2 storage is estimated by dividing the sum of the annualized capital costs (arrived at using a capital recovery factor) and the annual O&M cost by the product of the capacity factor and the design flow rate and adding any additional M&V cost and injection fees associated with site closure.

Illustrative Case Studies

The reservoir descriptions used in the performance model for the four illustrative case studies are listed in Table 27 and were previously used to illustrate the behavior of the performance model. The cost model parameters used in the case study are listed in Table 31 and are the same for each case for ease of comparisons. The design CO_2 flow rate and the capital recovery factor will be varied parametrically as part of the analysis.

The levelized cost of CO_2 storage predicted by the aquifer storage model is presented in Figure 70 for the four cases across a range of mass flow rates. For a design injection rate of 5 Mt CO_2 per year, the levelized cost of CO_2 storage is $0.82 per tonne CO_2 for the Purdy-Springer case; $8.85 per tonne CO_2 for the Joffre-Viking case; $0.35 per tonne CO_2 for the Liberty-Frio case; and, $0.75 per tonne CO_2 for the Lake Wabamun-Mannville case. Figure 71 shows the same results on an expanded scale for the three lowest-cost sites.

Table 31.   Cost model parameter values used in the four case studies.

Project Parameter	Deterministic Value
Capital Recovery Factor (%)	15
O&M Costs	
Compression Energy Cost ($/MWh)	40
Operating Monitoring & Verification ($/tonne)	0.02
Injection Fee ($/tonne)	0
Closure Cost ($)	0
Site Characterization Cost	
Geophysical Cost ($/km2)	38,610
Test Well Spacing (km2/well)	65
Test Well Cost ($/well)	3,000,000
Consulting Services (% of Total)	30
Capital Cost Escalation Factors	
Drilling & Completion	1.0
Injection Well Equipment	1.0
Compression Equipment	1.0
O & M Cost	1.0
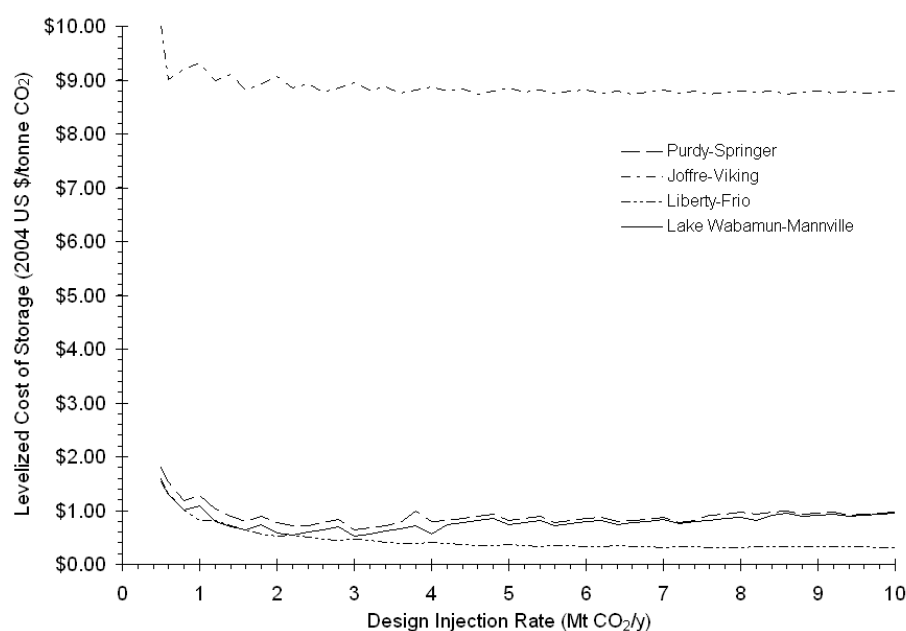
Figure 70. Levelized cost of CO_2 storage for the four cases across a range of design injection rates.

Several observations can be made from Figure 70 and Figure 71. First, the levelized cost of storage in the Joffre-Viking case is substantially higher than for any of the other cases. Second, the three "low-cost" cases show different behavior with increasing injection rates: the storage cost for the Liberty-Frio case continually declines over the range shown, whereas the cost for both Lake Wabamun-Mannville case and the Purdy-Springer case goes through a minimum at between 2 and 3 Mt CO_2 per year (shown most clearly by the smoothed curves). These differences in cost can be explained largely by examining the breakdown of total capital cost for each of the projects, shown in Figure 72 for 5 Mt CO_2 per year.
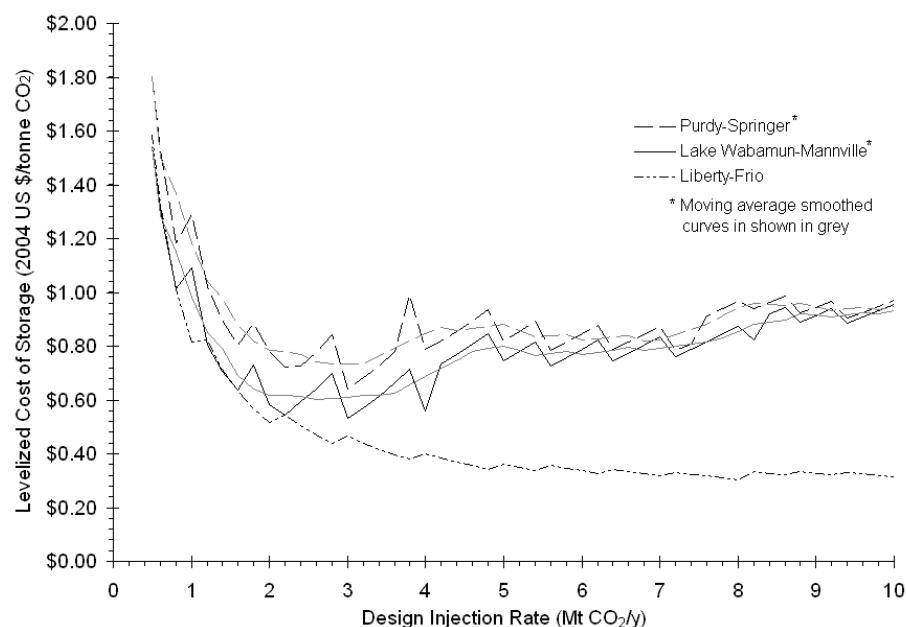
Figure 71.   Levelized cost of CO_2 storage for the three low-cost cases shown in Figure 70 across a range of design injection rates. Smoothed curves are shown in grey for the Purdy-Springer and the Lake Wabamun-Mannville cases.
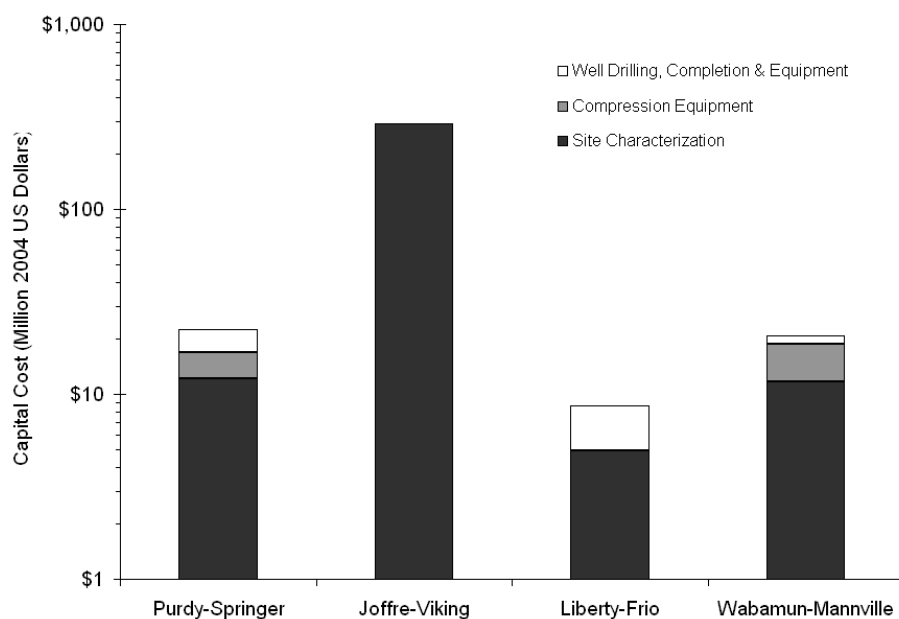
Figure 72.   Breakdown of capital cost for each of the four cases at 5 Mt per year CO_2. Note the logarithmic scale.

As the CO_2 injection rate increases, a trade-off between site characterization cost and compression cost (including resulting energy cost) occurs in the two intermediate cases, resulting in the minimums shown in Figure 71. For all four cases at 5 Mt CO_2 per year, Figure 72 shows that the capital cost of site characterization dominates the total capital cost. For the Joffre-Viking case the cost of site characterization represents nearly all of the capital cost because the aquifer properties (i.e., underpressured, relatively thin net sand, and high porosity) results in an abnormally large footprint for site characterization (i.e., almost 2600 km[2]). Conversely, the cost of site characterization for the Liberty-Frio site is much lower despite the high permeability of the Frio Sandstone because of the expansive net sand (i.e. aquifer net thickness),

which translates into a relatively small footprint (i.e., less than 50 km^2).[17] The Purdy-Springer and Wabamun Mannville cases are intermediate between these two cases; the cost of compression equipment being a more significant factor.

Model Sensitivity Analysis Results

To assess the sensitivity of the model to changes in multiple performance and economic parameters, uniform distributions were assigned to a number of parameters and the model was used to estimate the levelized cost of CO_2 storage over a Monte Carlo simulation for the Lake Wabamun-Mannville case. Uniform distributions were selected to represent uncertainty or variability because there is no prior information that would suggest choosing a more complex distribution (such as a triangular or lognormal distribution). Twelve performance model parameters and seven cost model parameters were assigned distributions; both the parameters and the distributions for the parameter values are listed in Table 32.

Table 32.   The uncertainty distributions for parameters considered in the sensitivity analysis of the Lake Wabamun-Mannville case.

Model Parameter	Uncertainty Distribution
Performance Model Parameters	
Planning Horizon (years)	Uniform (10,30)
$P_{wb,max}$ (% of p_{frac})	Uniform (80,90)
Depth (m)	Uniform (1435,1580)[a]
G_p (MPa/km)	Uniform (7.93,10.63)[a]
G_T (K/km)	Uniform (20,30)[b]
Net Sand (m)	Uniform (35.5,74.2)[a]
ϕ (%)	Uniform (8,15)[c]
X_{brine} (ppm$_w$)	Uniform (53369,90639)[a]
Cost Model Parameters	
Geophysical Cost ($/km^2)	Uniform (28958, 48263)[d]
Test Well Cost ($/well)	Uniform (2250000, 3750000)[d]
Capital Recovery Factor (%)	Uniform (10,20)
Energy Cost ($/MWh)	Uniform (40,20)
Operating Monitoring & Verification ($/tonne)	Uniform (0.01,0.03)[e]
Capital Cost Escalation Factors	
Escalation Factor for Drilling & Completion	Uniform(1.0,1.5)[d]
Escalation Factor for Injection Well Equipment	Uniform(1.0,1.5)[d]
Escalation Factor for O & M Cost	Uniform(0.75,1.25)[e]
Escalation Factor for Compression	Uniform(0.75,1.25)[e]

---

[17] The method used to estimate the aerial extent of the plume may not be appropriate for the Liberty-Frio case because the low velocity of the injected CO_2 means that buoyancy may be a large factor that can not be neglected [39]. Nordbotten et al [39] present a more complex alternative method that accounts for buoyancy which could be used in this scenario.

The Dykstra-Parsons coefficient was used as discussed in Describing Reservoir Heterogeneity to generate unique layered reservoirs for each of 1,000 Monte Carlo trials. The distributions for depth, geothermal and pressure gradients (G_p and G_T, respectively), net sand, porosity (ϕ), and total dissolved solids (X_{brine}) were derived from the Lake Wabamun dataset provided by the Alberta Geological Survey [38]. From these 1,000 trials cumulative distribution functions (CDF) were generated showing the breakeven CO_2 price, the net CO_2 utilization, and the cumulative mass of CO_2 stored.

Figure 73 shows the CDF for the levelized cost of CO_2 storage. The median cost of CO_2 storage is $0.95 per tonne CO_2, with a 90% confidence interval of $0.55 to $1.81 per tonne CO_2. Note that these results exclude 429 cases where the model could not meet the required injection rate using fewer than 100 injectors. In such scenarios, a project developer would likely look at other sequestration targets or use horizontal drilling to reduce the number of wells required.
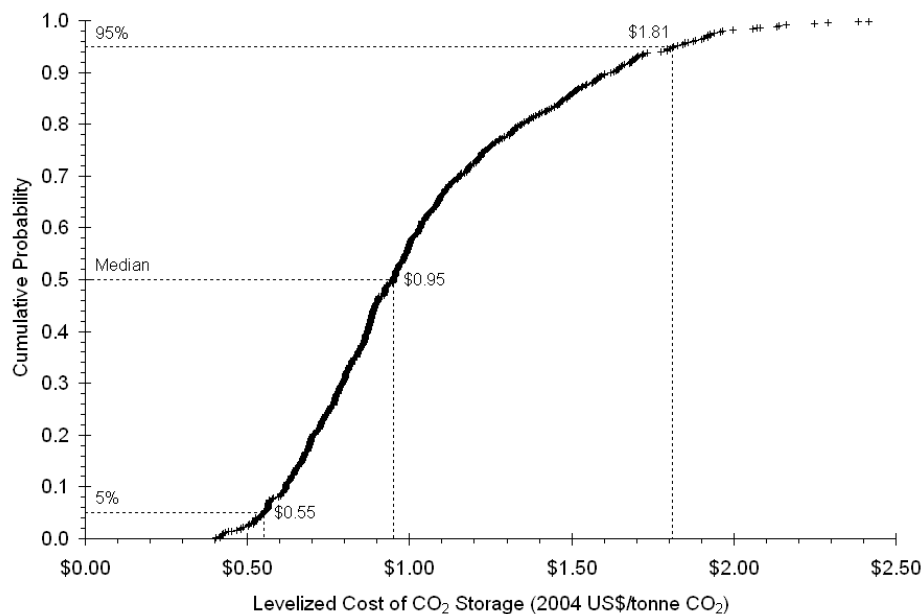
Figure 73. CDF for the levelized cost of CO_2 storage for the Lake Wabamun-Mannville case.
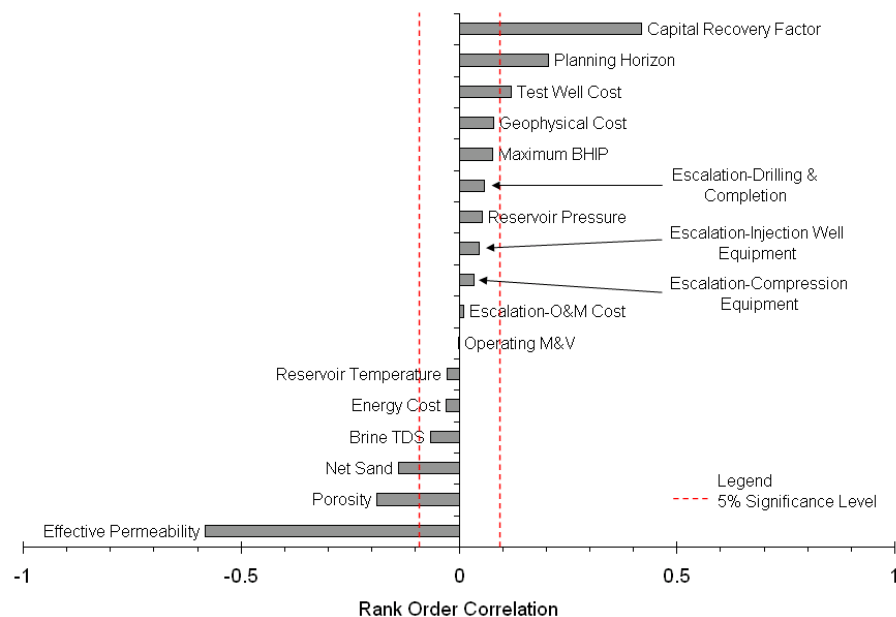
Figure 74.   Rank-order correlation between the results of the Monte Carlo sensitivity analysis and the parameters assigned uniform distributions.

Results of the Monte Carlo trials can also be used to assess the sensitivity of storage cost to the model parameters assigned uniform distributions. The measure used to assess the sensitivity is the Spearman rank-order correlation (r_s) [51]. The value of the rank order correlation coefficient for each model parameter is shown in Figure 74. The dashed vertical lines to the left and the right of the y-axis indicate the 5% significance level ($r_s = \pm 0.07$); thus rank-order correlation coefficients smaller than this value are not statistically significant at the 5% level. Figure 74 shows that the strongest correlation with the levelized cost of CO_2 storage is the effect of the effective permeability ($r_s = -0.58$) and, followed by the capital recovery factor ($r_s = 0.41$), planning horizon ($r_s = 0.21$), and porosity ($r_s = -0.19$). Following these, other significant rank-order correlation coefficients (by decreasing magnitude) are net sand thickness and test well cost.

Comparison with Other Models

The IPCC Special Report on Carbon Capture and Storage (SRCCS) [7] cited three studies as the basis for their estimates of aquifer storage costs, which ranged from $0.2 to $6.2 per tonne CO_2 excluding monitoring, verification & closure costs. Of those studies, only Bock et al. present a method [9] that related cost to the geology of a target formation. Bock et al. [9] used a correlation presented by Law and Bachu [11] to estimate the number of wells required for a design flow rate. The correlation developed by Law and Bachu [11] relates mass injection rate to reservoir permeability, k; net aquifer thickness, h; pressure difference between the initial pressure, p_i, and the BHIP, p_{wb}; and, CO_2 viscosity. That correlation, however, did not account for interactions between injection wells and, as Figure 47 shows, significantly overestimates the injectivity of a multi-well system.
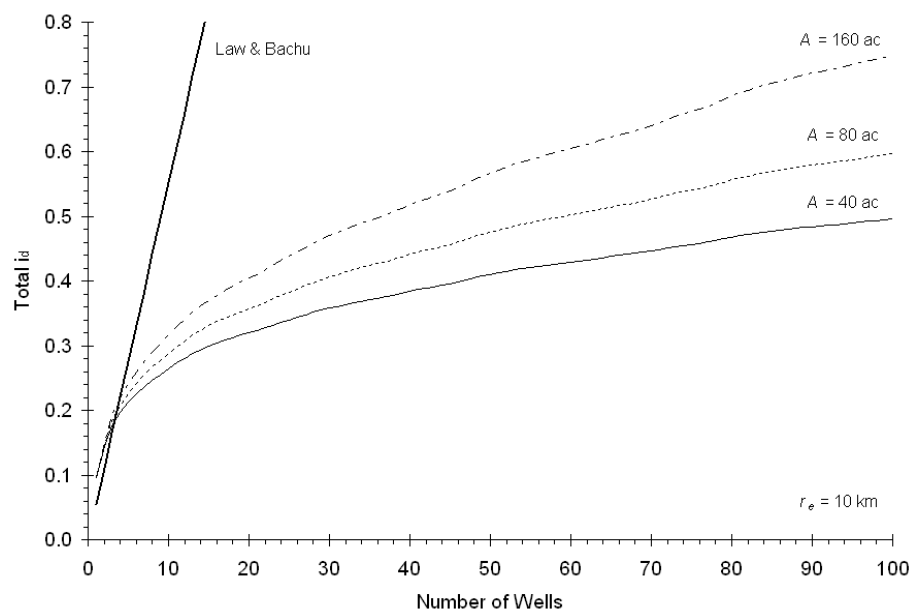
Figure 75. The total injectivity for systems with 1 to 100 wells on 40, 80, and 160 acre spacing with a constant pressure radius where $p_e = p_i$ at 10 km, compared with results of the correlation developed by Law & Bachu [11].

The costs used by the Bock et al. model [9] for well drilling and completion, and for injection equipment are based on the same data used in the model presented here (i.e., the EIA Oil and Gas Lease Equipment and Operating Cost index [43]); however, the cost of site characterization used by Bock et al. [9] was a fixed value substantially smaller than the values typically found here. Nor do Bock et al. report the stand alone values of storage cost; rather, they report only a combined cost of CO_2 transport and storage, so that systematic comparisons are not possible.

Overall, the results presented here are generally similar to the IPCC cost ranges for onshore CO_2 storage in aquifers. However, the case studies used here to estimate the cost of aquifer storage are different than those used in the three publications cited by the IPCC. Based on those prior studies, however, the IPCC concluded that the largest component of the storage cost was the cost of well drilling, completion and equipping [7]. In contrast, the examples presented here show these to be the smallest portion of the total cost of storage when current site characterization costs are accounted for.

References

1.   Bachu, S., *Screening and ranking of sedimentary basins for sequestration of CO₂ in geological media in response to climate change.* Environmental Geology, 2003. **44**: p. 277-289.
2.   Bachu, S. and K. Haug, *In-Situ Characteristics of Acid-Gas Injection Operations in the Alberta Basin, Western Canada: Demonstration of CO₂ Geological Storage*, in *The CO₂ Capture and Storage Project (CCP) for Carbon Dioxide Storage in Deep Geologic Formations for Climate Change Mitigation*, S. Benson, Editor. 2004, Elsevier Science.
3.   Bachu, S. and W.D. Gunter. *Overview of Acid-Gas Injection Operations in Western Canada*. in *7th International Conference on Greenhouse Gas Control Technologies*. 2004. Vancouver, Canada: Elsevier Science.
4.   Papanikolau, N., et al., *Safe storage of CO₂: experience from the natural gas storage industry*, in *8th International Conference on Greenhouse Gas Control Technologies*. 2006, Elsevier Science: Trondheim, Norway.
5.   Benson, S.M., et al., *Lessons Learned from Natural and Industrial Analogues for Storage*. 2002, Lawrence Berkley National Laboratory: Berkley, CA.
6.   Keith, D.W., et al., *Regulating the Underground Injection of CO₂*. Environmental Science & Technology, 2005. **39**: p. 499A-505A.

7. Benson, S., et al., *Underground geological storage*, in *IPCC Special Report on Carbon Dioxide Capture and Storage*, B. Metz, et al., Editors. 2005, Cambridge University Press: Cambridge, U.K.

8. Hendriks, C.F., *Carbon dioxide removal from coal fired power plants*. 1 ed. 1994: Kluwer Academic Publishers.

9. Bock, B., et al., *Economic Evaluation of CO_2 Storage and Sink Enhancement Options*. 2003, TVA Public Power Institute: Muscle Shoals, AL.

10. Allinson, W.G., D.N. Nguyen, and J. Bradshaw, *The Economics of Geological Storage of CO_2 in Australia*. APPEA Journal, 2003. **43**: p. 623-636.

11. Law, D.H.S. and S. Bachu, *Hydrogeological and Numerical Analysis of CO_2 Disposal in Deep Aquifers in the Alberta Sedimentary Basin*. Energy Conversion & Management, 1996. **37**(6-8): p. 1167-1174.

12. Wildenborg, T., et al. *Cost Curves for CO_2 Storage: European Sector*. in *7th International Conference on Greenhouse Gas Control Technologies*. 2004. Vancouver, Canada: Elsevier Science.

13. Craft, B. and M. Hawkins, *Applied Petroleum Reservoir Engineering*. 1st ed. Prentice-Hall Chemical Engineering Series. 1959, Englewood Cliffs, NJ: Prentice-Hall. 437.

14. Freeze, R.A. and J.A. Cherry, *Groundwater*. 1979, Englewood Cliffs, N.J.: Prentice-Hall. xvi, 604 p.

15. Bachu, S., et al., *CO_2 storage capacity estimation: Methodology and gaps*. International Journal of Greenhouse Gas Control, 2007. **1**(4): p. 430-443.

16. Chevron Australia, *Draft Environmental Impact Statement/Environmental Review and Management Programme for the Proposed Gorgon Development*. 2005, Chevron Austraila Pty Ltd: Perth, Australia.

17. Brigham, W., *Doublets and Other Allied Well Patterns*. 2000, Stanford University Petroleum Research Institute: Stanford, CA.

18. Press, W.H., *Numerical recipes in C : the art of scientific computing*. 2nd ed. 1992, Cambridge; New York: Cambridge University Press. xxvi, 994 p.

19. Selby, S.M., ed. *Standard Mathematical Tables*. 16th ed. 1968, The Chemical Rubber Co.: Cleveland, OH.

20. Nordbotten, J.M., M.A. Celia, and S. Bachu, *Analytical solutions for leakage rates through abandoned wells*. Water Resources Research, 2004. **40**(4).

21. Dake, L.P., *Fundamentals of reservoir engineering*. 1 ed. 1978: Elsevier.

22. Shafeen, A., et al., *CO_2 sequestration in Ontario, Canada. Part II: cost estimation*. Energy Conversion & Management, 2004. **45**: p. 3207-3217.

23. Pizarro, J.O.S. and L.W. Lake, *Understanding Injectivity in Heterogeneous Reservoirs*, in *SPE/DOE Improved Oil Recovery Symposium*. 1998, Society of Petroleum Engineers: Tulsa, OK.

24. Heller, J.P. and J.J. Taber, *Influence of Reservoir Depth on Enhanced Oil Recovery by CO_2 Flooding*, in *Permian Basin Oil & Gas Recovery Conference of the Society of Petroleum Engineers*. 1986, Society of Petroleum Engineers: Midland. TX.

25. Lake, L.W. and J.L. Jensen, *Review of heterogeneity measures used in reservoir characterization*. 1989, Society of Petroleum Engineers: Richardson, TX. p. 40.

26. Willhite, G.P., *Waterflooding*. SPE Textbook Series. 1986, Richardson, TX: Society of Petroleum Engineers. 326.

27. Jensen, J.L., D.V. Hinkley, and L.W. Lake, *A Statistical Study of Reservoir Permeability: Distributions, Correlations, and Averages*. SPE Formation Evaluation, 1987. **2**(4): p. 461-468.

28. Freeman, J. and R. Modarres, *Inverse Box-Cox: The power-normal distribution*. Statistics & Probability Letters, 2006. **76**(8): p. 764-772.

29. Gunter, W.D., et al., *Aquifer Disposal of CO_2-Rich Gases: In the Vicinity of the Sundance and Genesee Power Plants*. 1993, Alberta Department of Energy: Edmonton, AB.

30. Gunter, W.D., et al., *Central Alberta: CO_2 Disposal Into Alberta Basin Aquifers - Phase II*. 1994, Alberta Department of Energy: Edmonton, AB.

31. Hovorka, S.D., *Optimal Geological Environments for Carbon Dioxide Disposal in Saline Aquifers in the United States*. 1999, Bureau of Economic Geology, University of Texas at Austin: Austin, TX. p. 63 p.

32. Simlote, V.N. and E.M. Withjack, *Estimation of Tertiary Recovery by CO_2 Injection--Springer A Sand, Northeast Purdy Unit*. Journal of Petroleum Technology, 1981(May): p. 808-818.

33. Stephenson, D.J., A.G. Graham, and R.W. Luhning, *Mobility Control Experience in the Joffre Viking Miscible CO_2 Flood*. SPE Reservoir Engineering, 1993(August): p. 183-188.

34. Alberta Geological Survey. *Major Basin Units for CO_2 Sequestration*. 2005 [cited 2007 December 29]; Available from: http://www.ags.gov.ab.ca/website/co2_formation/viewer.htm.

35.   Hovorka, S.D., C. Doughty, and M.H. Holtz, *Testing Efficiency of Storage in the Subsurface: Frio Brine Pilot Experiment*, in *7th International Conference on Greenhouse Gas Control Technologies*. 2004: Vancouver, Canada.

36.   Hovorka, S.D., et al., *Evaluation of Brine-Bearing Sands of the Frio Formation, Upper Texas Gulf Coast for Geological Sequestration of CO2*, in *First National Conference on Carbon Sequestration*. 2001, National Energy Technology Lab: Washington, DC.

37.   Holtz, M.H., et al., *Geologic Sequestration in Saline Formations: Frio Brine Storage Pilot Project, Gulf Coast Texas*, in *Fourth Annual Conference on Carbon Capture & Sequestration*. 2005: Alexandria, VA.

38.   Alberta Geological Survey. *Test Case for Comparative Modelling of CO2 Injection, Migration and Possible Leakage - Wabamun Lake Area, Alberta, Canada*. 2006 May 1 [cited 2007 December 29]; Available from: http://www.ags.gov.ab.ca/activities/wabamun/wabamun_base.html.

39.   Nordbotten, J.N., M.A. Celia, and S. Bachu, *Injection and Storage of CO2 in Deep Saline Aquifers: Analytical Solution for CO2 Plume Evolution During Injection.* Transport in Porous Media, 2005. **58**: p. 339-360.

40.   Tombari, J., Schlumberger Limited. *RE: Site Characterization Costs for GS.* Personal Communication, 21 December 2007.

41.   American Petroleum Institute, *Joint Association Survey on Drilling Costs*. 2002, American Petroleum Institute: Washington, DC. p. 111.

42.   Lewin & Associates Inc., *Economics of Enhanced Oil Recovery*. 1981, Department of Energy: Washington, DC. p. 123.

43.   Energy Information Administration. *Oil and Gas Lease Equipment and Operating Costs 1988 Through 2006*. 18 June 2007 [cited 26 September 2007]; Available from: http://www.eia.doe.gov/pub/oil_gas/natural_gas/data_publications/cost_indices_equipment_production/current/coststudy.html.

44.   Advanced Resources International, *Basin Oriented Strategies for CO2 Enhanced Oil Recovery: Permian Basin*. 2006, US Department of Energy: Arlington, VA. p. 117.

45.   Perry, R.H., D.W. Green, and J.O. Maloney, *Perry's chemical engineers' handbook*. 7th ed. 1997, New York: McGraw-Hill.

46.   Woodhill Engineering Consultants, *Pipeline Transmission of CO2 and Energy: Transmission Study - Report*. 2002, IEA Greenhouse Gas R&D Programme: Stoke Orchard, UK.

47.   Wilson, E.J., S.J. Friedmann, and M.F. Pollak, *Research for deployment: Incorporating risk, regulation, and liability for carbon capture and sequestration.* Environmental Science & Technology, 2007. **41**(17): p. 5945-5952.

48.   Benson, S.M., et al. *Monitoring Protocols and Life-Cycle Costs for Geologic Storage of Carbon Dioxide*. in *7th International Conference on Greenhouse Gas Control Technologies*. 2004. Vancouver, Canada: Elsevier Science.

49.   Smith, L., et al., *Carbon Dioxide Sequestration in Saline Formations- Engineering and Economic Assessment Final Technical Report*. 2001, Battelle Memorial Institute: Columbus, OH. p. 93.

50.   McCoy, S.T. and E.S. Rubin, *Models of CO2 Transport and Storage Costs and Their Importance in CCS Cost Estimates*, in *Fourth Annual Conference on Carbon Capture and Sequestration*. 2005: Alexandria, VA.

51.   Morgan, M.G., M. Henrion, and M. Small, *Uncertainty : a guide to dealing with uncertainty in quantitative risk and policy analysis*. 1990, Cambridge: Cambridge University Press. 332.

Conclusions

In this report models have been developed to estimate the performance and cost of CO_2 transport by pipeline, CO_2 storage through enhanced oil recovery, and CO_2 storage in saline aquifers. Each of the models was used to estimate cost and performance for a range of cases involving CO_2 transport and storage. Moreover, the sensitivity of cost to input parameter changes was quantified using the probabilistic assessment capabilities of the models. Sections Pipeline Transport of CO_2 – Results and Implications through CO_2 Storage in Deep Saline Aquifers – Results and Implications summarize results from each of the models and discuss the implications of these results. Sections Limitations of These Results and Future Work review the limitations of the results and suggest several directions for future work.

Pipeline Transport of CO$_2$—Results and Implications

Figure 76 summarizes results from the CO_2 pipeline transport model based on inputs listed in the Modeling CO_2 Transport by Pipeline chapter. This figure illustrates how the cost of pipeline transport varies with distance, design capacity, and region of construction. Economies of scale in CO_2 transport are clearly evident in Figure 76, suggesting that it may be more efficient to encourage hub-and-spoke transport systems rather than point-to-point systems to transport large amounts of CO_2. In either case, current regulations for CO_2 pipelines may have to be revised and expanded to effectively regulate a large infrastructure for transport of CO_2.
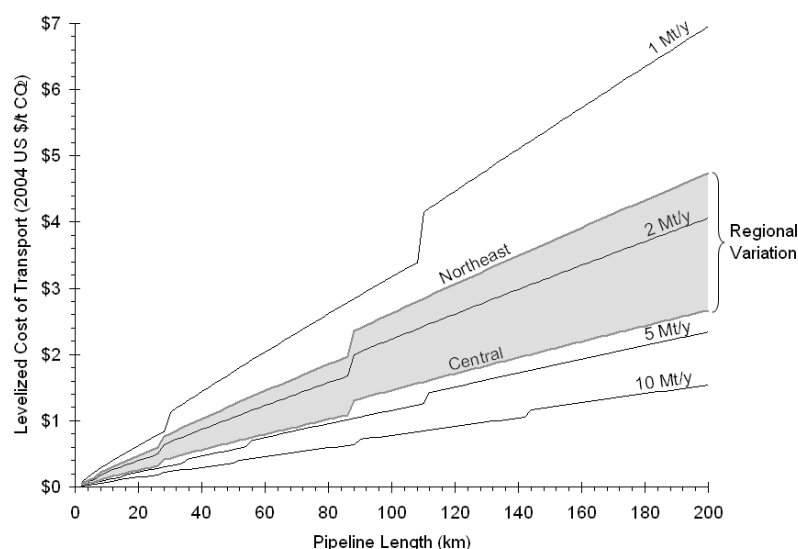
Figure 76. Illustrative results for the levelized cost of CO_2 transport (in constant 2004 US dollars) over a range of pipeline design capacities and pipeline distances.

CO$_2$ Storage through Enhanced Oil Recovery—Results and Implications

Unlike the cases of CO$_2$ transport or saline aquifer storage, it is not possible to estimate a meaningful levelized cost of CO$_2$ storage for CO$_2$-flood EOR. This is because the CO$_2$ storage function of this process has traditionally been a secondary effect of oil recovery—the main motivation for this process. However, the breakeven cost of CO$_2$ (i.e., the cost of CO$_2$ at which the project has a net present value of zero) can be interpreted as the highest price a CO$_2$-flood developer would be willing to pay for CO$_2$ delivered to the site based on the assumed benchmark oil price (and numerous other factors). The amount of oil produced, CO$_2$ stored, and the breakeven CO$_2$ prices for four cases examined with the EOR model are shown in Table 33.

Table 33.   Results for the four EOR case studies from the Enhanced Oil Recovery (EOR) chapter showing cumulative oil produced in million barrels (mmbbl), cumulative CO$_2$ stored, the CO$_2$ storage rate (tonnes per barrel), and the breakeven CO$_2$ price for two West Texas Intermediate (WTI) oil prices.

Field	Oil Produced (mmbbl)	CO$_2$ Stored (Mt)	CO$_2$ Storage Rate (t/bbl)	Breakeven CO$_2$ Price ($/tonne CO$_2$)	
				$50/bbl (WTI)	$100/bbl (WTI)
Northeast Purdy Unit	36	5.8	0.16	$83	$315
SACROC Unit, Kelly-Snyder Field	402	83.3	0.21	$120	$310
Ford Geraldine Unit	13	2.3	0.18	$34	$243
Joffre Viking Pool	23	3.3	0.14	$123	$392

Across the range of oil prices experienced over the last several years (since about 2004), the breakeven prices for CO$_2$ estimated from the case studies range from a low of $34 per tonne CO$_2$ ($1.79 per mscf CO$_2$) to a high of $392 per tonne CO$_2$ ($20.75 per mscf CO$_2$). These results emphasize the wide range of EOR project profitability and the wide range in the amount of CO$_2$ that can be stored through EOR projects—although it should be noted that projects like the SACROC Unit, with fairly large CO$_2$ storage capacity are the exception; most operating EOR projects have smaller CO$_2$ storage capacities. These results also suggest that there is ample profit incentive to early entrants who are able to provide CO$_2$ for new EOR projects because typical CO$_2$ capture costs are much lower than the prices shown in Table 33.

The results from these case studies also highlight that, for many EOR projects, the rate of CO$_2$ storage and the total capacity for CO$_2$ storage are very small in relation to the rate and amount of CO$_2$ produced by a modern coal-fired power plant (i.e., 2 to 3 Mt CO$_2$ per year for 500 MW of coal fired capacity). This highlights that the viability of CO$_2$-flood EOR as a means to mitigate CO$_2$ emissions hinges on whether there are fields remaining that are amenable to CO$_2$-flooding that can accept these large amounts of CO$_2$ at practical rates. In a study of the Alberta and Williston Basins (Western Canada), Bachu and Shaw found that the majority of EOR-related CO$_2$ storage capacity is in a very small fraction of reservoirs and that when reservoirs with total capacities of less than 1 Mt CO$_2$ were excluded, only 2% of reservoirs were suitable for CO$_2$ storage [1]. The results would likely be similar for other sedimentary basins. Consequently, CO$_2$-flood EOR alone will not be the solution for mitigating emissions on a large-scale.

In addition, the results of the case studies show that the CO$_2$ storage rate in tonnes per bbl oil is relatively small compared to the CO$_2$ emissions produced from the consumption of the oil. One typical barrel of light oil[18] contains approximately 0.7 tonnes C, which if fully oxidized produces 1.2 tonnes of CO$_2$ (excluding emissions associated with the additional energy used in oil refining, such as from hydrotreating). This compares to the CO$_2$ storage rates in Table 33 of 0.14 to 0.21 tonnes CO$_2$ per barrel of oil produced. Thus, CO$_2$ stored in any of the case study projects would not offset emissions from the combustion of oil produced from the project. On the other hand, if the marginal barrel of oil displaced by CO$_2$-flood EOR production were from a carbon-intensive source, oil sands for example [2], CO$_2$-flood EOR would result in a net emissions reduction compared with consumption of the marginal barrel. Thus, whether CO$_2$-flood EOR results in a net emission of CO$_2$ is sensitive to the source of the hydrocarbon that EOR production is assumed to displace on the supply curve.

---

[18] Assuming that one kilogram of oil contains 0.84 kilograms of carbon with a gravity of 35 to 40°API (equivalent to the carbon content of decane, C$_{10}$H$_{22}$).

CO$_2$ Storage in Deep Saline Aquifers—Results and Implications

Results of the aquifer storage case studies show a large range of variability in the cost per tonne of CO$_2$ stored, driven primarily by differences in aquifer geology and petrophysical properties. For a design injection rate of 5 Mt CO$_2$ per year, the levelized cost of CO$_2$ storage ranged from \$0.35 per tonne CO$_2$ for the Liberty-Frio case to \$8.85 per tonne CO$_2$ for the Joffre-Viking case. Considering only the costs of well drilling and completion, and injection equipment, the capital cost of all of the cases was relatively similar; however, inclusion of the cost of site characterization changed the results greatly. For all of the cases, the largest portion of the total levelized cost (ranging from 45% for Liberty-Frio to 98% for Joffre-Viking) was the cost of site characterization. The importance of assumptions regarding site characterization cost (and the implied methods of site characterization) to the levelized cost of CO$_2$ storage in saline aquifers has not been previously demonstrated.

The large contribution of site characterization cost to the levelized cost of storage implies that requirements for site characterization imposed by a regulatory framework should be carefully considered. Requirements for high-resolution characterization methods (e.g. 3D-seismic, as assumed here) or larger areas of review will increase the levelized cost of storage. However, the upfront cost requirements for characterization could be managed by, for example, limiting the area of review to the area impacted for a specified time horizon (e.g., the planning horizon for a project), with provision for further characterization prior to extension of the operation past the original planning horizon.

Limitations of These Results

The results for CO$_2$ transport and storage costs presented here are based on a limited number of illustrative case studies. While the models can be applied to a wider range of cases, caution must be exercised when applying the results presented here to different situations. For example, the effect of pipeline routing on transport cost is not considered by the pipeline transport model. Thus, it is entirely possible that the cost of a pipeline in a nominally high-cost region (e.g., Northeast US) could be lower than the cost of a particular pipeline in a generally lower-cost region (e.g., Central US) depending on the pipeline routing because of factors such as complex terrain, river crossings, and high population densities. Other tools are available that allow such details of pipeline routing to be considered (e.g., Zhang et al. [3]), and can be used in conjunction with this model to develop more accurate cost estimates. Thus, cost differences between regions should be interpreted only as being broadly representative.

Similarly, the illustrative cases for both EOR and aquifer storage were selected based on available data. While descriptions of a large number of CO$_2$-flood EOR projects have been published, particularly in *Society of Petroleum Engineers* journals, the data available on saline aquifers suited to CO$_2$ injection are much sparser. Consequently, the four EOR cases represent a range of typical projects based on those that have been developed to date, while the two additional aquifer storage cases may not cover as broad a range of potential projects. Thus, it is possible that some storage projects, particularly aquifer storage projects, could exhibit considerably different cost behavior.

In addition, the CO$_2$-flood EOR model was developed to answer questions about the cost of EOR storage in cases where a reservoir-specific answer is desired but limited information is available; or, where an answer is desired with minimal effort and cost. Far more accurate estimates can be made using more advanced models [4], particularly if a history-matched model of the reservoir is available. Such estimates are far more time-consuming and costly to obtain, but, are necessary to support investment decisions on EOR projects. Conversely, where there is inadequate information to even apply the less-complex model presented here, rule-of-thumb based methods are more appropriate (e.g., see Bock et al. [5]). Similarly, the aquifer storage model presented here fills the niche where adequate data is available to apply the model, but the insufficient to support analysis using more complex simulators (e.g. see Pruess et al. [6]).

Future Work

All of the models developed here are suitable for use in addressing a variety of questions related to policies and projects for carbon capture and storage. Perhaps the most pressing need for future work, however, concerns the development of data needed to estimate CO$_2$ storage costs. Given the necessary geological data to allow storage cost from site to site to be differentiated, the models developed here could be used to perform source-sink matching and to generate regional cost

curves. However, data characterizing aquifers at the project-level scale appropriate for use of the screening model developed here are not widely available. While the US Department of Energy (DOE)—though its Regional Carbon Sequestration Partnerships—has produced a "Carbon Sequestration Atlas of the United States and Canada," [7] the data in that atlas are too small-scale for use in the type of model developed here. Thus, it is currently difficult to estimate the practical capacity available for CO_2 storage at local scales [8], or to generate reliable cost curves (i.e., the cost of storing increasing amounts of CO_2) on a national scale. Thus, collection, aggregation, and application of the model to this required data is a significant area for future research.

The CO_2 transport and storage models presented here can also be used to assess the impact of regulatory requirements on the cost of CCS. Future work could analyze a number of alternative regulatory scenarios to examine their impact on cost. This type of analysis could be used as part of a benefit-cost analysis, or a cost-effectiveness analysis, of proposed regulations for CO_2 capture and storage. The models developed here would be valuable tools to help evaluate different proposals.

References

1.   Bachu, S. and J. Shaw, *Evaluation of the CO_2 sequestration capacity in Alberta's oil and gas reservoirs at depletion and the effect of underlying aquifers.* Journal of Canadian Petroleum Technology, 2003. **42**(9): p. 51-61.
2.   Brandt, A.R. and A.E. Farrell, *Scraping the bottom of the barrel: greenhouse gas emission consequences of a transition to low-quality and synthetic petroleum resources.* Climatic Change, 2007. **84**(3-4): p. 241-263.
3.   Zhang, H., W. Li, and H. Herzog, *MIT CO_2 Pipeline Transport and Cost Model.* 2007, Massachusetts Institute of Technology: Carbon Capture and Sequestration Technologies Program: Boston, Massachusetts.
4.   Gerritsen, M.G. and L.J. Durlofsky, *Modeling fluid flow in oil reservoirs.* Annual Review of Fluid Mechanics, 2005. **37**: p. 211-238.
5.   Bock, B., et al., *Economic Evaluation of CO_2 Storage and Sink Enhancement Options.* 2003, TVA Public Power Institute: Muscle Shoals, AL.
6.   Pruess, K., et al., *Numerical Modeling of Aquifer Disposal of CO_2*, in *SPE/EPA/DOE Exploration and Production Environmental Conference.* 2001, Society of Petroleum Engineers: San Antonio, TX.
7.   National Energy Technology Lab, *Carbon Sequestration Atlas of the United States and Canada.* 2007, Pittsburgh, PA: US Department of Energy. 86.
8.   Bachu, S., et al., *CO_2 storage capacity estimation: Methodology and gaps.* International Journal of Greenhouse Gas Control, 2007. **1**(4): p. 430-443.

Estimation of Physical Properties

Physical properties are the attributes of a substance that can be measured directly or indirectly through experimentation, such as density, enthalpy, and viscosity. Estimation of the physical properties of CO_2 and CO_2-containing mixtures is of critical importance in the design of transport and injection systems for carbon capture and storage as well as the behavior of injected CO_2 in the subsurface. Additionally, in the case of enhanced oil recovery (EOR), it is necessary to know the physical properties of crude oils at reservoir conditions. This appendix discusses the methods employed to estimate physical properties of both CO_2 and CO_2-containing mixtures and crude oils in the models developed in this report.

Physical Property Estimation for Pure Fluids and Fluid Mixtures

Fluids are a phase of matter, capable of flowing under an applied shear stress (i.e., they will flow from high pressure to low pressure) and can be either gaseous or liquid. A pure fluid consists of only one substance (e.g., Hg or CO_2). Conversely, a fluid mixture, such as acid gas, contains more than one substance (e.g., in the case of acid gas, H_2S, CO_2, and other minor constituents) and its physical properties are a function of composition. While crude oils are fluid mixtures, they contain on the order of hundreds of hydrocarbon components, as well as non-hydrocarbon impurities, and can not easily be treated in the same way as a pure fluid or simple fluid mixture. Consequently, they are treated separately in Properties of Crude Oils. The following sections discuss pressure-volume-temperature relationships (PVT) for pure fluids and simple fluid mixtures, thermodynamic property and transport property estimation for these mixtures, and finishes by comparing the accuracy of different calculation methods.

Pressure-Volume-Temperature Relationships

Equations of state (EOS) relate the pressure, volume and temperature of pure fluids and fluid mixtures. The relationship between pressure, p, molar volume, v, and temperature, T, can be expressed by the compressibility, Z:

$$Z = \frac{pv}{RT} \tag{68}$$

where R is the universal (or ideal) gas constant. When $Z = 1.0$, Equation 68 reduces to the familiar ideal gas law. However, for real gases (or liquids) Z is generally less than 1, and near the critical point Z changes rapidly with pressure and temperature. Thus for a typical single-phase, real-gas system where pressure and temperature are fixed, Equation 68 shows that the compressibility must be estimated to calculate the density of the system (or vice versa).

To describe both liquids and gases, an EOS must be at least cubic in V and to be analytically tractable must be no greater than quartic in V [1]. An EOS that fits these requirements was proposed by van der Waals over a century ago and was the first cubic EOS [2]. To date, there are over 400 parameterizations of the cubic EOS proposed in literature [2], however, only small number of these equations are commonly used.

generalized cubic EOS can be written [1]:

$$p = \frac{RT}{v-b} - \frac{\Theta(v-\eta)}{(v-b)(v^2 + \delta v + \varepsilon)}$$

For all of the parameterizations of the cubic EOS discussed here, $\eta = b$, thus this generalized equation reduces to Equation 69.

$$p = \frac{RT}{v-b} - \frac{\Theta}{v^2 + \delta v + \varepsilon} \qquad (69)$$

In Equation 69, b, δ, ε, and Θ are fluid specific parameters that vary depending on the parameterization used.

To solve the cubic EOS analytically for compressibility using the cubic equation, it must be rewritten in terms of Z, and set equal to zero:

$$Z^3 + (\delta' - B' - 1)Z^2 + [\Theta' + \varepsilon' - \delta'(B'+1)]Z - \varepsilon'(B'+1) + \Theta'B' = 0$$

where the dimensionless parameters are defined.

$$B' = \frac{bp}{RT} \quad \delta' = \frac{\delta p}{RT} \quad \Theta' = \frac{\Theta p}{RT} \qquad \varepsilon' = \varepsilon\left(\frac{P}{RT}\right)^2 \qquad (70)$$

The parameterizations available in the models are listed in Table 34, Table 35, and Table 36. These parameterizations represent a range from those commonly used in the process and reservoir engineering fields, such as Soave, 1972 (commonly referred to as SRK) or Peng and Robinson, 1976, to more recent and less commonly used parameterizations, such as Twu et al, 1995. In the remainder of this discussion, the custom of referring to different parameterizations as EOS will be followed. For example, the Peng and Robinson parameterization will be referred to as the Peng and Robinson EOS.

Table 34.   The seven cubic EOS available in the models developed for this report.

EOS	δ	ε	Θ
Redlich & Kwong (1949)	b	0	$a\alpha(T_r)$
Wilson (1964)	b	0	$a\alpha(T_r)$
Soave (1972)	b	0	$a\alpha(T_r)$
Peng & Robinson (1976)	$2b$	$-b^2$	$a\alpha(T_r)$
Soave (1984)	$2c$	c^2	$a\alpha(T_r)$
Patel, Teja & Valderrama (1990)	$b+c$	$-bc$	$a\alpha(T_r)$
Twu et al. (1995)	$2b$	$-b^2$	$a\alpha(T_r)$

The $\alpha(\omega,T_r)$ term listed in Table 35 is referred to as the attractive term of the cubic EOS, and is the only temperature dependent term in the equations of state presented here. However, the attractive term is dependent on the reduced temperature, T_r, which is the temperature relative to the fluid critical temperature, T/T_c. In addition, the attractive term is a function of the Pitzer acentric factor, ω, which relates to the vapor pressure of a pure species measured at a fixed T_r.

Table 35. *The temperature-dependent attractive terms for the cubic EOS available in the models developed for this report.*

EOS	$\alpha(\omega, T_r)$
Redlich & Kwong (1949)	$1\big/T_r^{1/2}$
Wilson (1964)	$\left[1+(1.57+1.62\omega)(1/T_r-1)\right]T_r$
Soave (1972)	$\left[1+\left(0.48+1.574\omega-0.176\omega^2\right)\left(1-\sqrt{T_r}\right)\right]^2$
Peng & Robinson (1976)	$\left[1+\left(0.37464+1.54226\omega-0.2699\omega^2\right)\left(1-\sqrt{T_r}\right)\right]^2$
Soave (1984)	$\left[1+\left(0.4998+1.5928\omega-0.19563\omega^2+0.025\omega^2\right)\left(1-\sqrt{T_r}\right)\right]^2$
Patel, Teja & Valderrama (1990)	$\left[1+\left(0.46283+3.58230\omega Z_c+8.19417\omega^2 Z_c^2\right)\left(1-\sqrt{T_r}\right)\right]^2$
Twu et al. (1995)	$T_r^{-0.171813}e^{\left[0.125283\left(1-T_r^{1.77634}\right)\right]}+...$ $...\omega\left\{T_r^{-0.607352}e^{\left[0.511614\left(1-T_r^{2.20517}\right)\right]}-T_r^{-0.171813}e^{\left[0.125283\left(1-T_r^{1.77634}\right)\right]}\right\}$

Table 36. *Coefficients for the cubic EOS listed in Table 34.*

EOS	$\dfrac{ap_c}{(RT_c)^2}$	$\dfrac{bp_c}{RT_c}$	$\dfrac{cp_c}{RT_c}$
Redlich & Kwong (1949)	0.42748	0.08664	-
Wilson (1964)	0.42748	0.08664	-
Soave (1972)	0.42748	0.08664	-
Peng & Robinson (1976)	0.45724	0.0778	-
Soave (1984)	0.42188	0.08333	0.04167
Patel, Teja & Valderrama (1990)	$0.66121-0.76105Z_c$	$0.02207+0.20868Z_c$	$0.57765-1.87080Z_c$
Twu et al. (1995)	0.457236	0.0778	-

All of the parameters for the cubic EOS discussed thus far have been in terms of pure component properties—ω, T_c, and P_c. To accommodate fluid mixtures, mixing rules must be used that define the cubic EOS parameters based on the pure fluid parameters. While there are a number of more modern mixing rules available, many of which are reviewed by Valderrama [2], simple van der Waals-type rules [1, 3] have been used here.

$$b_m = \sum_{i=1}^{n} y_i b_i$$

$$\Theta_m = \sum_{i=1}^{n}\sum_{j=1}^{n} y_i y_j \Theta_{ij}$$

$$\Theta_{ij} = \begin{cases} \Theta_i\,, & \text{if } i=j \\ \sqrt{\Theta_i \Theta_j}\left(1-k_{ij}\right)\!, & \text{if } i\neq j \end{cases}$$

(71)

Where *y* represents the mole fraction of the component, and *n* is the number of components in the system.

Estimation of Real Fluid Thermodynamic Properties

Thermodynamic properties or potentials are a measure of the amount of energy stored in a system. In this context, properties of interest are the enthalpy, H, entropy, S, heat capacity at constant pressure, C_p, and at constant volume C_v.

With the exception of ideal-gas heat capacity, C_p^{ig}, these properties are not directly measurable; rather they are derived from pressure-volume-temperature relationships. Moreover, excepting C_p, it is not possible to estimate absolute values of these properties; only differences can be defined. These properties are referred to as state properties.

For ease of calculation, these state properties are estimated as departures from the ideal gas value. For any generic thermodynamic state property, M, the departure function is defined as:

$$M^d = M^{ig} - M \qquad (72)$$

where M^{ig} is the ideal gas value of the thermodynamic property and M is the real gas value.

The departure functions for enthalpy and entropy are generated from the departure function for Gibbs free energy, G^d. It can be shown that [3]:

$$d\left(\frac{G^d}{RT}\right) = \frac{v^d}{RT}\,dp - \frac{H^d}{RT^2}\,dT$$

Thus at constant temperature:

$$d\left(\frac{G^d}{RT}\right) = \frac{v^d}{RT}\,dp$$

The departure function for volume is simply defined:

$$\frac{v^d}{RT} = \frac{(1-Z)}{p}$$

and, making the appropriate substitution:

$$\frac{G^d}{RT} = \int_0^p (1-Z)\frac{dp}{p}$$

The enthalpy departure function can then be derived:

$$\frac{H^d}{RT} = -T\left[\frac{\partial\left(G^d/RT\right)}{\partial T}\right]_p$$

$$= -T\left\{\frac{d}{dT}\left[\int_0^p (1-Z)\frac{dp}{p}\right]\right\}_p$$

$$= T\int_0^p \frac{dZ}{dT}\Big|_p \frac{dp}{p}$$

And, from the definition of Gibbs free energy:

$$\frac{S^d}{R} = T\int_0^p \frac{dZ}{dT}\Big|_p \frac{dp}{p} - \int_0^p (1-Z)\frac{dp}{p}$$

Therefore, based on Equation 69:

$$\frac{G^d}{RT} = -\frac{\Theta}{RT\left(\delta^2 - 4\varepsilon\right)^{1/2}} \ln\left[\frac{2v + \delta - \left(\delta^2 - 4\varepsilon\right)^{1/2}}{2v + \delta + \left(\delta^2 - 4\varepsilon\right)^{1/2}}\right] + \ln\left[Z\left(1 - \frac{b}{v}\right)\right] - Z + 1 \qquad (73)$$

$$\frac{H^d}{RT} = \frac{T\,d\Theta/dT - \Theta}{RT\left(\delta^2 - 4\varepsilon\right)^{1/2}} \ln\left[\frac{2v + \delta - \left(\delta^2 - 4\varepsilon\right)^{1/2}}{2v + \delta + \left(\delta^2 - 4\varepsilon\right)^{1/2}}\right] - Z + 1 \qquad (74)$$

$$\frac{S^d}{R} = -\frac{d\Theta/dT}{R\left(\delta^2 - 4\varepsilon\right)^{1/2}} \ln\left[\frac{2v + \delta - \left(\delta^2 - 4\varepsilon\right)^{1/2}}{2v + \delta + \left(\delta^2 - 4\varepsilon\right)^{1/2}}\right] + \ln\left[Z\left(1 - \frac{b}{v}\right)\right] \qquad (75)$$

The derivative of Θ is the product of a and the derivative of the attractive term, α. Table 37 shows the first derivatives of the attractive term for all of the equations of state discussed here. The $f(\omega)$ term present in several of the derivatives represents the polynomial term containing the Pitzer acentric factor and can be identified by comparing the results with those in Table 35.

Table 37.   Derivatives of the attractive term used in the estimation of thermodynamic properties

EOS	$\partial\alpha/\partial T$
Redlich & Kwong (1949)	$-\dfrac{1}{2TT_r^{1/2}}$
Wilson (1964)	$\dfrac{\alpha}{T} - \dfrac{f(\omega)}{T}$
Soave (1972)	$-f(\omega)\sqrt{\dfrac{\alpha}{TT_c}}$
Peng & Robinson (1976)	$-f(\omega)\sqrt{\dfrac{\alpha}{TT_c}}$
Soave (1984)	$-f(\omega)\sqrt{\dfrac{\alpha}{TT_c}}$
Patel, Teja & Valderrama (1990)	$-f(\omega, Z_c)\sqrt{\dfrac{\alpha}{TT_c}}$
Twu et al. (1995)	$\dfrac{T_r^{-0.171813}}{T_c} e^{\left[0.125283\left(1 - T_r^{1.77634}\right)\right]}\left(\dfrac{0.171813}{T_r} + 0.222545 T_r^{0.77634}\right)(\omega - 1) - \ldots$ $\ldots \omega \dfrac{T_r^{-0.607352}}{T_c} e^{\left[0.511614\left(1 - T_r^{2.20517}\right)\right]}\left(\dfrac{0.607352}{T_r} + 1.12820 T_r^{1.20517}\right)$

The equation for heat capacity at constant volume can be integrated following substitution of Equation 69 to arrive at the departure function for C_v:

$$C_v^d = T\int_v^\infty \left[\left(\frac{\partial^2 p}{\partial T^2}\right)_v\right]_T dv$$

$$= \frac{T\,d^2\Theta/dT^2}{\left(\delta^2 - 4\varepsilon\right)^{1/2}} \ln\left[\frac{2v + \delta - \left(\delta^2 - 4\varepsilon\right)^{1/2}}{2v + \delta + \left(\delta^2 - 4\varepsilon\right)^{1/2}}\right] \qquad (76)$$

At ideal gas conditions, the difference between C_p and C_v simplifies to the ideal gas constant, R. This relationship is written fully as [1]:

$$C_p = C_v - T\left(\frac{\partial p}{\partial T}\right)_V^2 \Big/ \left(\frac{\partial p}{\partial V}\right)_T$$

Table 38.   Second derivatives of the attractive term used in the estimation of heat capacity.

EOS	$\partial\alpha/\partial T$
Redlich & Kwong (1949)	$-\dfrac{3}{4T^2 T_r^{1/2}}$
Wilson (1964)	0
Soave (1972)	$\dfrac{f(\omega)}{2T}\left(\dfrac{f(\omega)}{T_c} + \sqrt{\dfrac{\alpha}{TT_c}}\right)$
Peng & Robinson (1976)	$\dfrac{f(\omega)}{2T}\left(\dfrac{f(\omega)}{T_c} + \sqrt{\dfrac{\alpha}{TT_c}}\right)$
Soave (1984)	$\dfrac{f(\omega)}{2T}\left(\dfrac{f(\omega)}{T_c} + \sqrt{\dfrac{\alpha}{TT_c}}\right)$
Patel, Teja & Valderrama (1990)	$\dfrac{f(\omega,Z_c)}{2T}\left(\dfrac{f(\omega,Z_c)}{T_c} + \sqrt{\dfrac{\alpha}{TT_c}}\right)$
Twu et al. (1995)	$\dfrac{(\omega-1)}{TT_c}e^{\left[0.125283\left(1-T_r^{1.77634}\right)\right]}\left(0.096298 T_r^{0.604527} - 0.049526 T_r^{2.38087} - ...\right.$ $...\left.0.201333 T_r^{-1.171813}\right) + \omega\dfrac{e^{\left[0.511614\left(1-T_r^{2.20517}\right)\right]}}{TT_c}\left(0.010754 T_r^{0.597818} + ...\right.$ $...\left.1.27283 T_r^{2.80299} + 0.976228 T_r^{-1.607352}\right)$

Rewriting the above relationship in terms of departure functions results in the relation below, which can be integrated with the substitution of Equation 69 for *p:*

$$C_p^d = R + T\int_v^\infty \left[\left(\frac{\partial^2 p}{\partial T^2}\right)_v\right]_T dv + T\left(\frac{\partial p}{\partial T}\right)_V^2 \Big/ \left(\frac{\partial p}{\partial V}\right)_T$$

$$= R + \frac{T\,d^2\Theta/dT^2}{\left(\delta^2 - 4\varepsilon\right)^{1/2}} \ln\left[\frac{2v + \delta - \left(\delta^2 - 4\varepsilon\right)^{1/2}}{2v + \delta + \left(\delta^2 - 4\varepsilon\right)^{1/2}}\right] - T\frac{\left(\dfrac{R}{v-b} - \dfrac{d\Theta/dT}{v^2 + \delta v + \varepsilon}\right)^2}{\dfrac{RT}{(v-b)^2} - \dfrac{\Theta(2v+\delta)}{\left(v^2 + \delta v + \varepsilon\right)^2}} \qquad (77)$$

Solving Equations 77 and 76 to arrive at the constant volume and pressure heat capacity requires the second derivative of the attractive term of the cubic equation of state. The second derivatives are given in Table 38.

To calculate thermodynamic properties of mixtures, the mixing rules presented as Equation 71 have to be expanded to include the first and second derivatives of the attractive parameter. The mixing rule for the first derivative of T is given as Equation (78, while the second derivative is listed as Equation 79.

$$\frac{d\Theta_m}{dT} = \sum_{i=1}^{n}\sum_{j=1}^{n} y_i y_j \frac{d\Theta_{ij}}{dT}$$

$$\frac{d\Theta_{ij}}{dT} = \begin{cases} \dfrac{d\Theta_i}{dT}, & if\ i = j \\ \dfrac{\left(1-k_{ij}\right)}{2\sqrt{\Theta_i\Theta_j}}\left(\Theta_i\dfrac{d\Theta_j}{dT}+\Theta_j\dfrac{d\Theta_i}{dT}\right), & if\ i \neq j \end{cases} \tag{78}$$

$$\frac{d^2\Theta_m}{dT^2} = \sum_{i=1}^{n}\sum_{j=1}^{n} y_i y_j \frac{d^2\Theta_{ij}}{dT^2}$$

$$\frac{d^2\Theta_{ij}}{dT^2} = \begin{cases} \dfrac{d^2\Theta_i}{dT^2}, & if\ i = j \\ \dfrac{\left(1-k_{ij}\right)}{2\sqrt{\Theta_i\Theta_j}}\left(\Theta_i\dfrac{d^2\Theta_j}{dT^2}+\dfrac{d\Theta_j}{dT}\dfrac{d\Theta_i}{dT}+\Theta_j\dfrac{d^2\Theta_i}{dT^2}\right)-... \\ \qquad ...\dfrac{\left(1-k_{ij}\right)}{4\Theta_i\Theta_j\sqrt{\Theta_i\Theta_j}}\left(\Theta_i\dfrac{d\Theta_j}{dT}+\Theta_j\dfrac{d\Theta_i}{dT}\right)^2, & if\ i \neq j \end{cases} \tag{79}$$

Estimation of Ideal Gas Properties

As discussed in Estimation of Real Fluid Thermodynamic Properties, Thermodynamic properties of real fluids are calculated as departures from the ideal gas behavior. Thus, this section briefly identifies the methods used to calculate the ideal-gas values of enthalpy, entropy, and constant pressure heat capacity.

Aly and Lee [4] proposed a set of accurate self-consistent equations for to calculating enthalpy, entropy and heat capacity. The form of the Aly and Lee equations have been adopted by many organizations, such as the AIChE sponsored DIPPR® 801 project, which maintains a database of critically evaluated process design data. The equations for heat capacity, enthalpy, and entropy are reproduced below for convenience.

$$C_p^{ig} = A + B\left[\frac{C/T}{\sinh\left(C/T\right)}\right]^2 + D\left[\frac{\left(E/T\right)}{\cosh\left(E/T\right)}\right]^2 \tag{80}$$

$$H^{ig} = \int_0^T C_p^{ig}\,dT$$

$$= AT + BC\coth\left(\frac{C}{T}\right) - DE\tanh\left(\frac{E}{T}\right) + HCON \tag{81}$$

$$S_{ig} = \int_0^T \frac{C_p^{ig}}{T} dT - \ln \frac{p}{p_\circ}$$

$$= A\ln(T) + B\left\{\frac{C}{T}\coth\left(\frac{C}{T}\right) - \ln\left[\sinh\left(\frac{C}{T}\right)\right]\right\} - ... \qquad (82)$$

$$...D\left\{\frac{E}{T}\tanh\left(\frac{E}{T}\right) - \ln\left[\cosh\left(\frac{E}{T}\right)\right]\right\} + SCON - \ln\frac{p}{p_\circ}$$

In Equations 80, 81, and 82, tabulated constants are represented by variables A through E, and $HCON$ and $SCON$ are integration constants, the value of which depends on the reference enthalpy and entropy chosen. The tabulated constants can be found in a number of different data compilations such as the DIPPR® 801 database or National Institute of Standards and Technology TRC publications.

Estimation of Transport Properties

Estimation of transport properties is important for understating flow and heat transfer processes, such as those encountered in CO_2 pipelines and injection strings. Transport properties of interest in this context are viscosity and thermal conductivity. The methods used to estimate viscosity and thermal conductivity of real gases in this work were proposed by Chung et al., [5] and modified for high pressure application by Reid, Prausnitz, and Poling [1]. However, the details of the calculation methods will be not be reproduced here as, while being relatively simple to implement, the calculation of thermal conductivity and viscosity involve over a dozen equations each.

Comparison of Cubic EOS

Designing CO_2 transport and injection systems requires most accurate properties data available. Thus, the best cubic EOS for design applications will be the most accurate across the range of conditions that are encountered in transport and injection systems. As discussed in the Modeling CO_2 Transport by Pipeline chapter, CO_2 pipeline systems operates at pressures between approximately 8 MPa and 15 Mpa at roughly atmospheric temperatures. In the CO_2 injection string, similar ranges of pressure would likely be encountered, but the temperatures will range from atmospheric to temperatures on the order of 100°C.

The accuracy of the EOS described here was assessed by comparing physical properties of pure-CO_2 calculated by the parameterizations against the same properties calculated by the EOS of Span and Wagner[6] and the transport property correlations of Vesovic et al. [7]. The EOS of Span and Wagner is considered the "reference" EOS for pure CO_2 and is estimated to be within ±0.03% to ±0.05% of the true value for compressibility. Similarly, the correlations of Vescovic et al. are the reference correlations for viscosity and thermal conductivity, and are estimated to have an error of less than 2% in range of conditions considered/

The physical properties compared for each cubic EOS in Figure 77 are, from left to right, the compressibility, enthalpy, entropy, heat capacity (at both constant pressure and constant volume), viscosity, and thermal conductivity. Each parameterization was assessed across the same range of pressure—7 MPa to 15 MPa—and the same range of temperature—between 270 K and 370 K.
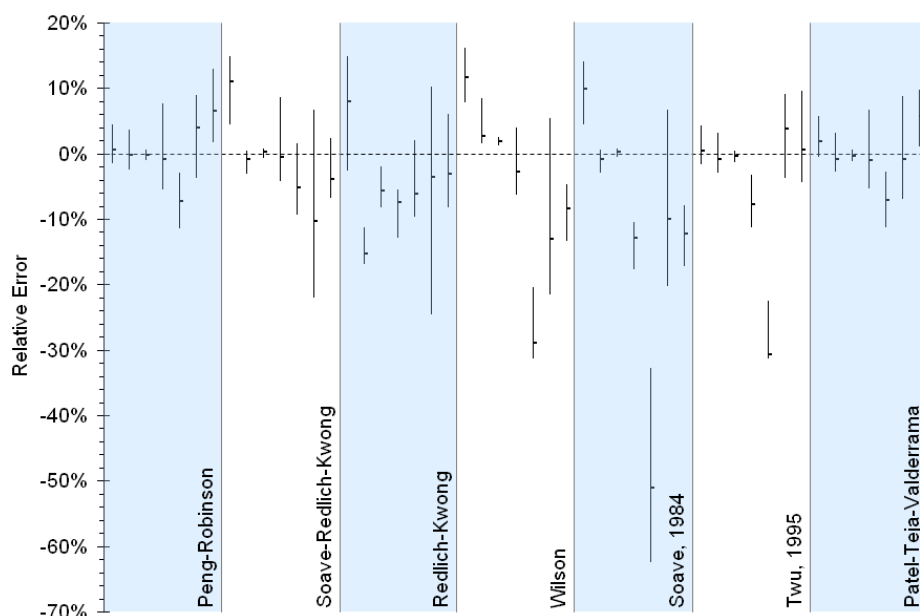
Figure 77. Relative error (i.e., the difference between the estimated and actual values, divided by the actual value) for seven parameters, estimated with the seven cubic EOS presented here. For each EOS, the seven lines correspond to (from left to right) Z, H, S, Cp, Cv, η, and λ. The upper end of each line corresponds to the first quartile; the lower end to the third quartile; and, the dash-mark to the median.

The measures compared in Figure 77 are the medial, 25th percentile, and 75th percentile relative errors. The 25th and 75th percentile errors have been chosen as a basis for comparison as opposed to the minimum and maximum errors for two reasons: the range of temperatures includes the critical point where all EOS are notoriously inaccurate, and; the enthalpy crosses zero in this range of conditions, and thus is subject to extremely large relative errors (as the relative error is normalized to the absolute value of the enthalpy). Table 39 presents the numerical results in more detail.

Based on this analysis, the EOS proposed by Peng and Robinson (PR) is the most accurate, followed closely by the Patel-Teja-Valderamma (PTV) EOS. This agrees with general process engineering industry practice, in which the Peng-Robinson EOS is the standard. Thus, while all seven of the equations of state are available in each model developed in this report, all of the models default to using the PR EOS, and all of the results presented here are based on properties predicted with the PR EOS.

Table 39.   *The median, first and third quartile relative error for seven estimated parameters for all seven cubic EOS presented here.*

Parameter	Measure	PR	SRK	RK	W	S84	T95	PTV
Z Error	Median	0.5	11.0	8.0	11.7	9.9	0.5	1.8
	Q1	-1.5	4.4	-2.6	7.8	4.4	-1.7	-0.5
	Q3	4.4	14.9	14.9	16.2	14.0	4.2	5.8
H Error	Median	-0.3	-0.9	-15.4	2.7	-0.8	-0.8	-0.8
	Q1	-2.5	-3.1	-16.9	1.5	-3.0	-3.0	-2.8
	Q3	3.7	0.4	-11.4	8.4	0.6	3.1	3.2
S Error	Median	-0.2	0.2	-5.7	1.9	0.3	-0.4	-0.3
	Q1	-1.1	-0.7	-8.2	1.3	-0.6	-1.3	-1.2
	Q3	0.5	0.7	-1.9	2.6	0.8	0.4	0.6
C_P Error	Median	-0.9	-0.5	-7.5	-2.8	-12.9	-7.8	-1.1
	Q1	-5.5	-4.3	-12.8	-6.4	-17.7	-11.3	-5.3
	Q3	7.7	8.6	-5.4	4.0	-10.5	-3.3	6.7
C_V Error	Median	-7.3	-5.2	-6.1	-28.9	-51.0	-30.7	-7.2
	Q1	-11.5	-9.4	-9.7	-31.3	-62.5	-31.4	-11.3
	Q3	-2.3	1.6	2.1	-20.5	-32.8	-22.6	-2.8
η Error	Median	4.0	-10.4	-3.6	-13.0	-10.0	3.8	-0.8
	Q1	-3.8	-22.0	-24.6	-21.5	-20.3	-3.7	-6.9
	Q3	9.0	6.7	10.2	5.4	6.7	9.2	8.7
λ Error	Median	6.5	-3.9	-3.1	-8.4	-12.2	0.7	5.7
	Q1	1.8	-6.8	-8.2	-13.3	-17.3	-4.4	1.0
	Q3	12.9	2.4	6.0	-4.7	-7.9	9.6	9.8

Properties of Crude Oils

Crude oils are complex mixtures of hydrocarbons, ranging from light ends (e.g., CH_4 and C_2H_6) to polyaromatic hydrocarbons (e.g., pyrene), organometalic compounds (e.g., porphyrins), and heteroatomic compunds (e.g. thiophene). While advances have been made in lumping large groups of constituents into pseudocomponents, and modeling crude oils using cubic EOS [2], this requires assay results for the specific oil. The alterative to using EOS is to use generic correlations for crude oil properties.

In the modeling work performed in this report, only two crude oil properties are of interest: oil viscosity and oil formation volume factor. Density of the crude oil (i.e., the API gravity), and the gas-oil ratio must be known to asses these properties.

Estimation of Oil Viscosity

Crude oil is categorized as "live" or "dead" depending on whether the oil contains gases in solution. At initial reservoir conditions, oil is considered to be live and, thus, contains light ends that are liberated as the reservoir pressure falls and oil is brought to the surface. Correlations for live-oil viscosity are based on the dead-oil viscosity, which is a correlated with temperature and API gravity. Live oil viscosity is then a function of the dead oil viscosity and the gas-oil ratio, R_s (i.e., the ratio of produced gas to produced oil).

The correlations tested for the dead-oil viscosity are listed in Table 40, including the region of the oils used in developing the correlation. Typical results from at each correlation at two temperatures for a range of API gravities are shown in Figure 78

Table 40.   The correlations tested for dead-oil viscosity and the valid temperature and API gravity ranges for these correlations.

Correlation	Oil Region	Temperature Range (^{o}F)	API Gravity Range
Beal [8]	California	100 – 220	10.1 – 52.2
Beggs & Robinson [9]	N/A	70 – 295	16 – 58
Glaso [10]	North Sea	100 – 300	20.1 – 45.8
Egbogah & Ng [11]	N/A	41 – 176	5 – 58
Labedi [12]	African	100 – 306	32.2 – 48.0
Kartoatmodjo & Schmidt [13]	Worldwide	75 – 320	14.4 – 58.9
Petrosky & Farshad [14]	Gulf of Mexico	114 – 288	25.4 – 46.1
Elsharkawy & Alikhan [15]	Middle East	100 – 300	19.9 – 48.0
Naseri et al. [16]	Iran	105 – 295	17 – 44
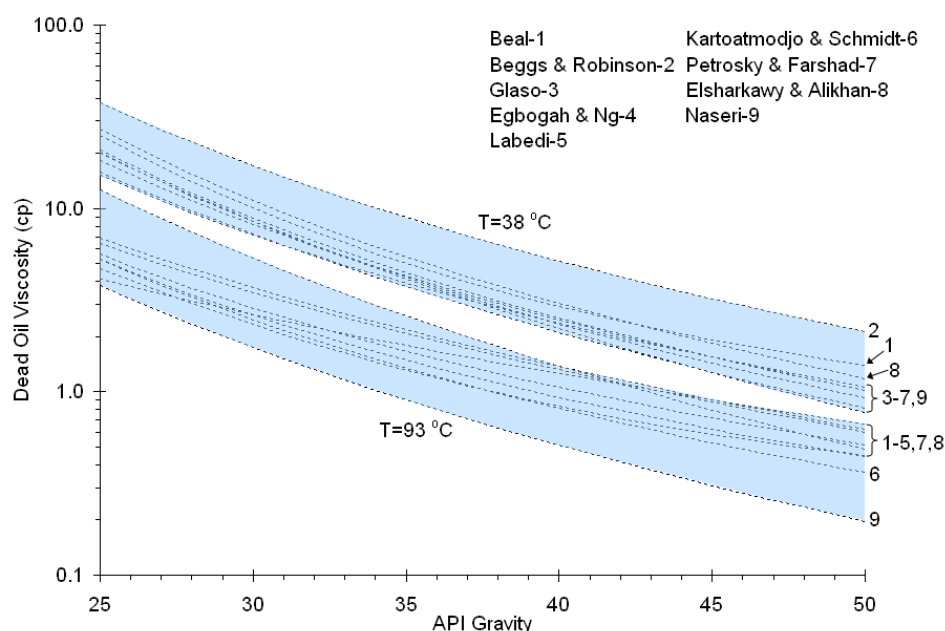
Figure 78.   Typical results for the dead-oil viscosity correlations available in the models, showing the range of possible viscosities depending on the correlation chosen, the API gravity, and the system temperature.

The viscosity estimated with these correlations is strongly dependent on both the system temperature and the type of crude oil used to develop the correlation, as can be seen in Figure 78 (note the logarithmic scale). However, even when these factors are known, the estimated dead-oil viscosity can only be considered an order of magnitude estimate [17].

Correlations for live-oil viscosity are listed in Table 41, including the region of the oils used in developing the correlation and the valid range of gas-oil ratios for the correlation (in industry standard units of standard cubic feet, scf, per stock-tank barrel, STB). Typical results from each correlation for two temperatures and a range of gas-oil ratios are shown in Figure 79.

For a given dead oil viscosity and gas-oil ratio, variation in the predicted live-oil viscosity between correlations is much smaller than the corresponding variation for the dead-oil viscosity. Moreover, the large difference between dead-oil viscosities (for a given API gravity) estimated by the different correlations shown in Figure 78 is reduced somewhat in the calculation of the live-oil viscosity. For example, at 38 ^{o}C, a 30° API crude oil could have a viscosity ranging from 17 cp to 7 cp depending on the correlation used. Under saturated conditions, the same oil with a gas-oil ratio of 1100 scf/STB would have a live-oil viscosity between 1.6 cp and 0.7 cp, depending on the live-oil correlation chosen.

Table 41.   The correlations tested for live-oil viscosity and the valid temperature and API gravity ranges for these correlations.

| Correlation	Number	Region	R_s Range (scf/STB)
Chew & Connally [18]	1	California	51 – 3544
Beggs & Robinson [9]	2	N/A	20 – 2,070
Kartoatmodjo & Schmidt [13]	3	North Sea	0 – 2,890
Petrosky & Farshad [14]	4	Middle East	21 – 1,885
Elsharkawy & Alikhan [15]	5	African	10 – 3,600
Dindoruk & Christman [19]	6	Worldwide	133 – 3,050
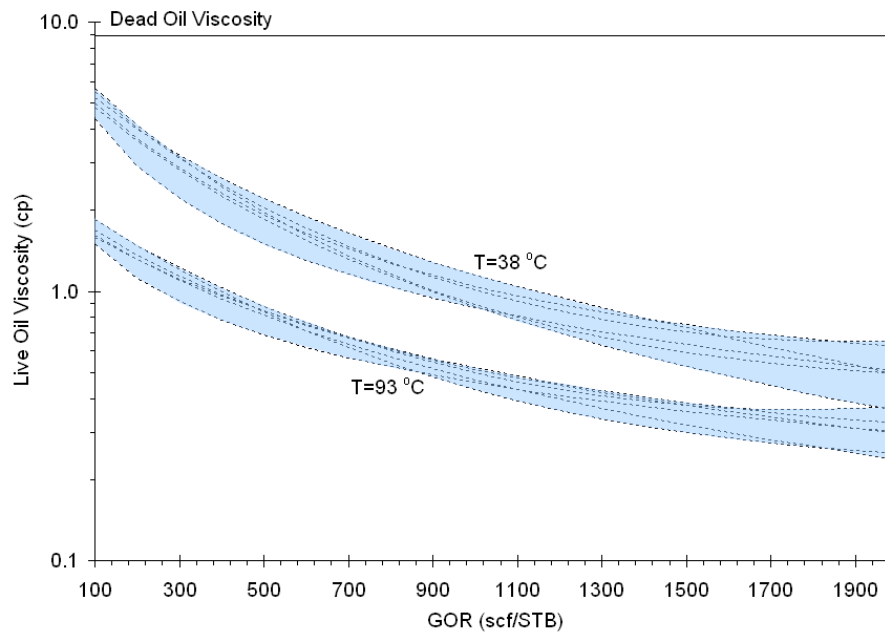
Figure 79. Typical results for the live-oil viscosity correlations available in the models, showing the range of possible viscosities depending on the correlation chosen, Rs, and the system temperature.

Estimation of Oil Formation Volume Factor

As discussed previously, oil at reservoir conditions contains dissolved gas (in proportion to the gas-oil ratio). At the surface, where the oil is under near-atmospheric pressures and temperatures (i.e., stock-tank conditions), gas is liberated from solution, and the volume of oil decreases relative to the volume at reservoir conditions. The ratio of oil volume at reservoir conditions to volume at stock-tank conditions is known as the formation volume factor, B_o.

The correlation for the formation volume factor used in this work is the Standing correlation (reproduced in [17]). Using the gas-oil ratio, R_s, the gas and oil specific gravities, γ_g and γ_o, respectively, and the reservoir temperature in °F, T_F, the formation volume factor at or below the bubble point, B_{ob}, can be predicted:

$$B_{ob} = 0.9759 + 12\left(10^{-5}\right)C_{Bob}^{1.2}$$

$$C_{Bob} = R_s \sqrt{\frac{\gamma_g}{\gamma_o}} + 1.25 T_F \qquad (83)$$

At pressures above the bubble point, the formation volume factor can be estimated from Equation 83 using:

$$B_o = B_{ob} \exp\left[\kappa_o\left(p_b - p\right)\right] \qquad (84)$$

Where, p_b is the bubble point pressure in psia, and κ_o is the isothermal compressibility of the oil (psia⁻¹).

When bubble point pressure and isothermal compressibility are not known, they can be calculated using Equations 85 and 86, developed by Standing, and Vazquez and Beggs [17].

$$p_b = 18.2\left(C_{pb} - 1.4\right)$$

$$C_{pb} = 10^{\left(0.00091 T_F - 0.0125 \gamma_{API}\right)} \left(\frac{R_s}{\gamma_g}\right)^{0.83} \tag{85}$$

$$\kappa_o = \frac{\left(-1443 + 5R_s + 17.2 T_F - 1180 \gamma_g + 12.61 \gamma_{API}\right)}{10^5 p} \tag{86}$$

The estimated bubble point is estimated to and accuracy of approximately 15%, while the estimated isothermal compressibility may be in error by as much as 50% at high pressures (i.e., approaching the maximum pressure of the correlation, which is 9500 psia or 66 MPa) [17].

References

1. Poling, B.E., J.M. Prausnitz, and J.P. O'Connell, *The Properties of Gases and Liquids.* 5 ed. 2001: McGraw-Hill Book Company.
2. Valderrama, J.O., *The State of the Cubic Equations of State.* Industrial and Engineering Chemistry Research, 2003. **42**(8): p. 1603-1618.
3. Smith, J.M., H.C. van Ness, and M.M. Abbott, *Introduction to Chemical Engineering Thermoynamics.* 6 ed. 2001, New York, NY: McGraw-Hill Higher Education. 660.
4. Aly, F.A. and L.L. Lee, *Self-consistent equations for calculating the ideal gas heat capacity, enthalpy, and entropy.* Fluid Phase Equilibria, 1981. **6**(3-4): p. 169-179.
5. Chung, T.H., et al., *Generalized Multiparameter Correlation for Nonpolar and Polar Fluid Transport Properties.* Industrial and Engineering Chemistry Research, 1988. **27**: p. 671-679.
6. Span, R. and W. Wagner, *A New Equation of State for Carbon Dioxide Covering the Fluid Region from the Triple Point Temperature to 1100K at Pressures up to 800 Mpa.* Journal of Physical and Chemical Reference Data, 1996. **25**(6): p. 1509-1596.
7. Vesovic, V., et al., *The Transport-Properties of Carbon-Dioxide.* Journal of Physical and Chemical Reference Data, 1990. **19**(3): p. 763-808.
8. Beal, C., *The Viscosity of Air, Water, Natural Gas, Crude Oil and Its Associated Gases at Oil Field Temperatures and Pressures.* Transactions of the American Institute of Mining and Metallurgical Engineers, 1946. **165**: p. 94-115.
9. Beggs, H.D. and J.R. Robinson, *Estimating the Viscosity of Crude Oil Systems.* Journal of Petroleum Technology, 1975: p. 1140-1141.
10. Glaso, O., *Generalized Pressure-Volume-Temperature Correlations.* Journal of Petroleum Technology, 1980: p. 785-795.
11. Egbogah, E.O. and J.T. Ng, *An improved temperature-viscosity correlation for crude oil systems.* Journal of Petroleum Science and Engineering, 1990. **5**: p. 197-200.
12. Labedi, R., *Improved correlations for predicting the viscosity of light crudes.* Journal of Petroleum Science and Engineering, 1992. **8**: p. 221-234.
13. Kartoatmodjo, T. and Z. Schmidt, *Large data bank improves crude physical property correlations.* Oil and Gas Journal, 1994. **92**(27): p. 51-55.
14. Petrosky, G.E. and F.F. Farshad, *Viscosity Correlations for Gulf of Mexico Crude Oils*, in *Production Operations Symposium.* 1995, Society of Petroleum Engineers: Oklahoma City, OK.
15. Elsharkawy, A.M. and A.A. Alikhan, *Models for predicting the viscosity of Middle East crude oils.* Fuel, 1999. **78**: p. 891-903.
16. Naseri, A., M. Nikazar, and S.A. Mousavi Dehghani, *A correlation approach for prediction of crude oil viscosities.* Journal of Petroleum Science and Engineering, 2005. **47**: p. 163-174.
17. McCain, W.D., *Reservoir-Fluid Property Correlations-State of the Art.* Society of Petroleum Engineers Reservoir Engineering, 1991: p. 266-271.
18. Chew, J.N. and C.A. Connally, *A Viscosity Correlation for Gas-Saturated Crude Oils.* Transactions of the American Institute of Mining and Metallurgical Engineers, 1959. **216**: p. 23-25.

19.   Dindoruk, B. and P.G. Christman, *PVT Properties and Viscosity Correlations for Gulf of Mexico Oils.* Society of Petroleum Engineers Reservoir Evaluation and Engineering, 2004: p. 427-437.

Oil Recovery Methods

Oil recovery methods can be grouped into conventional and enhanced methods. Conventional recovery involves production of oil through natural reservoir pressure caused by gas expansion (i.e., gas drive) or water influx (i.e., waterdrive), through pumping (i.e., artificial lift). Conventional recovery also encompasses waterflooding, where water is injected into the reservoir to maintain reservoir pressure and displace residual oil. Conventional recovery ceases when the oil production rate is too low to offset the cost of operating the field. At this point, typically 40% to 60% of the original oil in place (OOIP) remains trapped in the reservoir [1].

Enhanced oil recovery (EOR) methods allow additional oil to be economically extracted from the reservoir above that extracted via conventional production, and can generally be categorized into three broad classes: thermal, chemical, and gas [2]. Thermal methods include steam and hot water injection, and in-situ combustion. Chemical recovery methods include polymer and surfactant flooding. Gas methods include injection of both miscible and immiscible gases, such as light hydrocarbons (e.g., propane, butane), CO_2, and flue gases.

CO_2 can be used in two distinct EOR processes: immiscible and miscible flooding. In the immiscible CO_2-flood process, the CO_2 acts to improve oil recovery by dissolving in the oil, causing it to swell, and reducing both density and viscosity of the oil [2]. In the miscible CO_2-flooding process, reservoir pressure is high enough to cause the CO_2 to become completely miscible with the reservoir oil, greatly increasing displacement efficiency in areas contacted by the displacing fluid [2, 3].

Under field conditions, miscible CO_2-flooding allows an additional 10 to 15% of the OOIP to be recovered [1]. Immiscible CO_2-flooding does not increase recovery efficiencies to the same extent as miscible flooding and, to date, has been employed infrequently [4]. However, the miscible CO_2-flooding process can only be implemented on reservoirs that meet a number of screening criteria. Table 42, describes screening criteria suggested by a number of authors.

For miscibility to develop between the reservoir oil and injected CO_2, the reservoir pressure must be greater than the minimum miscibility pressure (MMP) for the reservoir oil. This criteria is explicitly addressed by the criteria proposed by the National Petroleum Council [5] and Shaw and Bachu [5]. All of the other authors criteria presented in Table 42 imply that MMP must be greater than reservoir pressure. In addition to MMP, oil density (reflected by the API gravity) and residual saturation to waterflooding, S_{or}, are important screening criteria.

A large number of papers discuss methods to estimate MMP (e.g. Holm and Josendal [6], Yellig and Metcalfe [7], Wang and Orr [8]). Additionally, an overview of miscibility, laboratory measurement of MMP, and MMP predictive methods can be found in monographs by Stalkup [3] and Green and Willhite [2].

Table 42.   Proposed screening criteria for miscible CO_2-flooding compiled by Shaw and Bachu [9], modified to include criteria proposed by Stalkup [3] and Kovscek [10], as well as a more recent NPC report [5].

Criterion	Geffen (1973)	Lewin et al. (1976)	McRee (1977)	Iyoho (1978)	OTA (1978)	Carcoana (1982)	Stalkup (1983)	Taber & Martin (1983)	NPC (1984)	Taber et al. (1997)	Shaw & Bachu (2001)	Kovscek (2002)
Crude Oil Criteria												
ρ (°API)	>30	>30	>35	30-45	i) <27 ii) 27-30 iii)>30	>40	>27	>26	>25	i)22-27.9 ii) 28-31.9 iii) 32-39.9 iv) >40	27-48	>22
μ (mPa s)	<3	<12	<5	<10	<12	<2	<12	<15		<10		
Reservoir Criteria												
T (°C)						<91					31-120	
p (MPa)	7.6	10.3				8.3						
G (kPa/m)												<17.4
k (md)			>5	>10		>1						
d (m)		>914	>607	>762	i) >2195 ii) >1676 iii) >762	< 2987		>607		i) >1219 ii) >1006 iii) >853 iv) >762		
S_{or}	>0.25	>0.25	>0.25	>0.25		>0.30	>0.20	>0.30		>0.20	>0.25	
C (kg/m^3)												>10
kh (m^3)												>10^{-14}
$S_o\Phi$												>0.05
p/MMP									>1		>0.95	

References

1. Blunt, M.F., F.J. Fayers, and F.M. Orr, *Carbon Dioxide in Enhanced Oil Recovery.* Energy Conversion & Management, 1993. **34**(9-11): p. 1197-1204.
2. Green, D.W. and G.P. Willhite, *Enhanced Oil Recovery.* SPE Textbook Series. 1998, Richardson, TX: Society of Petroleum Engineers. 545.
3. Stalkup Jr., F.I., *Miscible Displacement.* 1983, Dallas: Society of Petroleum Engineers. 204.
4. Moritis, G., *CO_2 injection gains momentum.* Oil & Gas Journal, 2006. **104**(15): p. 37-41.
5. National Petroleum Council, *Enhanced Oil Recovery.* 1984.
6. Holm, L.W. and V.A. Josendal, *Mechanisms of Oil Displacement by Carbon Dioxide.* Journal of Petroleum Technology, 1974(December): p. 1427-1438.
7. Yellig, W.F. and R.S. Metcalfe, *Determination and Prediction of CO2 Minimum Miscibility Pressures.* Journal of Petroleum Technology, 1980: p. 160-168.
8. Wang, Y. and J.F.M. Orr, *Analytical calculation of minimum miscibility pressure.* Fluid Phase Equilibria, 1997. **139**(1-2): p. 101-124.
9. Shaw, J. and S. Bachu, *Screening, evaluation, and ranking of oil reservoirs suitable for CO_2-flood EOR and carbon dioxide sequestration.* Journal of Canadian Petroleum Technology, 2002. **41**(9): p. 51-61.
10. Kovscek, A.R., *Screening Criteria for CO_2 Storage in Oil Reservoirs.* Petroleum Science and Technology, 2002. **20**(7-8): p. 841-866.

Numerical Modeling of the Wellbore Environment

Estimating the pressure drop across a CO_2 injection well (or any segment of an injection well) begins with a total energy balance on the flowing fluid, which can be written:

$$dH + \frac{g}{g_c} dh + \frac{u}{g_c} du = dQ + dW \qquad (87)$$

In Equation 87: H is the fluid enthalpy; h is height relative to the well bottom; g is acceleration due to gravity; g_c is a conversion factor for converting force units (in SI, equal to unity); u is fluid velocity; Q is heat transfer; and, W is flow work.

Because there is no flow work being done (i.e., pump or turbine work) and the kinetic energy change is negligible, both dW and du can be eliminated. Thus, Equation 87 accounts for pressure-volume work (dH), changes in potential energy (dh), and heat transfer. Equation 87 can then be integrated in the direction of flow (i.e., from point 1, upstream, to point 2, downstream) to yield:

$$H_2 - H_1 + \frac{g}{g_c}(h_2 - h_1) = Q \qquad (88)$$

Pressure does not appear explicitly in Equation 88; however, enthalpy is a function of pressure and temperature. Since the upstream pressure and temperature are known, the upstream enthalpy can be calculated (see the Estimation of Physical Properties chapter for the analytical relationship between enthalpy, pressure, temperature). Thus, assuming the heat transfer term is known, Equation 88 can be rearranged to solve for the enthalpy of the downstream fluid.

Because the downstream enthalpy is a function of pressure and temperature, a second energy balance must be used to determine the downstream pressure. Equation 89 shows the differential form of this mechanical energy balance. Equation 89 accounts for changes in kinetic energy, pressure-volume work, changes in potential energy, and energy loss due to skin friction in a flow system.

$$\frac{c}{g_c v} du + \frac{1}{v} dp + \frac{g}{g_c v^2} dh + \frac{2 f_F c^2}{g_c D_i} dL = 0 \qquad (89)$$

In Equation 89: c is a constant equal to the product of density, ρ, and fluid velocity, u; g is acceleration due to gravity; g_c is the conversion factor converting force units (in the SI system of units, this is equal to unity); v is the specific volume of fluid; p is pressure; f_F is the fanning friction factor; D_i is the pipeline diameter; and L is tubing length.

Following the derivation in Pipe Segment Engineering and Design in the Modeling CO_2 Transport by Pipeline chapter, Equation 89 is simplified (i.e., assuming kinetic energy changes are negligible and average compressibility), and solved for downstream pressure resulting in:

$$p_2 = \sqrt{p_1^2 - \frac{2g p_{ave}^2 M (h_2 - h_1)}{g_c Z_{ave} R T_{ave}} - \frac{64 Z_{ave} R T_{ave} f_F \dot{m}^2 \Delta L}{g_c \pi^2 D_i^5 M}} \qquad (90)$$

where: p_{ave} is average pressure; T_{ave} is average temperature; R is the ideal gas constant; M is the fluid molecular weight; Z_{ave} is the fluid compressibility calculated at p_{ave} and T_{ave}; $\dot{m}$ is the mass flow rate; and, ΔL is the tubing segment length.

The average temperature, T_{ave}, required in Equation 90 is calculated using Equation 91. Because pressure varies non-linearly along the pipeline, the average pressure, P_{ave}, is calculated using Equation 92 [1].

$$T_{ave} = \frac{T_1 + T_2}{2} \qquad (91)$$

$$P_{ave} = \frac{2}{3} \left(p_2 + p_1 - \frac{p_2 p_1}{p_2 + p_1} \right) \qquad (92)$$

Using Equation 90, the downstream pressure can be calculated following the iterative method described in Pipe Segment Engineering and Design in the Modeling CO2 Transport by Pipeline chapter. Thus, both pressure and enthalpy are known at the well bottom, and temperature can therefore be estimated using a root finding algorithm (e.g., van Wijngaarden-Deker-Brent) on Equation 91.

As noted previously, the heat transfer term in Equation 88 must also be calculated to arrive at the BHIP. The heat transfer calculations follow the approach outlined by Willhite [2] with the solution for transient radial heat transfer to the surrounding rock proposed by Ramey [3]. Figure.80 shows the important parameters relevant to the heat transfer problem over a cross-section of the wellbore.

As Figure.80 shows, the wellbore is simplified to: tubing, containing the flowing fluid; an annulus between the casing and tubing, filled with brine; cement between the formation and the sandface; and, the surrounding rock. Resistance to heat transfer from the tubing and casing is ignored, as the conductivity of the steel used in the tubing and casing is at least an order of magnitude larger than any other conductivity in the system.

If only radial heat transfer is considered, the heat transfer between the flowing fluid and the wellbore can be written as:

$$Q = \frac{(T_r - T_b)}{\sum R_{th}} \qquad (93)$$

In Equation 93, T_b is the bulk temperature of the flowing fluid, T_r is the temperature of the undisturbed rock, and R_{th} is resistance to heat transfer. In this case, the bulk temperature of the flowing fluid is calculated as the average of the upstream and downstream temperatures (i.e, Equation 91). If the temperature of the rock is higher than the temperature of the flowing fluid, energy is transferred to the fluid, and q is greater than zero.

The temperature of the undisturbed rock at depth, d, is calculated using the geothermal gradient, G:

$$T_r = T_s + Gd \qquad (94)$$

where, T_s is the surface temperature and G is typically approximately 25 °C per kilometer [4, 5].

Neglecting radiative heat transfer between the tubing and casing, the expression for resistance to heat transfer needed in Equation 93 is derived by Willhite as [2]:

$$\sum R_{th} = \frac{1}{\pi \Delta L k_b Nu_D} + \frac{\ln(r_c/r_t)}{2\pi \Delta L k_a Nu_\delta} + \frac{\ln(r_{wb}/r_c)}{2\pi \Delta L k_c} + \frac{f(t)}{2\pi \Delta L k_r} \qquad (95)$$

where: k is the thermal conductivity of the bulk tubing fluid (b), annulus fluid (a), concrete (c), and rock (r); Nu is the Nusselt number with characteristic length of the tubing diameter (D) and tubing-annulus gap (δ); r are the radii defined in Figure.80; and, $f(t)$ is the time function developed by Ramey [3].
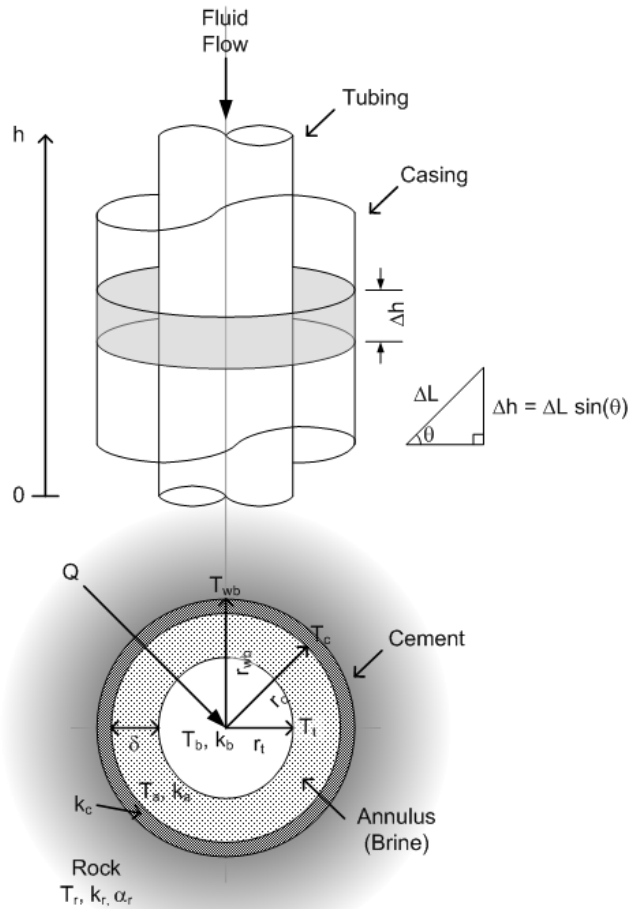
Figure.80.   Cross-section of the wellbore showing important parameters relevant to the wellbore heat transfer problem.

From left to right, the terms in Equation 95 account for heat transfer between the flowing fluid and the tubing (via forced convection), across the annular space (via natural convection), and across the cement into the formation (via conduction). The Nusselt number for forced convection is calculated using the correlation of Sieder & Tate [6] and the for natural convection, using the correlation of MacGregor & Emery [7]. Properties of the casing fluid, required to calculate the annular Nusselt number, are estimated using the correlations of Batzle & Wang presented by Adams & Bachu [8].

The BHIP and bottomhole temperature are calculated using a finite-difference method: the wellbore is broken into *n* segments, and the pressure and temperature are calculated at the bottom of each segment (starting from the wellhead conditions) using Equations 88, 90, and 93. Because the heat transfer term (Equation 93) is a function of the flowing bulk fluid properties, which are related by temperature and pressure to the downstream enthalpy calculated from Equation 88, an iterative solution method is required for each segment. The iteration scheme is illustrated is Figure 81.

P_1, T_1, T_{rock}
$\Delta L, \Delta h$
m
ε
$D_{tubing}, D_{casing}, D_{wellbore}$
k_c, k_f, α_{rock}

| INITIAL TEMPERATURE $T_{2,old} = T_1$ | MECHANICAL ENERGY BALANCE $p_2 = f(Re, F_f, \Delta L)$ | TEMPERATURE UPDATE $T_{2,old} = T_{2,new}$ |

PRESSURE CHECK
Single phase flow
$p_2 > p_{sat}$

CALCULATE AVERAGES
T_{ave}, p_{ave}

ANNULAR FLUID PROPERTIES

ESTIMATE HEAT TRANSFER
$q = f(T_{ave}, p_{ave})$

TOTAL ENERGY BALANCE
$H_2 = H_1 - g\Delta H + q/m$

TOTAL ENERGY BALANCE
$H_2 = H_1 - g\Delta H + q/m$

INTERVAL TEMPERATURE
$T_{2,new} = f(H_2, p_2)$

$T_{2,new} - T_{2,old} <$ Tolerance?

YES   NO

P_2, T_2

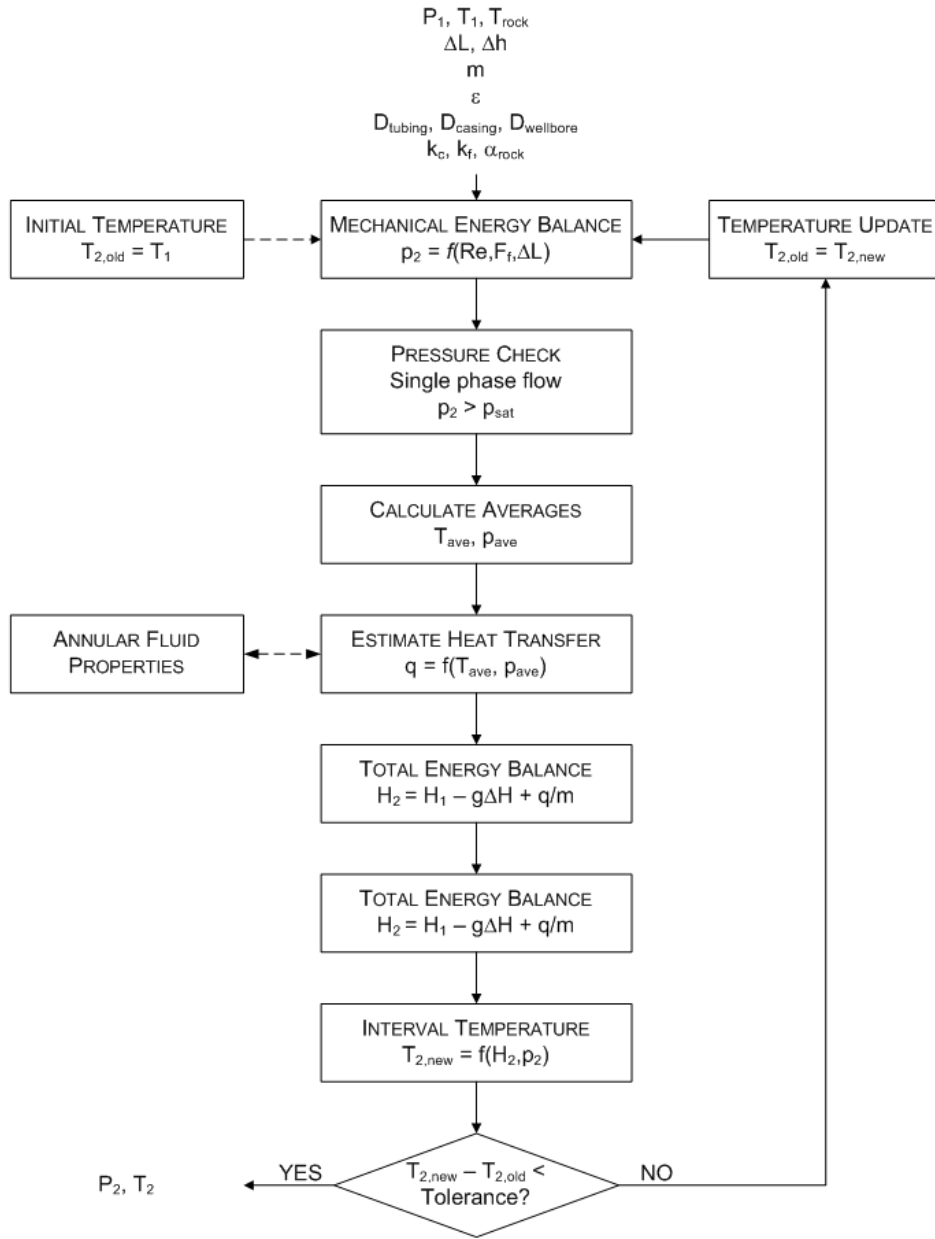*Figure 81.   The iteration scheme used to solve for the downstream pressure over a segment of the wellbore.*

Thus, Equations 88, 90, 93 and the iteration scheme presented in Figure 81 combine to for the wellbore flow model. Using the wellbore flow model with the illustrative parameter values presented in Table 43 for different mass flow rates generates the pressure distribution shown in Figure 82.

Table 43.   Illustrative values for the wellbore flow model parameters.

| Model Parameters	Deterministic Value
Well Completion	
Wellbore Length (m)	1000
Wellbore Angle (θ)	90
Tubing Diameter (m)	0.076
Casing Diameter (m)	0.152
Wellbore Diameter (m)	0.254
Pipe Roughness (mm)	0.0457
Annulus Salt Concentration (ppm$_w$)	100000
Cement Thermal Conductivity (W/m K)	0.87
Geological	
Ground Temperature (^oC)	13.79
Geothermal Gradient (^oC)	10.3
Rock Thermal Conductivity (W/m K)	2.6
Rock Thermal Diffusivity (m^2/d)	0.09
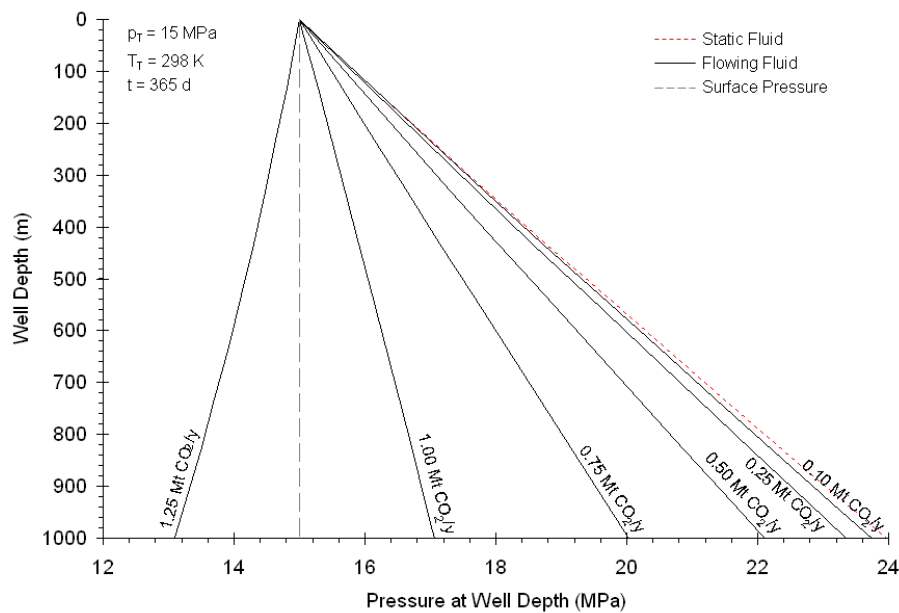
Figure 82.   Results from the wellbore flow model for pressure as a function of depth for mass flow rates between 0.1 Mt CO$_2$ per year and 1.25 Mt CO$_2$ per year.

The results in Figure 82 show that increasing the mass flow rate reduce the bottom hole pressure for all well depths at fixed wellhead conditions. At flow rates between 1 and 1.25 Mt per year of CO$_2$ injected, the pressure gradient becomes negative, resulting in BHIP lower than the wellhead pressure. At the other extreme, flow rates less than 0.1 Mt CO$_2$ per year result in flowing pressure losses so small that the BHIP is nearly the same as hydrostatic fluid pressure.
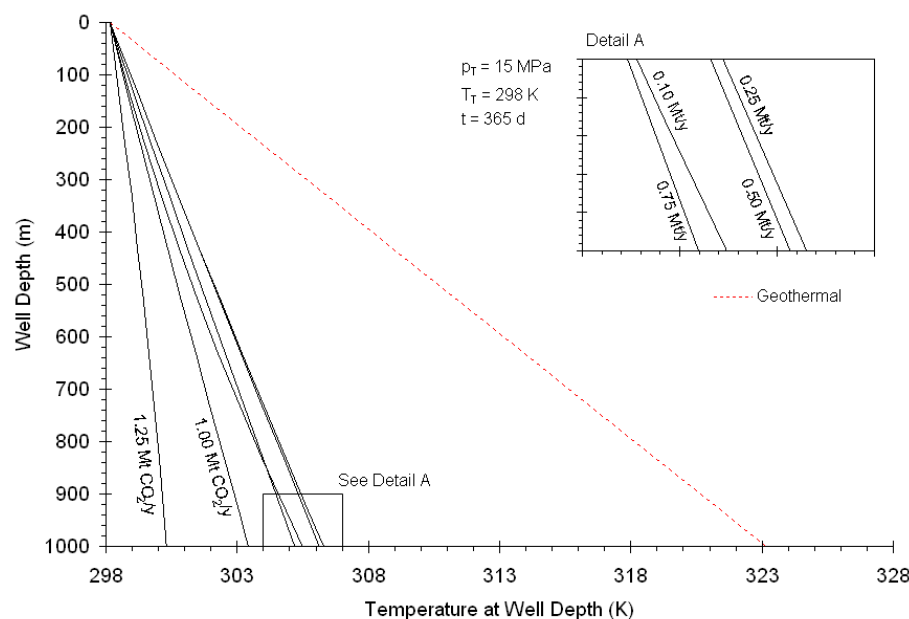
Figure 83. Results from the wellbore flow model for temperature as a function of depth for mass flow rates between 0.1 Mt CO$_2$ per year and 1.25 Mt CO$_2$ per year.

While the relationship between pressure and mass flow rate is monotonic, the relationship between temperature and mass flow rate is more complex, as Figure 83 shows. At flow rates between 1 Mt CO$_2$ per year and 1.25 Mt CO$_2$ per year, bottomhole temperature decreases with increasing flow rates. At lower mass flow rates, temperature passes through a maximum between 0.5 Mt CO$_2$ per year and 0.25 Mt CO$_2$ per year.

Because of the strong dependence of injection rates on BHIP, the pressure is much more important than temperature in the context of the EOR performance model developed here. Thus, it is important to know how the well completion and geological parameters affect the BHIP. Figure 84 presents the results of a sensitivity analysis on heat transfer related parameters in the wellbore flow model, where parameter value differences are relative to the base values listed in Table 43, with a mass flow rate of 0.5 Mt CO$_2$ per year, time of 365 days, wellhead pressure of 15 MPa, and wellhead temperature of 298 K.

Parameters included in Figure 84 do not include the tubing, casing and wellbore diameters, as they are not independent parameters (e.g., smaller tubing means smaller casing can be used). Figure 84 shows that changes to the parameters related to the heat transfer calculation (Equation 93) have a very small influence on the calculated BHIP. For example, a 50% change in the surface temperature changes the calculated BHIP by only 16 kPa. Moreover, the BHIP is less sensitive to changes in all other heat transfer related parameters.

Figure 85 shows the sensitivity of BHIP to changes in wellbore flow model non-heat transfer related parameter values, where base values are defined in Table 43. Of the parameters considered in Figure 85, BHIP is least sensitive to materials roughness—200 kPa for a 50% change—and most sensitive to surface pressure—9 MPa for a 50% change. The sensitivity of BHIP to changes in heat transfer related parameters is at least an order of magnitude smaller than the sensitivities shown in Figure 85. Thus relatively speaking, BHIP is nearly insensitive to changes in heat transfer related parameter values.

Figure 84.   Sensitivity of BHIP to changes in the heat transfer related input parameter values listed in Table 43, where the difference from the base parameter value is calculated as (x-x$_{base}$)/x$_{base}$.
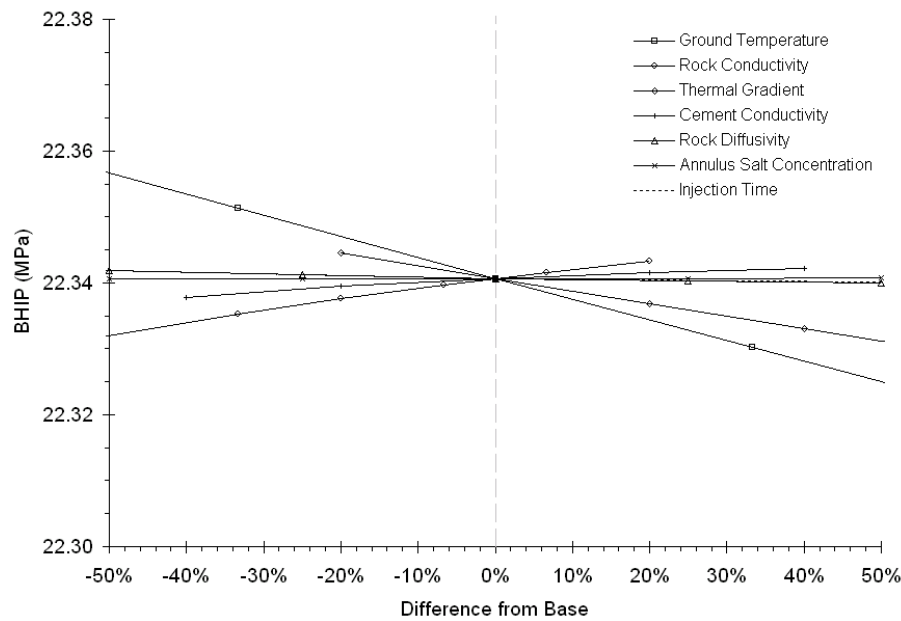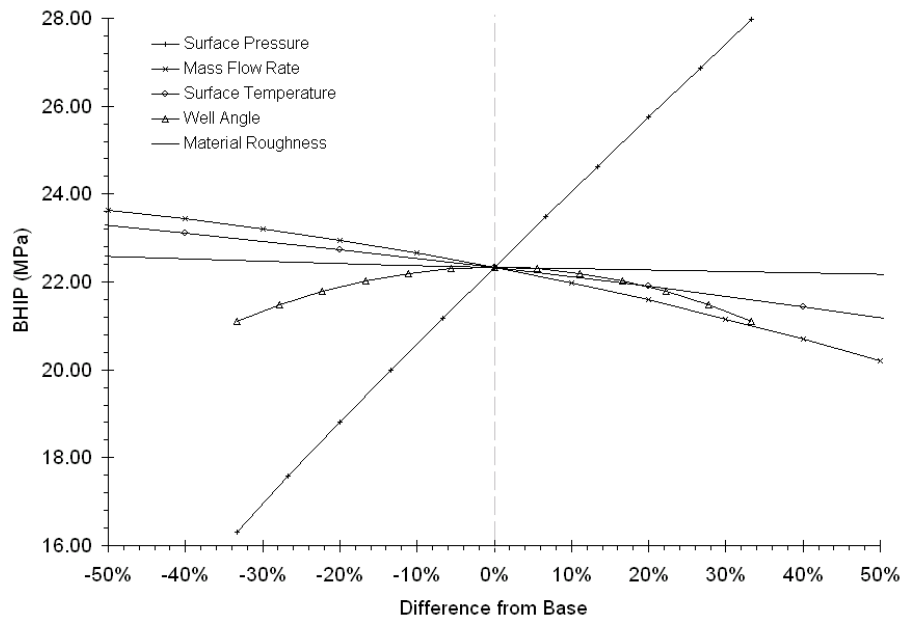

Figure 85. Sensitivity of BHIP to changes in non-heat transfer related input parameter values listed in Table 43, where the difference from the base parameter value is calculated as (x-x$_{base}$)/x$_{base}$.

References

1. Mohitpour, M., H. Golshan, and A. Murray, *Pipeline Design & Construction*. 1st ed. 2003, New York, NY: ASME Press.
2. Willhite, G.P., *Over-all Heat Transfer Coefficients in Steam and Hot Water Injection Wells*. Journal of Petroleum Technology, 1967(May): p. 607-615.
3. Ramey, H.J., *Wellbore Heat Transmission*. Journal of Petroleum Technology, 1962(April): p. 427-435.
4. Bachu, S., *Screening and ranking of sedimentary basins for sequestration of CO_2 in geological media in response to climate change*. Environmental Geology, 2003. **44**: p. 277-289.
5. Holloway, S. and D. Savage, *The Potential for Aquifer Disposal of Carbon Dioxide in the UK*. Energy Conversion & Management, 1993. **34**(9-11): p. 925-932.
6. Holman, J.P., *Heat Transfer*. 9th ed. 2002, New York, NY: McGraw-Hill.
7. Macgregor, R.K. and A.F. Emery, *Free Convection through Vertical Plane Layers - Moderate and High Prandtl Number Fluids*. Journal of Heat Transfer, 1969. **91**(3): p. 391.
8. Adams, J.J. and S. Bachu, *Equations of state for basin geofluids: algorithm review and intercomparison for brines*. Geofluids, 2002. **2**(4): p. 257-271.

Arial Extent of CO₂ Plume Size in Aquifer Injection

Methods to estimate the aerial extent of a CO_2 plume were developed by both Saripalli and McGrail [1] and Nordbotten et al [2]. Both these methods are extensions of the Buckley-Leverett equation [3], describing the immiscible displacement of one fluid by another, solved for a radial system. However, these authors make different assumptions about the displacement of brine by CO_2. Saripalli and McGrail [1] implicitly assume that the displacement is stable (i.e. the endpoint mobility ratio, M, is less than one) while Nordbotten et al [2] assume that the displacement is unstable, and significant viscous fingering occurs. Assuming equal endpoint relative permeabilities (k_{rw} and k_{rc} for brine and CO_2, respectively), the mobility ratio in displacement of brine by CO_2 will be much greater than ten. Thus, the approach taken by Nordbotten et al [2] is more appropriate for this type of displacement.

While the results obtained by Nordbotten et al [2] agree broadly with Buckley-Leverett theory, their derivation is difficult to follow and does not follow typical conventions in the reservoir engineering field. For convenience, their result is derived here using the similar assumptions—namely, effects of capillary pressure are negligible, fluids are incompressible, and the reservoir petrophysical properties are homogeneous—using arguments analogous to those used by Dake [3] for an unstable, horizontal displacement.
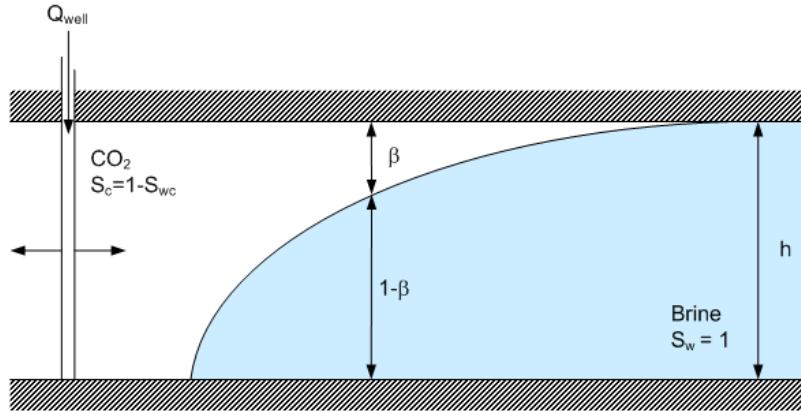

Figure 86.   Geometry of a system where CO₂ is displacing brine.

The system modeled is illustrated in Figure 86. For a differential cylindrical volume of this system, the volumetric balance on the CO_2 phase can be written:

$$\varphi \frac{\partial \overline{S}_c(r,t)}{\partial t} + \nabla \cdot q_c(r,t) = 0 \tag{96}$$

where: $\bar{S}_c$ is the vertically averaged saturation of CO_2, φ is the reservoir porosity, q_c is the flux of CO_2, r represents radial distance from the injection well, and t is time. Assuming drainage (i.e., CO_2 is displacing brine in a brine-wet reservoir), the vertically averaged saturation of CO_2, $\bar{S}_c$, is defined as:

$$\bar{S}_c = \beta(1 - S_{wc}) \tag{97}$$

Darcy's law for the brine and CO_2 phases can be written as:

$$q_c = -K\beta\lambda_c\nabla p_c \tag{98}$$

$$q_w = -K(1-\beta)\lambda_w\nabla p_w \tag{99}$$

In equations 98 and 99 K is the intrinsic permeability of the reservoir, β is the fraction of the reservoir thickness invaded by the CO_2 plume, λ is the phase mobility (k_r/u), and ∇p is the pressure gradient.

Since the fluids are incompressible ($\nabla \cdot q = 0$), the flux into the system equals the flux out of the system and the total apparent flux, q_t, is:

$$q_t = \frac{Q_{well}}{A} = q_c + q_w$$

where: Q_{well} is the injection rate of CO_2 into the system and A is the area across which the flux occurs. Assuming capillary pressure is negligible and, therefore $\nabla p_c = \nabla p_w = \nabla p$ and substituting equations 98 and 99, we arrive at:

$$\frac{Q_{well}}{A} = -K[\beta\lambda_c + (1-\beta)\lambda_w]\nabla p \tag{100}$$

Solving equation 100 for pressure gradient, results in:

$$\nabla p = -\frac{Q_{well}}{KA[\beta\lambda_c + (1-\beta)\lambda_w]}$$

which can then be substituted into equation 98, to arrive at the flux of the CO_2 phase as a function of the injection rate.

$$q_c = \frac{\beta\lambda_c}{\beta\lambda_c + (1-\beta)\lambda_w}\left(\frac{Q_{well}}{A}\right) = f_c\frac{Q_{well}}{A} \tag{101}$$

In equation 101, the term referred to as f_c is the fractional flow of the carbon dioxide phase in the system. Substituting this equation into the volumetric balance, 96, yields:

$$\varphi\frac{\partial\bar{S}_c}{\partial t} + \nabla \cdot \left(f_c\frac{Q_{well}}{A}\right) = 0$$

Writing the divergence operator for a cylindrical coordinate system gives:

$$\varphi\frac{\partial\bar{S}_c}{\partial t} + \frac{1}{r}\frac{\partial}{\partial r}\left(rf_c\frac{Q_{well}}{2\pi rh}\right) = 0$$

Simplifying results in:

$$\varphi\frac{\partial\bar{S}_c}{\partial t} + \frac{Q_{well}}{2\pi rh}\frac{\partial f_c}{\partial r} = 0 \tag{102}$$

Applying the chain rule to the fractional flow equation, the $\partial f_c/dr$ can be rewritten:

$$\frac{\partial f_c}{dr} = \frac{\partial f_c}{\partial \bar{S}_c} \times \frac{\partial \bar{S}_c}{\partial r} = f_c{}' \frac{\partial \bar{S}_c}{\partial r}$$

Upon substitution into 102, we arrive at a statement of the Buckley-Leverett equation for a radial system:

$$\frac{\partial \bar{S}_c}{\partial t} + \frac{Q_{well} f_c{}'}{2\pi r h \varphi} \frac{\partial \bar{S}_c}{\partial r} = 0 \qquad (103)$$

This equation was solved by Woods and Comer [4] for the boundary conditions, $r = r_w$ at $t = 0$, resulting in:

$$r(\bar{S}_c) = \sqrt{\frac{f_c{}' Q_{well} t}{\pi h \varphi} + r_w^2} \qquad (104)$$

If vertically averaged saturation of the CO_2 phase was not assumed (i.e., 97), determination of $f_c{}'$ would require an assumption of the shape of the relative permeability curves for the CO_2-brine system and particular reservoir rock. However, because we are operating under the assumption that saturation is a linear average of phase saturations (i.e., 97), $f_c{}'$ can be expressed via the chain rule as:

$$f_c{}' = \frac{df_c}{d\beta} \times \frac{d\beta}{d\bar{S}_c} = \frac{\lambda_w \lambda_c}{[\lambda_w + \beta(\lambda_c - \lambda_w)]^2} \left(\frac{1}{1 - S_{wc}} \right)$$

Substituting this into the above equation, we arrive at an expression for the radial distance as a function of the fraction of the formation height invaded by the CO_2 plume:

$$r(\beta) = \sqrt{\frac{\lambda_w \lambda_c Q_{well} t}{\pi h \varphi (1 - S_{wc})[\lambda_w + \beta(\lambda_c - \lambda_w)]^2} + r_w^2} \qquad (105)$$

Assuming that the injection well radius is much smaller than the radius of the CO_2 plume, the maximum extent of the CO_2 plume occurs at $\beta = 0$:

$$r_{max} = \sqrt{\frac{\lambda_c Q_{well} t}{\pi h \varphi \lambda_w (1 - S_{wc})}} \qquad (106)$$

With the residual water saturation in the invaded area, S_{wc}, set to zero, equation 106 is the same as that presented by Nordbotten et al [2]. As concluded by Nordbotten et al [2], this equation is a reasonably accurate estimate of the maximum extent of plume spread under conditions where buoyancy caused by the density difference between CO_2 and brine is relatively small in relation to viscous and pressure forces.

References

1.   Saripalli, P. and P. McGrail, *Semi-analytical approaches to modeling deep well injection of CO_2 for geological sequestration.* Energy Conversion & Management, 2002. **43**: p. 185-198.
2.   Nordbotten, J.N., M.A. Celia, and S. Bachu, *Injection and Storage of CO_2 in Deep Saline Aquifers: Analytical Solution for CO_2 Plume Evolution During Injection.* Transport in Porous Media, 2005. **58**: p. 339-360.
3.   Dake, L.P., *Fundamentals of reservoir engineering.* 1 ed. 1978: Elsevier.
4.   Woods, E.G. and A.G. Comer, *Saturation Distribution and Injection Pressure for a Radial Gas-Storage Reservoir.* Journal of Petroleum Technology, 1962(December): p. 1389-1393.

CO$_2$ Price Conversion Table

Table 44.   Conversions between CO$_2$ price metrics used in this thesis

$/mscf	$/tonne CO$_2$	$/tonne C
$0.50	$9.45	$34.63
$0.53	$10.00	$36.64
$1.00	$18.90	$69.27
$1.50	$28.35	$103.90
$2.00	$37.81	$138.54
$2.50	$47.26	$173.17
$3.00	$56.71	$207.81
$3.50	$66.16	$242.44
$4.00	$75.61	$277.08
$4.50	$85.06	$311.71
$5.00	$94.52	$346.35
$5.29	$100.00	$366.44